

Mathematical methods for the study of electrochemical systems

Lisa Stephens

A thesis submitted to McGill University
in partial fulfillment of the requirements for the degree of
Doctor of Philosophy

Department of Chemistry, McGill University

Montreal, Quebec, Canada

August 2019

© Lisa Stephens, 2019. All rights reserved.

“It’s still magic even if you know how it’s done.”
—Terry Pratchett, *A Hat Full of Sky*

Abstract

Science is iterative. We build on the foundations of scientists who came before us to lay the groundwork for those that will come after us. We develop theories, schematics, and equations to model interesting systems from the subatomic to celestial scales, and then refine them until our predictions match reality. For all the unanswered questions we have, there are a lot of things we have figured out. This thesis is based on that premise: a few fundamental equations describe a broad scope of electrochemical systems, and we can use these to build mathematical models that help us understand and optimize materials, sensors, and techniques.

Steel rusts. One of the biggest design challenges facing infrastructure projects is corrosion, the set of surface oxidation processes that eat away at the material slowly over time. In investigating the corrosion properties of new materials, there is a disconnect between the short-term experiments of a lab scale and the long-term use these materials will be subjected to. The usual strategy for bridging this gap is to accelerate corrosion through harsh solutions or high potentials, but an alternative is developing models to predict the state of the material days, months, or years in the future. This conserves not only materials but the non-renewable resource often overlooked: time.

Macro stems from micro. The visible surface evolution we see is the result of invisible processes. This is true for corroding surfaces, battery materials, and biological systems. We need sensors on the same scale to understand material behaviour; however, as with the materials they are being used to test, electrode response depends on size. Microelectrodes

exhibit a different response time, diffusion profile, and reactivity to their larger counterparts. Measurements made using them must be interpreted in the context of the probe geometry used for correct interpretation of the information they provide. This can be done through the use of generalizable models that can be used by experimentalists and theoreticians alike.

Every system has a limit. For electrochemical systems this is often surface stability, noisy collection environments, and instrumental precision and accuracy. If we understand the origins of these limitations and model their effect, we can correct for them – fix blurry images, design more precise instruments, and obtain better data. Where neighbouring fields have grappled with the same challenge, we can learn from their approaches and adapt the algorithms they use to treat electrochemical images.

Résumé

La science est itérative. Nous bâtissons sur les fondements des scientifiques qui nous ont précédés pour façonner les bases de ceux qui nous suivront. Nous développons des théories, des schémas et des équations pour modéliser des systèmes intéressants des échelles subatomique à astronomique, puis nous les raffinons jusqu'à ce que nos prédictions correspondent à la réalité. L'assortiment de nos questions sans réponse s'appuie sur des concepts déjà résolus. Cette thèse est basée sur cette prémisse: quelques équations fondamentales décrivent un large éventail de systèmes électrochimiques et nous pouvons les utiliser pour construire des modèles mathématiques qui nous aident à comprendre et à optimiser les matériaux, capteurs et techniques.

L'acier rouille. L'un des plus grands défis de conception auxquels sont confrontés les projets d'infrastructure est la corrosion, l'ensemble des processus d'oxydation de surface qui rongent lentement le matériau. En étudiant les propriétés de corrosion de nouveaux matériaux, il existe un décalage entre les expériences à court terme à échelle d'un laboratoire et l'utilisation à long terme de ces matériaux. La stratégie habituelle pour combler cet écart consiste à accélérer la corrosion grâce à des solutions rigoureuses ou à des potentiels élevés. Une autre solution consiste à mettre au point des modèles permettant de prédire l'état sur des jours, des mois ou des années. Cela préserve non seulement les matériaux, mais une ressource non renouvelable souvent négligée: le temps.

L'échelle macrométrique provient de l'échelle micrométrique. L'évolution de la surface visible que nous voyons est le résultat de processus invisibles. Ceci est vrai pour les surfaces

corrodées, les matériaux de batterie et les systèmes biologiques. Nous avons besoin de capteurs à la même échelle pour comprendre le comportement de ces matériaux. Cependant, comme pour les matériaux sur lesquels ils sont testés, la réponse des électrodes dépend de leur taille. Les microélectrodes présentent un temps de réponse, un profil de diffusion et une réactivité différents de ceux de leurs homologues de plus grandes dimensions. Les mesures effectuées doivent donc être interprétées dans le contexte de la géométrie de la sonde utilisée pour une interprétation correcte des informations fournies. Cela peut être fait en employant des modèles généralisables qui peuvent être utilisés aussi bien par les expérimentateurs que par les théoriciens.

Chaque système a une limite. Pour les systèmes électrochimiques, il s'agit souvent de la stabilité de surface, des environnements de collecte bruyants et de la précision instrumentale. Si nous comprenons les origines de ces limitations et modélisons leurs effets, nous pouvons les corriger: correction des images floues, conception d'instruments plus précis et ainsi l'obtention de meilleures données. Là où des domaines connexes ont été confrontés au même défi, nous pouvons tirer des leçons de leurs approches et adapter les algorithmes qu'ils utilisent pour traiter les images électrochimiques.

Acknowledgments

Finishing a PhD is a little like running a marathon, with one significant difference: it isn't an individual race. It takes a village. There are a lot of people who have cheered from the sidelines or passed out water or tagged in for a leg, more names than I have space for. There are a few people I want to mention here, but if you played a role in getting me to this point, no matter how large, thank you.

I want to start by thanking my family. My parents, Doug and Heather, taught me kindness, curiosity, and strength. I am incredibly proud to be your daughter. You have always supported whatever I wanted to do, even when I have had no idea what I wanted to do (in other words, most of the time). My sister, Marianne. Whether it is cooking or politics or Zelda, midnight or noon, you have always been there for me. It's a stroke of luck that you're the older sibling, because it means I've had a best friend from day one.

I've been in school for a long time at this point, and had some pretty wonderful teachers along the way. My high school chemistry and math teachers Mr. Chatten, Mr. Quinlan, and Ms. Bevan gave me the foundation I needed for everything that came after. My Queen's chemistry family, Derek Esau, James Fan, Timothy Hutama, Zac Mah, and Robert Teuma-Castelletti, kept the passion alive through the slog of undergrad. Meaghan Sherban, a formal teacher in her own right at this point, but someone who has taught me things not covered in any curriculum over twenty years of friendship.

Thank you to all members of the Mauzeroll Group past, present, and honorary who have made my graduate school experience a great one. For the past four years I have been an

undercover computational chemist in an experimental lab, and picked up an incalculable amount of things from all of you by osmosis. Samuel Perry, I couldn't have asked for a better mentor in my first two years. I loved that you were equally willing to talk COMSOL simulations or Marvel comics. Samantha Perry, you have the biggest heart of anyone I know. Thank you for welcoming me into your life with such open arms. Samantha Gateman, through the ups and downs of grad school, you've been a copilot on this wild ride.

To the unfortunate souls that have had to share an office with me, thank you for creating an environment where I could laugh and learn. Jeremy Dawkins, your relentlessly positive attitude has done absolute wonders for my motivation. Thank you for introducing me to microelectronics, convincing me to switch from MATLAB to Python, and being just as much of a technology nerd as I am. Sebastian Skaanvik, we've had many, many discussions in the office over the past few years. I admire your dedication to both scientific rigour and the origins of a song at ukelele club. William Odette, you are equally as passionate about philosophy as are you are about chemistry. Thanks for sharing some of that with me. Siba Moussa, your innate curiosity reminds me everything there is to love about science when projects get hard and results seem inexplicable. I couldn't have asked for better labmates over the years than Anielli Pasqualetti, David Polcari, Karlie Potts, Malak Dayeh, Mohammadreza Ghavidel, Tomer Noyhouzer, Waldemir Paschoalino Jr., Yani Pan, and Yuanjiao Li.

To the upstairs office, apologies for the distractions I managed to bring to you. Nicholas Payne, who shares my passion for programming, graphic design, and Nintendo. You have shared your time, your ideas, and your knowledge with me. You are a great scientist but an even better friend. Isabelle Beaulieu, you're the glue that keeps us together. Whether it

is a Tuesday movie or grocery shopping or celebratory drinks, thank you for always being there for me. Andrew Danis, thank you for always being willing to follow the math. Captain America doesn't come from Brooklyn, he comes from Vermont.

Finally, I'd like to thank my supervisor, Janine Mauzeroll. For four years now I have been turning up in your office full of caffeine and research plans on tangents that had nothing to do with what I was supposed to be working on, and you have always, always been encouraging. From you I have learned how to manage not just a research project but people. Thank you for your guidance and support, both academically and personally.

Contents

Preface	i
Abstract	i
Résumé	iii
Acknowledgments	v
List of Figures	xiv
List of Tables	xvii
List of Equations	xix
List of Abbreviations	xxi
List of Symbols	xxiii
Author Contributions	xxvi
 Thesis Outline	 1
 1 Introduction	 3
1.1 Principles of Electrochemistry	5
1.1.1 From Chemistry to Electrochemistry	5
1.1.2 Mass Transfer: the Nernst-Planck Equation	6
1.1.3 Thermodynamics of Reaction: the Nernst Equation	8
1.1.4 Kinetics of Reaction: the Butler-Volmer Equation	10
1.1.5 Non-Faradaic Processes: Double Layer Capacitance	13
1.2 Mathematical Methods	14
1.2.1 Numerical Modelling	18
1.2.1.1 Symmetry Simplifications	19
1.2.1.2 Numerical Methods	20
1.2.1.3 Solving the System	21
1.2.1.4 Initial Values, Parameters, and Boundary Conditions	26

1.2.1.5	Mesh Optimization	27
1.2.1.6	Steady State Solutions	28
1.2.2	Approximation Equations	29
1.2.3	Software and Algorithms	31
1.2.4	Motivation: From Measurement to Interpretation	32
1.3	Techniques	32
1.3.1	Scanning Electrochemical Microscopy (SECM)	33
1.3.1.1	Modes of SECM	35
1.3.1.2	Mathematical Methods	37
1.3.1.2.1	Numerical Models.	37
1.3.1.2.2	Approximation Equations.	38
1.3.1.2.3	Software and Algorithms.	39
1.3.2	Potentiodynamic Polarization (PDP)	41
1.3.2.1	Corrosion Mechanisms	42
1.3.2.2	Mathematical Methods	43
1.3.2.2.1	Numerical Models.	43
1.3.2.2.2	Approximation Equations.	44
1.3.2.2.3	Software and Algorithms.	45
1.4	Summary	46
2	Development of a Model for Experimental Data Treatment of Diffusion and Activation Limited Polarization Curves for Magnesium and Steel Alloys	55
2.1	Introduction	57
2.2	Experimental	59
2.2.1	Materials	59
2.2.2	Instrumentation	60
2.2.3	Data Collection and Procedure for Tafel Fits	60
2.3	Results and Discussion	61
2.3.1	Factors Influencing Choice of Model Geometry	61
2.3.2	Decoupling Activation and Diffusion-Controlled Contributions to Current	64
2.3.2.1	Extraction of Initial Model Inputs E_{corr} , j_{corr} , β_a , β_c	64

2.3.2.2	Optimization of Kinetic and Corrosion Parameters	66
2.3.3	Evaluation of Statistical Metrics for Goodness of Fit	70
2.3.4	Analysing Diffusion-Limited Current Densities in Terms of Solution Mass Transport	75
2.4	Conclusions	82
3	Altered Spatial Resolution of Scanning Electrochemical Microscopy In- duced by Multifunctional Dual Barrel Microelectrodes	87
3.1	Introduction	90
3.2	Experimental Section	92
3.2.1	Finite Element Simulations	92
3.2.2	Hardware and Solver Parameters	96
3.2.3	Data Analysis	96
3.3	Results and Discussion	97
3.3.1	Effect of Tip-Substrate Distance	97
3.3.2	Effect of Feature Size	100
3.3.3	Effect of Electrolyte Composition	102
3.3.4	Effect of Feature Shape	104
3.4	Additional Considerations	108
3.5	Conclusions	109
4	Evaluating the Use of Edge Detection in Extracting Feature Size From Scanning Electrochemical Microscopy Images	115
4.1	Introduction	118
4.2	Experimental	120
4.2.1	Substrate Fabrication	120
4.2.2	Cell Culture	121
4.2.3	Electrochemical Experiments	121
4.2.4	Instrumentation	122
4.2.5	Finite Element Simulations	122
4.2.6	Data Analysis	122
4.3	Results and Discussion	123
4.3.1	Substrates Displaying Positive Feedback	123
4.3.2	Substrates Displaying Negative Feedback	127

4.3.3	Substrates Displaying Non-Ideal Behavior	132
4.4	Conclusions	134
5	Flux: New Software for Analysing SECM Data	139
5.1	Introduction	141
5.2	Implementation	143
5.3	Approach Curves	143
5.3.1	Normalization	144
5.3.2	Calibrating Tip-Substrate Distance	146
5.3.3	Fitting R_g , κ	147
5.4	Images	148
5.4.1	Slope Correction	149
5.4.2	Edge Detection	151
5.5	Voltammetry	151
5.5.1	Cyclic Voltammetry	151
5.5.1.1	Formal Potential	151
5.5.2	Chronoamperograms	152
5.5.2.1	Response Time	152
5.6	Conclusions	154
6	Conclusions	157
6.1	Summary and Future Work	158
6.2	Final Thoughts	166
	Appendices	171
A	Supporting Information for Chapter 1	173
A.1	Introduction	174
A.2	Code Outline	174
A.3	Usage Notes	175
A.4	MATLAB Script	175
B	Supporting Information for Chapter 2	183
B.1	Mathematical Description of Model Physics	184
B.1.1	3D Model: Incorporating Effects of Overpotential	184

B.1.2	2D Model: Incorporating Effects of Overpotential and Concentration Gradients	188
B.1.3	Parameters	192
B.1.4	Mesh Density	193
B.2	Additional Results	195
B.2.1	Variation in Transport Numbers with Time	195
B.2.2	Effects of Scan Rate and Range	196
B.3	Calculation of Goodness of Fit Statistics	196
C	Supporting Information for Chapter 3	201
C.1	Detailed Description of Model	202
C.2	Validation of Linear Interpolation	206
C.3	Validation of Mesh and Solver Tolerance	207
D	Supporting Information for Chapter 4	211
D.1	Electrochemical Setup	212
D.2	Finite Element Model	213
D.3	Enlarged Second Derivatives	215
D.4	Atomic Force Microscopy	216
D.5	Asymmetrical Reactive Features	217
D.6	Accuracy and Feature Size	218
D.7	Effect of Groove Spacing	219
D.8	Scanning Ion Conductance Microscopy	220
D.9	Effect of Mediator Concentration	222
E	Supporting Information for Chapter 5	225
E.1	Overview	226
E.1.1	Introduction	226
E.1.2	Class Structure	227
E.1.3	Setting Up the User Interface	228
E.2	Importing Files	231
E.2.1	HEKA / .asc	232
E.2.2	HEKA / .mat	233
E.2.3	Biologic / .txt	235

E.2.4	CH Instruments / .txt	237
E.2.5	Sensolytics / .dat	239
E.3	Analysing the Data	241
E.3.1	Normalization	241
E.3.2	Tip-Substrate Distance Calibration	242
E.3.3	Fitting R_g , κ	242
E.3.4	Slope Correction	244
E.3.5	Edge Detection	244
E.3.6	Formal Potential	246
E.3.7	Response Time	247

List of Figures

1.1	Homogeneous versus heterogeneous reactions.	6
1.2	Fermi levels of the electrode at various applied potentials.	9
1.3	Potential energy diagram for the reduction of ferricyanide.	11
1.4	Electrical double layer and charging currents.	13
1.5	Mathematical model for the reduction of ferricyanide.	15
1.6	Meshing a model geometry.	18
1.7	Evolution of potential, concentration, and current over discrete model time steps.	26
1.8	Comparison of three different meshes applied to the same system.	28
1.9	Schematic of an SECM approach curve.	30
1.10	Equation vs. software based methods for performing a linear regression. . . .	31
1.11	Schematic of a SECM instrument.	34
1.12	Modes of SECM.	36
1.13	General shape of an approach curve for the three feedback cases.	39
1.14	Schematic of a PDP experiment.	41
1.15	Overview of various corrosion mechanisms.	42
2.1	Model geometry depicted in 2D-axisymmetric (A) and 3D (B) space.	63
2.2	Experimental and simulated polarization curves.	69
2.3	Weighted and unweighted comparison statistics for a polarization curve performed on pure Mg.	72
2.4	Simulated concentration profiles during a polarization curve performed on pure Mg.	78
2.5	Simulated concentration profiles during a polarization curve performed on SS444.	81

3.1	Schematic of the feedback and redox competition processes possible for a dual-barrel probe.	93
3.2	Effect of tip-substrate distance on the shape distortion.	99
3.3	Effect of feature size on the shape distortion.	101
3.4	Effect of electrolyte composition on the shape distortion.	103
3.5	Effect of feature shape on the shape distortion.	107
3.6	Reduced shape distortion under optimal experimental conditions.	110
4.1	Edge detection on a model substrate with constant topography and variable reactivity.	125
4.2	Edge detection on an experimental substrate with constant topography and variable reactivity.	128
4.3	Edge detection on a model substrate with constant reactivity and variable topography.	130
4.4	Edge detection on an experimental substrate with constant reactivity and variable topography.	131
4.5	Edge detection on a group of HEK cells.	133
5.1	Flux interface for processing approach curves.	145
5.2	Flux interface for processing images.	150
5.3	Voltammetric data processed in Flux.	153
6.1	Schematic of SICM and SECCM.	165
A.1	Script output for the default set of parameters.	180
A.2	Script output for $k_0 = 5$ m/s and all other parameters having default settings.	181
A.3	Script output for $k_0 = 5$ m/s, $npts.t = 5000$, and all other parameters having default settings.	181
B.1	Geometry and mesh used for all 3D and 2D-axisymmetric geometries.	194
B.2	Variation in simulated transport numbers with time.	195
B.3	Effect of scan rate on the simulated concentration profiles.	196
C.1	Sampling grid used to construct maps.	202
C.2	Simulation geometry and boundary conditions.	204
C.3	Meshing parameters for 3D model.	204

C.4	Effect of electrode orientation.	205
C.5	Residuals analysis of linear interpolation method.	206
C.6	Validation of 3D model using approach curves.	208
D.1	Schematic of the integrated electrochemical/optical microscope.	212
D.2	3D simulation geometry and mesh.	214
D.3	Enlarged plot of the second derivatives.	215
D.4	AFM data of the Au/SiO ₂ interface.	216
D.5	Edge detection on SECM images of asymmetrical reactive features.	217
D.6	Accuracy study of edge detection for various size features.	218
D.7	Effectiveness of edge detection for topographical grooves.	219
D.8	SICM data for the Si/SU-8 substrate.	221
D.9	Effect of mediator concentration.	222

List of Tables

1	List of abbreviations.	xxi
2	List of Latin symbols.	xxiii
3	List of Greek symbols.	xxv
1.1	Comparison of analytical and numerical solutions to a system of model equations.	17
1.2	Dimensionality of model geometries and their corresponding coordinate systems.	19
1.3	Comparison of numerical modelling methods.	20
1.4	Overview of the approximation equations developed for feedback mode.	39
2.1	Simulation-optimized Tafel parameters for the four alloys tested.	68
2.2	Comparison summary statistics for the goodness of fit statistics examined: residuals, % difference, and chi-squared.	73
2.3	Summary of the Tafel parameters obtained for pure Mg at different scan rates.	74
3.1	Recommended experimental parameters for reduced shape distortion	110
B.1	Model parameters held constant during Tafel optimization.	192
B.2	Bulk concentrations and diffusion coefficient of aqueous species in solution.	193
D.1	Pipette pulling parameters.	220
E.1	Python packages used in Flux.	226
E.2	Tkinter/Python widgets used in building the Flux graphical user interface.	229

List of Equations

1.1	Nernst-Planck equation	7
1.2	Fick's first law of diffusion	7
1.3	Gibbs free energy of reaction	8
1.4	Standard potential and Gibbs free energy of reaction	9
1.5	Nernst equation	10
1.6	Arrhenius equation	11
1.7	Butler-Volmer equation	12
1.14	Discretization of potential and rate constant for a LSV	22
1.20	Discretization of concentration change due to chemical reaction	23
1.22	Calculation of current for the discretized system	24
1.26	Discretization of concentration change due to diffusion	24
1.27	Equivalence of discretized and continuous variables for small interval size	27
1.32	Randles-Sevcik equation	29
1.34	Theoretical steady state current for a disk microelectrode.	35
1.35	Tafel equation	45
1.36	Calculation of Tafel slope from transfer coefficient	45
2.1	Contributions to current density	64
2.3	Current distribution within the electrolyte.	64
2.7	Overpotential experienced by the working electrode	65
2.9	Revised Tafel equation incorporating mass transport limited current density	66
2.13	Net flux of species accounting for chemical reaction and mass transport	76
4.1	Average time for a species to diffuse a given distance	124
5.2	Beta factor describing back diffusion to a disk microelectrode	146
5.3	Approximation equation for negative feedback at a disk microelectrode	147

5.4	Approximation equation for positive feedback at a disk microelectrode	148
5.6	Approximation equation for mixed feedback at a disk microelectrode	148

List of Abbreviations

Table 1 – List of abbreviations used throughout the thesis.

Abbreviation	Full Name
1D	One dimensional
2D	Two dimensional
3D	Three dimensional
AFM	Atomic force microscopy
AR	Aspect ratio
BEM	Boundary element method
CE	Counter electrode
CV	Cyclic voltammogram
DC	Direct current
DMEM	Dulbecco's modified Eagle medium
FcMeOH	(Hydroxymethyl)ferrocene (also known as ferrocenemethanol)
FDM	Finite difference method
FEM	Finite element method
FVM	Finite volume method
HEK	Human embryonic kidney cells
HEPES	(4-(2-hydroxyethyl)-1-piperazineethanesulfonic acid)
HOMO	Highest occupied molecular orbital
IUPAC	International Union of Pure and Applied Chemistry
LOG	Laplacian of Gaussian
LSV	Linear sweep voltammetry
LUMO	Lowest unoccupied molecular orbital
NDE	Negative difference effect
OCP	Open circuit potential

Table 1 – Continued from previous page.

Abbreviation	Full Name
PBS	Phosphate-buffered saline
PDE	Partial differential equation
PDP	Potentiodynamic polarization
PSF	Point spread function
RAM	Random access memory
RE	Reference electrode
SCE	Saturated calomel electrode
SDM	Scanning droplet methods
SECCM	Scanning electrochemical cell microscopy
SECM	Scanning electrochemical microscopy
SEM	Scanning electron microscopy
SG-TC	Substrate generation - tip collection
SICM	Scanning ion conductance microscopy
SIM	Structured illumination microscopy
SMCM	Scanning micropipette contact method
SPM	Scanning probe microscopy
SSD	Solid state drive
WE	Working electrode

List of Symbols

Table 2 – List of Latin symbols.

Symbol	SI Units	Meaning
a	m	Electroactive radius (microelectrode)
A	m ²	Electroactive area
b	m	Electroactive radius (substrate feature)
c_i	mol m ⁻³	Concentration of species i
c_{dl}	F m ⁻²	Double layer capacitance
d	m	Tip-substrate distance for a microelectrode
D_i	m ² s ⁻¹	Diffusion coefficient of species i
E	V	Potential (boundary)
f_R	-	Fraction of electroactive species in form R
F	C m ⁻¹	Faraday's constant
G	J mol ⁻¹	Gibbs free energy
h	-	Number of total data points
i	A	Current
i_{ss}	A	Steady-state current at a microelectrode
j	A m ⁻²	Current density
J	mol m ⁻² s ⁻¹	Boundary flux
k	m s ⁻¹	Heterogeneous rate constant
K	-	Equilibrium constant
L	-	Normalized tip-substrate distance (d/a)
M_i	g mol ⁻¹	Molar mass of species i
n	-	Number of electrons
\vec{n}	-	Normal vector
N_i	mol m ⁻³ s ⁻¹	Mass transport flux of species i

Table 2 – Continued from previous page.

Symbol	SI Units	Meaning
Ni_T	-	Normalized current (i/i_{ss})
Q	C	Charge
r	-	Residual (statistics)
r_{glass}	m	Glass radius of microelectrode
s_v	m^{-1}	Active specific surface area (surface area/volume)
R	$\text{J mol}^{-1} \text{ C}^{-1}$	Gas constant
R_g	-	Normalized glass radius of microelectrode (r_{glass}/a)
R_i	$\text{mol m}^{-3} \text{ s}^{-1}$	Net flux of species i
s	m	Height of topographical substrate feature
t	s	Time
T	K	Temperature
u_i	$\text{m}^2 \text{ s}^{-1} \text{ V}^{-1}$	Ionic mobility
\vec{v}	m s^{-1}	Normal velocity
v	-	Stoichiometric coefficient
W	-	Pre-exponential factor (Arrhenius)
x_{pos}	m	X-position of microelectrode
y_{pos}	m	Y-position of microelectrode
z_i	-	Charge of species i

Table 3 – List of Greek symbols.

Symbol	SI Units	Meaning
α	-	Transfer coefficient
β	V	Tafel slope
$\beta(R_g)$	-	Back-diffusion to a microelectrode
χ^2	-	Chi-squared goodness of fit statistic
δ	-	Normalized height of substrate topographical feature (s/a)
ϵ	-	Volume fraction
η	V	Overpotential
κ	-	Normalized heterogeneous rate constant (ka/D)
γ_i	-	Activity coefficient
ν	V s ⁻¹	Scan rate
ϕ	V	Potential (domain)
ρ_i	g m ³	Density of species i
σ	S m ⁻¹	Conductivity
u_i	m ² s ⁻¹ V ⁻¹	Ionic mobility

Contributions

All of the work in this thesis was performed under the supervision of Professor Janine Mauzeroll. She provided guidance on all projects and corrections on all manuscripts.

Chapter 1

Author Contributions: This chapter was written by Lisa Stephens (LS).

Contributions to Original Knowledge: This chapter provides an introduction to the processes involved in an electrochemical system from the perspective of a mathematical modeller. A generalizable procedure for translating a conceptual understanding to a system of equations and three methods of using these equations to extract quantitative information are presented.

Publication Information: Portions of the text have been reproduced from:

Stephens, L.I.; Mauzeroll, J. Demystifying Mathematical Modelling of Electrochemical Systems. *Journal of Chemical Education* **2019**, 96(10), 2217-2224.

Chapter 2

Author Contributions: LS designed and tested the model presented in this chapter, and performed all experimental validation unless otherwise noted. Dr. Samuel Perry (SP) provided guidance throughout the project and helped correct the manuscript. Samantha Gatmean (SG) performed the experiments on stainless steel 444 and contributed to the writing in the section discussing this material. Dr. Robert Lacasse (RL) and Dr. Robert Schulz (RS) provided useful feedback on the manuscript. This work was part of a collaboration with HydroQuebec.

Contributions to Original Knowledge: The model presented in this chapter improves upon the procedure of traditional Tafel fitting by incorporating an additional parameter that describes the effect of mass transport limitations. This extends the quantitative ability of a technique commonly used to test novel materials for their corrosion properties.

Publication Information: The text in this chapter is reproduced from:
Stephens, L.I.; Perry, S.C.; Gateman, S.M.; Lacasse, R.; Schulz, R.; Mauzeroll, J. Development of a Model for Experimental Data Treatment of Diffusion and Activation Limited Polarization Curves for Magnesium and Steel Alloys. *Journal of the Electrochemical Society* **2017**, 164(11), E3576-E3582.

Chapter 3

Author Contributions: LS designed and tested the model presented in this work. All writing and manuscript correction was performed by LS.

Contributions to Original Knowledge: The model presented in this chapter provides the first extensive theoretical treatment of a dual barrel multifunctional microelectrode. The effect of controllable experimental variables on the final image produced is used to provide recommendations for future experimental work.

Publication Information: The text in this chapter is reproduced from:
Stephens, L.I.; Mauzeroll, J. Altered Spatial Resolution of Scanning Electrochemical Microscopy Induced by Multifunctional Dual Barrel Microelectrodes. *Analytical Chemistry* **2018**, 90(11), 6796-6803.

Chapter 4

Author Contributions: LS developed the idea and procedure for treating SECM images using edge detection algorithms, designed and tested the model, and wrote the manuscript. NP assisted with the experiments on the Au/Si substrate. Sebastian Skaanvik (SS) cultured the HEK cells and assisted with their SECM imaging. David Polcari (DP) and Matthias Geissler (MG) fabricated the Si and Au/Si substrates respectively. All of the above provided substantial feedback on the written manuscript.

Contributions to Original Knowledge: This chapter presents the first use of edge detection algorithms applied to an electrochemical imaging technique. A connection is made between the image formation procedure and theoretical basis of edge detection.

Publication Information: The text in this chapter is reproduced from: Stephens, L.I.; Payne, N.A.; Skaanvik, S.A.; Polcari, D.; Geissler, M.; Mauzeroll, J. Evaluating the Use of Edge Detection in Extracting Feature Size from Scanning Electrochemical Microscopy Images. *Analytical Chemistry* **2019**, 91(3), 2312-2318.

Chapter 5

Author Contributions: LS programmed the software described in this chapter. The data used to test it was contributed by a combination of the author, NP, SS, and instrument manufacturers.

Contributions to Original Knowledge: This chapter presents the first open source software specialized to SECM data analysis. Existing data treatment procedures are incorporated into a graphical user interface to simplify the process of extracting quantitative

information from the measured current.

Publication Information: The text in this chapter is reproduced from:

Stephens, L.I.; Mauzeroll, J. Flux: New Software for Analysing SECM Data. *Journal of the Electrochemical Society* **2019**, 166(16), H861-H865.

Thesis Outline

The main objective of this thesis was to develop mathematical techniques for studying electrochemical systems from materials and theoretical perspectives. The models, equations, and software described in the remaining chapters were developed to predict the long-term behaviour of novel materials, interpret the results of imaging techniques with minimal prior theoretical treatment, and standardize data treatment methodologies.

Chapter 1 presents an introduction to the mathematical methods and electrochemical characterization techniques used in the body of the thesis. In particular, the theory and equations behind numerical modelling, approximation equations, and software as they have been applied to the techniques of scanning electrochemical microscopy (SECM) and potentiodynamic polarization (PDP) are introduced.

Chapter 2 focuses on PDP, a macroscale characterization technique that is used to study a material's bulk corrosion properties. The shape of these curves depends strongly on the local corrosion mechanism of the metallic surface. Inconsistencies in the literature procedures for treating this data quantitatively have given rise to a need for data analysis methods which can be systematically employed.

Chapter 3 introduces multifunctional microelectrodes, a new class of probe recently developed to extend the imaging capabilities of SECM, an electrochemical scanning probe technique. These probes allow SECM to be performed in tandem with dedicated topography techniques to resolve the topography-reactivity convolution of traditional SECM, or for the

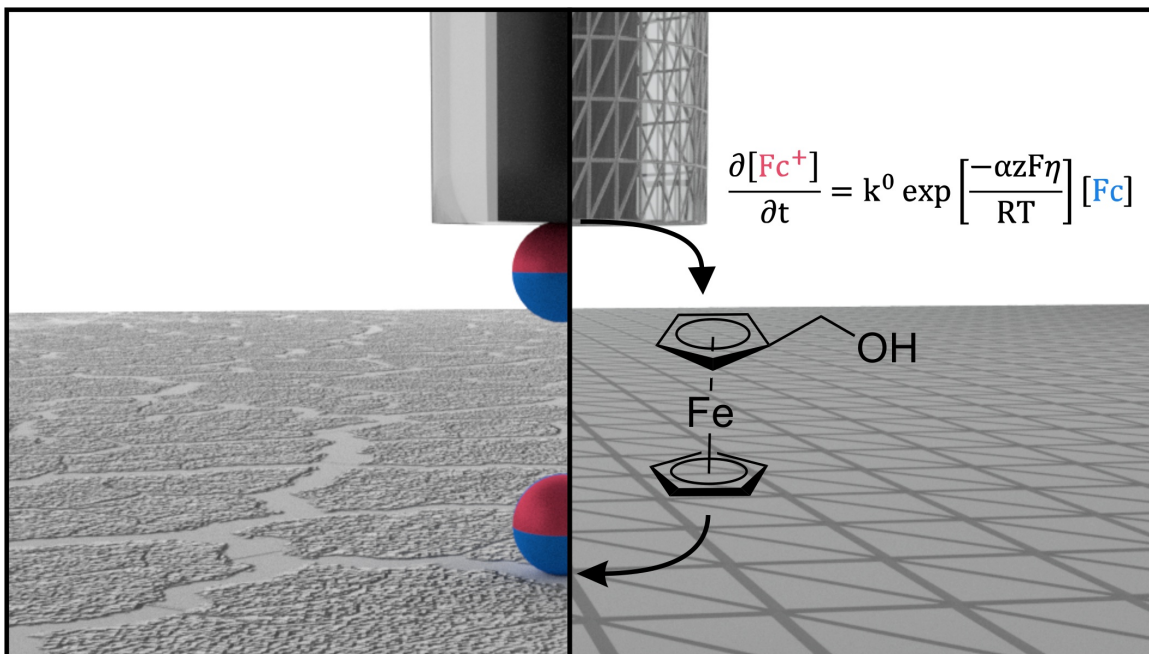
monitoring of two signals at separate potentials for enhanced chemical selectivity. The model predicts that the asymmetric shape of these probes can produce distortions in the images they generate under select conditions, and outlines the optimal experimental conditions to minimize these distortions.

Chapter 4 proposes a strategy for improving the resolution of SECM images based on image processing algorithms. Traditionally, some degree of blurring is unavoidable in an SECM image due to the non-contact detection strategy; this blurring makes the location of local features hard to determine precisely. An integrated experiment/modelling approach is used to demonstrate that edge detection algorithms can recover the true feature shape with high precision, provided there is strong contrast in the original SECM image.

Chapter 5 integrates the SECM theory and data treatment methodologies introduced in previous chapters into an open-source Python-based software called Flux. This software supports normalization, non-linear curve fitting, and performance metric extraction of both simulation and experimental data sets.

Chapter 1

Introduction



Chapter Preface

This chapter will introduce the concepts, equations, and existing literature surrounding the mathematical methods used in the body of the thesis. It is split into three sections which can be read independently.

The first section will introduce the theory behind electrochemical processes in terms of their relationships to traditional chemical concepts of thermodynamics and kinetics as well as the fundamental equations that link these concepts to experimentally measurable quantities. The second section will introduce the mathematical methods used in this work and how they can be used to treat electrochemical systems involving multiple processes. These are numerical modelling, approximation equations, and software/algorithm development. The third section will introduce the electrochemical techniques used in this thesis, with a focus on how they have been treated mathematically in the current literature.

Portions of the work presented in this chapter have been adapted from:

Stephens, L.I.; Mauzeroll, J. Demystifying Mathematical Modelling of Electrochemical Systems. *Journal of Chemical Education* **2019**, 96(10), 2217-2224.

1.1 Principles of Electrochemistry

Electrochemistry is the transfer of electrons across interfaces resulting in an electrochemical potential change. The involvement of the interface makes this process a heterogeneous reaction, in contrast to single-phase homogeneous reactions. The change in electrochemical potential may result in a chemical reaction that can modify surfaces, catalyse transformations, or generate light. This section will introduce the major concepts involved in an electrochemical reaction.

1.1.1 From Chemistry to Electrochemistry

In a homogeneous reaction, one or more reactants undergo a chemical change, causing a rearrangement in the electronic configuration of the reactants (Figure 1.1 A). In a heterogeneous reaction, an electrode serves as one of these reactants, allowing electrons to be added or removed to the system at the electrode/electrolyte interface through an external circuit (Figure 1.1 B). Though this modifies the local charge, both electronic and ionic charge are conserved over the entire system. Electronic charge is conserved by means of a second electrode in the circuit that performs the opposite reaction (in the example given, an oxidation would occur at the electrode not pictured). Ionic charge is conserved by means of mass transfer of ions in the electrolyte.

In both homogeneous and heterogeneous reactions, two requirements are present for the reaction to proceed spontaneously: (1) the reactants must be close enough for an electron transfer to occur; (2) the reactants must have sufficient energy to react. If both requirements

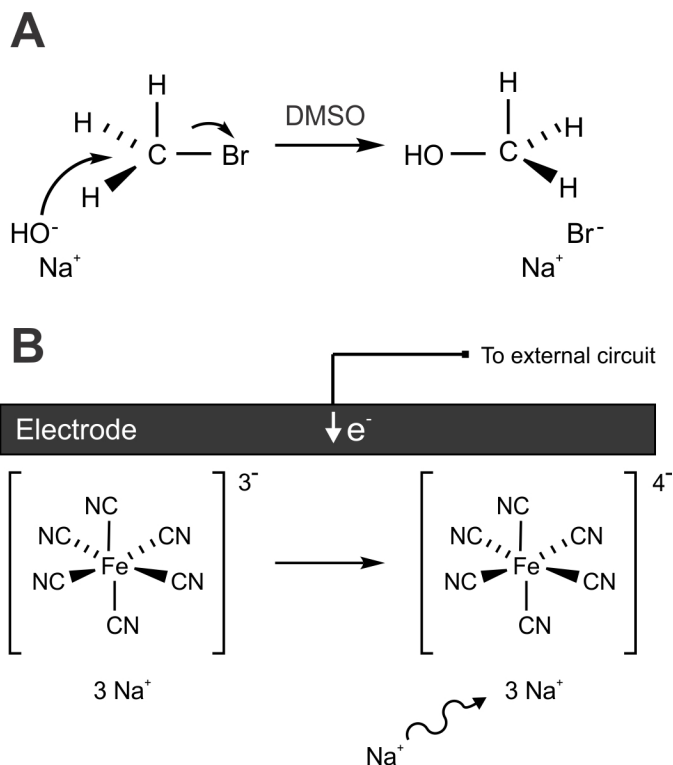


Figure 1.1 – (A) An example of a homogeneous reaction: an S_N2 reaction between bromomethane and hydroxide. (B) An example of a typical heterogeneous reaction: the reduction of $\text{Fe}(\text{CN})_6^{3-}$ to form $\text{Fe}(\text{CN})_6^{4-}$. Only the half-cell reaction has been shown for comparison.

are met, the reaction proceeds and the movement of electrons through the circuit generates an electrical current.

1.1.2 Mass Transfer: the Nernst-Planck Equation

The first requirement for reaction is that the reactants are close enough for an electron transfer to occur. This requires mass transfer of the reactants to the electrode surface, which takes place according to the Nernst-Planck equation. In 1D, this is:¹

$$J_j(x) = -D_j \frac{\partial c_j}{\partial x} - \frac{z_j F D_j c_j}{RT} \frac{\partial \phi(x)}{\partial x} + c_j v(x) \quad (1.1)$$

Where $J_j(x)$ is the mass transfer flux, D_j the diffusion coefficient, c_j the concentration, and z_j the charge of species j . x refers to the distance from the electrode surface, with $x = 0$ being the electrode/electrolyte interface. F is Faraday's constant, R the universal gas constant, T the temperature, ϕ the electric potential, and v the solution velocity. The first term corresponds to a diffusional process, where mass transfer is proportional to a concentration gradient. The second term corresponds to a migrational process, where mass transfer is proportional to an electric potential gradient. The third term corresponds to a convection process, where mass transfer is proportional to solution velocity.

This is the most general form of the mass transfer equation commonly used, but it can be simplified in several ways depending on the experimental setup. In the absence of external stirring, the solution velocity is approximately zero and convection is negligible. In the presence of a large relative electrolyte concentration, the electric potential gradient in solution is approximately zero and migration is negligible. If both of these conditions are met, the Nernst-Planck equation simplifies to Fick's first law of diffusion:¹

$$J_j(x) = -D_j \frac{\partial c_j}{\partial x} \quad (1.2)$$

As a consequence of this equation, whenever species are consumed at the electrode surface

as a result of an electrochemical reaction, a concentration gradient develops near the electrode surface and diffusion of the reactant to the electrode surface occurs.

1.1.3 Thermodynamics of Reaction: the Nernst Equation

The second requirement for reaction is that the reactants must have sufficient energy to react. This can be controlled by altering the potential applied to the electrode; this in turn alters the Fermi levels of the electrons in the electrode, and favours oxidation or reduction accordingly (Figure 1.2).¹ If the electrode is polarized at the equilibrium potential of a redox couple, then the energy level of the electrons in the electrode falls in between the lowest unoccupied molecular orbital (LUMO) and highest occupied molecular orbital (HOMO) of the analyte and no net reaction occurs. If polarized more negative than the equilibrium potential, the energy level of the electrons in the electrode increases and donation of an electron from electrode to analyte (reduction) is favoured. Conversely, if polarized more positive than the equilibrium potential, the energy level of the electrons in the electrode decreases and donation of an electron from analyte to electrode (oxidation) is favoured.

The position of this equilibrium potential is dependent on the Gibbs free energy of the reactant and product species. For the reaction $A + e^- \rightarrow B$ where A is the oxidized and B the reduced species, the Gibbs free energy of reaction is given by:

$$\Delta G = G_B - G_A - G_{e^-} \quad (1.3)$$

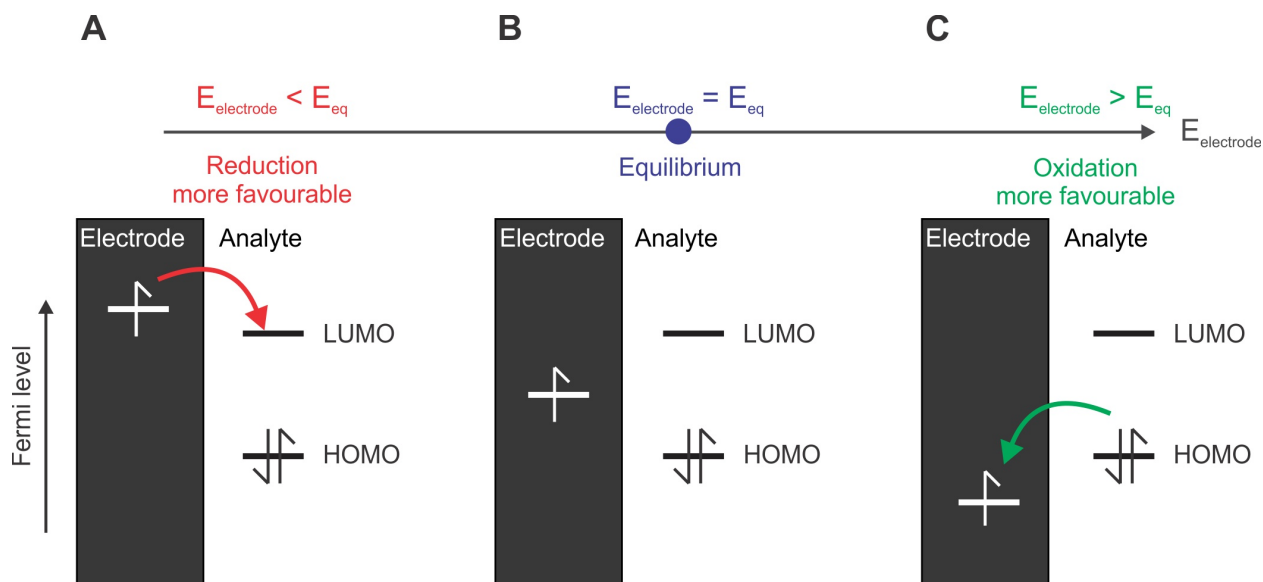


Figure 1.2 – Schematic of the Fermi level of the electrode as a function of applied potential giving rise to an (A) reduction, (B) equilibrium, or (C) oxidation of a species in the analyte.

This is in turn related to the standard potential of reaction according to:¹

$$\Delta G^0 = -nFE_{\text{rxn}}^0 \quad (1.4)$$

Where ΔG^0 is the Gibbs free energy under standard conditions, n is the number of electrons transferred during the reaction, and E_{rxn}^0 is the standard potential of reaction.

In the majority of cases, an electrochemical reaction does not take place under standard conditions. The relationship between the standard potential and equilibrium potential exhibited by the system is described by the Nernst equation:¹

$$E_{\text{eq}} = E_{\text{rxn}}^0 - \frac{RT}{nF} \ln \frac{\gamma_B c_B}{\gamma_A c_A} \quad (1.5)$$

Where E_{eq} is the equilibrium potential and γ_i is the activity coefficient of species i .

In this way, altering either the electrode potential or the concentration ratio of the oxidized and reduced species controls whether the reaction is energetically favourable. If this condition is met, how quickly the reaction will occur is in turn determined by the kinetics of reaction.

1.1.4 Kinetics of Reaction: the Butler-Volmer Equation

The energy profile of a chemical reaction is typically depicted in the form of a potential energy diagram (Figure 1.3), which looks at the energy of the system as a function of the critical reaction coordinate during a particular chemical reaction. For a reaction to occur, the reactants must pass through a high-energy atomic configuration before forming the lower energy products. This high-energy configuration might be called either a transition state or activated complex, depending on the nuance of the theory used; here, the phrase transition state will be used.

The energy difference between the reactants and products is referred to as the total energy of reaction (ΔG_{rxn}), and is related to the thermodynamics of reaction as discussed in 1.1.3. The energy difference between the reactants and transition state is referred to as the activation energy (ΔG^\ddagger), and is related to the kinetics of reaction.

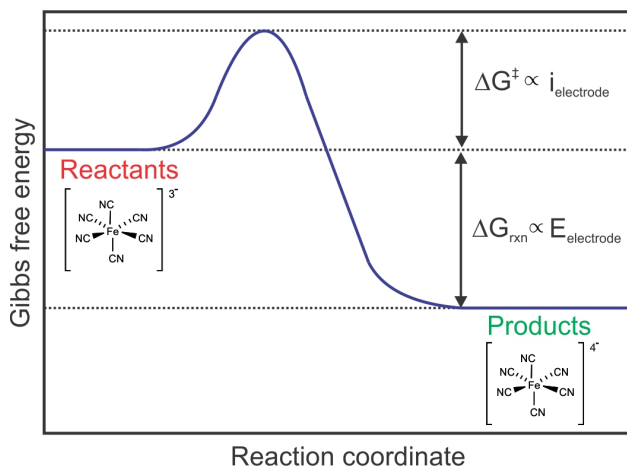


Figure 1.3 – Potential energy diagram of the reduction of ferricyanide, showing the mapping between quantities expressed in terms of Gibbs free energy and their electrochemical counterparts.

The Arrhenius equation links the rate constant to the activation energy as follows:¹

$$k = W e^{-\Delta G^\ddagger / RT} \quad (1.6)$$

Where k is the rate constant of reaction and W is a pre-exponential factor.

When this reaction occurs and an electron is transferred across the electrode/electrolyte interface, a current may be measured, and so it is convenient to think about the rate of reaction in terms of the current rather than an absolute rate. To do this, the rate constant must be converted to a rate by accounting for the concentration and stoichiometry of reaction, and all quantities must be converted to their electrochemical forms. This is done through the Butler-Volmer equation, which links the kinetics and thermodynamics of an electrochemical

reaction together as follows:¹

$$i = F A k [C_O(0, t) e^{-\alpha \eta F / RT} - C_R(0, t) e^{(1-\alpha) \eta F / RT}] \quad (1.7)$$

Where i is the current, A the electrode area, $C_j(0, t)$ the concentration of species j at the electrode surface, α the transfer coefficient, and η the overpotential. t refers to time, with $t = 0$ being the initial condition of the system. The overpotential is $\eta = E_{\text{app}} - E_{\text{eq}}$, where E_{app} is the applied potential. This can be thought of as the potential required for a reaction to progress at a certain rate.

The Butler-Volmer equation unifies the rate of both oxidation and reduction reaction; if these are treated separately, it can be rewritten as follows:

$$i = F A k_0 \exp\left[\frac{-\alpha \eta F}{RT}\right] C_O(0, t) - F A k_0 \exp\left[\frac{(1-\alpha) \eta F}{RT}\right] C_R(0, t) \quad (1.8)$$

$$i = k_{\text{red}} C_O(0, t) - k_{\text{ox}} C_R(0, t) \quad (1.9)$$

As a consequence of Equations 1.7-1.9, as the electrode potential increases, the activation energy of reaction decreases, and the reaction begins to occur more quickly. This results in a larger current being measured.

In combination with mass transport, these two fundamental relationships of potential/thermodynamics and current/ kinetics can be used to design and optimize any electrochemical system. The nature of this optimization depends on the characteristics of the system. In

the field of corrosion, the ideal material will be stable as fabricated and therefore resistant to oxidation: this corresponds to a high equilibrium potential and low reaction current. In the field of electrocatalysis, the ideal material will generate a large amount of product for minimal energy input: this corresponds to a low overpotential and high reaction current. One of the methods of interpreting electrochemical data in terms of these fundamental equations is the use of mathematical methods.²⁻⁹

1.1.5 Non-Faradaic Processes: Double Layer Capacitance

Up to now the discussion of electrochemical systems has focused on processes resulting in an oxidation or reduction reaction at the electrode/electrolyte interface, which are collectively known as Faradaic processes. However, contributions from other effects can also generate a measurable current; these are known as non-Faradaic processes.

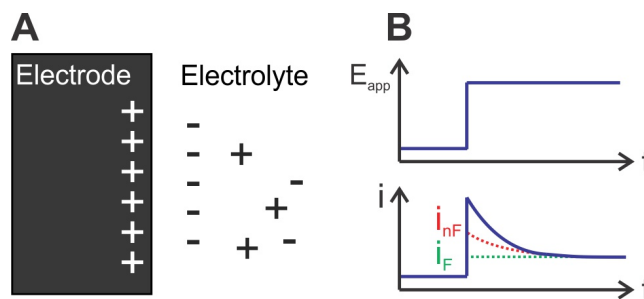


Figure 1.4 – (A) Schematic of the organization of ions in the double layer. (B) Contribution of non-Faradaic and Faradaic processes to the total current in a potential step experiment.

When a potential is applied to the electrode surface, a net charge develops on the surface of the electrode (Figure 1.4 A). In the adjacent electrolyte, oppositely charged ions arrange themselves in a compact layer to balance this charge. This in turn creates a layer of charge

in solution that is balanced by the formation of a second layer of diffuse charge. Collectively this organization of ions in the electrolyte is known as the double layer and it acts as a capacitor, storing charge. When the potential at the electrode surface is changed, the ions in the double layer rearrange accordingly, generating a charging current according to:¹

$$i_{\text{nF}} = \frac{E_{\text{app}}}{R_s} e^{-t/R_s C_{\text{dl}}} \quad (1.10)$$

Where i_{nF} is the non-Faradaic (charging) current, E_{app} is the applied potential, R_s is the solution resistance, and C_{dl} is the double layer capacitance. The total current measured at any potential is the sum of both Faradaic and non-Faradaic contributions ([Figure 1.4 B](#)). The larger the concentration of electrolyte, the smaller the solution resistance and the smaller the non-Faradaic contribution, but its effects are always present to some degree. This contribution can be corrected for through blank subtraction (collecting a voltammogram with no analyte present) or curve fitting (linear regression to a region of the voltammogram where no Faradaic response is present to estimate the potential - charging current relationship).

1.2 Mathematical Methods

The previous section introduced the individual processes that take place in an electrochemical system and their mathematical descriptions. Many of these equations are coupled to one another through a shared variable such as the diffusion coefficient or local concentration, and so analysing an electrochemical system in its entirety requires treating them as a complete set through the construction of a mathematical model.

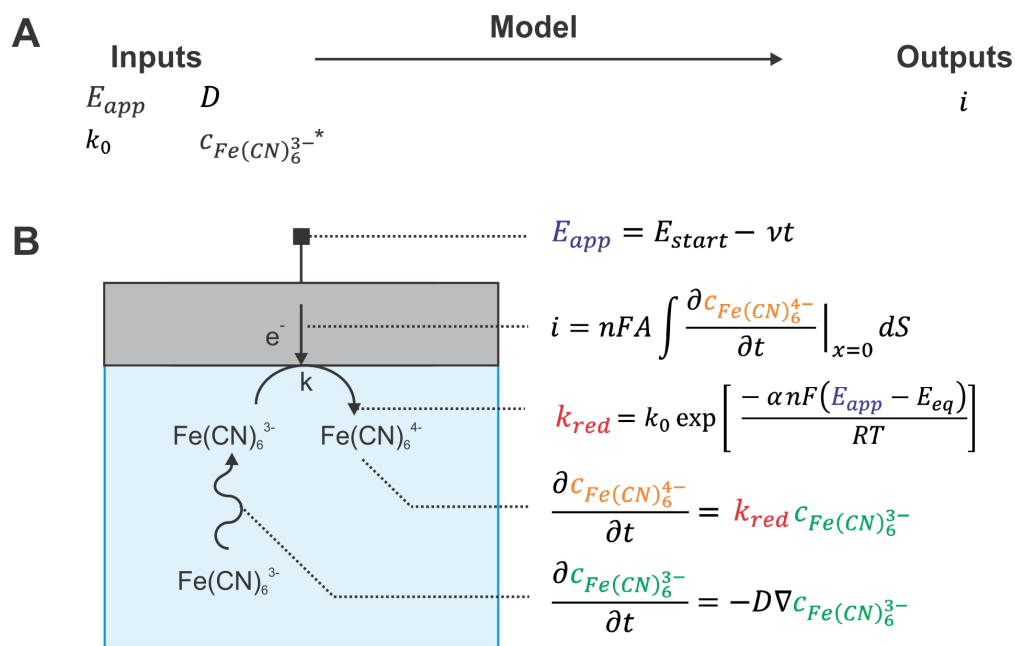


Figure 1.5 – Model for the reduction of $Fe(CN)_6^{3-}$ during a linear sweep voltammogram. (A) Mapping of input experimental parameters to output model result. (B) Schematic and model equations.

When this model is solved, inputs corresponding to the initial experimental conditions will be converted to outputs containing the desired unknown. This may be a measurable variable such as the current, or a non-measurable variable such as the concentration at a specific point in solution.

A model for the reduction of ferricyanide during a linear sweep voltammogram (LSV) is given in Figure 1.5. This includes several coupled processes; though many of these occur simultaneously, for the purposes of explanation they can be expressed in chronological order as follows:

- The applied potential at the working electrode is decreased as a function of time.

- As the applied potential decreases, the rate constant for reduction increases.
- As the rate constant increases, $\text{Fe}(\text{CN})_6^{3-}$ is reduced to form $\text{Fe}(\text{CN})_6^{4-}$.
- When reduction takes place, an electron is transferred from the external circuit and a current is measured.
- As $\text{Fe}(\text{CN})_6^{3-}$ is depleted in the vicinity of the electrode, more $\text{Fe}(\text{CN})_6^{3-}$ diffuses in.

There are two basic approaches to solving this system of equations ([Table 1.1](#)). In an analytical approach, these equations are solved precisely to yield a new set of equations describing the output at any point in space or time. In a numerical approach, these equations are solved approximately to yield a set of values for the output at predefined points in space or time. Though an analytical approach provides the best accuracy, it is computationally challenging and not always possible using current calculus techniques. Using a numerical approach reduces the need for simplifying assumptions, and so allows more complex systems to be modelled. Examples of standard modelling assumptions include the following:

- Symmetry. Equations are simplified to the minimum viable dimensionality. (See [1.2.1.1](#) for more details.)
- Uniformity. Vector-based properties of the system such as the diffusion coefficient and porosity are assumed to be isotropic. Variations in nanoscale properties such as surface roughness are assumed to be negligible and a constant value is used.
- Simplicity. Species that do not participate in a Faradaic reaction at the electrode are

excluded from the model. Double layer effects and the associated charging current can be treated as negligible.

Table 1.1 – Comparison of analytical and numerical solutions to a system of model equations.

	Analytical	Numerical
Accuracy	Exact	Approximate
Output	Equation	Values
Assumptions required	Many	Few
Difficulty of solution	Challenging	Easier

1.2.1 Numerical Modelling

In a numerical approach, the continuous equations of space and time are discretized. This is done by first building up a model geometry in terms of its constituent spatial components (Figure 1.6 A). A domain encloses a given area or volume, and corresponds to a material with continuous properties (electrolyte, glass, metal, etc.) Domains are connected by boundaries, where interactions between domains can occur (electron transfer, fluid flow, etc.) or boundary conditions can be set (fixed concentrations, zero flux, etc.). These boundaries and domains are then split up into a series of small segments in a process known as meshing (Figure 1.6 B). The nodes where adjacent segments meet define the mesh points where the model variables will be explicitly calculated. We can assign an address to these new boxes in two ways: either according to the value of the model variable (e.g. $x = 5 \mu\text{m}$) or according to an integer index (e.g. $j = 1$).

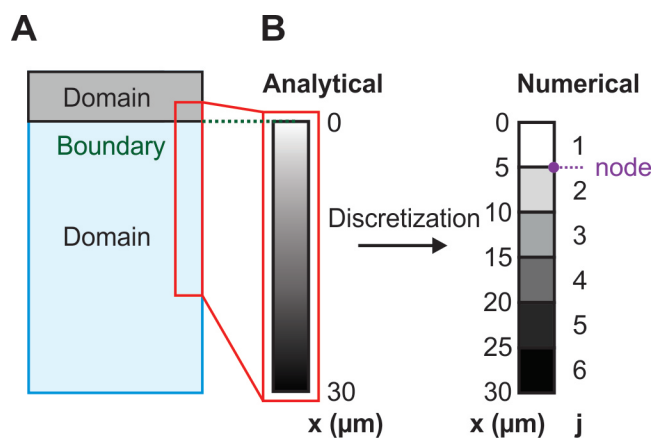
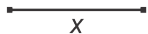
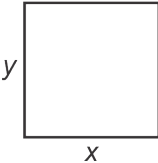
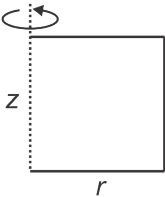
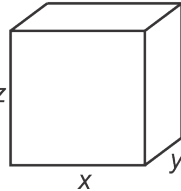


Figure 1.6 – (A) Components of a model geometry (B) Discretization of the electrolyte domain to form a mesh, in preparation for a numerical approach to solving the model equations.

1.2.1.1 Symmetry Simplifications

A 3D model geometry is the most representative of the true experimental system, but the most difficult to solve. To simplify the math involved, we can take advantage of any symmetry present in the system to rewrite the spatial equations in a simpler coordinate system (Table 1.2). If the system possesses a central axis of symmetry, a 2D-axisymmetric geometry can be used. If the system possesses a plane of symmetry, a 1D or 2D geometry can be used.

In the context of electrochemistry, the appropriate coordinate system is often determined by the mass transport profile of the system. Mass transport to a macroelectrode takes place via linear diffusion, and so a 1D or 2D geometry can be used. A microelectrode exhibits radial diffusion, and requires a 2D-axisymmetric geometry at minimum. A 3D geometry can handle even more complex diffusion patterns, but this flexibility comes at a high computational cost. Table 1.2 – Dimensionality of model geometries and their corresponding coordinate systems.

	→ Increasing computational cost			
	1D	2D	2D-axisymmetric	3D
Schematic				
Coordinate system	x	x, y	r, z	x, y, z
Applicable diffusion pattern	Linear	Linear	Linear, radial	All
Examples	2,3	4,5	6,7	8,9

1.2.1.2 Numerical Methods

A variety of numerical methods have been developed including the boundary element method (BEM),¹⁰ finite difference method (FDM),^{1,11} finite element method (FEM),¹² and finite volume method (FVM).¹³ A comparison of these methods can be found in [Table 1.3](#). The main differences between them include which geometry components are meshed, how the equations are expressed, what is calculated at the nodes connecting mesh segments, and restrictions on the compatible systems. In many cases BEM is computationally more efficient than the finite methods, but as the domain is not meshed, variables varying within a domain such as a concentration profile are not accessible. The finite methods are very similar to one another, with slight differences between them; FDM expresses equations in difference rather than integral form, and FVM calculates the flux rather than value of model variables.

Table 1.3 – Comparison of numerical modelling methods.

	Boundary element	Finite difference	Finite element	Finite volume
Meshed components	Boundary	Boundary, domain	Boundary, domain	Boundary, domain
Variable calculated	Value	Value	Value	Flux
Equation form	Integral	Difference	Integral	Integral
Advantages	Low computational cost	Simple equation form	Most robust	Variables are conserved
Disadvantages	Small surface area/volume ratio needed	Requires regular geometry	High computational cost	Requires regular geometry
Electrochemical applications	SECM ¹⁴	SECM ¹	SECM ^{19,20}	Corrosion ²³
	Corrosion ¹⁵	Corrosion ¹⁶	Fuel cells ²¹	Fuel cells ²⁴
		Voltammetry ¹⁷	Batteries ²²	Batteries ²⁵
		Membrane transport ¹⁸		

All of these methods have previously been used in electrochemical modelling, but the

finite element method is currently one of the most popular. This preference is in part due to the rise of user-friendly software packages like COMSOL Multiphysics (commercial)²⁶ and OpenFOAM (open source),²⁷ which have lowered the entry barrier significantly.

1.2.1.3 Solving the System

Putting the meshed geometry together with one of the numerical techniques discussed above, the model equations can then be solved. This section will focus on the finite difference solution for simplicity, but the iterative treatment of the meshed geometry and time steps is similar among all of the numerical methods.

Still using our system of $\text{Fe}(\text{CN})_6^{3-}$ undergoing reduction during a linear sweep voltammogram (Figure 1.5), a numerical value for the current-potential relationship can be calculated.¹ First, the time is discretized into a series of k steps of size Δt . Combining these time steps with our already meshed 1D geometry of j total segments of size Δx , we can rewrite the model equations of Figure 1.5 in their finite difference forms. For conciseness of notation, c_{red} and c_{ox} refer to $c_{\text{Fe}(\text{CN})_6^{4-}}$ and $c_{\text{Fe}(\text{CN})_6^{3-}}$ respectively. The procedure is as follows:

1. For a given time step k , the potential and rate constant are calculated.

$$E_{app}(t) = E_{start} - \nu t \quad (1.11)$$

$$E_{app}(t + \Delta t) = E_{app}(t) - \nu \Delta t \quad (1.12)$$

$$k_{red}(t) = k_0 \exp \left[\frac{-\alpha n F (E_{app} - E_{eq})}{RT} \right] \quad (1.13)$$

$$k_{red}(t + \Delta t) = k_0 \exp \left[\frac{-\alpha n F (E_{app}(t + \Delta t) - E_{eq})}{RT} \right] \quad (1.14)$$

2. The concentrations of c_{ox} and c_{red} in box 1 ($x = 0$) are updated based on an electrochemical reaction occurring at the boundary.

$$\left. \frac{\partial c_{red}}{\partial t} \right|_{x=0} = k_{red} c_{ox} \quad (1.15)$$

$$\frac{c_{red}(0, t + \Delta t) - c_{red}(0, t)}{\Delta t} = k_{red}(t + \Delta t) c_{ox}(0, t) \quad (1.16)$$

$$c_{red}(0, t + \Delta t) = c_{red}(0, t) + \Delta t k_{red}(t + \Delta t) c_{ox}(0, t) \quad (1.17)$$

$$\left. \frac{\partial c_{ox}}{\partial t} \right|_{x=0} = -k_{red} c_{ox} \quad (1.18)$$

$$\frac{c_{ox}(0, t + \Delta t) - c_{ox}(0, t)}{\Delta t} = -k_{red}(t + \Delta t) c_{ox}(0, t) \quad (1.19)$$

$$c_{ox}(0, t + \Delta t) = c_{ox}(0, t) - \Delta t k_{red}(t + \Delta t) c_{ox}(0, t) \quad (1.20)$$

3. The current associated with reaction is calculated. (Note: In its most general form, the current is calculated as the integral over all mesh points at the electrode/electrolyte boundary. In the 1D case, only one point fulfills this criteria.)

$$i = nF \left. \frac{\partial c_{red}}{\partial t} \right|_{x=0} \quad (1.21)$$

$$i(t) = nF \left[\frac{c_{red}(0, t + \Delta t) - c_{red}(0, t)}{\Delta t} \right] \quad (1.22)$$

4. The concentrations of c_{ox} and c_{red} in all boxes are updated based on diffusion. For a given box of position x , the concentration gradient is calculated using the adjacent boxes in positions $x + \Delta x$ and $x - \Delta x$.

$$\frac{\partial c_{ox}(x, t)}{\partial t} = \frac{\partial J(x, t)}{\partial x} \quad (1.23)$$

$$\frac{c_{ox}(x, t + \Delta t) - c_{ox}(x, t)}{\Delta t} = \frac{J(x + \Delta x/2, t) - J(x - \Delta x/2, t)}{\Delta x} \quad (1.24)$$

$$\frac{c_{ox}(x, t + \Delta t) - c_{ox}(x, t)}{\Delta t} = \frac{D}{\Delta x^2} [c_{ox}(x + \Delta x, t) - 2c_{ox}(x, t) + c_{ox}(x - \Delta x, t)] \quad (1.25)$$

$$c_{ox}(x, t + \Delta t) = c_{ox}(x, t) + \frac{D\Delta t}{\Delta x^2} [c_{ox}(x + \Delta x, t) - 2c_{ox}(x, t) + c_{ox}(x - \Delta x, t)] \quad (1.26)$$

This discretization uses a three point central difference approach for space and a two point forward difference approach for time. In general, the former yields the smallest error and the most accurate results.²⁸ However, it requires the calculation of a point before and after the point of interest ($x + \Delta x$, $x - \Delta x$). In space, this is possible to calculate for all points except the domain boundaries, which have a separate boundary condition defined. In time, this is not possible at the value $t = 0$. Here a forward difference approach must be used instead, where only a point after the point of interest and the point itself are used ($t + \Delta t$, t).

Due to the higher error associated with the discretization of time, if Δt is not sufficiently

small the error in the approximation could become progressively worse with time. An alternative to this approach might be to use a Taylor expansion to calculate higher order forward differences.²⁸ This reduces the error associated with forward differencing but is more computationally expensive.

5. A step Δt is taken forward in time. The concentration profiles at the end of step k are taken as the initial conditions for step $k + 1$. The new potential and rate constant are calculated, and Steps 1-3 (Equations 1.11-1.25) are repeated.

A schematic of this potential \rightarrow concentration \rightarrow current relationship is given in [Figure 1.7](#). At $k = 0$, the system starts with a uniform concentration in all boxes. At $k = 1$, the reduction reaction begins to occur, the concentrations of reactant and product change in $j = 1$, and a rise in current is calculated. In this region, the rate of reaction is dominated by the rate constant of reaction and is therefore activation limited. As the reaction progresses for $k \geq 2$, the concentration of reactant is depleted in the vicinity of the electrode and needs to diffuse in from further away in solution for the reaction to progress. At the same time, the product begins to diffuse away. A significant concentration gradient develops near the electrode, affecting the concentration in a greater number of boxes over time. Consequently, the calculated current begins to decrease. In this region, the rate of reaction is dominated by the concentration of reactant and is therefore mass transport limited.

A sample MATLAB implementation of Equations 11-26 is available in [Appendix A](#).

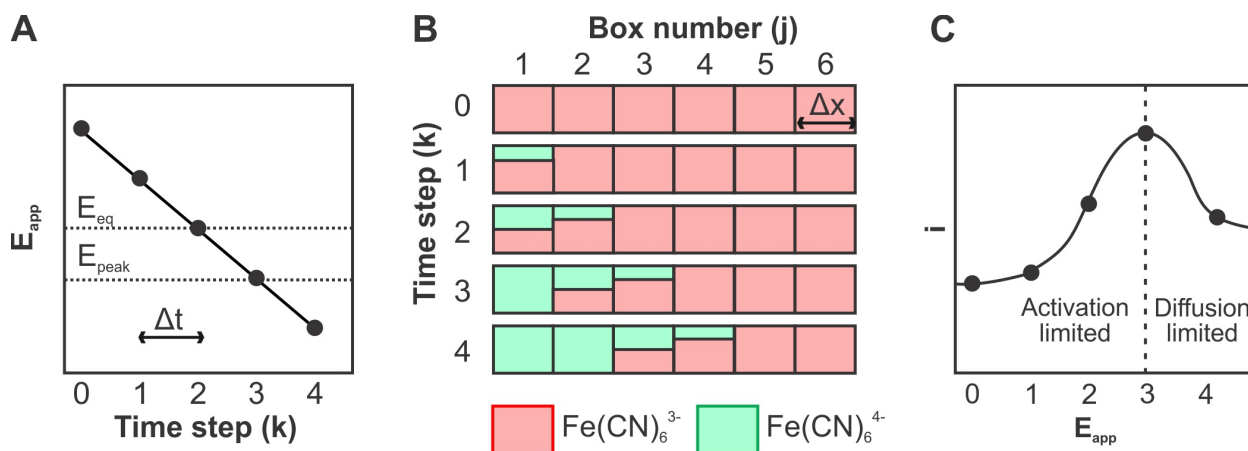


Figure 1.7 – Schematic of a finite difference model. (A) Discretization of time steps. (B) Concentration profile as a function of box number and time step. (C) Output currents.

1.2.1.4 Initial Values, Parameters, and Boundary Conditions

In general, the discretized equations of space and time have an iterative form, where the values of the present step depend on the values of the previous step. This presents a challenge for the initial time point, where no previous step exists.

Numerical models such as these require a set of initial conditions, or specific values of the model variables at $t = 0$ that are allowed to change as time progresses. In the case of our LSV, we assumed that only $Fe(CN)_6^{3-}$ was present initially; expressed as a fraction of the total concentration, this corresponds to initial conditions of $c_{ox}(x, t = 0) = 1$ and $c_{red}(x, t = 0) = 0$.

Our model also contains a set of constants that do not change with space or time, but are still related to the experimental conditions. For example, E_{start} and ν correspond to the initial value of the potential waveform and scan rate of the CV waveform respectively. Examining how a calculated result changes as one of these parameters changes is commonly

referred to as a parametric sweep; for example, this might be done to examine peak current as a function of scan rate.

The last thing that is required for a model is a set of boundary conditions. Similar to the initial conditions, these are a set of rules that define the value of a model variable, but over all time points as opposed to $t = 0$. For example, if we assume our electrolyte domain is sufficiently large, the concentrations in the box furthest from the electrode surface will not be affected by the chemical reaction. Expressed as a fraction of the total concentration, this corresponds to $c_{ox}(x = j, t) = 1$ and $c_{red}(x = j, t) = 0$.

1.2.1.5 Mesh Optimization

In our iterative discretized numerical model, the smaller the values of Δx and Δt , the more accurate the result. This is in line with the traditional transition from a limit to an integral:

$$\lim_{\Delta x \rightarrow 0} \sum_{i=1}^n f(x) \Delta x = \int_a^b f(x) dx \quad (1.27)$$

Our initial model used a uniformly coarse mesh ([Figure 1.8](#)). A simple alternative with greater accuracy might be a uniformly dense mesh; however, this adds significant computational cost. Both of these strategies use a constant value of Δx ; in practice, this is not required by all of the finite methods. A good compromise might therefore be a non-uniform mesh, which is dense close to the electrode surface where a concentration gradient is developing and coarse far from the surface where concentrations are not changing. This approach

strikes a balance between model accuracy and computational cost.

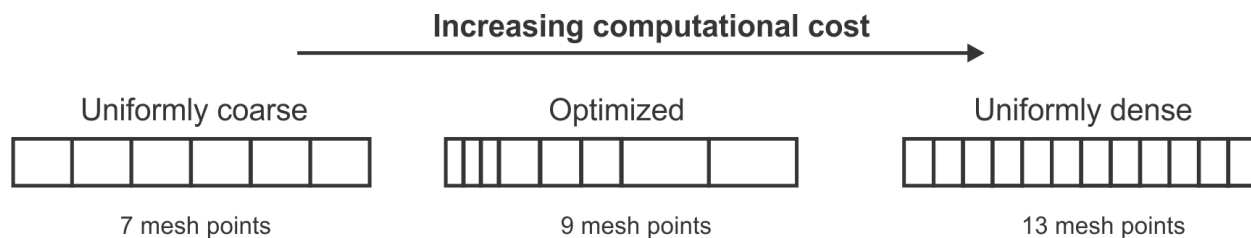


Figure 1.8 – Comparison of three different meshes applied to the same system.

In addition to accuracy, both the mesh and the simulation parameters contribute to solution stability. For the model system described previously to have a stable solution, the following condition must be met:¹

$$\frac{D\Delta t}{\Delta x^2} < 0.5 \quad (1.28)$$

If this is not true, then more than half the species in a given box will be moved to an adjacent box in a given time step, and the solution error will become progressively worse with every time step.

1.2.1.6 Steady State Solutions

The shape of the voltammogram in [Figure 1.7 C](#) is characteristic of a macroelectrode, which experiences linear diffusion. If a microelectrode was used instead, a radial diffusion profile would develop and the currents in the diffusion-limited region would exhibit a steady state value. In this case, the following condition would be true:

$$\frac{\partial c_{ox}(x, t)}{\partial t} = \frac{\partial J(x, t)}{\partial x} = 0 \quad (1.29)$$

One method for calculating the steady state solution is the Newton-Raphson method,²⁹ which estimates the roots of an equation using an iterative derivative calculation.

$$c_{n+1} = c_n - \frac{f(c_n)}{f'(c_n)} \quad (1.30)$$

$$c_{n+1} = c_n - f(c_n) \frac{c_n - c_{n-1}}{f(c_n) - f(c_{n-1})} \quad (1.31)$$

Where n is the iteration number and $f(c)$ is the right hand side of [Equation 1.26](#). This procedure is repeated until the concentration reaches a stable value, meaning that the change in the value between iterations is less than the convergence criterion.

1.2.2 Approximation Equations

Numerical modelling is not the only method of interpreting and predicting results. In many models, a parametric sweep is performed to examine the effect of a model input on a calculated result. When an equation exists that describes this relationship, the model can be compared to theory. In the case of our LSV, the Randles-Sevcik equation describes the relationship between peak current and scan rate:³⁰

$$i_{peak} = 0.4463nFAc_{red} \left(\frac{nF\nu D}{RT} \right)^{\frac{1}{2}} \quad (1.32)$$

In most cases, the effect of a given parameter is not known but is instead the object of the study. In these cases, an arbitrary equation may be fit to the parameter-result relationship to describe the results. The constants in these equations are not directly linked to theory in the same way as equations derived from first principles, but they allow the model to be generalized and used directly by experimentalists. An example of this includes the approximation equation developed for a negative feedback approach curve (Figure 1.9) in scanning electrochemical microscopy:³¹

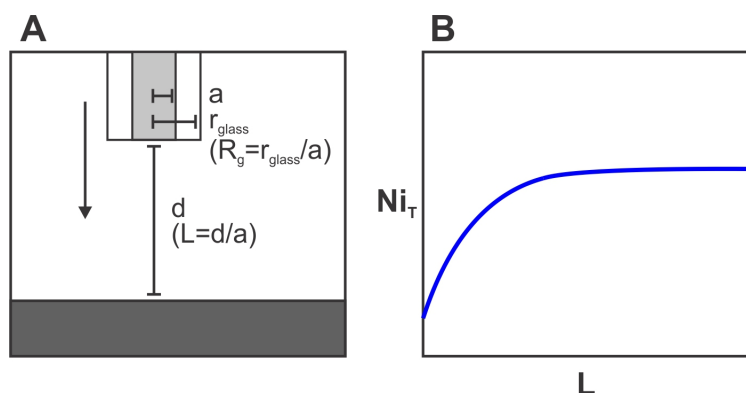


Figure 1.9 – (A) Schematic (B) Normalized current-distance relationship for a negative feedback approach curve in scanning electrochemical microscopy.

$$Ni_T = \frac{\left[\frac{2.08}{R_g^{0.358}} \left(L - \frac{0.145}{R_g} \right) + 1.585 \right]}{\frac{2.08}{R_g^{0.358}} (L + 0.0023R_g) + 1.57 + \frac{\ln R_g}{L} + \frac{2}{\pi R_g} \ln \left(1 + \frac{\pi R_g}{2L} \right)} \quad (1.33)$$

Where Ni_T is the normalized current at a microelectrode, R_g the normalized glass radius, and L the normalized tip-substrate distance. An extended discussion of scanning electrochemical microscopy and approach curves will be given in later sections. Though many of the constants in this equation do not have physical meaning, it is still useful. An experimental

approach curve displaying negative feedback can be fit to extract a geometric parameter of the electrode, R_g .

1.2.3 Software and Algorithms

Once developed and tested, these equations have a fixed form that can be integrated into software code. This isolates the adjustable parameters in the equation and allows existing algorithms to be used to extract them.

An example of this is linear regression (Figure 1.10). A well-defined set of equations determines the best fit slope and intercept for any set of paired x, y points; however, every data analysis software or programming language also has an algorithm which implements these equations and returns only the desired values to the user.

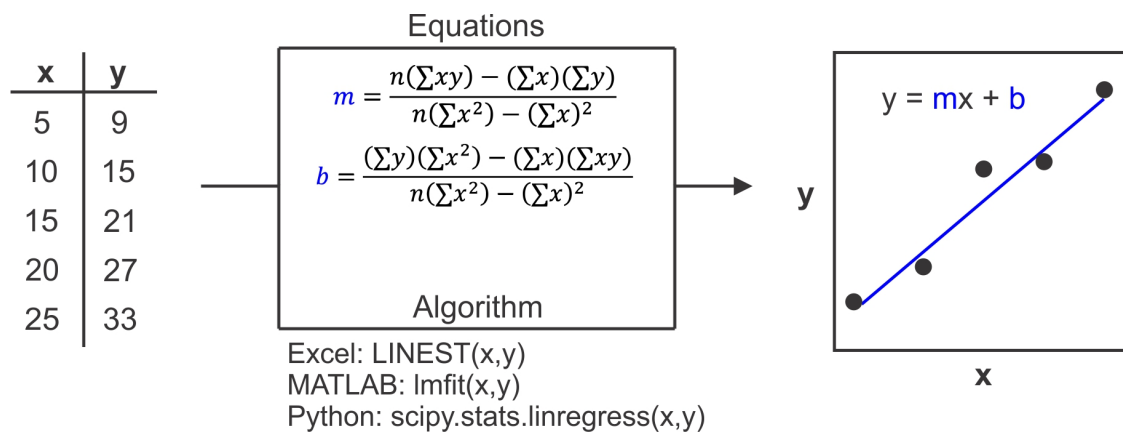


Figure 1.10 – Equation vs. software based methods for performing a linear regression.

In general, an algorithm-based approach makes theory that has already been developed easier to use.

1.2.4 Motivation: From Measurement to Interpretation

The previous sections have introduced the conceptual theory behind individual processes occurring in an electrochemical system and mathematical methods for solving the set of model equations that link these processes together. Putting it all together, there are two essential reasons to use these methods:

1. The interpretation of existing results. Electrochemical measurements are made in terms of potential, current, and resistance; in contrast, the desired unknown is typically along the lines of a kinetic rate constant or local pH. Converting quantities we can measure to quantities we are interested in relies on methods such as these.
2. The prediction of future results. Lab scale measurements take place over short times and small scales, but the desired applications involve long times and large scales. Mathematical modelling allows us to extrapolate current results to predict future behaviour, which conserves limited resources including time, materials, and money.

These three mathematical methods of approximation-based treatment, model-based treatment, and software-based treatment have been used in [Chapter 2](#); [Chapter 3](#), [Chapter 4](#); and [Chapter 5](#) respectively.

1.3 Techniques

Building on the concepts and equations introduced previously, this section will focus on the experimental electrochemical techniques used in the remainder of the thesis. This discussion

will emphasize the specific parameter-result relationships probed by each technique, with a focus on how quantitative information can be extracted from these relationships using various mathematical methods.

1.3.1 Scanning Electrochemical Microscopy (SECM)

Scanning electrochemical microscopy (SECM) is a non-contact scanning probe technique invented independently by two groups in 1986^{32,33} which can be used to measure the local topography and electrochemical activity of surfaces. A number of recent book chapters and literature reviews have discussed the operational principles of the technique^{34–37} as well as its applications in the field of biology,^{38–40} corrosion,^{41–43} and energy.^{44–46}

In SECM, a microelectrode is connected to a positioning system ([Figure 1.11 A](#)) that allows it to be moved relative to the sample of interest, where X and Y movement are parallel to the sample (lateral scan) and Z movement is perpendicular to the sample (approach/retraction). When positioned close to the surface of the sample, the concentration gradient and subsequent mass transfer profile of electroactive species to the surface of the microelectrode is affected by the local properties of the sample surface.

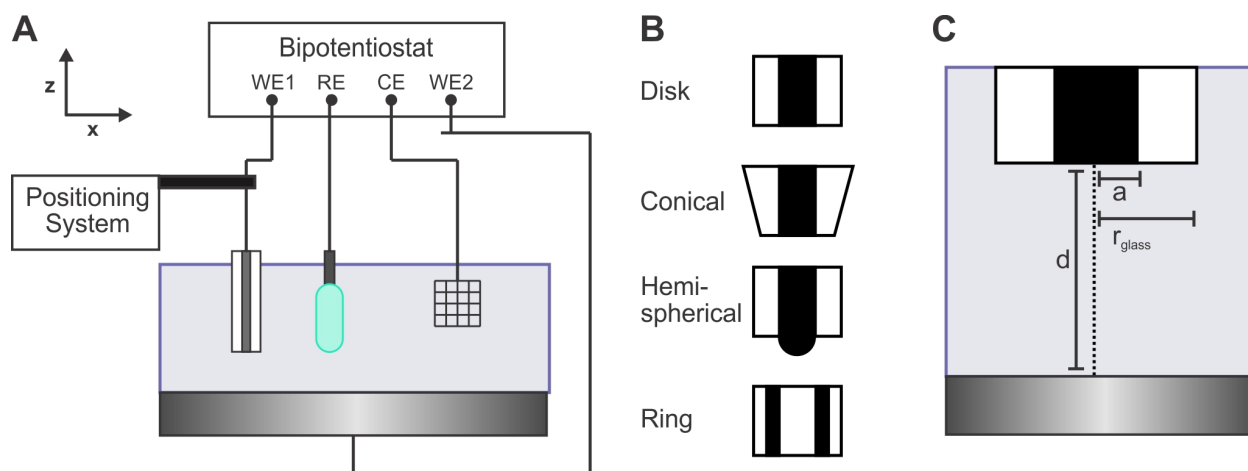


Figure 1.11 – (A) Schematic of a scanning electrochemical microscope. (B) Variations in shape among microelectrode geometries. (C) Critical geometric parameters of a disk microelectrode.

To be classified as a microelectrode, the probe must have a μm^2 electroactive area. A number of probe geometries meeting this definition have been fabricated (Figure 1.11 B). Standard probe geometries include disk,⁴⁷ conical,⁴⁸ hemispherical,⁴⁹ and ring⁵⁰ geometries. In many cases, these forms have been extended to create multifunctional microelectrodes that allow two signals to be measured simultaneously. Probes with two microelectrodes have been fabricated with ring-disk⁵¹ and dual^{52–54}/quad⁹ barrel geometries, and probes that incorporate a microelectrode into a non-electrochemical sensor include modified AFM tips^{55,56} and optical fibres.⁵⁷

For a singular SECM experiment, the most common geometry is the disk microelectrode due to its ease of fabrication⁴⁷ and well-defined behaviour.¹ A conductive material such as Pt wire is encased in an insulating material such as glass, leaving only a circular electroactive area exposed to the electrolyte. When operating under diffusion limited conditions, a radial

or hemispherical diffusion profile to the tip develops. Disk microelectrodes are described by two geometric parameters (Figure 1.11 C): a , the radius of the microelectrode; and R_g , the normalized glass radius (r_{glass}/a). The other critical geometric parameter of the system is the tip-substrate distance d , which may be normalized to the radius as well as $L = d/a$.

The steady state current expected when $d \gg a$ is:⁵⁸

$$i_{ss} = 4nFD_Rc_R^*a\beta(R_g) \quad (1.34)$$

Where n is the number of electrons and $\beta(R_g)$ is a parameter depending on the scaled glass radius, R_g . Often, raw currents are scaled to the steady state value according to $Ni_T = i/i_{ss}$ in order to compare experiments with different probe geometries or mediator concentrations. Within the SECM literature, these are referred to as normalized although the scale after this correction does not have an upper bound of 1; the term normalized will still be used in this thesis to be consistent with the literature.

1.3.1.1 Modes of SECM

SECM can be performed in a number of modes that vary according to which electrochemical quantity is measured (current, potential, or impedance), where the electroactive species being detected is generated, and whether or not the detection reaction is reversible. The three modes used in this thesis are feedback, generation-collection, and redox competition.

Feedback mode⁶ (Figure 1.12 A) is one of the oldest and most popular modes of SECM,

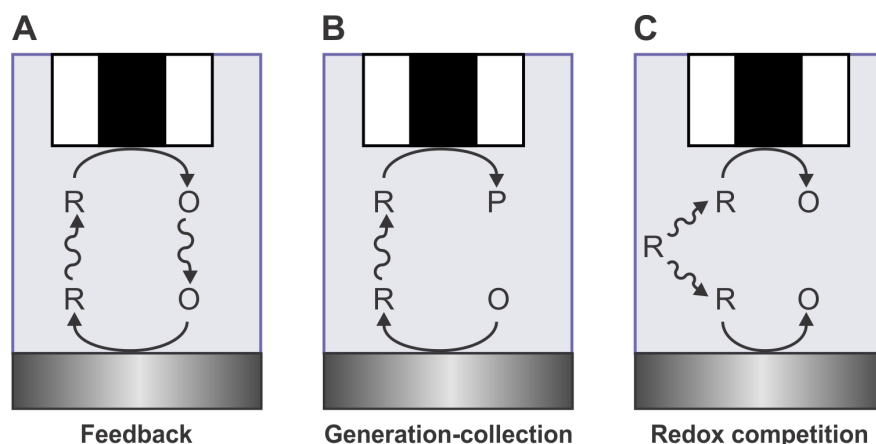


Figure 1.12 – Schematic of the SECM modes used in the thesis. (A) Feedback mode (B) Substrate generation - tip collection mode (C) Redox competition mode.

named for the feedback loops which form between the microelectrode and sample surface. This mode makes use of a redox mediator that can be reversibly oxidized or reduced. The electrode is polarized with a high overpotential for oxidation or reduction of this mediator, such that the rate of reaction is diffusion limited and a steady state state current develops. The microelectrode is then approached to the surface.

If the surface is insulating or nonreactive, diffusion of the mediator to the surface is hindered, and the current decreases. This is known as negative feedback. If the surface is conductive or reactive, the mediator may undergo a second reaction at the surface to regenerate the mediator in its original oxidation state, making it available to react at the microelectrode again, and the current increases. This is known as positive feedback. If the surface falls in between these two cases, supporting a reaction but at a kinetically limited rate, this is known as mixed feedback. This mode is generally used to identify locally reactive features^{59–61} and perform quantitative kinetic studies.^{62–64}

In the two generation-collection modes (Figure 1.12 B) of tip generation - substrate collection⁶⁵ and substrate generation - tip collection,⁷ the redox mediator undergoes an irreversible reaction at one of the surfaces. These modes are generally used for quantifying electrocatalytic activity⁶⁶⁻⁶⁸ and detecting flux from the sample surface.⁶⁹⁻⁷¹

In redox competition mode,⁷² both the microelectrode and sample surface support oxidation or reduction of the redox mediator and so compete for the reactant. This mode is generally used for quantifying electrocatalytic activity⁷³⁻⁷⁵ and monitoring localized corrosion processes.⁷⁶⁻⁷⁸

A number of additional SECM modes beyond these three have been developed including potentiometric,⁷⁹ alternating current,⁸⁰ and shear force,⁸¹ but are not the focus of this thesis.

1.3.1.2 Mathematical Methods

All three of the mathematical methods discussed earlier have been used to analyse SECM experiments, with the goal of these methods being to convert the electrode position - Faradaic current relationship to a quantitative value for the surface height (topography) or rate constant (reactivity).

The majority of these methods have been focused on the feedback mode,³⁵ but a growing body of work has analysed the generation-collection^{7,82} and redox competition⁸³ modes as well.

1.3.1.2.1 Numerical Models. Numerical models have been a part of SECM analysis since the inception of the technique. The initial paper on feedback mode SECM⁶ used a 2D-

axisymmetric model solved using the finite element method to calculate the concentration profile of mediator in solution for different electrode heights during positive and negative feedback measurements. Later models would extend this work to understand the effect of the electrode in terms of its R_g ;^{31,84} the mediator in terms of its diffusion coefficient,⁸⁵ partition coefficient,⁸⁶ and charge transfer kinetics across liquid-liquid interfaces;^{87,88} and the sample surface in terms of its kinetics,⁸⁹ roughness,⁹⁰ and porosity.⁹¹

In addition to analysing these parameter-result relationships in a general sense, modelling has been used to extract the kinetic parameters of specific systems. This is typically done by performing a parametric sweep on a kinetic parameter to simulate a family of curves, followed by comparison of the experimental data to this family of curves to determine the best match.^{61,92–94}

Most of these works have employed 2D-axisymmetric geometries for simplicity, but as more complex probe geometries lacking the required symmetry have been fabricated, a switch to 3D models has been needed. This approach has been used for push-pull probes^{8,95} and multifunctional microelectrodes.^{52,53} Even for axisymmetric disk microelectrodes, the nature of specific surfaces has required the use of a 3D model.⁹⁶

1.3.1.2.2 Approximation Equations. Numerical modelling can be used to investigate the relationship between an electrode, electrolyte, or surface parameter and the measured current; however, this strategy requires all experimental results to be run through the model for quantitative use. This complication has motivated the development of approximation equations (also commonly called analytical approximations; this term will not be used here

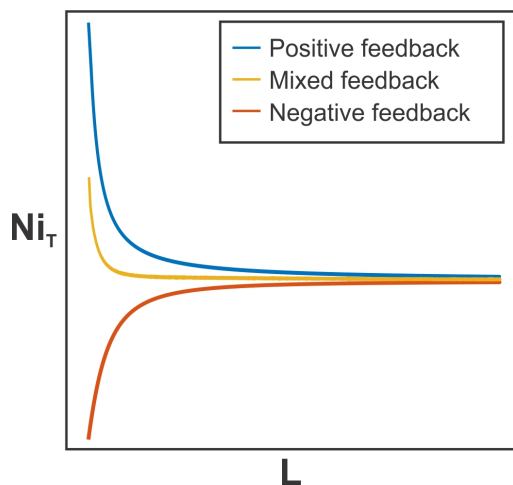


Figure 1.13 – General shape of an approach curve for the three feedback cases.

Table 1.4 – Overview of the approximation equations developed for feedback mode.

Probe Geometry	Mode	References
Disk	Steady state	97,98
	Negative feedback	31
	Positive feedback	99
	Mixed kinetics	20
Conical	Steady state	100
Hemispherical	Steady state	101,102
	Negative feedback	88
	Positive feedback	88

to avoid confusion with an analytical approach to modelling), which summarize model results and allow them to be used directly by experimentalists.

Most of the development effort has focused on developing equations that generalize the current-distance relationship in an approach curve for a particular feedback case (Table 1.4).⁵⁸

The approximation equation describing a negative feedback approach curve for a disk microelectrode is given in Equation 1.33. This expresses the result (normalized current) in terms of two properties (normalized tip-substrate distance and normalized glass radius).

1.3.1.2.3 Software and Algorithms. The approximation equations work well for treating one dimensional data like approach curves, but more complex data treatment procedures are often needed for two dimensional data like images; this is where software and algorithms have been useful.¹⁰³

One of the challenges of feedback mode SECM is separating the contributions of topogra-

phy and reactivity to the measured current. Experimental strategies for resolving this have included changing the setup to use a topography sensitive mode of SECM^{80,81} or combining feedback mode SECM with a dedicated topography technique like AFM^{55,104} or SICM.^{105,106} Alternatively, an algorithm-based strategy has been employed that separates the two contributions by using a negative feedback image to correct a mixed feedback image for topography, thereby generating a new image containing only the kinetic contributions.¹⁰³

Within an individual image, the spatial resolution is primarily determined by the size of the microelectrode, and so efforts to improve the resolution of the technique have focused on the fabrication of smaller probes.^{107,108} Early on, the potential of image processing for improving resolution was also recognized.^{109,110} These methods applied a Laplacian of Gaussian (LOG) filter to the raw SECM image to reduce the effects of diffusional blurring and produce sharper edges. This approach is similar in concept to point spread function (PSF) based deconvolution that has seen widespread usage in super-resolution fluorescence techniques such as structured illumination microscopy (SIM).¹¹¹ A PSF based approach was applied to SECM images four years after the initial image processing papers.⁹⁰ While these filters were able to describe the relationship between the ideal (non-blurred) image and the convoluted observed one, they also contained a set of arbitrary parameters that needed to be optimized for each individual image. These were likely related but were not explicitly connected to the probe geometry and size, making this method hard to generalize. In general this approach did not see widespread usage, likely due to concurrent advances in electrode fabrication and instrumentation achieving the same goal.^{107,108,112} However, this strategy still offers unique benefits including retroactive data treatment.

1.3.2 Potentiodynamic Polarization (PDP)

Poteniodynamic polarization (PDP) is a voltammetric technique used for the characterization of materials, which has been used in the fields of electrocatalysis^{113,114} and corrosion.^{115–117} In this thesis PDP is used for the characterization of corroding materials, and so the discussion in this section will focus primarily on a corrosion interpretation.

In a PDP experiment, the material of interest is incorporated into an electrochemical cell as the working electrode and linearly polarized while monitoring the logarithm of the current (Figure 1.14). For historical reasons, a mix of plotting conventions is used when displaying these curves: both $\log(i)$ vs. V ¹¹⁸ and V vs. $\log(i)$ ¹¹⁹ are regularly used.

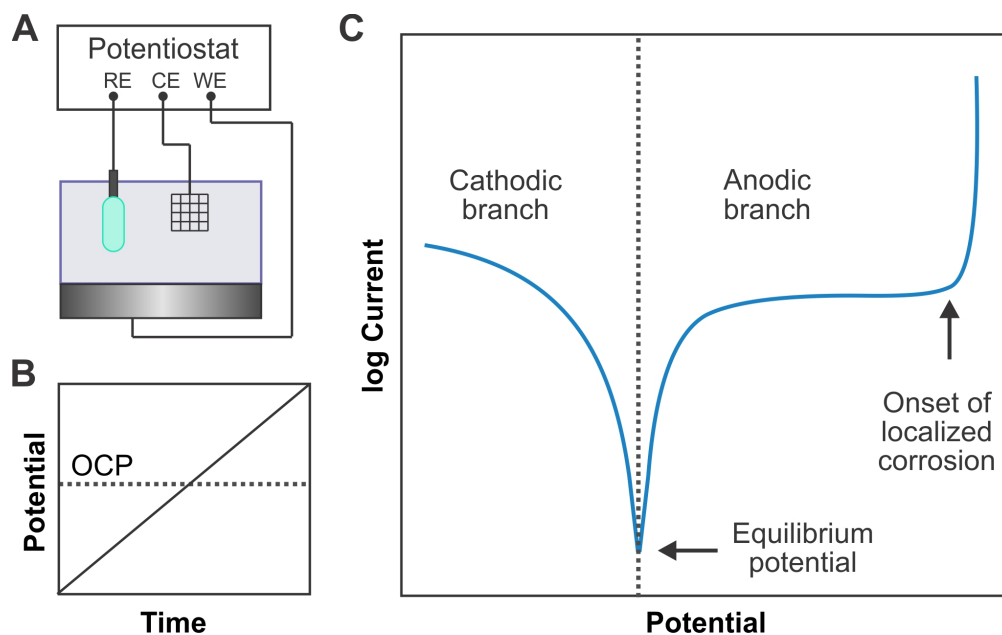


Figure 1.14 – Schematic of a PDP experiment. (A) Electrode configuration of the electrochemical cell. (B) Potential waveform. (C) PDP plot.

The bounds of the potential sweep are chosen relative to the open-circuit potential (OCP)

of the material. Before any changes are made to the surface induced by polarization, this OCP is equal to the equilibrium potential or E_{corr} of the system. Depending on the procedure, the potential will be linearly increased starting from E_{corr} ¹²⁰ or negative to this value.¹¹⁵ In the latter case, the potential waveform will pass through the OCP, testing the material under conditions where a net oxidizing and net reducing reaction is occurring at the surface. Under these conditions, the curve displays a V-shape, and can be split into anodic and cathodic branches.

1.3.2.1 Corrosion Mechanisms

There is a lot of interest in modelling corroding systems for optimizing material design^{3,121} and predicting material behaviour.^{122,123} The scale of these models is dependent on the underlying corrosion mechanism.

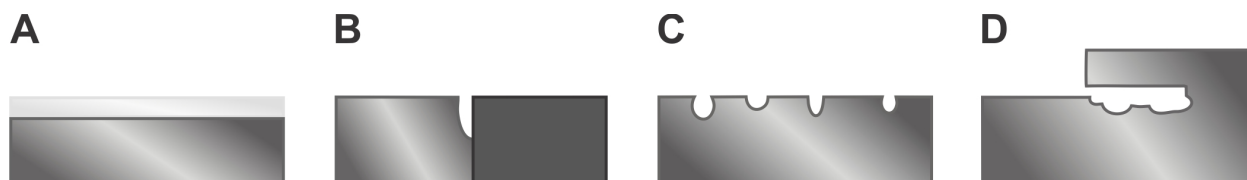


Figure 1.15 – Overview of common corrosion mechanisms. (A) Uniform corrosion (B) Galvanic corrosion (C) Pitting corrosion (D) Crevice corrosion.

Under ambient conditions, a nanoscale layer of oxidized material separates a metallic material from its environment; this is known as a passive film.¹²⁴ When this passive film is removed or weakened by mechanical or chemical means, the metallic surface is exposed to the electrolyte directly and can oxidize further in a process known as corrosion. If this happens evenly across the surface, it is known as uniform corrosion ([Figure 1.15 A](#)). If this

happens at the interface of two dissimilar materials, with the more active of the two being preferentially corroded, it is known as galvanic corrosion (Figure 1.15 B). In many cases this film breakdown happens not uniformly but locally. If this occurs at single, isolated points on the surface where degradation spreads out evenly from the point, it is known as pitting corrosion (Figure 1.15 C). If this occurs in small regions where degradation spreads out along a preferential direction, it is known as crevice corrosion (Figure 1.15 D).

1.3.2.2 Mathematical Methods

1.3.2.2.1 Numerical Models. Depending on the corrosion mechanism involved, mathematical models of a corroding material span a wide range of size scales. In a microscale approach, atoms are considered explicitly. The model geometry therefore considers their finite size and packing arrangement, and the corresponding physics considers their individual behaviour. In a macroscale approach, the atoms are instead treated as a collection with uniform properties. The model geometry therefore considers them as a surface, and the physics does not distinguish between the role of individual atoms.

Microscale models are concerned with describing stochastic, isolated events at the surface, and so are suitable for the study of localized corrosion processes. These are generally used for mechanistic studies of pitting^{125–127} and crevice^{121,125} corrosion. These models use a detailed level of theory, and seek to relate parameters such as the concentration of point defects in the passive film,^{126,128} potential drop across the semiconducting passive film,^{122,127} and adsorption equilibrium constant of inhibiting species¹²⁹ to outputs such as the probability of event initiation and rate of localized propagation.

While an atom-based microscale model is useful for studying localized processes,¹³⁰ it has poor scalability. A surface-based macroscale model is generally used for studying uniform^{2,131,132} or galvanic^{5,133} corrosion. These models use a coarser level of theory, and seek to relate properties such as the anode/cathode area ratio,¹³⁴ mixed potential,⁵ and diffusion coefficient of reactants² to outputs such as the equilibrium potential and current density, E_{corr} and i_{corr} respectively. This approach can model materials on a scale that more closely resembles their ultimate application. The increase in size of the model geometry means that considering microscale processes is no longer feasible. Considering a case where the model equations are meant to be solved numerically using discretization, a uniform mesh element size of 10 nm (a point defect) would mean that 100 elements would be needed to simulate 1 μm and 1 000 000 to simulate 1 cm.

Historically PDP has been performed as a macroscale technique that samples the evolution of entire surfaces. Features associated with localized processes are visible on these graphs – for example, the onset of pitting corrosion at a breakdown potential¹¹⁵ – but are not interpreted with a detailed level of theory. However, the development of scanning probe techniques such as scanning electrochemical cell microscopy (SECCM)¹³⁵ allows a single electrolyte droplet to be moved around the surface, forming a small scale electrochemical cell at each landing point. This has recently been applied for corrosion applications,¹³⁶ and may change the level of modelling applied to this technique in the future.

1.3.2.2.2 Approximation Equations. The most well known approximation equation for analysis of a PDP experiment is the Tafel equation,¹³⁷ which expresses a linear relation-

ship between the overpotential applied and the resulting current.

$$\eta = a + \beta \log(i) \quad (1.35)$$

Where a is a fitting constant and β is the Tafel slope. This slope can be converted to a transfer coefficient according to:¹¹⁴

$$\beta = -\frac{\alpha n F}{2.3 RT} \quad (1.36)$$

1.3.2.2.3 Software and Algorithms. In combination with the Tafel approximation, algorithmic procedures for treating PDP curves to extract corrosion metrics have been developed.

The basic procedure is as follows: a Tafel line is first fit to each branch of the PDP. These lines are then extrapolated to their intersection, which corresponds to the E_{corr} and i_{corr} of the material.^{115,118} While straightforward in principle, this method does not work well for materials that do not display ideal Tafel behaviour.^{117,138} This is further complicated by inconsistencies or incomplete guidelines for selecting the Tafel region to fit,^{30,115,139} which have a significant effect on the final values.

1.4 Summary

In general, electrochemical systems can be decomposed into a series of individual processes and then treated mathematically in order to convert measurable quantities like potential and current to quantities of interest such as rate constants of individual reactions. The relevant processes that need to be considered depend on the technique being used and the parameter-result relationships it is sensitive to.

Chapter 2 uses an equation-based approach to analyse PDP.

Chapter 3 and **Chapter 4** use a model-based approach to analyse SECM in the context of multifunctional microelectrodes and image processing respectively. **Chapter 5** uses a software-based approach to integrate existing data treatment theory and procedures into a user-friendly form.

References

- [1] Bard, A. J.; Faulkner, L. R. *Electrochemical Methods: Fundamentals and Applications*, 2nd ed.; John Wiley & Sons: New York, NY, USA, 2001.
- [2] Melchers, R. *Corrosion Science* **2003**, *45*, 923–940.
- [3] Ansari, T. Q.; Xiao, Z.; Hu, S.; Li, Y.; Luo, J. L.; Shi, S. Q. *npj Computational Materials* **2018**, *4*, 1–10.
- [4] Duddu, R. *Computational Mechanics* **2014**, *54*, 613–627.
- [5] Deshpande, K. B. *Corrosion Science* **2010**, *52*, 3514–3522.
- [6] Kwak, J.; Bard, A. J. *Analytical Chemistry* **1989**, *61*, 1221–1227.
- [7] Martin, R. D.; Unwin, P. R. *Analytical Chemistry* **1998**, *70*, 276–284.

-
- [8] Bondarenko, A.; Cortés-Salazar, F.; Gheorghiu, M.; Gáspár, S.; Momotenko, D.; Stanica, L.; Lesch, A.; Gheorghiu, E.; Girault, H. H. *Analytical Chemistry* **2015**, *87*, 4479–4486.
- [9] Nadappuram, B. P.; McKelvey, K.; Byers, J. C.; Güell, A. G.; Colburn, A. W.; Lazenby, R. A.; Unwin, P. R. *Analytical Chemistry* **2015**, *87*, 3566–3573.
- [10] Fulian, Q.; Fisher, A. C. *The Journal of Physical Chemistry B* **2002**, *102*, 9647–9652.
- [11] Compton, R.; Laborda, E.; Ward, K. *Understanding Voltammetry: Simulation of Electrode Processes*; Imperial College Press, 2013.
- [12] Nann, T.; Heinze, J. *Electrochemistry Communications* **1999**, *1*, 289–294.
- [13] Eymard, R.; Gallouet, T.; Herbin, R. *Handbook of Numerical Analysis* **2000**, *7*, 713–1018.
- [14] Fulian, Q.; Fisher, A. C.; Denuault, G. *The Journal of Physical Chemistry B* **1999**, *103*, 4387–4392.
- [15] Varela, F.; Kurata, Y.; Sanada, N. *Corrosion Science* **1997**, *39*, 775–788.
- [16] Doig, P. *Journal of the Electrochemical Society* **1979**, *126*, 2057.
- [17] Feldberg, S. W. *Journal of Electroanalytical Chemistry and Interfacial Electrochemistry* **1990**, *290*, 49–65.
- [18] Brumleve, T. R.; Buck, R. P. *Journal of Electroanalytical Chemistry and Interfacial Electrochemistry* **1978**, *90*, 1–31.
- [19] Nann, T.; Heinze, J. *Electrochimica Acta* **2003**, *48*, 3975–3980.
- [20] Cornut, R.; Lefrou, C. *Journal of Electroanalytical Chemistry* **2008**, *621*, 178–184.
- [21] Khaleel, M.; Lin, Z.; Singh, P.; Surdoval, W.; Collin, D. *Journal of Power Sources* **2004**, *130*, 136–148.
- [22] Garcia, R. E.; Chiang, Y.-M.; Craig Carter, W.; Limthongkul, P.; Bishop, C. M. *Journal of the Electrochemical Society* **2005**, *152*, A255.
- [23] Scheiner, S.; Hellmich, C. *Computer Methods in Applied Mechanics and Engineering* **2009**, *198*, 2898–2910.
- [24] Mazumder, S.; Cole, J. V. *Journal of the Electrochemical Society* **2003**, *150*, A1503.
- [25] Wiedemann, A. H.; Goldin, G. M.; Barnett, S. A.; Zhu, H.; Kee, R. J. *Electrochimica Acta* **2013**, *88*, 580–588.

- [26] Dickinson, E. J.; Ekström, H.; Fontes, E. *Electrochemistry Communications* **2014**, *40*, 71–74.
- [27] Jacobsen, N. G.; Fuhrman, D. R.; Fredsoe, J. *International Journal for Numerical Methods in Fluids* **2012**, *70*, 1073–1088.
- [28] Thomas, J. W. *Numerical Partial Differential Equations: Finite Difference Methods*; 1995; pp 5–39.
- [29] Thomas, J. W. *Numerical Partial Differential Equations: Finite Difference Methods*; 1995; pp 97–145.
- [30] Zoski, C. G. *Handbook of Electrochemistry*; Elsevier B.V.: Amsterdam, Netherlands, 2007.
- [31] Cornut, R.; Lefrou, C. *Journal of Electroanalytical Chemistry* **2007**, *608*, 59–66.
- [32] Liu, H.; Fan, F.; Lin, C.; Bard, A. *Journal of the American Chemical Society* **1986**, *108*, 3838–3839.
- [33] Engstrom, R.; Weber, M. *Analytical Chemistry* **1986**, *58*, 844–848.
- [34] Bard, A.; Mirkin, M. In *Scanning Electrochemical Microscopy*, 2nd ed.; Bard, A., Mirkin, M., Eds.; CRC Press, 2012; pp 1–647.
- [35] Polcari, D.; Dauphin-Ducharme, P.; Mauzeroll, J. *Chemical Reviews* **2016**, *116*, 13234–13278.
- [36] Zoski, C. G. *Journal of the Electrochemical Society* **2016**, *163*, H3088–H3100.
- [37] Izquierdo, J.; Knittel, P.; Kranz, C. *Analytical and Bioanalytical Chemistry* **2018**, *410*, 307–324.
- [38] Bergner, S.; Vatsyayan, P.; Matysik, F.-M. *Analytica Chimica Acta* **2013**, *775*, 1–13.
- [39] Holzinger, A.; Steinbach, C.; Kranz, C. *RSC Detection Science*; 2016; pp 125–169.
- [40] Filice, F. P.; Ding, Z. *Analyst* **2019**, *144*, 738–752.
- [41] Niu, L.; Yin, Y.; Guo, W.; Lu, M.; Qin, R.; Chen, S. *Journal of Materials Science* **2009**, *44*, 4511–4521.
- [42] Souto, R. M.; Lamaka, S. V. V.; Gonzalez, S.; Gonzalez, S. In *Microscopy: Science, Technology, Applications and Education*; Mendez-Vilas, A., Diaz, J., Eds.; Formatex: Badajoz, Spain, 2010; Vol. 3; pp 1769–1780.
- [43] Payne, N. A.; Stephens, L.; Mauzeroll, J. *CORROSION* **2017**, *73*, 2354.
- [44] Bertoncello, P. *Energy & Environmental Science* **2010**, *3*, 1620.
- [45] Schuhmann, W.; Bron, M. *Polymer Electrolyte Membrane and Direct Methanol Fuel Cell Technology: In Situ Characterization Techniques for Low Temperature Fuel Cells*; Elsevier, 2012; pp 399–424.
- [46] Ventosa, E.; Schuhmann, W. *Physical Chemistry Chemical Physics* **2015**, *17*, 28441–28450.

- [47] Danis, L.; Polcari, D.; Kwan, A.; Gateman, S. M.; Mauzeroll, J. *Analytical Chemistry* **2015**, *87*, 2565–2569.
- [48] Shao, Y.; Mirkin, M. V.; Fish, G.; Kokotov, S.; Palanker, D.; Lewis, A. *Analytical Chemistry* **1997**, *69*, 1627–1634.
- [49] Mauzeroll, J.; Hueske, E. A.; Bard, A. J. *Analytical Chemistry* **2003**, *75*, 3880–3889.
- [50] Lee, Y.; Amemiya, S.; Bard, A. J. *Analytical Chemistry* **2001**, *73*, 2261–2267.
- [51] Nebel, M.; Neugebauer, S.; Eckhard, K.; Schuhmann, W. *Electrochemistry Communications* **2013**, *27*, 160–163.
- [52] McKelvey, K.; Nadappuram, B. P.; Actis, P.; Takahashi, Y.; Korchev, Y. E.; Matsue, T.; Robinson, C.; Unwin, P. R. *Analytical Chemistry* **2013**, *85*, 7519–7526.
- [53] Nadappuram, B. P.; McKelvey, K.; Al Botros, R.; Colburn, A. W.; Unwin, P. R. *Analytical Chemistry* **2013**, *85*, 8070–8074.
- [54] Thakar, R.; Weber, A. E.; Morris, C. a.; Baker, L. A. *Analyst* **2013**, *138*, 5973.
- [55] Macpherson, J. V.; Unwin, P. R. *Analytical Chemistry* **2000**, *72*, 276–285.
- [56] Kueng, A.; Kranz, C.; Lugstein, A.; Bertagnolli, E.; Mizaikoff, B. *Angewandte Chemie International Edition* **2003**, *42*, 3238–3240.
- [57] Lee, Y.; Ding, Z.; Bard, A. J. *Analytical Chemistry* **2002**, *74*, 3634–3643.
- [58] Lefrou, C.; Cornut, R. *ChemPhysChem* **2010**, *11*, 547–556.
- [59] Paik, C. H.; White, H. S.; Alkire, R. C. *Journal of the Electrochemical Society* **2000**, *147*, 4120–4124.
- [60] Diaz-Ballote, L.; Veleva, L.; Pech-Canul, M. A.; Pech-Canul, M. I.; Wipf, D. O. *Journal of the Electrochemical Society* **2004**, *151*, B299–B303.
- [61] Gateman, S. M.; Stephens, L. I.; Perry, S. C.; Lacasse, R.; Schulz, R.; Mauzeroll, J. *npj Materials Degradation* **2018**, *2*, 5.
- [62] Bard, A. J.; Mirkin, M. V.; Unwin, P. R.; Wipf, D. O. *The Journal of Physical Chemistry* **1992**, *96*, 1861–1868.
- [63] Pierce, D. T.; Unwin, P. R.; Bard, A. J. *Analytical Chemistry* **1992**, *64*, 1795–1804.

- [64] Shen, Y.; Nonomura, K.; Schlettwein, D.; Zhao, C.; Wittstock, G. *Chemistry - A European Journal* **2006**, *12*, 5832–5839.
- [65] Lee, C.; Kwak, J.; Anson, F. C. *Analytical Chemistry* **1991**, *63*, 1501–1504.
- [66] Fernandez, J. L.; Bard, A. J. *Analytical Chemistry* **2003**, *75*, 2967–2974.
- [67] Minguzzi, A.; Alpuche-Aviles, M. A.; Lopez, J. R.; Rondinini, S.; Bard, A. J. *Analytical Chemistry* **2008**, *80*, 4055–4064.
- [68] Jung, C.; Sanchez-Sanchez, C. M.; Lin, C.-L.; Rodriguez-Lopez, J.; Bard, A. J. *Analytical Chemistry* **2009**, *81*, 7003–7008.
- [69] Bastos, A.; Simoes, A.; Gonzalez, S.; Gonzalez-Garcia, Y.; Souto, R. *Electrochemistry Communications* **2004**, *6*, 1212–1215.
- [70] Bastos, A.; Simoes, A.; Gonzalez, S.; Gonzalez-Garcia, Y.; Souto, R. *Progress in Organic Coatings* **2005**, *53*, 177–182.
- [71] Izquierdo, J.; Fernandez-Perez, B. M.; Filotas, D.; Ori, Z.; Kiss, A.; Martin-Gomez, R. T.; Nagy, Livia.; Nagy, G.; Souto, R. M. *Electroanalysis* **2016**, *28*, 2354–2366.
- [72] Eckhard, K.; Chen, X.; Turcu, F.; Schuhmann, W. *Physical Chemistry Chemical Physics* **2006**, *8*, 5359.
- [73] Eckhard, K.; Schuhmann, W. *Electrochimica Acta* **2007**, *53*, 1164–1169.
- [74] Karnicka, K.; Eckhard, K.; Guschin, D. A.; Stoica, L.; Kulesza, P. J.; Schuhmann, W. *Electrochemistry Communications* **2007**, *9*, 1998–2002.
- [75] Kundu, S.; Nagaiah, T. C.; Xia, W.; Wang, Y.; Dommele, S. V.; Bitter, J. H.; Santa, M.; Grundmeier, G.; Bron, M.; Schuhmann, W.; Muhler, M. *The Journal of Physical Chemistry C* **2009**, *113*, 14302–14310.
- [76] Santana, J.; Gonzalez-Guzman, J.; Fernandez-Merida, L.; Gonzalez, S.; Souto, R. *Electrochimica Acta* **2010**, *55*, 4488–4494.
- [77] Abodi, L. C.; Gonzalez-Garcia, Y.; Dolgikh, O.; Dan, C.; Deconinck, D.; Mol, J. M. C.; Terryn, H.; Deconinck, J. *Electrochimica Acta* **2014**, *146*, 556–563.
- [78] Thomas, S.; Cole, I. S.; Gonzalez-Garcia, Y.; Chen, M.; Musameh, M.; Mol, J. M. C.; Terryn, H.; Birbilis, N. *Journal of Applied Electrochemistry* **2014**, *44*, 747–757.

- [79] Horrocks, B. R.; Mirkin, M. V.; Pierce, D. T.; Bard, A. J.; Nagy, G.; Toth, K. *Analytical Chemistry* **1993**, *65*, 1213–1224.
- [80] Ballesteros K.B.; Schulte, A.; Calvo, E.; Koudelka-Hep, M.; Schuhmann, W. *Electrochemistry Communications* **2002**, *4*, 134–138.
- [81] Hengstenberg, A.; Kranz, C.; Schuhmann, W. *Chemistry - A European Journal* **2000**, *6*, 1547–1554.
- [82] Martin, R. D.; Unwin, P. R. *Journal of the Chemical Society, Faraday Transactions* **1998**, *94*, 753–759.
- [83] Ivanauskas, F.; Morkvenaite-Vilkonciene, I.; Astrauskas, R.; Ramanavicius, A. *Electrochimica Acta* **2016**, *222*, 347–354.
- [84] Galceran, J.; Cecilia, J.; Companys, E.; Salvador, J.; Puy, J. *The Journal of Physical Chemistry B* **2000**, *104*, 7993–8000.
- [85] Barker, A. L.; Unwin, P. R.; Amemiya, S.; Zhou, J.; Bard, A. J. *The Journal of Physical Chemistry B* **1999**, *103*, 7260–7269.
- [86] Barker, A. L.; Macpherson, J. V.; Slevin, C. J.; Unwin, P. R. *The Journal of Physical Chemistry B* **1998**, *102*, 1586–1598.
- [87] Liu, B.; Mirkin, M. V. *Journal of the American Chemical Society* **1999**, *121*, 8352–8355.
- [88] Selzer, Y.; Mandler, D. *The Journal of Physical Chemistry B* **2000**, *104*, 4903–4910.
- [89] Wipf, D. O.; Bard, A. *Journal of the Electrochemical Society* **1991**, *138*, 469.
- [90] Ellis, K. A.; Pritzker, M. D.; Fahidy, T. Z. *Analytical Chemistry* **1995**, *67*, 4500–4507.
- [91] Nugues, S.; Denuault, G. *Journal of Electroanalytical Chemistry* **1996**, *408*, 125–140.
- [92] Zhu, R.; Qin, Z.; Noël, J. J.; Shoesmith, D. W.; Ding, Z. *Analytical Chemistry* **2008**, *80*, 1437–1447.
- [93] Nowierski, C.; Noël, J. J.; Shoesmith, D. W.; Ding, Z. *Electrochemistry Communications* **2009**, *11*, 1234–1236.
- [94] Tefashe, U. M.; Snowden, M. E.; Ducharme, P. D.; Danaie, M.; Botton, G. A.; Mauzeroll, J. *Journal of Electroanalytical Chemistry* **2014**, *720-721*, 121–127.
- [95] Momotenko, D.; Qiao, L.; Cortés-Salazar, F.; Lesch, A.; Wittstock, G.; Girault, H. H. *Analytical Chemistry* **2012**, *84*, 6630–6637.

- [96] Li, M. S.; Filice, F. P.; Ding, Z. *Journal of Electroanalytical Chemistry* **2016**, *779*, 176–186.
- [97] Wightman, R.; Wipf, D. In *Electroanalytical Chemistry Volume 15*; Bard, A., Ed.; 1988; pp 267–253.
- [98] Fang, Y.; Leddy, J. *Analytical Chemistry* **1995**, *67*, 1259–1270.
- [99] Lefrou, C. *Journal of Electroanalytical Chemistry* **2006**, *592*, 103–112.
- [100] Zoski, C. G.; Mirkin, M. V. *Analytical Chemistry* **2002**, *74*, 1986–1992.
- [101] Myland, J. C.; Oldham, K. B. *Journal of Electroanalytical Chemistry and Interfacial Electrochemistry* **1990**, *288*, 1–14.
- [102] Daniele, S.; Ciani, I.; Battistel, D. *Analytical Chemistry* **2008**, *80*, 253–259.
- [103] Kuss, S.; Polcari, D.; Geissler, M.; Brassard, D.; Mauzeroll, J. *Proceedings of the National Academy of Sciences* **2013**, *110*, 9249–9254.
- [104] Kranz, C.; Friedbacher, G.; Mizaikoff, B.; Lugstein, A.; Smoliner, J.; Bertagnolli, E. *Analytical Chemistry* **2001**, *73*, 2491–2500.
- [105] Comstock, D. J.; Elam, J. W.; Pellin, M. J.; Hersam, M. C. *Analytical Chemistry* **2010**, *82*, 1270–1276.
- [106] Takahashi, Y.; Shevchuk, A. I.; Novak, P.; Murakami, Y.; Shiku, H.; Korchev, Y. E.; Matsue, T. *Journal of the American Chemical Society* **2010**, *132*, 10118–10126.
- [107] Fan, F.-R.; Demaille, C. In *Scanning Electrochemical Microscopy*, 2nd ed.; Bard, A. J., Mirkin, M. V., Eds.; Taylor & Francis, 2012; pp 25–47.
- [108] Amemiya, S. In *Electroanalytical Chemistry: A Series of Advances*; Bard, A., Zoski, C., Eds.; Electroanalytical Chemistry: A Series of Advances; CRC Press, 2015; pp 1–72.
- [109] Bartels, K. A.; Lee, C.; Bovik, A. C.; Bard, A. J. Digital restoration of scanning electrochemical microscope images. *Proceedings of SPIE*. 1991; pp 30–39.
- [110] Lee, C.; Wipf, D. O.; Bard, A. J.; Bartels, K.; Bovik, A. C. *Analytical Chemistry* **1991**, *63*, 2442–2447.
- [111] Gustafsson, M. G. L. *Journal of Microscopy* **2000**, *198*, 82–87.
- [112] Wipf, D. O.; Bard, A. J. *Analytical Chemistry* **1992**, *64*, 1362–1367.
- [113] Holewinski, A.; Linic, S. *Journal of the Electrochemical Society* **2012**, *159*, H864–H870.
- [114] Fang, Y.-H.; Liu, Z.-P. *ACS Catalysis* **2014**, *4*, 4364–4376.

- [115] Tait, W. S. *An introduction to electrochemical corrosion testing for practicing engineers and scientists*, 1st ed.; PairODocs Publications: Racine, WI, USA, 1994.
- [116] Rosborg, B.; Pan, J.; Leygraf, C. *Corrosion Science* **2005**, *47*, 3267–3279.
- [117] Shi, Z.; Liu, M.; Atrens, A. *Corrosion Science* **2010**, *52*, 579–588.
- [118] McCafferty, E. *Introduction to Corrosion Science*; Springer New York: New York, NY, 2010; pp 177–208.
- [119] Stern, M.; Geaby, A. L. *Journal of the Electrochemical Society* **1957**, *104*, 56.
- [120] ASTM, *Annual Book of ASTM Standards*; 2003.
- [121] Oldfield, J. W.; Sutton, W. H. *British Corrosion Journal* **1978**, *13*, 13–22.
- [122] Anderko, A.; McKenzie, P.; Young, R. D. *CORROSION* **2001**, *57*, 202–213.
- [123] Ahmad, S. *Cement and Concrete Composites* **2003**, *25*, 459–471.
- [124] Frankel, G.; Sridhar, N. *Materials Today* **2008**, *11*, 38–44.
- [125] Sharland, S. M.; Tasker, P. W. *Corrosion Science* **1988**, *28*, 603–620.
- [126] Laycock, N. J.; Noh, J. S.; White, S. P.; Krouse, D. P. *Corrosion Science* **2005**, *47*, 3140–3177.
- [127] Marcus, P.; Maurice, V.; Strehblow, H.-H. *Corrosion Science* **2008**, *50*, 2698–2704.
- [128] Lin, L. F. *Journal of the Electrochemical Society* **1981**, *128*, 1194.
- [129] Yang, S.; Macdonald, D. D. *Electrochimica Acta* **2007**, *52*, 1871–1879.
- [130] Qian, S. *Journal of the Electrochemical Society* **1990**, *137*, 435.
- [131] Nesic, S.; Postlethwaite, J.; Olsen, S. *CORROSION* **1996**, *52*, 280–294.
- [132] Nordsveen, M.; Nešić, S.; Nyborg, R.; Stangeland, A. *CORROSION* **2003**, *59*, 443–456.
- [133] Jia, J. X.; Song, G.; Atrens, A. *Corrosion Science* **2006**, *48*, 2133–2153.
- [134] Song, G.; Johannesson, B.; Hapugoda, S.; StJohn, D. *Corrosion Science* **2004**, *46*, 955–977.
- [135] Ebejer, N.; Schnippering, M.; Colburn, A. W.; Edwards, M. A.; Unwin, P. R. *Analytical Chemistry* **2010**, *82*, 9141–9145.
- [136] Yule, L. C.; Bentley, C. L.; West, G.; Shollock, B. A.; Unwin, P. R. *Electrochimica Acta* **2019**, *298*, 80–88.

-
- [137] Tafel, J. *Zeitschrift für Physikalische Chemie* **1905**, 50U.
- [138] Amin, M. A.; Khaled, K.; Fadel-Allah, S. A. *Corrosion Science* **2010**, 52, 140–151.
- [139] Frankel, G.; Landolt, D. In *Encyclopedia of Electrochemistry Volume 4: Corrosion and Oxide Films*; Bard, A. J., Stratmann, M., Frankel, G. S., Eds.; Wiley-VCH, 2003.

Chapter 2

Development of a Model for Experimental Data Treatment of Diffusion and Activation Limited Polarization Curves for Magnesium and Steel Alloys



Chapter Abstract

Most material characterization begins with a macroscale technique, which allows general trends in surface evolution to be identified and investigated further with later microscale techniques. PDP is well suited to this initial characterization as polarizing the sample allows natural corrosion processes to be accelerated and extensive degradation representative of long-term immersion to be induced. Furthermore, localized processes such as pitting corrosion give rise to characteristic features of these curves. Traditional Tafel analysis is commonly used to treat this data and extract quantitative parameters describing when the surface will begin to corrode and how quickly. While a powerful approach, literature guidelines for this quantitation are inconsistent, and often developed with a specific material exhibiting a small subset of corrosion mechanisms in mind.

This chapter presents a finite element model for the fitting of polarization curves to a diffusion-limited Tafel equation. This approach is applied to materials exhibiting different corrosion behaviour, demonstrating the versatility of this as a systematic approach. For a treated data set, implications of the extracted parameters for the concentration profile of electroactive species in solution are also discussed.

The work presented in this chapter is reproduced from:

Stephens, L.I.; Perry, S.C.; Gateman, S.M.; Lacasse, R.; Schulz, R.; Mauzeroll, J. Development of a model for experimental data treatment of diffusion and activation limited polarization curves for magnesium and steel alloys. *Journal of the Electrochemical Society* **2017**, 164(11), E3576-E3582.

2.1 Introduction

Models of corrosion are ubiquitous in the literature. Mathematical formulations of corrosion processes have been developed to describe pitting,^{1–4} galvanic,^{5–8} and uniform corrosion^{9–11} which in turn have been used to study factors influencing the rate of corrosion in specific systems including but not limited to chloride concentration in pitting initiation,^{12–14} oxygen diffusion in kinetic limitations,^{11,13,15,16} and sample geometry in crevice corrosion.^{16–18} These systems have been solved both analytically^{4,8} and numerically.^{4,5,7,15,17,19,20} Finding an analytical solution requires making simplifying assumptions such as a 1D-geometry, uniform surface reactivity, and negligible change in solution composition as a result of Faradaic reactions.⁸ This severely limits the scope of applicable systems. Numerical methods are by far the option of choice for any system with an added degree of complexity, whether that be a non-uniformly reacting surface, multi-dimensional geometry, or solution undergoing significant pH or other compositional changes which in turn affects the corrosion rate.

Numerical models of corrosion take one of two forms: (1) A model-first approach,^{12,13,18} which begins with a theoretical system and looks to predict material evolution, or (2) An experiment-first approach,^{11,17,21} which begins with a physical system and looks to explain observed behaviour. Both approaches begin with model inputs for the initial concentrations and diffusion coefficients of species in solution, metal and solution conductivity, and Tafel slopes. These Tafel slopes (β) are extracted from potentiodynamic polarization curves (PDPs), which can also be used to measure the corrosion potential (E_{corr}) and corrosion current density (j_{corr}) of the system. In practice, extraction of these parameters from exper-

imental data is problematic: the selection of the linear region is crucial for reproducibility and validity of analysis. If the linear region is selected based on a target R^2 value, the fitted region will be inconsistent between samples. Determining the potential at which to begin fitting is also problematic: Some recommend linear fitting begin 50 mV from E_{corr} and end after a one decade increase in current,²² while others suggest fitting can begin as far as 100 mV from E_{corr} over the same change in current.²³ Many textbooks on the subject do not specify this range at all^{24,25} as the linear region can change from metal to metal.

Significant discrepancies in the analysis method between materials exist: previous works have opted not to perform fitting,²⁶ perform a partial fit to a single branch,^{27–29} or perform a full fit to both branches in both ideal and non-ideal cases.^{23,30,31} If the two branches of the PDP are analysed separately, they often yield different values for the corrosion current density.³² Many use the value extracted exclusively from the cathodic branch as extensive surface changes and corrosion product formation occur in the anodic branch; however, the same issue may occur in the cathodic branch in acidic solutions or at potentials sufficiently negative to reduce the native passive film.²³ Fitting to the Tafel equation further assumes purely activation-controlled currents. If the reactions at the surface are under diffusion control, the fitting protocols discussed earlier cannot be used. Some work has been done to quantify systems of this nature involving iron³³ and copper,³⁴ but these have focused on a limited material scope or decoupled mass transport effects by introducing convection to the system. The agreement between corrosion current densities determined from both branches is also strongly dependent on experimental conditions used, such as the electrolyte and the scan rate.³² All of these factors are significant sources of error for the PDP technique,

which leads to poor agreement with other techniques such as mass loss and electrochemical impedance spectroscopy.

Herein, we present a material independent, finite element model that provides a systematic method for the more accurate data treatment of polarization curves. This is done through the incorporation of mass transport limiting current density to traditional Tafel kinetics. Experimental polarization curves are then fit through an iterative refinement process, with the experimental and simulated results statistically compared to validate model accuracy. This method is applicable to a broad material scope – specifically, extremely corrosion active magnesium alloys and extremely corrosion resistant steels have been presented here. As discussed previously, taking a numerical approach allows this model to be extended through the incorporation of complex, multi-component materials with asymmetrical geometries. Our model is therefore a significant improvement on those currently available in the literature, as ours is the first real example that offers reliable and reproducible comparison of the corrosion properties across such a broad range of materials regardless of the experimental approach.

2.2 Experimental

2.2.1 Materials

Magnesium rods (99.9% purity, 5 mm diameter) were obtained from Sigma Aldrich. Steel A516 rods (11.3 mm diameter) and AM60 Mg alloys (1 cm \times 1 cm) were obtained from

General Motors Canada. Stainless steel 444 samples were obtained from Hydro-Québec and machined into cylinders with 1 cm² surface area. All samples were fixed in cold mounting epoxy (Epofix, Streurs) and the metal face was exposed using a TegraPol-25 polishing wheel (Streurs) through a series of successive grinding steps with increasingly finer grits of SiC foils (800, 1200, 4000). This was followed by polishing with a 1 µm diamond suspension and a 0.05 µm alumina paste using an MD-chem polishing pad to obtain a mirror finish. Solutions were prepared with reagent grade NaCl (ACP) and nanopure water (18.2 MΩ-cm, Millipore).

2.2.2 Instrumentation

Electrochemical measurements were made using an ELProscan 1 system (HEKA Elektronik, Germany) with Potmaster software (version v2 x 66) and a VSP-300 system (Bio-Logic Science Instruments, France) with EC-Lab (version 11.01). A 1M Ag/AgCl reference electrode in a Luggin capillary was prepared following a literature procedure.²⁵ A commercial SCE reference electrode was used for the measurements on stainless steel 444. A platinum mesh was used as the counter electrode in all cases. The finite element models were built using COMSOL Multiphysics version 5.2a equipped with the Corrosion Module.

2.2.3 Data Collection and Procedure for Tafel Fits

Polarization curves were recorded in 0.10 M NaCl over a range of -300 mV to +300 mV relative to open-circuit potential. Initial values of E_{corr} , j_{corr} , β_a , and β_c for use in the parametric sweep were extracted from experimental data using MATLAB 2015b. A linear

fit was performed for each branch using a traditional Tafel fitting procedure where fitting began 50 mV from E_{corr} and ceased when the current density had increased one decade from the start point.²² These values were used as the initial guess of E_{corr} , j_{corr} , β_a , and β_c , which were then refined by simulating a parametric sweep and selecting the best statistical match. In cases where mass transfer limitations appeared to be present, a fifth parameter (j_{lim}) was included in the parametric sweep. The initial guess was then updated and the process was repeated using finer increments in the parametric sweep until further refinement yielded negligible improvement in the quality of the fit.

2.3 Results and Discussion

2.3.1 Factors Influencing Choice of Model Geometry

The geometry of a corroding system is ultimately three-dimensional: uneven oxide formation dependent on the crystallographic orientation, heterogeneous corrosion rates and microgalvanic corrosion associated with the underlying microstructure, and localized processes such as pitting and crevice corrosion all alter surface topography. In the context of a laboratory measurement, metal samples are polished to a smooth finish prior to testing and the topography changes minimally relative to the overall sample dimensions when testing under mild conditions.

The standard electrochemical cell during experimental corrosion measurements employs a three electrode setup where the metallic sample of interest serves as the working electrode

(WE). In a simulation, a combined reference and counter electrode (CE) can be used. An isolated region of the WE with well-defined surface area is exposed to the electrolyte through encasement of the sample in epoxy or the use of an O-ring. This geometry is depicted in [Figure 2.1](#). This cell possesses an axis of symmetry through the center of the sample. This enables the original 3D geometry to be simplified to its 2D-axisymmetric equivalent ([Figure 2.1 A](#)). This reduces the computational power needed to solve the mesh and aids in convergence, which is necessary when additional partial differential equations (PDEs) with a spatial dependence are incorporated into the system – in this case, mass transport of additional species in solution.

Simulations involving both 3D and 2D-axisymmetric geometries have been performed and are discussed in this work. For a description of the meshing technique employed for both geometries, refer to [Figure B.1](#). In general, the most appropriate geometry is determined by the goal of the simulation and computational power available to solve it. A 3D model is advantageous for asymmetric systems or localized corrosion processes, while a 2D-axisymmetric model is useful for a more detailed study of the individual reactions occurring during corrosion.

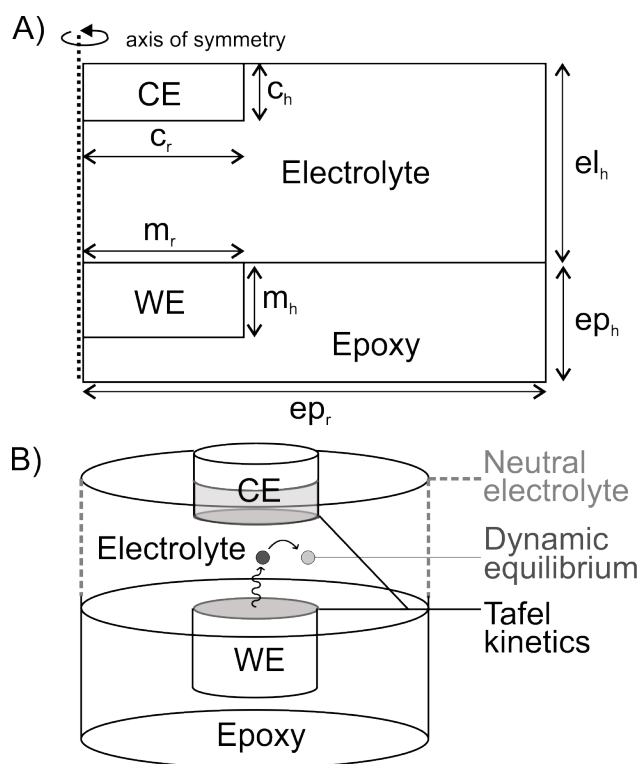


Figure 2.1 – Model geometry depicted in 2D-axisymmetric (A) and 3D (B) space. The dimensions were chosen such that the working electrode (WE) has an exposed surface area of 1 cm^2 , with $m_r = 0.564 \text{ cm}$, $m_h = 0.2 \text{ cm}$, $c_r = 0.564 \text{ cm}$, $c_h = 0.2 \text{ cm}$, $ep_r = 2 \text{ cm}$, $ep_h = 0.4 \text{ cm}$, $el_h = 2 \text{ cm}$. Tafel kinetics at the electrode/electrolyte interfaces in the WE and CE govern the currents measured at the WE. A boundary condition of electrolyte neutrality is applied to the walls of the container (dashed line). In versions of the model where the electrolyte composition is specified directly, a pH equilibrium is also specified within the electrolyte.

2.3.2 Decoupling Activation and Diffusion-Controlled Contributions to Current

2.3.2.1 Extraction of Initial Model Inputs \mathbf{E}_{corr} , \mathbf{j}_{corr} , β_a , β_c

A full description of the underlying equations used can be found in **Appendix B**. In a finite element formulation, the total current at the corroding surface is calculated according to:

$$i = \sum_m i_{loc,m} + i_{dl} \quad (2.1)$$

Where i is the overall current at the electrode surface, $i_{loc,m}$ is the Faradaic current associated with reaction m , and i_{dl} is the non-Faradaic current associated with double layer capacitance. The current distribution within the electrolyte is described by the following:

$$\nabla \cdot i_l = Q_l \quad (2.2)$$

$$i_l = -\sigma_l \nabla \phi_l \quad (2.3)$$

Where i_l is the current, Q_l the charge, σ_l the conductivity, and ϕ_l the electric potential within the electrolyte.

At high overpotentials, the Butler-Volmer equation simplifies to a linear Tafel expression.

$$\eta = \frac{RT}{\alpha F} \ln i_{corr} - \frac{RT}{\alpha F} \ln i \quad (2.4)$$

Where all variables are as defined in [1.1.4](#) and [1.3.2.2.2](#) More commonly, the Tafel slope (β) is reported rather than the transfer coefficient (α), as discussed in [1.3.2.2.2](#):

$$\beta_a = \frac{(1 - \alpha)nF}{2.3RT} \quad (2.5)$$

$$\beta_c = -\frac{\alpha nF}{2.3RT} \quad (2.6)$$

Where β_a and β_c are the anodic and cathodic Tafel slopes respectively, and n is the number of electrons transferred during reaction. The overpotential may be calculated as:

$$\eta = \phi_s - \phi_l - E_{corr} \quad (2.7)$$

Where ϕ_s , ϕ_l , and E_{corr} are the electrode, electrolyte, and corrosion potentials respectively.

Numerical analysis of a standard PDP takes advantage of these kinetics to extract four corrosion-relevant parameters from the Tafel region: these are β_a , β_c , E_{corr} , and j_{corr} (where j_{corr} is $i_{corr}/area$). In systems under activation control, these four parameters are sufficient for describing the shape of a polarization curve. In systems under diffusion control, the

reaction rate is limited by mass transport of reacting species to and from the electrode and so the current density plateaus at high overpotentials. Diffusion-limited currents are often observed while carrying out polarization measurements on a corroding sample where significant gas evolution occurs or extremely passivating oxide layers are present,²² as these phenomena reduce the availability of electroactive species at the metal/electrolyte interface. Under these conditions, an additional parameter is needed to adequately describe the rate of reaction: j_{lim} , the limiting current density. Depending on the underlying cause of this diffusion control, this may only apply to the anodic branch ($j_{lim,a}$) or cathodic ($j_{lim,c}$). The Faradaic current at the electrode surface may therefore be calculated as:

$$i_{loc} = \frac{i_{lim}i_{Tafel}}{i_{lim} + i_{Tafel}} \quad (2.8)$$

$$i_{Tafel} = i_{corr} \times 10^{\frac{\eta}{\beta_m}} \quad (2.9)$$

For a given reaction m , i_{loc} is the total Faradaic current, i_{lim} the mass transport contribution to current, and i_{Tafel} the activation contribution to current.

2.3.2.2 Optimization of Kinetic and Corrosion Parameters

A given PDP simulation was performed by linearly polarizing the WE from -300 mV to +300 mV relative to E_{corr} at 0.167 mV/s. A multi-parametric sweep was then performed that took the initial values of β_a , β_c , E_{corr} , and j_{corr} extracted from 2.3.2.1 and examined the effect of changing these in coarse increments. All combinations were examined statistically and

the best set of parameters was selected as the new input for a subsequent multi-parametric sweep using finer increments. In cases where diffusion control appeared to be present (initial values of $|\beta| > 240$ mV/decade, which would correspond to a process involving >4 electrons if it were purely kinetically controlled), traditional Tafel fitting procedures provided poor estimates of the corrosion kinetics. Therefore, a five-parameter sweep over a broader range was performed. The kinetics at the CE were assigned values corresponding to that of pure platinum: these are $j_{corr} = j_{exchange} = 0.794$ mA/cm², $E_{corr} = +1.188$ V vs. NHE, and idealized kinetics of $|\beta| = 118$ mV/decade,^{24,35} To aid in convergence, a boundary condition is applied to the walls of the container (the region of bulk solution) of $E_{electrolyte} = 0$ V.

The simulated PDPs for four different metallic systems and the corresponding experimental data to which they were fitted (Figure 2.2) demonstrate the broad material scope of the model, with excellent agreement found in all cases. The low E_{corr} and high j_{corr} of the two magnesium-based samples (Figure 2.2 A and B) are consistent with their poor corrosion resistance. The j_{corr} determined in this work is lower than those previously found in a Tafel analysis (80 μ A/cm² in this work compared to 120 μ A/cm²): notably, this value was extracted using only the cathodic branch and under the assumption of purely activation controlled kinetics,²⁸ an analytical procedure commonly used for Mg alloys including AM60.³⁶ Similar β_c values were found for the Mg alloys of 170-230 mV/decade; while a value for β_a was not given for direct comparison, the steep slope in this region and sharp contrast in the shapes of the anodic and cathodic branches are consistent with polarization curves reported on Mg and zinc-containing Mg alloys.^{37,38} Previous numerical analysis has been limited to the cathodic branch based on the analysis that since the hydroxide film formed on Mg and

Table 2.1 – Simulation-optimized Tafel parameters for the four alloys tested at 0.167 mV/s.

Alloy	E_{corr} (V vs. NHE)	j_{corr} ($\mu\text{A}/\text{cm}^2$)	β_a (mV/dec)	β_c (mV/dec)	$j_{lim,a}$ ($\mu\text{A}/\text{cm}^2$)	$j_{lim,c}$ ($\mu\text{A}/\text{cm}^2$)
Pure Mg	-1.192	80	10	-220	-	3000
AM60	-1.212	90	60	-120	-	60
Steel A516	-0.790	25	100	-220	-	-
S444	0.114	0.20	140	-200	0.50	-

Mg alloys is only partially protective, there is no single anodic or cathodic reaction occurring in each branch and so corrosion parameters extracted from Tafel analyses can be problematic.³⁹ This highlights the challenge of correctly interpreting the meaning of these values after they are extracted. As is, the currents measured are a convolution of multiple reactions occurring at the metal-solution interface. Their respective contributions can be elucidated using the concentration profile of each species in solution (Figure 2.4). This is particularly relevant for understanding the mass transport limited current densities that appear to be present in the cathodic branches for these samples, where hydrogen evolution is the dominant reaction. The aggressive formation of H_2 gas bubbles blocks the surface, effectively decreasing the surface area and resulting in a mass transport limited current density. No such limitation exists in the anodic branch where the dominant reaction is $\text{Mg}_{(s)}$ dissolution and so activation controlled reactions are observed.

In contrast to the Mg alloys, the dominant cathodic reaction for the steels tested (Figure 2.2 (C) and (D)) is oxygen reduction and no limiting current density is observed in the cathodic branch for these samples. It has previously been shown that oxygen reduction on

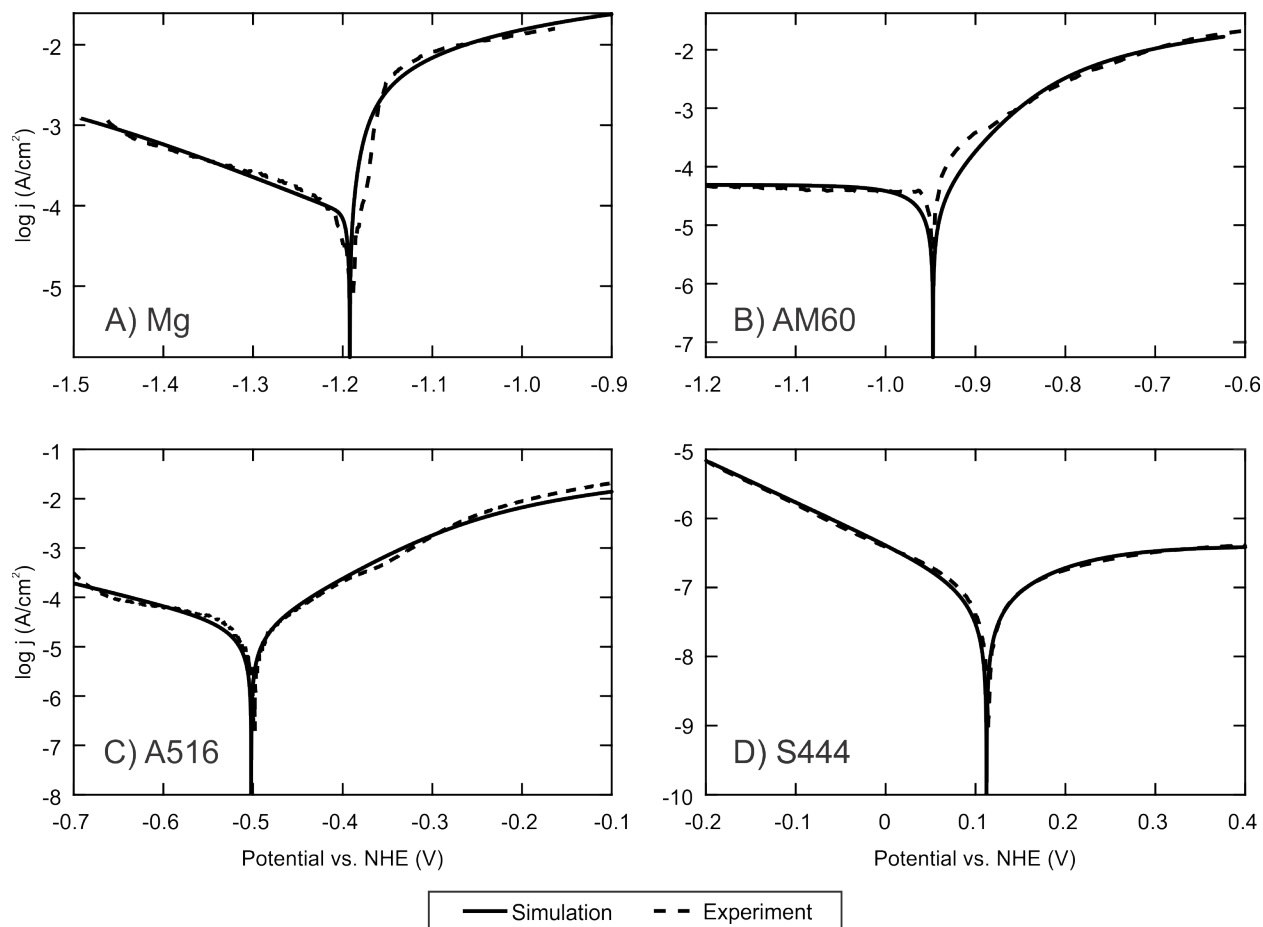


Figure 2.2 – Experimental and simulated polarization curves on (A) pure Mg, (B) magnesium alloy AM60, (C) carbon steel A516, and (D) stainless steel 444 performed at 0.167 mV/s in 0.10 M NaCl.

passivated stainless steel is activation-controlled within the Tafel region.⁴⁰ Higher j_{corr} values have been reported for S444^{41,42} as only the anodic branch was extrapolated. The extracted parameters in this work are consistent with the difference in corrosion susceptibility between carbon and stainless steels. This is further evidenced in the appearance of a mass transport limited current density in the anodic branch of the stainless steel. This is characteristic of a diffusion-controlled process where transport of reacting species to the metal surface is slowed

from surface blocking due to gas bubble formation or corrosion product restricting the electroactive species access to the metal surface. Such situations are typical explanations for diffusion-controlled processes occurring during the cathodic sweep of a PDP. As before, this deviation from an activation-controlled reaction rate poses a problem for traditional Tafel extraction that cannot decouple the two contributions.

In the anodic branch, however, the dominant reaction is metal dissolution. Therefore the limiting current density in the anodic branch for (Figure 2.2 D) arises due to the extremely passivating nature of the surface oxide layer that controls the rate of dissolution. Activation-controlled behaviour in the anodic branch of the carbon steel alloy shows that this material does not successfully passivate under the presented conditions and the metal dissolution is kinetically limited.

2.3.3 Evaluation of Statistical Metrics for Goodness of Fit

Examining the accuracy of a simulation with respect to theory or experimental data in a quantitative manner requires the selection of an appropriate goodness of fit statistic. Previous simulations of electrochemical experiments have considered a variety of metrics towards this end, including percent difference for chronoamperometry⁴³ and cyclic voltammetry,^{44,45} mean deviation for microelectrode approach curves,⁴⁶ and least-squares residuals analysis for impedance.⁴⁷ Given the non-linear nature of a polarization curve, there are a number of fit statistics that might be considered as candidates for determining the optimal fit. Of those mentioned earlier, percent difference and residuals are metrics that have previously been used in this context. Deviation would be most applicable in a system where a model

is being compared to a series of measurements rather than individual data sets as examined here. In addition to percent difference and residuals, the chi-squared goodness of fit test has been examined as a possible metric as it accounts for the number of parameters being fit.

In all tests, the largest discrepancy between experimental and simulated curves occurs in a narrow region around the corrosion potential where the model shows currents that are orders of magnitude smaller than experiment. This is due to the combination of two things. Firstly, when performing a linear sweep a potentiostat increases the potential in a discrete rather than continuous manner. This means that while a number of points immediately surrounding E_{corr} will be sampled, it is unlikely that a data point will be collected at exactly E_{corr} . It may be argued that measuring the initial open-circuit potential (OCP) of the sample serves this purpose, but this has two drawbacks: the OCP of an immersed sample often fluctuates even after an extended equilibrium time, and E_{corr} is measured over an actively corroding surface undergoing surface changes. Secondly, the assumption that electrode kinetics are Tafel in nature is most valid at high overpotentials. For small overpotentials, the current rather than the log current is proportional to potential; this is the regime of polarization resistance.²⁹ For this reason, the model is not expected to be a good fit in this region and so goodness of fit statistics should account for this. To this end, a weighting function has been developed (Figure 2.3 A) to place higher value on statistical comparison in the Tafel region as opposed to the polarization resistance region. A narrow region of 10 mV has been chosen to investigate the difference between weighted and unweighted values while retaining as much information as possible over the entire curve.

The potential dependence of the three chosen statistics for a PDP performed on pure

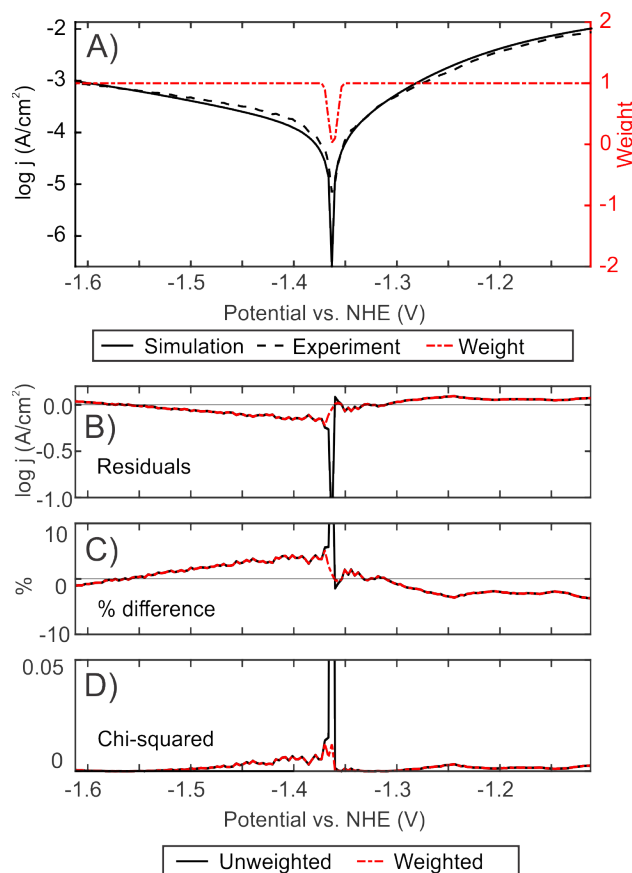


Figure 2.3 – Weighted and unweighted comparison statistics for a polarization curve on pure Mg performed at a scan rate of 10 mV/s in 0.10 M NaCl. The following parameters were simulated: $E_{corr} = -1.362$ V vs. NHE, $j_{corr} = 120 \mu\text{A}/\text{cm}^2$, $\beta_a = 80$ mV, $\beta_c = -220$ mV, $j_{lim,c} = 3000 \mu\text{A}/\text{cm}^2$.

Mg (Figure 2.3) communicate the same information about regions where the fit is better or worse. In practice, using these metrics to compare two sets of parameters and draw overall conclusions about goodness of fit requires summarizing the values for each point of comparison as an aggregate (residuals, chi-squared) or average (% difference). At this point, the differences between metrics becomes evident. The sum of residuals provides higher sensitivity for selecting between two possible sets of parameters. Percent difference is an

Table 2.2 – Summarized statistics for the data fits shown in [Figure 2.2](#) and [Figure 2.3](#). U refers to unweighted values, W refers to values determined using a weighting function which reduces the weight of values determined for $|\eta| < 10$ mV.

Alloy	Scan rate (mV/s)	Number of points	Sum of log residuals (A/cm ²)	% difference	Sum of chi- squared
Pure Mg	0.167	388	U: 10.91	U: 2.80%	U: 3.06
			W: 8.90	W: 2.60%	W: 2.50
	10	185	U: -1.44	U: 2.30%	U: 0.74
			W: 0.03	W: 2.13%	W: 0.34
AM60	0.167	186	U: -7.63	U: 2.76%	U: 1.32
			W: -6.18	W: 2.55%	W: 1.13
A516	0.167	171	U: 0.78	U: 2.61%	U: 1.18
			W: 1.29	W: 2.20%	W: 0.49
S444	0.167	797	U: 3.38	U: 0.49%	U: 0.44
			W: 5.43	W: 0.45%	W: 0.37

intuitive metric that is independent of the order of magnitude of currents observed and thus generalizable across samples. The chi-squared sum retains the proportionality of percent difference, though it loses the sensitivity to sign with respect to the simulation over- or underestimating measured currents. When the chi-squared goodness of fit test was used to examine goodness of fit, fits that appeared both good and poor passed the test, suggesting this is not a suitable metric for this system. Residuals and percent difference are better characterizations of goodness of fit, the former for comparing two fits and the latter for comparing the final fit to experimental results.

As seen in [Table 2.3](#), the fit for pure Mg samples scanned at 0.167 mV/s ([Figure 2.2 A](#))

Table 2.3 – Summary of the Tafel parameters obtained for pure Mg at different scan rates. Data corresponds to that shown in [Figure 2.2A](#) (0.167 mV/s) and [Figure 2.3](#) (10 mV/s).

Scan rate (mV/s)	E_{corr} (V vs. NHE)	j_{corr} ($\mu\text{A}/\text{cm}^2$)	β_a (mV/decade)	β_c (mV/decade)	$j_{lim,c}$ ($\mu\text{A}/\text{cm}^2$)
0.167	-1.192	80	10	-220	3000
10	-1.362	120	80	-220	3000

and 10 mV/s ([Figure 2.3](#)) is an excellent match statistically (<3% difference) though the fits are very different. The lower E_{corr} and higher β_a obtained for faster scan rates are consistent with previous methods studies,³² which explained this difference in terms of a disturbance in the charging current. If scanned too quickly, the double layer formed at the metal surface will not reach equilibrium before the measurement is taken and so the non-Faradaic contributions to the overall current will be larger. The larger this effect (the faster the scan rate), the larger the change in E_{corr} . This highlights one of the limitations of the model, which is reliance upon trusted experimental data. The extracted parameters are specific to a given data set, and so drawing conclusions about overall sample behaviour still requires a consideration of the experimental conditions and associated studies on reproducibility.

2.3.4 Analysing Diffusion-Limited Current Densities in Terms of Solution Mass Transport

A full description of the underlying equations used can be found in the Appendix B. The basic version of the model described earlier is suitable for data treatment, with good comparison between Tafel parameters determined using traditional methods and those optimized via simulation for activation-controlled systems. Furthermore, the model provides access to these parameters in diffusion-controlled systems where traditional methods fail. To understand these diffusion-limited current densities requires a detailed description of the chemical reactions involved and the environment both prior to and during corrosion, with the concentration, charge, and mobility of all electroactive species and the supporting electrolyte explicitly specified (Table B.1.3). The current distribution within the electrolyte is described by the following:

$$\nabla \cdot i_l = F \sum_i z_i R_i + Q_l \quad (2.10)$$

Where i_l is the current measured at the electrode/electrolyte interface, F is Faraday's constant, z_i and R_i are the charge and flux of species i respectively, and Q_l is the charge within the electrolyte.

The flux of species (Equation 2.11) is calculated as the sum of contributions from mass

transfer (Equation 2.12) and chemical reaction (Equation 2.13) as described by:

$$R_i = \frac{\partial c_i}{\partial t} + \nabla \cdot N_i \quad (2.11)$$

$$N_i = -D_i \nabla c_i - z_i u_i F c_i \nabla \phi_l \quad (2.12)$$

$$R_{i,m} = -\frac{\nu_{i,m} i_{loc,m}}{n_m F} \quad (2.13)$$

Where c_i is the concentration, D_i the diffusion coefficient, and u_i the mobility of species i . With respect to reaction m , $R_{i,m}$ is the flux of species i , $\nu_{i,m}$ the stoichiometry coefficient, $i_{loc,m}$ the Faradaic current, and n_m the number of electrons transferred during reaction. The total current at the electrode surface is calculated according to Equation 2.10.

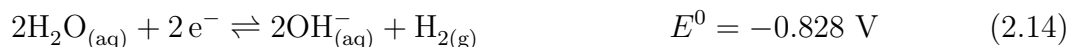
To reduce the computational power needed to solve this system, a 2D-axisymmetric geometry was used to reduce the dimensionality of the model. The polarization curves simulated previously were rerun in the new geometry to confirm neither the geometry nor the physics change affected the measured currents.

Accurate mass transport within solution was validated through comparison of calculated transport numbers to literature values available for electrolytes of equivalent concentration. These transport numbers were determined from a simulated chronoamperogram performed at $E_{corr} + 300$ mV. For a given ion in solution, this was calculated as the current associated with diffusive and migratory flux of this ion within the electrolyte domain relative to the total current within this domain. For an equivalent electrolyte concentration of 0.1 M NaCl, the

calculated transport numbers are 0.3963 and 0.6037 for Na^+ and Cl^- respectively compared to 0.3854 and 0.6146 in the literature;²⁴ these agree within 3%. The change in these values over the course of the experiment due to the formation of new charged species is negligible (Figure B.2)

The kinetics of reactions at the WE and CE are described using the same Tafel relationships as in 2.3.2.2 where the limiting current densities previously determined can now be analysed in terms of the reactions occurring at the surface. All standard potentials given are versus NHE.²⁴

For the Mg-based samples, the reactions considered were:



For the Fe-based samples, the reactions considered were:



The cathodic reaction is determined by the range of potentials considered: Mg begins corroding at potentials where the rate of hydrogen evolution is much faster than that of oxygen reduction, whereas the opposite is true for Fe. Further reactions of the metal cations to form solid oxides/hydroxides have not been included at this stage of model development,

but could be incorporated in the future. To understand the source of anodic and cathodic limiting current densities, a simulation was performed using the kinetic parameters previously extracted for pure Mg and S444 (Table 2.1). The concentration profiles of protons, metal ions, and dissolved gases were examined as a function of distance from the corroding sample in each case.

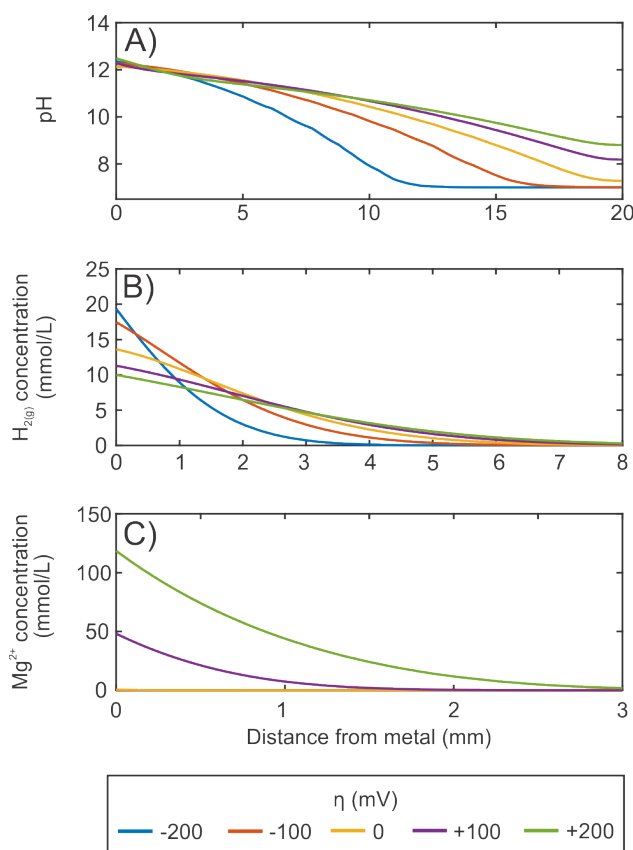


Figure 2.4 – Simulated distance-concentration relationship of (A) pH, (B) $\text{H}_{2(g)}$, and (C) Mg^{2+} during a PDP with the following Tafel parameters: $E_{corr} = -1.192$ V vs. NHE, $j_{corr} = 80 \mu\text{A}/\text{cm}^2$, $\beta_a = 10$ mV, $\beta_c = -220$ mV, $j_{lim,c} = 3000 \mu\text{A}/\text{cm}^2$. The concentration profiles for $\eta = -200, -100, 0, 100$ and 200 mV were sampled at $t = 600, 1200, 1800$ s, 2400 and 3000 s after the potential step respectively.

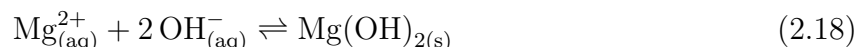
The concentration profiles calculated for a PDP on pure Mg (Figure 2.4) for $E < E_{corr}$

are important for examining the $j_{lim,c}$ observed in 2.3.2.2. When mass transport limited currents are present in the cathodic branch, possible causes include low availability of H_2O to react at the surface or blocking behaviour of the produced $H_{2(g)}$. Negligible Mg^{2+} has formed at these potentials and so transport of the metal ion through the oxide film is not a factor in this phenomenon. As the concentration of water as a solvent far exceeds everything else in solution and is essentially constant near the electrode, the most likely scenario is the produced $H_{2(g)}$ participating in surface blocking. This is consistent with the high activity of magnesium alloys towards hydrogen evolution.⁴⁸ This hypothesis could be verified by modifying the experimental setup to introduce convection or sonication. If this modification removed the diffusion limitation, it would provide strong evidence for the role of $H_{2(g)}$ formation in reducing the electroactive surface area. This modification would require careful monitoring of the corrosion product to ensure the agitation did not cause premature damage or delamination of this partially protective layer.

From the concentration profile of $H_{2(g)}$ observed in Figure 2.4 B, the region of high $H_{2(g)}$ concentration extends quite far into solution (mm scale) for a PDP performed at the slow scan rates suggested by standardized methods.⁴⁹ The size of this region will also depend on the scan rate and potential range employed: faster scans over a narrower potential range should see this effect to a lesser degree due to reduced hydrogen depletion near the electrode at the same overpotential. As the potential increases to give $E > E_{corr}$, the trend is consistent with previous time points. This is inconsistent with the negative difference effect (NDE) observed on Mg alloys, where the rate of hydrogen evolution increases with current density during anodic dissolution of the metal.⁴⁸ This is due to the applied kinetics being Tafel in nature: a

model that encompasses the NDE would require a more complex treatment of the cathodic reaction. The mechanism giving rise to the NDE has been debated since the 1950's, but theories proposed over the years include reductive desorption of adsorbed OH,⁵⁰ increase in the exchange current density during Mg dissolution,⁵¹ and presence of Fe inclusions acting as local cathodes.⁵²

As mentioned previously, the equations considered in this simulation do not currently include the formation of magnesium hydroxide:



This assumption should only effect the concentration profiles observed for where Mg^{2+} begins to be formed.

The concentration profiles calculated for a PDP on S444 (Figure 2.5) for $E > E_{\text{corr}}$ are of interest for examining the $j_{\text{lim},a}$ observed in 2.3.2.2. The mass transport limiting currents observed in this branch can be related to Equation 2.17 where Fe dissolution is the dominant reaction. Stainless steels are well known for their corrosion resistance in aqueous environments due to the high amounts of chromium present in the alloy.⁵³ Chromium forms a thin passivating oxide film over the metal surface. Fe dissolution is still the dominant reaction but the rate slows down due to hindered transport of species through this film. When a current plateau is observed in the anodic branch, this film is stable: current increases associated with pitting initiation and passive film breakdown are not observed until much higher overpotentials are applied than those simulated here.

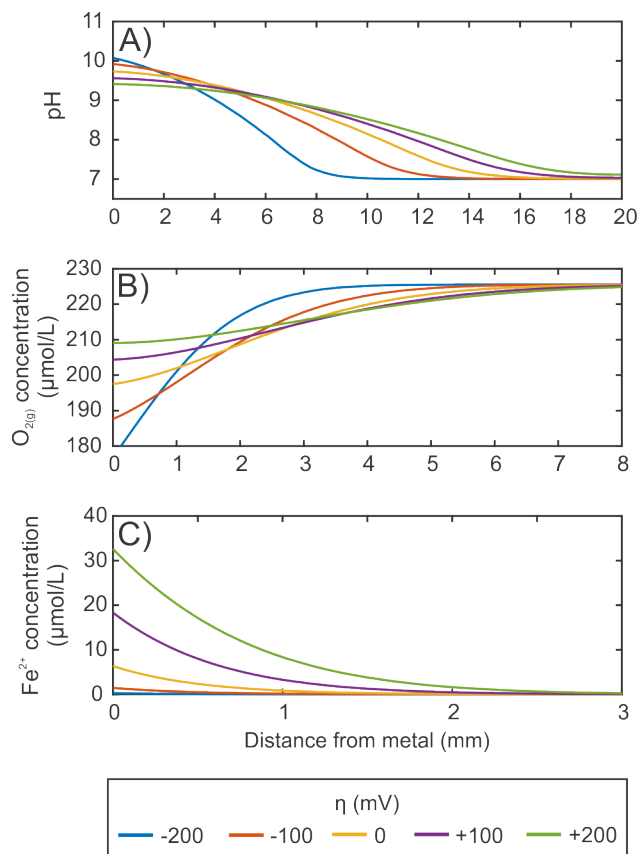


Figure 2.5 – Simulated distance-concentration relationship of (A) pH, (B) $O_{2(g)}$, and (C) Fe^{2+} during a PDP with the following Tafel parameters: $E_{corr} = -0.114$ V vs. NHE, $j_{corr} = 0.20 \mu\text{A}/\text{cm}^2$, $\beta_a = 140$ mV, $\beta_c = -200$ mV, $j_{lim,a} = 0.5 \mu\text{A}/\text{cm}^2$. The concentration profiles for $\eta = -200, -100, 0, 100$ and 200 mV were sampled at $t = 600, 1200, 1800$ s, 2400 and 3000 s after the potential step respectively.

The question is therefore whether it is the hindered transport of oxygen or of dissolved Fe^{2+} through the film that has the largest impact on the currents measured. [Figure 2.5](#) considers the concentration profiles of both these species in the absence of a passive film. Under these conditions, the region of high Fe^{2+} concentration is limited to a much smaller distance from the sample than that of low $O_{2(g)}$. This region will be compressed if diffusion away from the surface is hindered. This has the potential to produce a steep concentration

gradient, reducing the rate of further Fe dissolution.

2.4 Conclusions

The model developed in this work is able to treat polarization curves in a systematic fashion in order to extract information about the underlying corrosion properties. Traditional analytical procedures tend to treat the system as either activation-controlled and extract Tafel slopes or as diffusion controlled and extract a limiting current density; the ability to consider both contributions to current is useful for systems with intermediate behaviour that do not behave as either one of these two idealized cases. This allows for the analysis of a broader material scope. In this work, both extremely active magnesium-based alloys and extremely passivated stainless steels, ranging over 1 V difference in E_{corr} and two orders of magnitude difference in j_{corr} . The usefulness of common goodness of fit statistics has been assessed, with the sum of residuals and percent difference providing the strongest insight into the accuracy of the fits determined, with excellent agreement between simulation and experiment within 3% difference. The fits determined agree both with statistics and literature where comparison values are available, with similar Tafel slopes observed to previous studies on magnesium and similar corrosion currents observed to previous studies on stainless steel.

As presented, the model neglects the formation of solid species. Future work will build upon the model developed here in order to include the formation of oxides and hydroxides as a corrosion product, accounting for the corresponding effect on surface topography. The model may also be extended to examine localized corrosion processes such as pitting or micro

galvanic corrosion, though this would require considering a much smaller geometry to avoid generating meshes with unreasonably high element numbers as discussed in [1.3.2.2.1](#).

References

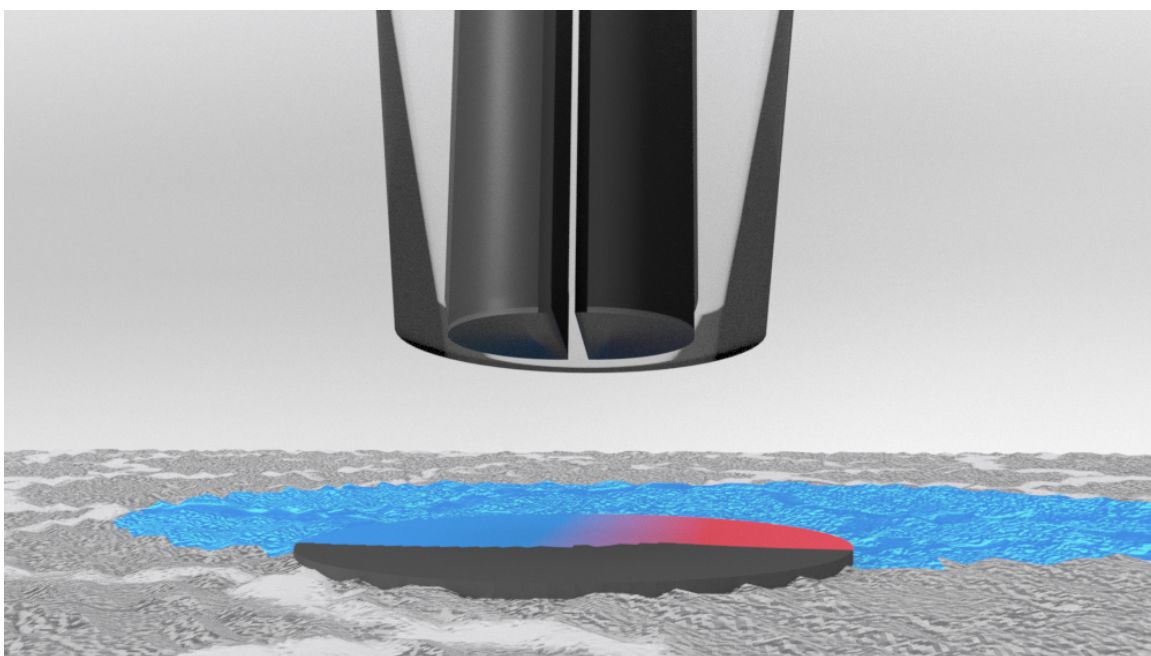
- [1] Sharland, S. M. *Corrosion Science* **1987**, *27*, 289–323.
- [2] Gunasegaram, D. R.; Venkatraman, M. S.; Cole, I. S. *International Materials Reviews* **2014**, *59*, 84–114.
- [3] Sridhar, N. *CORROSION* **2017**, *73*, 18–30.
- [4] Srinivasan, J.; Liu, C.; Kelly, R. G. *Journal of the Electrochemical Society* **2016**, *163*, C694–C703.
- [5] Atrens, A.; Shi, Z.; Song, G.-L. *Corrosion of Magnesium Alloys*; Elsevier, 2011; pp 455–483.
- [6] Stenta, A.; Basco, S.; Smith, A.; Clemons, C.; Golovaty, D.; Kreider, K.; Wilder, J.; Young, G.; Lillard, R. *Corrosion Science* **2014**, *88*, 36–48.
- [7] Munn, R. S.; Devereux, O. F. *CORROSION* **1991**, *47*, 618–634.
- [8] Song, G. L. *Corrosion Science* **2010**, *52*, 455–480.
- [9] Sun, W.; Nešić, S. *CORROSION* **2009**, *65*, 291–307.
- [10] Kahyarian, A.; Singer, M.; Nesic, S. *Journal of Natural Gas Science and Engineering* **2016**, *29*, 530–549.
- [11] Melchers, R. *Corrosion Science* **2003**, *45*, 923–940.
- [12] Gaudet, G. T.; Mo, W. T.; Hatton, T. A.; Tester, J. W.; Tilly, J.; Isaacs, H. S.; Newman, R. C. *American Institute of Chemical Engineers Journal* **1986**, *32*, 949–958.
- [13] Laycock, N. J.; Newman, R. C. *Corrosion Science* **1997**, *39*, 1771–1790.
- [14] Marcus, P.; Maurice, V.; Strehblow, H. H. *Corrosion Science* **2008**, *50*, 2698–2704.
- [15] Martín-Pérez, B.; Pantazopoulou, S.; Thomas, M. *Computers & Structures* **2001**, *79*, 1251–1264.
- [16] Walton, J. C. *Corrosion Science* **1990**, *30*, 915–928.
- [17] Song, F. M.; Jones, D. A.; Kirk, D. W. *CORROSION* **2005**, *61*, 145–152.
- [18] Keating, A.; Nešić, S. *CORROSION* **2001**, *57*, 621–633.
- [19] Walton, J.; Cragnolino, G.; Kalandros, S. *Corrosion Science* **1996**, *38*, 1–18.

-
- [20] Jia, J. X.; Song, G.; Atrens, A. *Corrosion Science* **2006**, *48*, 2133–2153.
- [21] Jia, J. X.; Atrens, A.; Song, G.; Muster, T. H. *Materials and Corrosion* **2005**, *56*, 468–474.
- [22] Tait, W. S. *An introduction to electrochemical corrosion testing for practicing engineers and scientists*, 1st ed.; PairODocs Publications: Racine, WI, USA, 1994.
- [23] Poorqasemi, E.; Abootalebi, O.; Peikari, M.; Haqdar, F. *Corrosion Science* **2009**, *51*, 1043–1054.
- [24] Bard, A. J.; Faulkner, L. R. *Electrochemical Methods: Fundamentals and Applications*, 2nd ed.; John Wiley & Sons: New York, NY, USA, 2001.
- [25] Zoski, C. G. *Handbook of Electrochemistry*; Elsevier B.V.: Amsterdam, Netherlands, 2007.
- [26] Song, G.; Atrens, A.; Dargusch, M. *Corrosion Science* **1998**, *41*, 249–273.
- [27] Zhao, M. C.; Schmutz, P.; Brunner, S.; Liu, M.; Song, G.-l.; Atrens, A. *Corrosion Science* **2009**, *51*, 1277–1292.
- [28] Shi, Z.; Liu, M.; Atrens, A. *Corrosion Science* **2010**, *52*, 579–588.
- [29] Bard, A. J., Stratmann, M., Frankel, G. S., Eds. *Encyclopedia of Electrochemistry Volume 4: Corrosion and Oxide Films*; Wiley-VCH, 2003.
- [30] Xu, L.; Cheng, Y. *Corrosion Science* **2013**, *73*, 150–160.
- [31] Ge, J.; Isgor, O. B. *Materials and Corrosion* **2007**, *58*, 573–582.
- [32] Zhang, X. L.; Jiang, Z. H.; Yao, Z. P.; Song, Y.; Wu, Z. D. *Corrosion Science* **2009**, *51*, 581–587.
- [33] Flitt, H. J.; Schweinsberg, D. P. *Corrosion Science* **2005**, *47*, 3034–3052.
- [34] Mansfeld, F.; Liu, G.; Xiao, H.; Tsai, C.; Little, B. *Corrosion Science* **1994**, *36*, 2063–2095.
- [35] Sawyer, D. T.; Sobkowiak, A.; Roberts, J. L. *Electrochemistry for Chemists*, 2nd ed.; John Wiley & Sons: New York, NY, USA, 1995; p 207.
- [36] Liu, W.; Cao, F.; Chen, A.; Chang, L.; Zhang, J.; Cao, A. *CORROSION* **2012**, *68*, 045001–1 – 045001–14.
- [37] Song, G.; Atrens, A.; Wu, X.; Zhang, B. *Corrosion Science* **1998**, *40*, 1769–1791.
- [38] King, A. D.; Birbilis, N.; Scully, J. R. *Electrochimica Acta* **2014**, *121*, 394–406.
- [39] Song, G.; Atrens, A. *Advanced Engineering Materials* **2003**, *5*, 837–858.

-
- [40] Babić, R.; Metikoš-Huković, M. *Journal of Applied Electrochemistry* **1993**, *23*, 352–357.
- [41] Cheng, Y. F.; Rairdan, B. R.; Luo, J. L. *Journal of Applied Electrochemistry* **1998**, *28*, 1371–1375.
- [42] Bitondo, C.; Bossio, A.; Monetta, T.; Curioni, M.; Bellucci, F. *Corrosion Science* **2014**, *87*, 6–10.
- [43] Cutress, I. J.; Dickinson, E. J. F.; Compton, R. G. *Journal of Electroanalytical Chemistry* **2010**, *638*, 76–83.
- [44] Davies, T. J.; Moore, R. R.; Banks, C. E.; Compton, R. G. *Journal of Electroanalytical Chemistry* **2004**, *574*, 123–152.
- [45] Ordeig, O.; Banks, C. E.; Davies, T. J.; del Campo, J.; Muñoz, F. X.; Compton, R. G. *Journal of Electroanalytical Chemistry* **2006**, *592*, 126–130.
- [46] Kuss, C.; Payne, N. A.; Mauzeroll, J. *Journal of the Electrochemical Society* **2016**, *163*, H3066–H3071.
- [47] Liu, C.; Bi, Q.; Leyland, A.; Matthews, A. *Corrosion Science* **2003**, *45*, 1243–1256.
- [48] Song, G.; Atrens, A.; Stjohn, D.; Nairn, J.; Li, Y. *Corrosion Science* **1997**, *39*, 855–875.
- [49] ASTM, *Book of Standards Volume 03.02 Corrosion of Metals; Wear and Erosion*; ASTM International: West Conshohocken, PA, 2004; pp 1–5.
- [50] Taylor, C. D. *Journal of the Electrochemical Society* **2016**, *163*, C602–C608.
- [51] Frankel, G.; Samaniego, A.; Birbilis, N. *Corrosion Science* **2013**, *70*, 104–111.
- [52] Williams, G.; Birbilis, N.; McMurray, H. *Electrochemistry Communications* **2013**, *36*, 1–5.
- [53] Olsson, C. O. A.; Landolt, D. *Electrochimica Acta* **2003**, *48*, 1093–1104.

Chapter 3

Altered Spatial Resolution of Scanning Electrochemical Microscopy Induced by Multifunctional Dual Barrel Microelectrodes



Chapter Abstract

Chapter 2 focused on the macroscale characterization of surface activity or passivity that can be observed by PDP. This technique can also be used to identify the onset of localized processes, for which microscale techniques like SECM are more suitable for further investigation. In **Chapter 2**, the parameterization of the current-potential relationship allowed the contribution of mass transport limitations to be separated from the overall current measured. SECM has the same challenge of signal convolution, where both local topography and reactivity contribute to the signal measured. Multifunctional microelectrodes are a class of probe designed to separate out convoluted signals such as these by incorporating a second sensor into the same device. Though several different geometries of these have been developed, straightforward adaptation of a pyrolytic deposition procedure for creating carbon microelectrodes has made dual-barrel probes created from theta pipettes a popular design choice.

This chapter presents a 3D finite element model for examining the theoretical behaviour of dual-barrel microelectrodes for use in SECM operating in a tandem feedback / generation-collection configuration. The signal measured from a microelectrode is known to be highly sensitive to the electrode shape, as this shape determines the diffusion profile of electroactive species. This model compares simulated SECM images of the same substrate imaged using both standard and multifunctional microelectrode. It reveals that dual-barrel electrodes can produce imaging distortions under select conditions, and outlines a set of experimental conditions where this effect is strongest.

The work presented in this chapter is reproduced from:

Stephens, L.I.; Mauzeroll, J. Altered spatial resolution of scanning electrochemical microscopy induced by multifunctional dual barrel microelectrodes. *Analytical Chemistry* **2018**, 90(11), 6796-6803.

3.1 Introduction

Multifunctional microelectrodes have promising applications in the field of high speed electrochemical imaging, allowing local *in situ* measurements of kinetics, pH, and topography to be performed consecutively rather than concurrently.^{1,2} The challenges associated with aligning microscopy techniques are eliminated by integrating multiple electrodes (probes) into the same sensor. A broad range of multifunctional probe geometries have been fabricated, including modified AFM tips,³⁻⁵ crescent moons,⁶⁻⁸ multi-barrel,⁹⁻¹⁴ and disk^{15,16} geometries that are suitable for tandem techniques involving scanning electrochemical microscopy (SECM),^{14,17} scanning ion conductance microscopy (SICM),^{2,6-8,10-13,17} scanning droplet methods (SDM),^{9,12,15,18} atomic force microscopy (AFM),^{1,4,5,19,20} and others.¹⁵ These techniques have been used to study substrates such as nanoparticles and nanocrystals,^{10,12,13,18} corroding materials,^{3,21} single membrane pores,^{4,5,7,17} and biological samples.^{11,14,16,20} Despite this extensive development in multifunctional microelectrodes, the relationship between probe shape and response remains underdeveloped for multifunctional microelectrodes outside of discussions of probe size.

Since an SECM signal is a result of local fluxes to the entire electrode surface, the currents measured are strongly influenced by the shape as well as the size of the probe. Traditional quantitative procedures for extraction of local kinetics using SECM²² and topography extraction using SICM²³ are based on symmetrical disk-shaped probes, which have a well-defined hemispherical diffusion pattern. This allows data collected using different probes to be compared, which is not possible for multifunctional probes. Though multifunctional probes also

display a steady state current that can be used for normalization, the theory connecting the probe shape to this steady state current is less developed.¹⁷ Commonly, the currents and distances are not normalized because the critical probe dimension to use could be either the major and minor radius. In these cases, numerical simulations can be used to quantify changes in local reactivity. The lack of symmetry in many of these geometries necessitates a change from the 2D-axisymmetric models commonly used²⁴ to more computationally intensive 3D models. 3D numerical models have been used to study disk,¹⁶ modified AFM,²⁵ and multi barrel^{11,13,14} multifunctional microelectrodes. However, previous efforts have focused on fitting a particular experiment rather than a generalized description of probe behaviour.

In this work, we use 3D finite element modelling to systematically study the relationship between probe geometry, experimental conditions, and current response for dual-barrel electrodes used in SECM feedback mode measurements. A model substrate containing local reactive features is used to examine the effects of tip-substrate distance, feature size, electrolyte composition, and feature shape. The electrode shape has been observed to have a significant influence on the spatial resolution of the technique, with the non-uniform diffusion profile to the electrode surface producing distortions in the shape of the imaged feature, leading to erroneous conclusions about the local reactivity of the substrate. The relationship between diffusion profile and image blurring in SECM has been noted previously for disk shaped probes, and the same approach of image correction using a point spread function could be applied to these systems in the future.²⁶

A set of conditions under which the distortion at dual barrel multifunctional probes occurs is proposed; in short, this effect is strongest at small tip-substrate distances (as commonly

employed in feedback measurements) for features equal to or smaller than the size of probe. This poses a challenge for optimizing experimental measurements, which must balance the improved sensitivity at small distances with the more accurate feature resolution at large distances.

3.2 Experimental Section

3.2.1 Finite Element Simulations

A full 3D model was built using COMSOL Multiphysics version 5.3 to simulate probes of varying geometry based on the dual barrel geometry motif, with an isolated electrode in each barrel (see supporting information for full model details). Three geometries have been investigated ([Figure 3.1 i](#)): a disk, single barrel, and dual barrel electrode. Though the single barrel electrode simulated does not have multifunctional capability, it is provided for comparison as an intermediate geometry between the disk and dual barrel electrodes.

Due to the additional computational difficulty associated with solving 3D geometries where symmetry simplifications cannot be made, this work has focused on systems where diffusion is the dominant mass transport mechanism in solution. Both convection and migration are assumed to be negligible. These physics reduce the computational time and so allow the effect of various experimental variables on the relationship between probe geometry and current response to be studied more comprehensively. This methodology may be extended in the future to include migrational effects, allowing it to be used to study techniques such

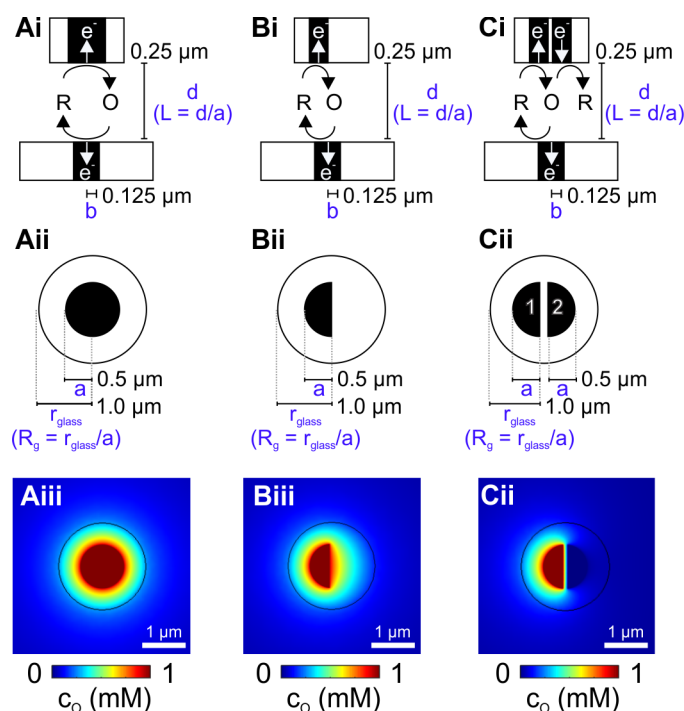


Figure 3.1 – Schematic of the feedback and redox competition processes possible between a model substrate consisting of a flat conductive disk in insulating surroundings and (A) Disk (B) Single barrel and (C) Dual barrel electrode geometries. (i) Substrate dimensions and normalization procedures used. Parameter names are given in blue, their values in black. In all cases, tip-substrate distance and r_{glass} have been normalized to the electrode radius a for comparison to the disk. (ii) Electrode dimensions. (iii) Steady state concentration profile of species O in the plane of the electrode/electrolyte interface.

as SICM.

To investigate this relationship, current maps have been calculated for each probe geometry during a feedback based SECM measurement over a model substrate consisting of a circular conductive disk (herein referred to as a substrate feature) in an insulating bulk matrix. At close tip-substrate distances, a positive feedback loop forms between electrode and substrate feature, and a negative feedback loop between electrode and bulk substrate. In the case of the dual barrel electrode, the response under generation-collection conditions

is investigated (Figure 3.1 Cii), where the oxidized species produced at the first electrode (O) is then reduced again at the second. Under these conditions, two additional processes are possible: redox competition with the substrate feature and generation-collection with the other electrode. In this case, the concentration profiles at the electrode surface (Figure 3.1 ii) show differences between all three geometries, and the uniform shape and size of the diffusion layer to the disk electrode is not observed for either of the barrel geometries, with a reduction in size present at the corners along the flat side of the electrode.

This work has considered the effect of four experimental variables on these measurements (Figure 3.2 i-ii): tip-substrate distance (L), feature size (b), electrolyte composition (f_R), and feature shape, where L is the tip-substrate distance d normalized by the electrode radius a , b is the radius of the reactive substrate feature, and f_R is the fraction of mediator initially in the reduced form ($f_O = 1 - f_R$). For comparison to disk-shaped measurements, distance normalization and R_g calculation is based on the electrode radius (Figure 3.1). Currents have not been normalized to a steady state, to highlight the different current scales between electrode geometries. The standard set of initial conditions were selected based on the usual size of dual barrel electrodes with radii between 100 - 1000 nm^{10,14} and basic tenets of feedback-based measurements, where the best spatial resolution is obtained at the smallest tip-substrate distances. These starting conditions were $a = 500$ nm, $R_g = 2$, $L = 0.5$, $b = 250$ nm, and $f_R = 1$, where R_g is the normalized radius of the insulating glass sheath.

The current for each electrode position was calculated by solving the steady state Nernst-Planck equation under the mass transport conditions described earlier (Equation 3.1). The

electrode position was rastered to generate a current map of the substrate.

$$\frac{\partial c_i}{\partial t} = 0 = \nabla \cdot (D_i \nabla c_i) + R_i \quad (3.1)$$

Where c_i , D_i , and R_i are the concentration, diffusion coefficient, and reaction-induced flux of species i respectively. It is assumed that $D_O = D_R = D$, with ferrocenemethanol chosen as a model redox mediator and therefore $D = 6.7 \times 10^{-10} \text{ m}^2/\text{s}$.²⁷

At the electrode surface, a diffusion-controlled oxidation takes place (Equation 3.2). At the surface feature and second electrode in the dual barrel, a diffusion-controlled reduction takes place (Equation 3.3). At all other surfaces, a no flux boundary condition is applied (Equation 3.4).

$$R_O = k_{\text{tip}} \times c_R \quad R_R = -k_{\text{tip}} \times c_R \quad (3.2)$$

$$R_O = -k_{\text{tip}} \times c_O \quad R_R = k_{\text{tip}} \times c_O \quad (3.3)$$

$$R_O = 0 \quad R_R = 0 \quad (3.4)$$

Where k_{tip} is the rate constant at the electrode, set to an arbitrarily large value of 1×10^4 as is typical in simulations of feedback mode SECM.^{25,28}

A sufficiently large electrolyte volume of $100a$ in all directions is modelled such that the concentrations of oxidized and reduced species at the edge are not influenced by the reactions

at the tip, and so a concentration boundary condition is applied at the edges as follows:

$$c_O = c_{O,bulk} \quad c_R = c_{R,bulk} \quad (3.5)$$

Where $c_{R,bulk} = 1$ mM and $c_{O,bulk} = 0$ mM.

3.2.2 Hardware and Solver Parameters

All simulations were performed on a high-performance computer consisting of a dual core Intel i7 processor (3.40 GHz) equipped with 12 GB of RAM and an SSD. A relatively dense mesh consisting of approximately 100,000 finite elements was introduced to the geometry, with maximum size restrictions of $0.075a$ applied to all reacting boundaries and maximum growth rate of 1.3 applied within the electrolyte. The relative solver tolerance was set to 1×10^{-10} . Under these conditions, each current map took approximately 12 hours to calculate. Accurate mesh behaviour and solver tolerance were determined through comparison of approach curves with a disk electrode over a uniformly reacting substrate to the analytical approximations for pure feedback behavior (Figure C.6).²²

3.2.3 Data Analysis

All data was analysed using MATLAB 2017b. Each current map consisted of 2601 evenly spaced data points (51x51 grid). Contour plots and aspect ratios were constructed from interpolated maps, after verifying the differences between the interpolated and directly calculated maps were negligible (Figure C.5).

3.3 Results and Discussion

3.3.1 Effect of Tip-Substrate Distance

The tip to substrate distance is arguably the most significant experimental parameter in feedback mode SECM, since the electrode needs to be close enough for a feedback loop to form. The greatest sensitivity is therefore obtained for $L < 1$, when species produced at the surface are within the hemispherical diffusion profile of a disk-shaped electrode.

Under these conditions of small L (Figure 3.2 Ai), the disk electrode shows both high sensitivity (contrast in current magnitude between regions of different reactivity) and high spatial accuracy (similarity in appearance between true and apparent shapes). In contrast, for the single and dual barrel electrodes (Figure 3.2 B-D), sensitivity is maximized at small L as expected, but spatial accuracy is decreased in two respects: the feature is compressed along the minor axis of the electroactive area, distorting the shape, and there is an offset of the apparent feature center. Both these changes are explained by the altered diffusion profile to the electrode tip. The size of the diffusion region to a symmetrical probe is uniform in shape and size (Figure 3.1 iii), but not for a dual barrel probe, meaning that at small tip-substrate distances the signal is strongly dependent on the orientation of the electrode over the substrate. At larger distances, diffusional broadening of the signal overwhelms the effect of the altered diffusion profile, producing a more accurate shape. This dependence on orientation also produces the offset in apparent position of the feature; the feedback loop cannot form until the probe reaches a position where it can interact with the substrate,

and the same response is not observed when either the glass or the generation-collection electrode are the dominant regions over the feature instead. This therefore has implications for electrode positioning methods. In this work, the position of the electrode is specified based on the center of the insulating glass sheath. Depending on the orientation of the electrode (Figure C.4), at electrode positions where the disk can form a feedback loop, either negative feedback or a redox competition process is occurring instead. This observation has implications for aligning SECM measurements with other microscopy techniques; an alignment via microscope might center the glass over the feature, while an alignment via an electrochemical signal might center the electroactive area over the feature.

As the electrode moves further away from the surface, the diffusion region widens, and this effect becomes less pronounced. This effect is monitored using isocurrent contours, extracted from maps at equally spaced L values of 0.25, 0.50, 0.75, and 1.00 (Figure 3.2 ii). The contours shown are rings of constant current, which outline the profile of the observed feature shape. In all cases, the contours extracted are $95 \pm 1\%$ of the maximum current calculated. Slight broadening is observed in the contours due to the reduced spatial resolution of the measurement at larger distances, when the contribution from the surrounding insulating matrix is proportionally higher. Notably, the compression of the circular feature for the two barrel-derived geometries is reduced at these distances; while the observed feature shape is not perfectly circular as in the true geometry, it is significantly closer, as evidenced by the maps at $L = 1$ (Figure 3.2 iii). While this has some promise for identifying experimental conditions suitable for use with existing probes, it poses a challenge: feedback sensitivity must be balanced with spatial accuracy. This has significant implications for quantitative

applications of SECM that rely on the high sensitivity including the extraction of local kinetics.²⁹

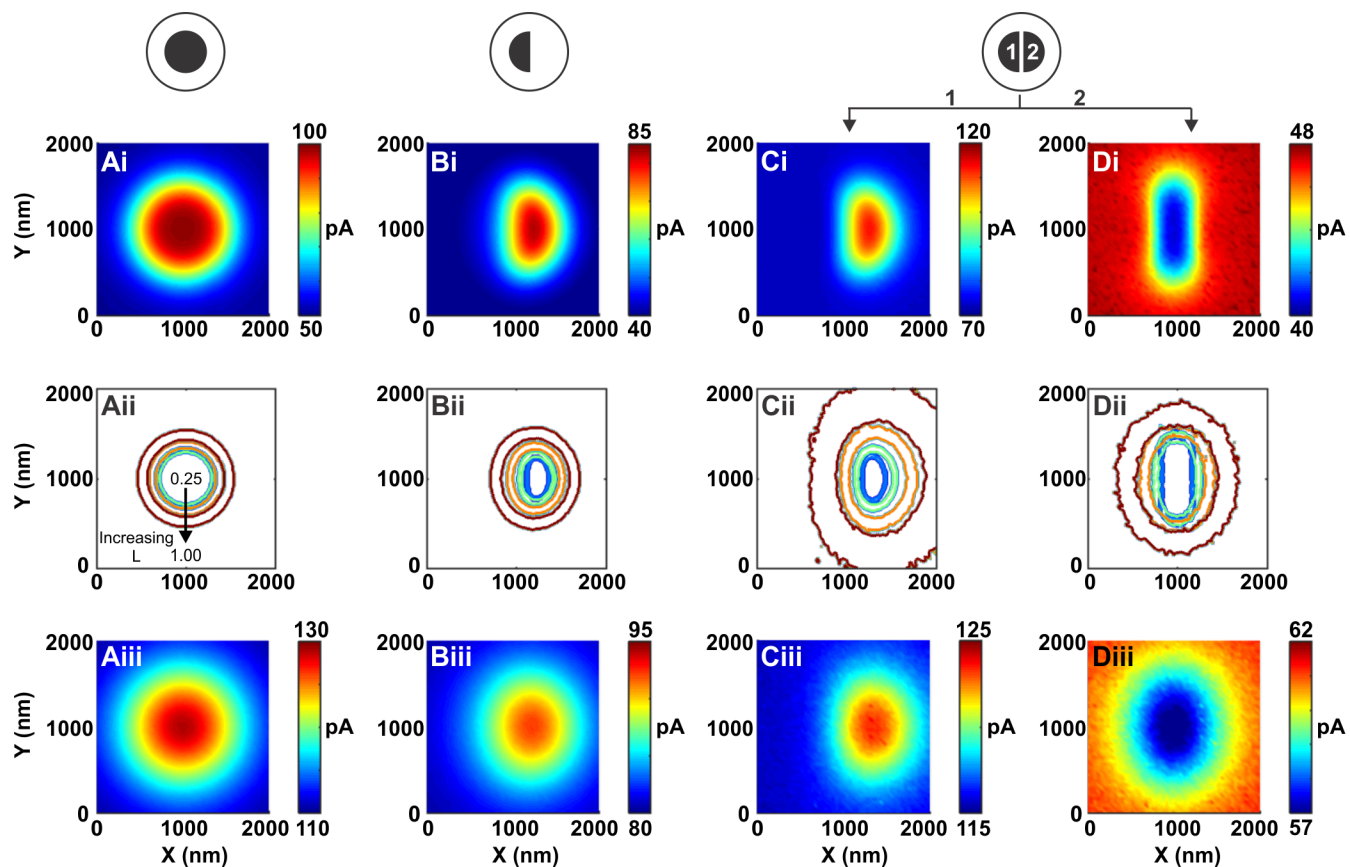


Figure 3.2 – Effect of tip-substrate distance on the current response of (A) Disk (B) Single barrel (C) Dual barrel (feedback) (D) Dual barrel (generation-collection) electrode geometries. The electrodes were oriented over the feature as pictured in Figure 3.1 during all calculations. (i) $L = 0.25$. (ii) Isocurrent contours of $95 \pm 1\%$ of the maximum (reduction) or minimum (oxidation) currents observed within maps of $L = 0.25, 0.5, 0.75, \text{ and } 1.00$. (iii) $L = 1.00$. All other parameters were held constant, with $b = 250$ nm, $a = 500$ nm, $R_g = 2$, and $f_R = 1$.

3.3.2 Effect of Feature Size

After the tip to substrate distance, the feature size has the largest influence on the measurement quality. In general, an experiment is usually designed so that the probe is smaller than the feature being imaged for optimal spatial resolution. This has spurred interest in nano-electrode fabrication.³⁰ This is particularly true for quantitative applications, as many of the methods for extracting local reactivity assume an approach curve sees a uniform substrate,²² an approximation which is only valid for small probes imaging large features. However, the hard restriction on minimum feature size is not probe size but a signal distinguishable from noise. Provided care is taken to minimize noise through the use of vibration isolating tables and Faraday cages, it is possible to use multifunctional probes to image features of the same or smaller size.¹⁰

As noted previously, under the standard set of conditions used in this work of $L = 0.5$ and $b = a/2$, a distortion in the circular feature is observed for the single and dual barrel electrodes (Figure 3.3 i). The extent of this distortion can be monitored through the aspect ratio (AR), which is calculated as the width/height of the $95 \pm 0.1\%$ isocurrent contour (Figure 3.3 ii). For a circular feature, this should be 1 regardless of feature size, as observed for the disk geometry (Figure 3.3 A). For the single and dual barrel electrodes, an $AR < 1$ is observed for a feature smaller to or equal to the probe radius, with a trend towards the ideal value. Notably, as the size ratio increases further, rather than asymptotically approaching the ideal ratio an $AR > 1$ is observed instead. As with tip-substrate distance, this relationship can be explained by the altered diffusion profile to the probe. The concentration profile in

the vicinity of the electrode/electrolyte interface (Figure 3.1 ii) does not extend evenly into solution from the electrode surface, but is broader along the minor radius of the single and dual barrel probes.

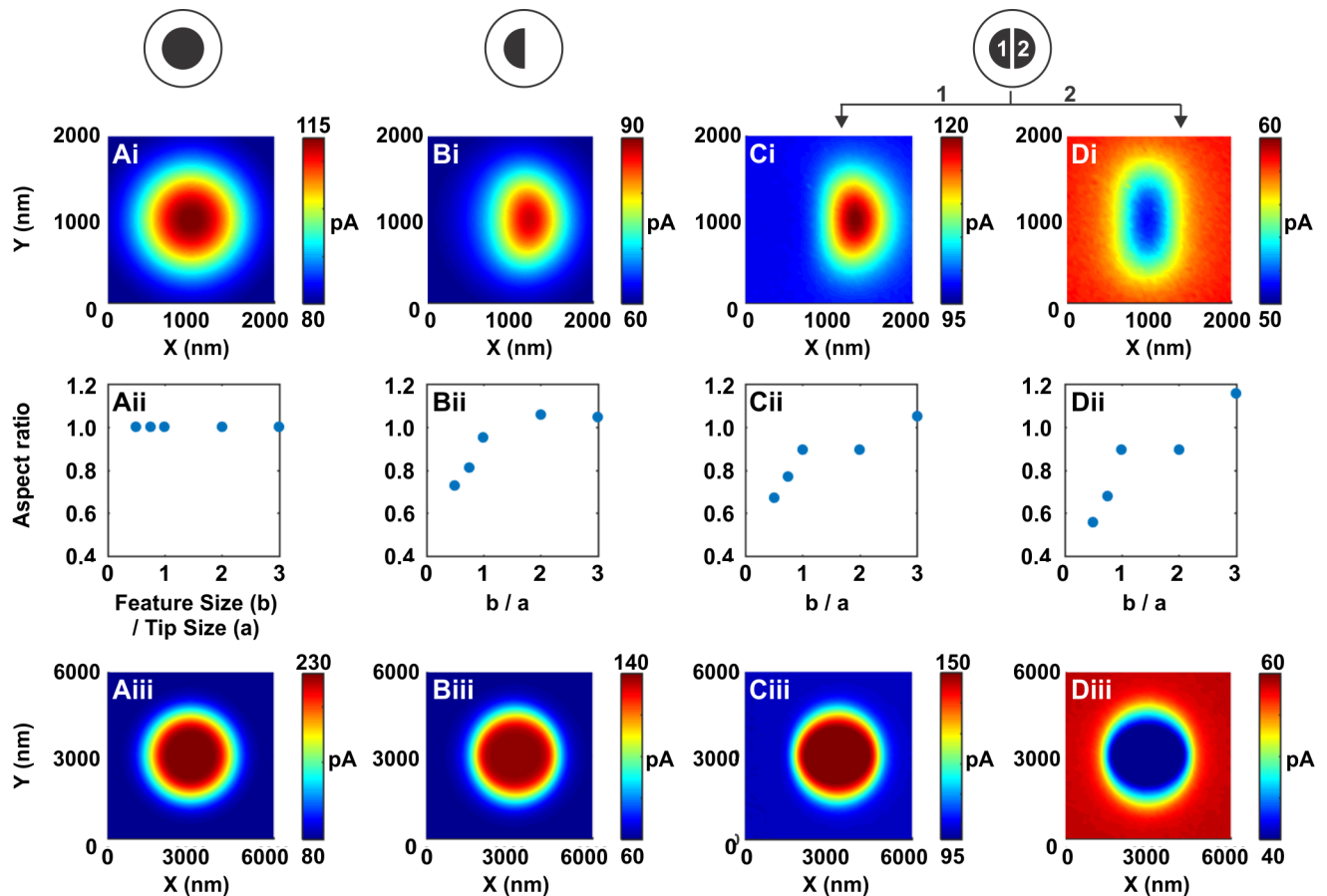


Figure 3.3 – Effect of feature size on the current response of (A) Disk (B) Single barrel (C) Dual barrel (feedback) (D) Dual barrel (generation-collection) electrode geometries. The electrodes were oriented over the feature as pictured in Figure 3.1 during all calculations. (i) $b = a/2$. (ii) Aspect ratio of the feature as it gets larger relative to the size of probe. (iii) $b = 3a$. All other parameters were held constant, with $L = 0.5$, $a = 500$ nm, $R_g = 2$, and $f_R = 1$.

3.3.3 Effect of Electrolyte Composition

In feedback mode measurements, typically only one oxidation state of the redox mediator is initially present in solution, with the other species in the redox couple only formed upon reaction. This is also usually the case in generation-collection mode measurements, where the oxidation state formed depends on the electrode and/or substrate potential being applied. However, the role of electrolyte composition is unclear when combining these two measurements. In the case of mediators with two stable oxidation states such as $\text{Fe}(\text{CN})_6^{3-}/\text{Fe}(\text{CN})_6^{4-}$, it is possible for both mediators to initially be present in solution.

Under these conditions, the electrolyte composition has a significant impact on the spatial resolution of the generation-collection but not feedback signal (Figure 3.4). When $f_O = 0$ as in a normal feedback measurement, the generation-collection signal is compressed (Figure 3.4 Bi). As the initial value of f_O increases, the observed shape of the substrate feature significantly broadens. When $f_O = f_R$ (Figure 3.4 iii), the shape of the generation-collection signal is significantly closer to the actual substrate feature. When O is the dominant species in solution (Figure 3.4 iv), the spatial resolution of the feedback signal has not been significantly affected but the generation-collection signal shows a more evenly distributed signal consistent with the uniform reactivity of the feature.

Altering the electrolyte composition is not a trivial change for feedback measurements, as changing the initial R/O ratio alters the overpotential and therefore the reaction rate. Polarization of the probe and substrate must still employ a high overpotential to ensure the process remains diffusion limited. When the surrounding matrix is not a pure insulator but

possesses some reactivity, the possibility of side reactions and planar diffusion under these altered conditions needs to be considered as well. However, for a case such as this, the enhanced resolution of the generation-collection probe under these conditions makes this a worthwhile time investment.

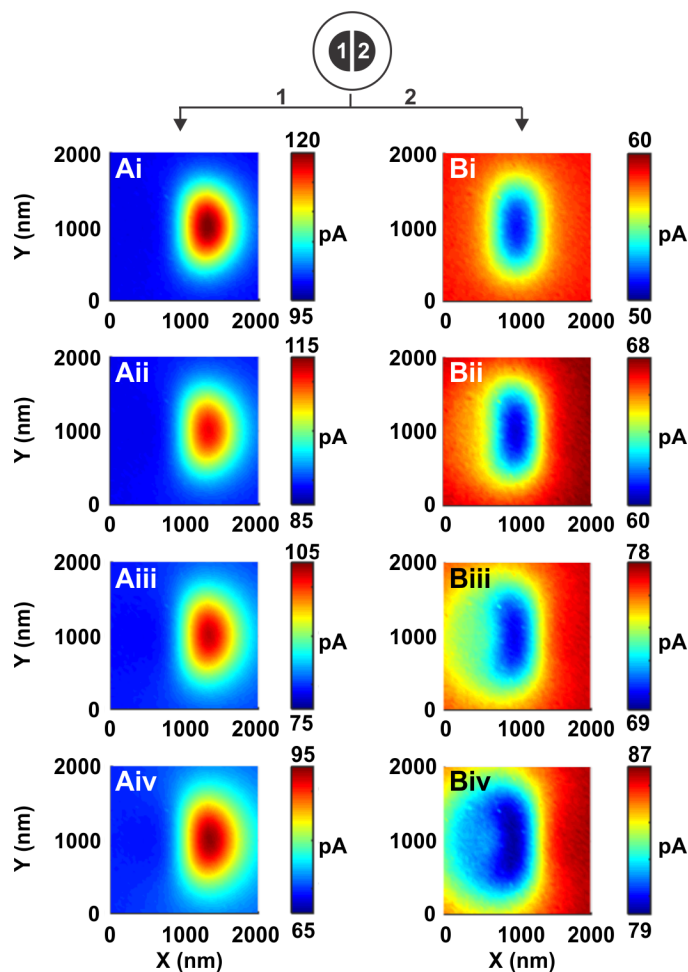


Figure 3.4 – Effect of electrolyte composition on the current response of the (A) Dual barrel (feedback) and (B) Dual barrel (generation-collection) electrodes. The electrodes were oriented over the feature as pictured in Figure 3.1 during all calculations. (i) $f_R = 1.00$, (ii) $f_R = 0.75$, (iii) $f_R = 0.50$, (iv) $f_R = 0.25$. $f_O = 1 - f_R$. All other parameters were held constant, with $L = 0.5$, $b = 250$ nm, $a = 500$ nm, and $R_g = 2$.

3.3.4 Effect of Feature Shape

The discussion so far has focused on variables that are controlled during experimental design through careful selection of the probe size, probe positioning, and electrolyte composition. However, the last major consideration is the substrate itself. To characterize the effect of feature shape, a range of feature shapes have been selected with unique characteristics (Figure 3.5): a square feature with sharp vertices, a crescent moon feature with a high aspect ratio, an array feature with multiple reacting elements in close proximity, and a ring feature with a discontinuous surface. Due to the additional complexity of these feature shapes, larger features have been selected than those used previously; namely, features the same size of the probe. Based on the AR observations in the previous section, spatial distortion is still expected to occur under these conditions.

Square or cubic features have previously been observed for precipitated nanocrystals.^{13,31} Of the three electrode geometries simulated, the dual barrel electrode demonstrates the closest response to the true shape (Figure 3.5 i), though this may be a byproduct of the broadening previously observed rather than true resolution. Though this is the largest feature shape tested in terms of area, the SECM images are furthest from the true geometry. This has to do with trying to resolve a challenging feature at the resolution limit. The challenge in observing sharp vertices of such shapes by simulation or experiment has been noted previously.³¹ For the simple case of a conductive region within insulating surroundings, this can be explained through edge effects. Current density is highest at the edges of an electrode because it is the distance of shortest diffusion for species diffusing from the bulk.

Although for the same total area a square feature has a larger perimeter than a circular feature's circumference, the shape of the edge plays a significant role. As noted previously, the presence of a sharp vertex creates an uneven diffusion profile to the reactive component of the surface, as evidenced by the concentration gradient extending over a larger distance far from a vertex and a smaller distance close to a vertex (Figure 3.1 Bii). This makes sharp corners challenging to resolve without a large discrepancy between probe and feature size.

Outside of regular geometric shapes, reactive features of a unique shape are often noted in the microstructure of complex alloys, with segregated phases of different reactivity forming during the cooling process which are observable using SECM.^{32–34} These often have highly irregular shapes with high aspect ratios,^{35–37} such as the crescent moon feature examined here (Figure 3.5 ii). As with the square feature, the dual barrel electrode appears to be better at resolving the true feature shape, displaying a sharper vertex where the feature looks closer to an oval with a disk electrode. This increased spatial resolution comes at the cost of signal strength, with a decrease in the measured feedback currents (a maximum of 120 pA and 94 pA for $f_R = 1$ and $f_R = 0.25$ respectively), as to be expected for the shallower concentration gradient associated with a lower initial concentration of species R .

Arrays of reactive features have long been of interest for nanoparticles and intentionally patterned nanostructures.^{17,38–40} In this work, an equally spaced 2×2 array of circular features has been simulated with a size and positioning at the edge of resolvability for the disk electrode (Figure 3.5 iii). When imaged using the single and dual barrel electrodes, they suffer from the same compression and shape distortion as observed previously. However, there is no impact on the ability to resolve individual elements of the array. Instead, the apparent

distance between adjacent elements has increased due to both the lateral compression in signal and smaller electroactive area of the probes. While the true feature shape would be obscured, this observation has the potential to be useful for pushing the ability of a system to resolve individual particles, which may be useful for tightly packed species.

The last feature shape investigated is a conductive ring ([Figure 3.5 iv](#)). While not commonly observed in a substrate, a number of ring-shaped microelectrodes have been used in SECM^{40–42} and SECM-SICM.¹⁷ As with the array, the dual barrel geometry improves the ability to resolve the insulating interior at the cost of shape accuracy and overall sensitivity. For the disk electrode, it is indistinguishable whether the central region is an insulator or region of lower activity. The contrast between the conductive ring and central insulator is clearer for both the single and dual barrel geometries, with the best contrast obtained for the feedback signal of the dual barrel ([Figure 3.5 C iv](#)).

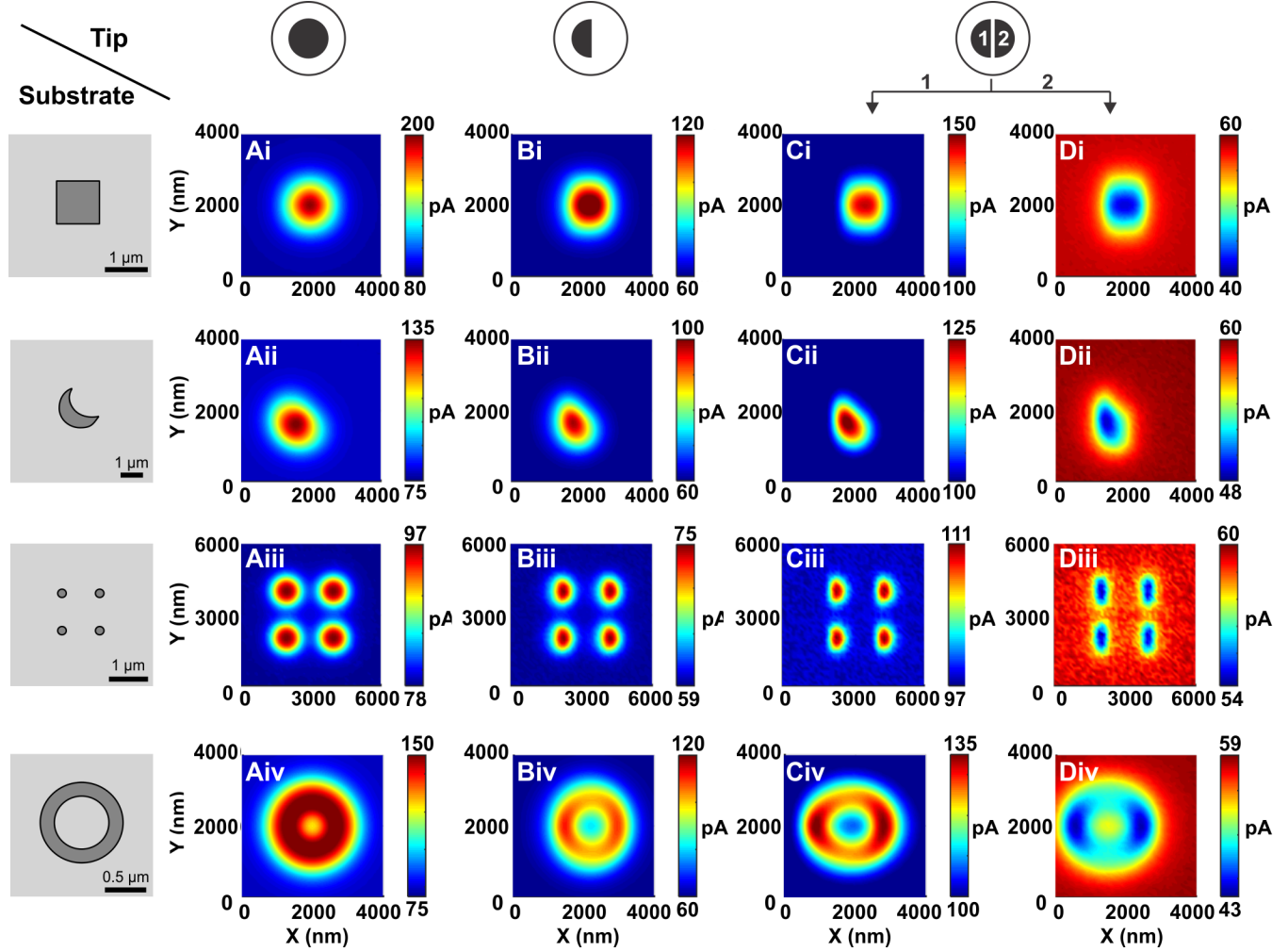


Figure 3.5 – Effect of feature shape on the current response of the (A) Disk, (B) Single barrel, (C) Dual barrel (feedback) and (D) Dual barrel (generation-collection) electrodes. The electrodes were oriented over the feature as pictured in Figure 3.1 during all calculations. (i) Square of side length $2a$, (ii) Crescent moon of major radius $2a$, minor radius $0.01a$. (iii) Array of circular features with radius $a/3$ and center-center distance $2a$. (iv) Ring of inner radius $1.33a$, outer radius $2a$. All other parameters were held constant, with $L = 0.5$, $f_R = 1$, $a = 500$ nm, and $R_g = 2$.

3.4 Additional Considerations

The system considered here is an ideal one, which can be complicated by several factors. These electrodes are commonly fabricated through a process of pyrolytic carbon deposition^{13,14,43,44}; without further focused ion beam milling,¹⁷ the tip may not be perfectly flat, in turn influencing the diffusion profile to the tip that produces this shape distortion. Similarly, local variations in the topography or reactivity of the surface will also influence the diffusion field and spatial accuracy. However, this system provides a baseline of ideal behaviour that individual measurements may be compared to.

In terms of physics, here the only mass transport mechanism considered is diffusion. In the presence of an additional migration or convection component, this distortion may be reduced, amplified, or eliminated depending on the shape of the final concentration gradient to the electrode edge considering all components. With respect to convection, the one-directional flow induced by moving the electrode in a straight line would likely result in a simple translation of the concentration gradient and distortion would likely still be observed. In contrast, moving the electrode in a spiral pattern⁴⁵ would significantly alter the shape of the concentration gradient, smoothing out the extreme non-uniformity at the vertices such that distortion may be eliminated entirely. With respect to migration, under the conditions of SECM-SICM, the two signals are not determined by the mass transport of the same species, and the altered distortion depends on the degree to which these two species interact. A neutral SECM mediator would be less affected by the electric field in the SICM barrel than a charged mediator, and so stronger distortion would be expected in this case. However, the

asymmetry of both barrels is likely to create the same non-uniform concentration gradient such that distortion would still be possible. Migratory contributions to mass transport due to surface charge on the glass are also possible. Recent works have found this effect to be most significant in nanogap configurations where the tip-substrate distance is tens of nm, which employ a smaller nanoelectrode² or closer distance,⁴⁶ but may still have an effect on this system, and would be an important consideration for even narrower nanoelectrodes used in other systems.^{17,43}

3.5 Conclusions

In general, the finite element simulations suggest that the altered diffusion profile to the edge of a dual barrel electrode will give rise to compression artifacts in its imaging capability, creating a difference between the true and apparent shapes of local reactive features, effectively introducing a spatial distortion to the final SECM image obtained.

This effect is strongest when the size of the diffusion region surrounding the tip is approximately the same size as the feature being imaged. Suggested conditions for reduced spatial distortion are given in [Table 3.1](#) and a comparison of their effect for the dual barrel feedback electrode imaging the ring feature shown previously is demonstrated in [Figure 3.6](#). For the disk electrode, both sensitivity and spatial accuracy are optimal at close tip-substrate distances, leading to the best overall resolution under these conditions. In contrast, for the dual barrel electrode spatial distortion is strongest where sensitivity is highest; [Figure 3.6 A](#) has a more distorted shape, and erroneously suggests non-uniform reactivity over the feature.

To put some guidelines on the sensitivity of this phenomenon to the experimental conditions investigated here, a 10% error in the aspect ratio of a feature being imaged could occur in the presence of one or more of the following conditions: $L < 1$, $b/a < 2$, and/or $f_R > 0.5$; however, these limits are strongly dependent on each other, as all parameters contribute in tandem to the extent of distortion.

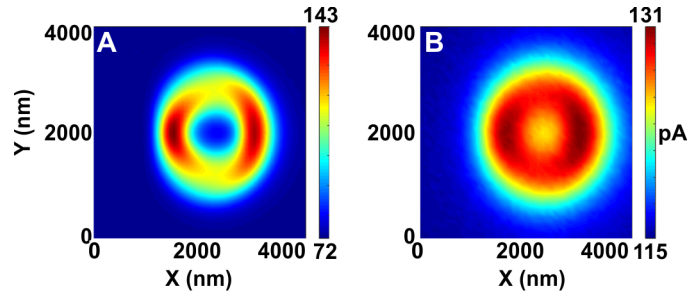


Figure 3.6 – Feedback signal of a dual barrel electrode (feedback signal) imaging a ring feature under (A) High ($L = 0.25$) and (B) Reduced ($L = 1$) spatial distortion. Sensitivity is highest where spatial distortion is strongest. All other parameters were held constant, with $a = 500$ nm, $R_g = 2$, and $f_R = 1$.

Table 3.1 – Recommended experimental parameters for reduced shape distortion

Parameter	Value
Tip-substrate distance	$L \geq 1$
Electrode size / feature size	$b/a \geq 1$
Electrolyte composition	$f_R \leq 1$

While these conditions occur at the limits of an experimental setup, they are well within the capability of current measurement methods (e.g. a nanoprobe imaging nanoparticles). Though many works do not state the exact tip-substrate distance used to generate a map, they are generally collected at $L \leq 1$, and the goal of instrumental improvements in noise

reduction and probe positioning is to get even closer. However, this work shows experimental design must balance the sensitivity obtained at close distances with the increased spatial accuracy obtained further away.

Overall, this phenomenon can be controlled through the careful selection of experimental conditions. For example, an increase in spatial accuracy of the feedback signal can be obtained by retracting the probe and in the generation-collection signal by having both oxidized and reduced forms of the mediator present in solution immediately. Furthermore, situations have been identified where the dual barrel probes outperform their disk counterparts in imaging particular features: these are the resolution of sharp vertices, spacing of densely packed array elements, and reactivity contrast in discontinuous regions.

The improved understanding of the relationship between probe geometry and current response allows the optimal probe dimensions for any given substrate to be determined. Furthermore, it lays the groundwork for further theory development in this vein towards generalization methods analogous to traditional disks, allowing the quantitative power of SECM to be combined with the high-speed benefits of multifunctional microelectrodes.

References

- [1] Kranz, C. *Analyst* **2014**, *139*, 336–352.
- [2] Page, A.; Perry, D.; Unwin, P. R. *Proceedings of the Royal Society A: Mathematical, Physical and Engineering Science* **2017**, *473*, 20160889.
- [3] Davoodi, A.; Pan, J.; Leygraf, C.; Norgren, S. *Journal of the Electrochemical Society* **2008**, *155*, C138.
- [4] Macpherson, J. V.; Unwin, P. R. *Analytical Chemistry* **2000**, *72*, 276–285.

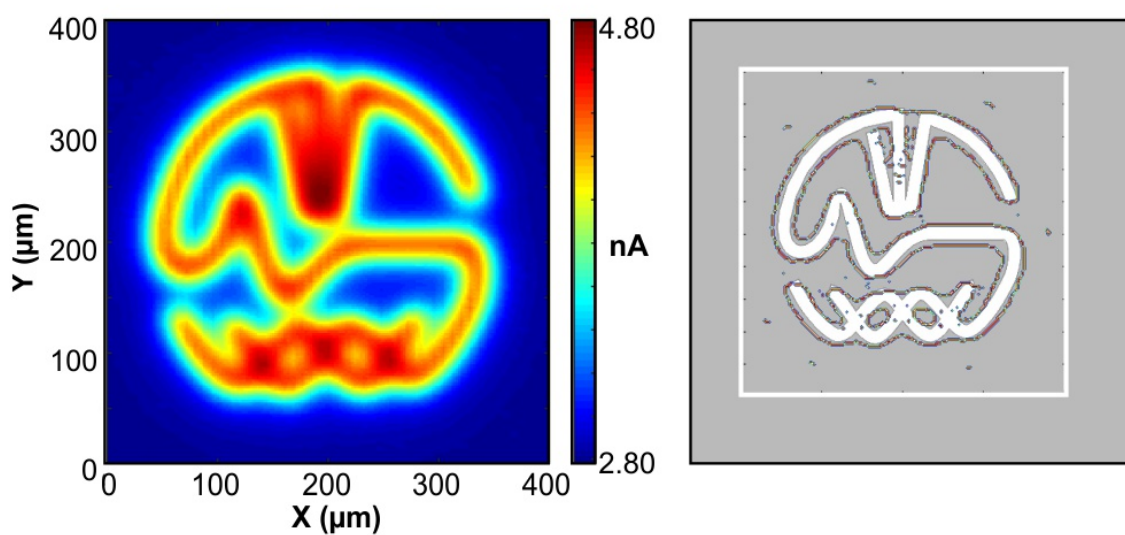
- [5] Kranz, C.; Friedbacher, G.; Mizaikoff, B.; Lugstein, A.; Smoliner, J.; Bertagnolli, E. *Analytical Chemistry* **2001**, *73*, 2491–2500.
- [6] Shi, W.; Baker, L. A. *RSC Advances* **2015**, *5*, 99284–99290.
- [7] Morris, C. a.; Chen, C.-C.; Baker, L. A. *Analyst* **2012**, *137*, 2933.
- [8] Comstock, D. J.; Elam, J. W.; Pellin, M. J.; Hersam, M. C. *Analytical Chemistry* **2010**, *82*, 1270–1276.
- [9] Snowden, M. E.; Güell, A. G.; Lai, S. C. S.; McKelvey, K.; Ebejer, N.; O’Connell, M. A.; Colburn, A. W.; Unwin, P. R. *Analytical Chemistry* **2012**, *84*, 2483–2491.
- [10] O’Connell, M. A.; Lewis, J. R.; Wain, A. J. *Chemical Communications* **2015**, *51*, 10314–10317.
- [11] Sen, M.; Takahashi, Y.; Matsumae, Y.; Horiguchi, Y.; Kumatani, A.; Ino, K.; Shiku, H.; Matsue, T. *Analytical Chemistry* **2015**, *87*, 3484–3489.
- [12] Nadappuram, B. P.; McKelvey, K.; Byers, J. C.; Güell, A. G.; Colburn, A. W.; Lazenby, R. A.; Unwin, P. R. *Analytical Chemistry* **2015**, *87*, 3566–3573.
- [13] Nadappuram, B. P.; McKelvey, K.; Al Botros, R.; Colburn, A. W.; Unwin, P. R. *Analytical Chemistry* **2013**, *85*, 8070–8074.
- [14] McKelvey, K.; Nadappuram, B. P.; Actis, P.; Takahashi, Y.; Korchev, Y. E.; Matsue, T.; Robinson, C.; Unwin, P. R. *Analytical Chemistry* **2013**, *85*, 7519–7526.
- [15] Badets, V.; Loget, G.; Garrigue, P.; Sojic, N.; Zigah, D. *Electrochimica Acta* **2016**, *222*, 84–91.
- [16] Bondarenko, A.; Cortés-Salazar, F.; Gheorghiu, M.; Gáspár, S.; Momotenko, D.; Stanica, L.; Lesch, A.; Gheorghiu, E.; Girault, H. H. *Analytical Chemistry* **2015**, *87*, 4479–4486.
- [17] Thakar, R.; Weber, A. E.; Morris, C. a.; Baker, L. A. *Analyst* **2013**, *138*, 5973.
- [18] Miller, T. S.; Macpherson, J. V.; Unwin, P. R. *Journal of Electroanalytical Chemistry* **2014**, *729*, 80–86.
- [19] Burt, D. P.; Wilson, N. R.; Weaver, J. M. R.; Dobson, P. S.; Macpherson, J. V. *Nano Letters* **2005**, *5*, 639–643.
- [20] Kueng, A.; Kranz, C.; Lugstein, A.; Bertagnolli, E.; Mizaikoff, B. *Angewandte Chemie International Edition* **2003**, *42*, 3238–3240.
- [21] Izquierdo, J.; Eifert, A.; Souto, R.; Kranz, C. *Electrochemistry Communications* **2015**, *51*, 15–18.

- [22] Lefrou, C.; Cornut, R. *ChemPhysChem* **2010**, *11*, 547–556.
- [23] Chen, C.-C.; Zhou, Y.; Baker, L. A. *Annual Review of Analytical Chemistry* **2012**, *5*, 207–228.
- [24] Sun, P.; Laforge, F. O.; Mirkin, M. V. *Physical Chemistry Chemical Physics* **2007**, *9*, 802–823.
- [25] Sklyar, O.; Kueng, A.; Kranz, C.; Mizaikoff, B.; Lugstein, A.; Bertagnolli, E.; Wittstock, G. *Analytical Chemistry* **2005**, *77*, 764–771.
- [26] Lee, C.; Wipf, D. O.; Bard, A. J.; Bartels, K.; Bovik, A. C. *Analytical Chemistry* **1991**, *63*, 2442–2447.
- [27] Anicet, N.; Bourdillon, C.; Moiroux, J.; Savéant, J.-M. *The Journal of Physical Chemistry B* **1998**, *102*, 9844–9849.
- [28] Kuss, C.; Payne, N. A.; Mauzeroll, J. *Journal of the Electrochemical Society* **2016**, *163*, H3066–H3071.
- [29] Polcari, D.; Dauphin-Ducharme, P.; Mauzeroll, J. *Chemical Reviews* **2016**, *116*, 13234–13278.
- [30] Shao, Y.; Mirkin, M. V.; Fish, G.; Kokotov, S.; Palanker, D.; Lewis, A. *Analytical Chemistry* **1997**, *69*, 1627–1634.
- [31] Blanchard, P.-Y.; Sun, T.; Yu, Y.; Wei, Z.; Matsui, H.; Mirkin, M. V. *Langmuir* **2016**, *32*, 2500–2508.
- [32] Asmussen, R. M.; Shoesmith, D. W. *CORROSION* **2014**, *70*, 1177–1180.
- [33] Jamali, S. S.; Moulton, S. E.; Tallman, D. E.; Forsyth, M.; Weber, J.; Wallace, G. G. *Corrosion Science* **2014**, *86*, 93–100.
- [34] Jensen, M. B.; Guerard, A.; Tallman, D. E.; Bierwagen, G. P. *Journal of the Electrochemical Society* **2008**, *155*, C324–C332.
- [35] Wang, W.-R.; Wang, W.-L.; Wang, S.-C.; Tsai, Y.-C.; Lai, C.-H.; Yeh, J.-W. *Intermetallics* **2012**, *26*, 44–51.
- [36] Ambat, R.; Aung, N. N.; Zhou, W. *Corrosion Science* **2000**, *42*, 1433–1455.
- [37] Wu, G.; Fan, Y.; Gao, H.; Zhai, C.; Zhu, Y. P. *Materials Science and Engineering: A* **2005**, *408*, 255–263.
- [38] Momotenko, D.; Page, A.; Adobes-Vidal, M.; Unwin, P. R. *ACS Nano* **2016**, *10*, 8871–8878.
- [39] Takahashi, Y.; Shevchuk, A. I.; Novak, P.; Murakami, Y.; Shiku, H.; Korchev, Y. E.; Matsue, T. *Journal of the American Chemical Society* **2010**, *132*, 10118–10126.

-
- [40] Lee, Y.; Ding, Z.; Bard, A. J. *Analytical Chemistry* **2002**, *74*, 3634–3643.
- [41] Kurulugama, R. T.; Wipf, D. O.; Takacs, S. A.; Pongmayteegul, S.; Garriss, P. A.; Baur, J. E. *Analytical Chemistry* **2005**, *77*, 1111–1117.
- [42] Lee, Y.; Amemiya, S.; Bard, A. J. *Analytical Chemistry* **2001**, *73*, 2261–2267.
- [43] Takahashi, Y.; Shevchuk, A. I.; Novak, P.; Zhang, Y.; Ebejer, N.; Macpherson, J. V.; Unwin, P. R.; Pollard, A. J.; Roy, D.; Clifford, C. A.; Shiku, H.; Matsue, T.; Klenerman, D.; Korchev, Y. E. *Angewandte Chemie International Edition* **2011**, *50*, 9638–9642.
- [44] Zhang, X.; Wang, H.; Morris, C.; Gu, C.; Li, M.; Baker, L. A.; Shao, Y. *ChemElectroChem* **2016**, *3*, 2153–2159.
- [45] Momotenko, D.; Byers, J. C.; McKelvey, K.; Kang, M.; Unwin, P. R. *ACS Nano* **2015**, *9*, 8942–8952.
- [46] Tan, S.-y.; Perry, D.; Unwin, P. R. *Journal of Electroanalytical Chemistry* **2018**, *819*, 240–250.

Chapter 4

Evaluating the Use of Edge Detection in Extracting Feature Size From Scanning Electrochemical Microscopy Images



Chapter Abstract

Chapter 3 presented an approach for extending the versatility of SECM through the use of multifunctional microelectrodes, which allow individual processes occurring in a system to be examined separately. It also discussed the relationship between microelectrode geometry, experimental conditions, and ultimate image resolution in SECM. Though an experiment can be optimized to improve spatial resolution, the final image produced will always contain some degree of diffusional blurring due to the non-contact methodology. Recent advances in the field of image processing have developed algorithms for detecting edges and isolating objects. These hold immense promise for use in SECM to compensate for this blur and improve resolution. This approach is complementary to that of multifunctional microelectrodes; where previously the use of a different type of sensor provided two signals, here one signal can be effectively split in two when analysed in the context of its location. Both of these approaches allow processes occurring simultaneously to be examined independent of one another.

This chapter presents an integrated experiment/modelling approach demonstrating the potential of edge detection algorithms to extract the boundaries of reactive features from SECM images for further analysis. The model is used to demonstrate that the inflection point in a 1D image corresponds well to the true feature edge, and that the Canny algorithm is well-suited to applying the same analysis in 2D. This approach has several benefits, including reducing the need for complementary microscopy techniques, revealing of hidden details embedded in the original image, and separating reactive features from their background for

further analysis.

The work presented in this chapter is reproduced from:

Stephens, L.I.; Payne, N.A.; Skaanvik, S.A.; Polcari, D.; Geissler, M.; Mauzeroll, J. Evaluating the use of edge detection in extracting feature size from scanning electrochemical microscopy images. *Analytical Chemistry* **2019**, 91(3), 2312-2318.

4.1 Introduction

Scanning electrochemical microscopy (SECM) is often cited as a technique with high spatial resolution,¹⁻⁴ which is frequently exploited to identify regions of local electrochemical activity on a surface.⁵⁻⁷ Though the approximate boundaries of these regions are reflected in spatial variations of the measured current, diffusional blurring gives rise to a sigmoidal transitional region at these boundaries, obscuring the exact position of the underlying edge. Accordingly, the preferred method of extracting the shape and size of a particular region has been optical or electron micrographs of the same or a similar region.⁸⁻¹⁰ For non-transparent samples, imaging the same region requires marking the sample for alignment purposes, which introduces additional challenges.^{11,12}

However, marking the sample is not the only option for extracting the boundaries of reactive or topographical features. In neighboring fields, features are isolated after the fact through image processing; in particular, edge detection algorithms that isolate individual features based on intensity gradients. These algorithms have been used in machine learning for facial detection and recognition,¹³ in medicine for isolating blood vessels in retinal images,¹⁴ and in astronomy for removing artifacts from telescope images,¹⁵ among other applications. Image processing has been successfully used in the past in SECM to improve resolution, most notably for filter-based deconvolution¹⁶ and the development of alternative electrode scanning patterns,¹⁷ though these methods require parameter optimization or new electrode scanning patterns to be programmed.

This work will demonstrate that the inflection point in a sigmoidal current profile in a

feedback mode SECM image is a strong indicator of the feature edge, and that importantly the spatial position of this point is insensitive to the tip-substrate distance or surface rate constant. This method is compatible with existing experimental imaging protocols with high sampling density, the major change is in post-processing. This procedure is most effective under conditions that produce maximum contrast in an image. This contrast is determined in part by the method of probe movement (in addition to the probe and surface characteristics); feedback mode imaging may be performed in either constant distance¹⁸ (fixed tip-substrate distance) or constant height¹⁹ (fixed z -position) configurations. Though constant distance mode can produce sharper images,²⁰ the alternate electrode movement pattern involved gives rise to a different current profile and so only the more common²¹ height mode will be discussed in this work. Modern edge detection algorithms are particularly suited to performing a contrast analysis on a 2D image. This approach may be used for revealing and amplifying finer details in SECM images, reducing the need for complicated alignment techniques, improving methods for thresholding images to separate features from background. The versatility of this approach has been demonstrated using both model substrates of constant topography or reactivity and complex cell agglomerates.

4.2 Experimental

4.2.1 Substrate Fabrication

An optically transparent cyclic olefin copolymer (Zeonor 1060R)²² was used as a base material for many of the substrates in this work. Zeonor 1060R (obtained in the form of pellets from Zeon Chemicals, Louisville, KY, USA) was injection-molded into 6 inch wafers (0.5 mm in thickness) using an Engel 150 apparatus operated at temperatures of between 127 and 134°C, an injection speed of 45 to 103 mm/s, and a pressure of 25 bar.

Au/SiO₂ substrates were produced as follows. First, the Zeonor wafer was covered with 10 nm of Cr and 50 nm of Au using e-beam evaporation (Kurt J. Lesker Company, Jefferson Hills, PA, USA). The wafer was then coated with HMDS, followed by 2 μ m of AZ 5214-E IR Photoresist (EMD, Somerville, NJ, USA). The wafer was baked at 95°C for 3 min using a ramp of 4°C/min. Resist was exposed to UV light at 365 nm (Hg i-line, 1250 mJ/cm²) through a Cr/quartz photo mask (Photronics, Inc.), using a Model 6200 mask aligner (EV Group, Schärding, Austria). Resist was developed in AZ 300 MIF Developer (EMD) followed by rinsing with DI water and drying with a stream of nitrogen gas. A thin layer (40 nm) of SiO₂ was subsequently deposited on the wafer using e-beam evaporation. Photoresist features were dissolved using Nano-Strip (KMG, Fort Worth, TX, USA). Disks (23.8 mm in diameter) comprising patterned Au/SiO₂ segments were cut off the wafer to obtain substrates for SECM measurements. Zeonor substrates for cell adhesion (23.8 mm in diameter) comprised an array of hydrophilic spots (12 μ m in diameter) and were prepared

according to published procedures.²³

Topographical features were generated on a silicon wafer using photolithography with SU-8 resist as described elsewhere.²⁴

4.2.2 Cell Culture

HEK293 cells were cultured in 75 cm² flasks (CELL+, SARSTEDT, Nümbrecht, Germany) and Dulbecco's Modified Eagle Medium (DMEM, Sigma Aldrich, Oakville, ON, Canada) supplemented with 9.1% fetal bovine serum (Thermo Fisher, Ottawa, ON, Canada) and 0.5 mg/mL primocin (InvivoGen, San Diego, CA, USA). Cells were incubated at 5% CO₂ and 37°C and were passed every 2-4 days with Trypsin/EDTA (Sigma Aldrich, 2.5 g/L and 1 g/L, respectively).

Cells were adhered to Zeonor 1060R slides treated with oxygen plasma as described previously²³ to give 12 µm round features for cell adhesion. Cells (8×10^5) were seeded on Zeonor slides 2 days before the SECM experiments. The Zeonor slides were then washed with PBS 2 times before it was mounted in the electrochemical cell and 2 mL imaging solution was added.

4.2.3 Electrochemical Experiments

SECM measurements were performed on ELProscan 1 and ELProscan 3 instruments (HEKA, Lambrecht/Pfalz, Germany), the latter equipped with an inverted microscope (schematic in [Figure D.1](#). 25 µm diameter Pt disk electrodes with $R_g \approx 3$ and 7 µm diameter carbon fiber electrodes with $R_g \approx 2$ were prepared according to a literature procedure.²⁵ Solutions

of either FcMeOH (Sigma Aldrich) in 0.1 M KCl (Fisher Scientific, Mississauga, ON) or $\text{Ru}(\text{NH}_3)_6\text{Cl}_3$ (Acros Organics/Thermo Fisher, Ottawa, ON) in DMEM^- were prepared depending on the substrate being imaged. A Ag/AgCl wire prepared from a 1 mm annealed Ag wire (99.99% Goodfellow, Mississauga, ON) and 0.5 mm diameter Pt wire (99.99%, Goodfellow) were employed as the reference and counter electrodes respectively. The substrates were not biased.

4.2.4 Instrumentation

SEM imaging was performed using a Hitachi SU3500 with an accelerating voltage of 15 keV and at a pressure of 30 Pa to reduce sample charging. Images were obtained using the topographical mode of the backscatter electron detector for enhanced contrast.

4.2.5 Finite Element Simulations

A 3D SECM model ([Figure D.2](#)) was built using COMSOL Multiphysics 5.3 to simulate surfaces with varying topography and reactivity, as detailed previously.²⁶ Currents were calculated by solving the steady-state Nernst-Planck equation under conditions of negligible convection and migration. Full model details may be found in the supporting information.

4.2.6 Data Analysis

All data was analysed using MATLAB 2017b. Experimental SECM images were slope corrected and linearly interpolated to a square grid at the scale of 1 pixel = 1 μm^2 to accommodate

the edge detection algorithm, which requires square pixels. For example, a $200\text{ }\mu\text{m} \times 200\text{ }\mu\text{m}$ map containing 2001×41 points initially would contain 200×200 points post-interpolation. The SECM images shown in figures reflect the interpolated data the edge detection algorithm was applied to, whereas the dimensions given in captions reflect the original sampling density and imaging time prior to interpolation. The Canny algorithm with default thresholds was used to extract edges from all 2D images. For the 1D line scans, the second derivative of each data set was numerically calculated and the zero-crossings identified graphically.

4.3 Results and Discussion

4.3.1 Substrates Displaying Positive Feedback

In the absence of significant topographical features, the currents at a disk microelectrode in feedback mode SECM are determined by the tip-substrate distance (d) and surface reactivity (k). These can be normalized as discussed in [3.2.1](#) as L ($L = d/a$) and κ ($\kappa = ka/D$) respectively. In a model system of local reactive features in insulating surroundings ([Figure 4.1 A](#)), decreasing the tip-substrate distance or increasing the feature reactivity relative to its surroundings increases the sensitivity of the measurement ([Figure 4.1 B-C](#)), producing a sharper contrast. An examination of the second derivative of the current reveals that though its magnitude depends on the specific experimental conditions, the locations at which it changes sign (zero-crossings) are the same in all cases (for larger size, see [Figure D.3](#)). Though this is model data, there is some noise present in the second derivative stemming from small errors

in the calculated current due to the iterative numerical solver used. Despite this noise, clear zero-crossings in the second derivative (inflection points in the original current profile) are present in the data. In the context of the true substrate geometry, the location of these inflection points agrees strongly with the feature edges.

This can be understood through the diffusional blurring inherent to feedback SECM, which causes local features to appear larger in SECM images than they are in reality. For a species to be detected, it must diffuse a minimum distance equal or greater to the tip-substrate distance. In the absence of a concentration gradient, the average time required to do this is described by:²⁷

$$t = \frac{x^2}{2D} \quad (4.1)$$

Where t is time. For a tip-substrate distance of 10 μm and diffusion coefficient of $6.7 \times 10^{-10} \text{m}^2/\text{s}$, the average diffusion time is 0.12 s. During this time, species from other regions can also diffuse to the surface and be detected. When a microelectrode approaches a local reactive feature, it will be detected well before the electrode is positioned above it; this begins when the feature enters the hemispherical diffusion field extending outwards from the electrode surface (positive rate of change, concave up). As the electrode crosses over the feature edge, the feature dominates the response and the current approaches its maximum value at the feature center (positive rate of change, concave down).

Though the inflection point is the same in all cases, noise has a stronger effect on measurements with low sensitivity. For this reason, modern edge detection algorithms often

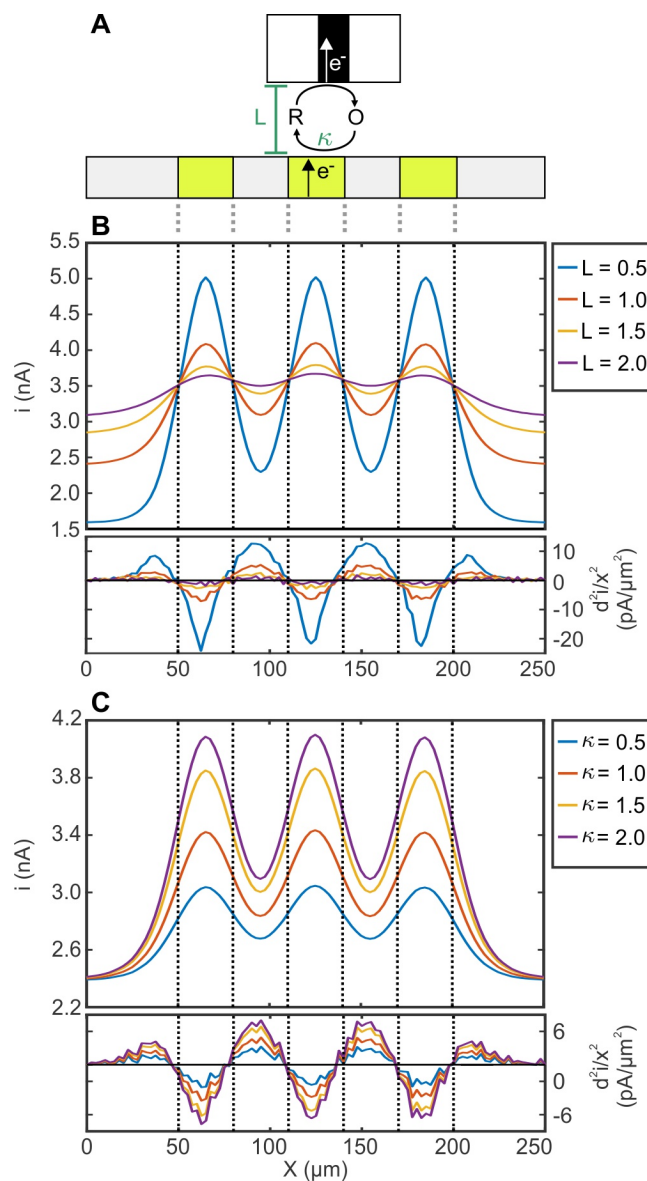


Figure 4.1 – (A) Schematic of the model system containing a substrate with constant topography and variable reactivity. (B) Simulated line scans over the model substrate at varying tip-substrate distances (constant $\kappa = 3$). (C) Simulated line scans over the model substrate with varying reactivity (constant $L = 1$). Dotted lines indicate the true feature edges.

include a smoothing step to prevent the identification of false positives (identified edges which do not truly exist). The Canny edge detection algorithm is one such example,²⁸ which was selected in this work to examine the effectiveness of using edge detection to precisely determine feature boundaries in SECM images. When compared to carrying out the same analysis by hand, the Canny algorithm is better able to handle noisy data. This is done through assigning each potential edge a strength based on the magnitude of the gradient. When several weak edges (shallow gradient) are detected very close to one another, a final thinning step then selects one based on optimal connectivity with strong edges in the vicinity.

To investigate the effectiveness of this approach on an experimental system, ideal substrates of geometrically precise conductive gold features in insulating surroundings were fabricated. These features were formed by patterned deposition of a thin (45 nm) layer of silicon oxide on a gold-coated substrate, producing negligible topological variation in the context of a 25 μm electrode in the final surface (Figure D.4). Three regions were selected for SECM imaging that contained features of different shapes and size scales (Figure 4.2 A-C). The detected edges from these SECM images were overlaid on optical micrographs of the same area, using the visible microelectrode in the optical image to match the scale and position of the two (Figure 4.2 D-F), assuming a 25 μm diameter wire.

This overlay shows strong agreement between the detected edges in the SECM image and the true feature geometry. In all cases, a rough outline of the features is visible in the initial SECM images; however, the exact size is hidden by the diffusional blur. Furthermore, the edge detection reveals both regular line spacing (Figure 4.2 A) and sharp corners (Figure 4.2 C) not apparent in the SECM images, which would normally require much smaller electrodes

to resolve. Isolated errors are present in the detected edges, most strongly in [Figure 4.2 A](#). These stem from artifacts in the original SECM image rather than errors in the edge detection, and are generally minimal. Overall, the edge detection accurately locates the feature boundaries for substrates with large variations in reactivity and minimal variations in topography, revealing hidden details encoded in the original SECM images. Though these samples were designed to be transparent for proof of concept, this approach is most powerful for applications where acquiring an optical image of the imaged area is technically challenging.

In general, optimal agreement is observed between the detected edge and true geometry when the original image is highly sampled; this is easily done in electrode scanning patterns based on line scans, but less common in some of the newer high-speed scanning patterns used in the voltage switching or hopping^{29,30} modes, which may image faster but often use lower sampling densities. Good performance is observed for more complex, asymmetrical features ([Figure D.5](#)). For both symmetric and asymmetric features, accuracy starts to diminish for features smaller than the electrode ([Figure D.6](#)).

4.3.2 Substrates Displaying Negative Feedback

In the absence of significant reactive features, the currents at a microelectrode are determined exclusively by the topography of the substrate. Though SECM can be used to image topography, sensitivity drops off quickly above $L \approx 1$, reducing the contrast in a constant height scan. Constant distance methods based on shear force retain enhanced contrast,^{31,32} but still require a non-reactive surface for a topography-only signal. This work will focus on

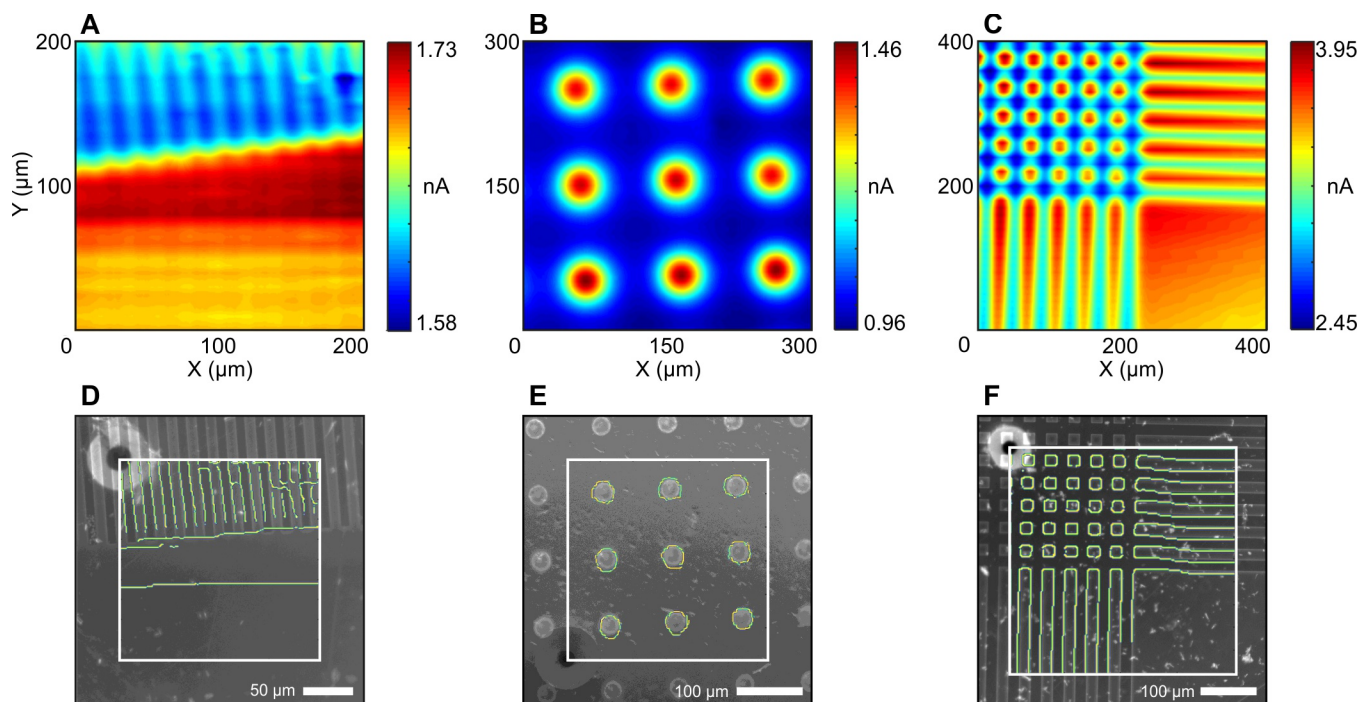


Figure 4.2 – Experimental SECM images of patterned gold features. (A) 10 μm width lines with 10 μm edge-edge spacing (2001 x 41 points, 15 minutes). (B) 30 μm diameter circles with 100 μm centre-centre spacing (3001 x 61 points, 30 minutes). (C) 20 μm squares with 20 μm edge-edge spacing (4001 x 41 points, 30 minutes). (D-F) Detected edges in the SECM image (bounded by the white box) overlaid on the corresponding microscope image of the scanned area. Substrates were imaged with a 25 μm disk Pt electrode polarized at 300 mV vs. Ag/AgCl in a solution of 0.5 mM (A,B) or 1 mM (C) FcMeOH in 0.1 M KCl. In all cases, the tip-substrate distance was approximately 10 μm .

the more common constant height methods; for consistency, the scan height L is defined as the distance between the electrode and highest point on the substrate. Alternate methods including multifunctional microelectrodes incorporating a topography-only channel such as atomic force microscopy (AFM),^{33,34} or scanning ion conductance microscopy (SICM)^{35,36} lift both of these limitations, providing both electrochemical and topographical contrast, but the theory relating their quantitative use for extracting rate constants is less well developed

than for disk electrodes.

In a model system of local topographical features in a non-reactive substrate (Figure 4.3 A), decreasing the tip-substrate distance or increasing the feature height increases the sensitivity of the measurement (Figure 4.3 B, E). As with κ , feature height s will be examined in the context of the electrode size, where $\delta = s/a$. $\delta > 0$ and $\delta < 0$ indicate local hills and valleys in the surface respectively. Compared to the reactivity-only case the reduced overall contrast manifests itself in smaller magnitudes of the second derivative, and a poorer signal/noise ratio. Consequently, these inflection points are more challenging to reliably identify among the noise (Figure 4.3 D, F), even when spaced further apart (Figure D.7). Smoothing the second derivative according to a 4-point moving average reveals that these inflection points do exist and tend to agree with the feature edges (Figure 4.3 D, G); however, this process also produces more false positives.

The effect of this reduced contrast was examined on silicon wafers etched to create grooves approximately 15 μm deep (for detailed topography, see SICM data in Figure D.8), corresponding to $\delta \approx 1.2$. As the substrates were not optically transparent, the SECM images were overlaid on SEM images of representative areas (Figure 4.4 A,D). This overlay demonstrates reasonable agreement between the detected edges and the true feature geometry; notably, this is much less precise than the reactivity-only case. The edge detection algorithm tends to overestimate the feature size. For the same separation distance between features which gave strong contrast in reactive features, a similar overestimation of feature size also occurs in model systems of both topographical valleys (Figure 4.4 B,E) and hills (Figure 4.4 C, F). Due to the reduced sensitivity of SECM to topographical changes, this procedure is less

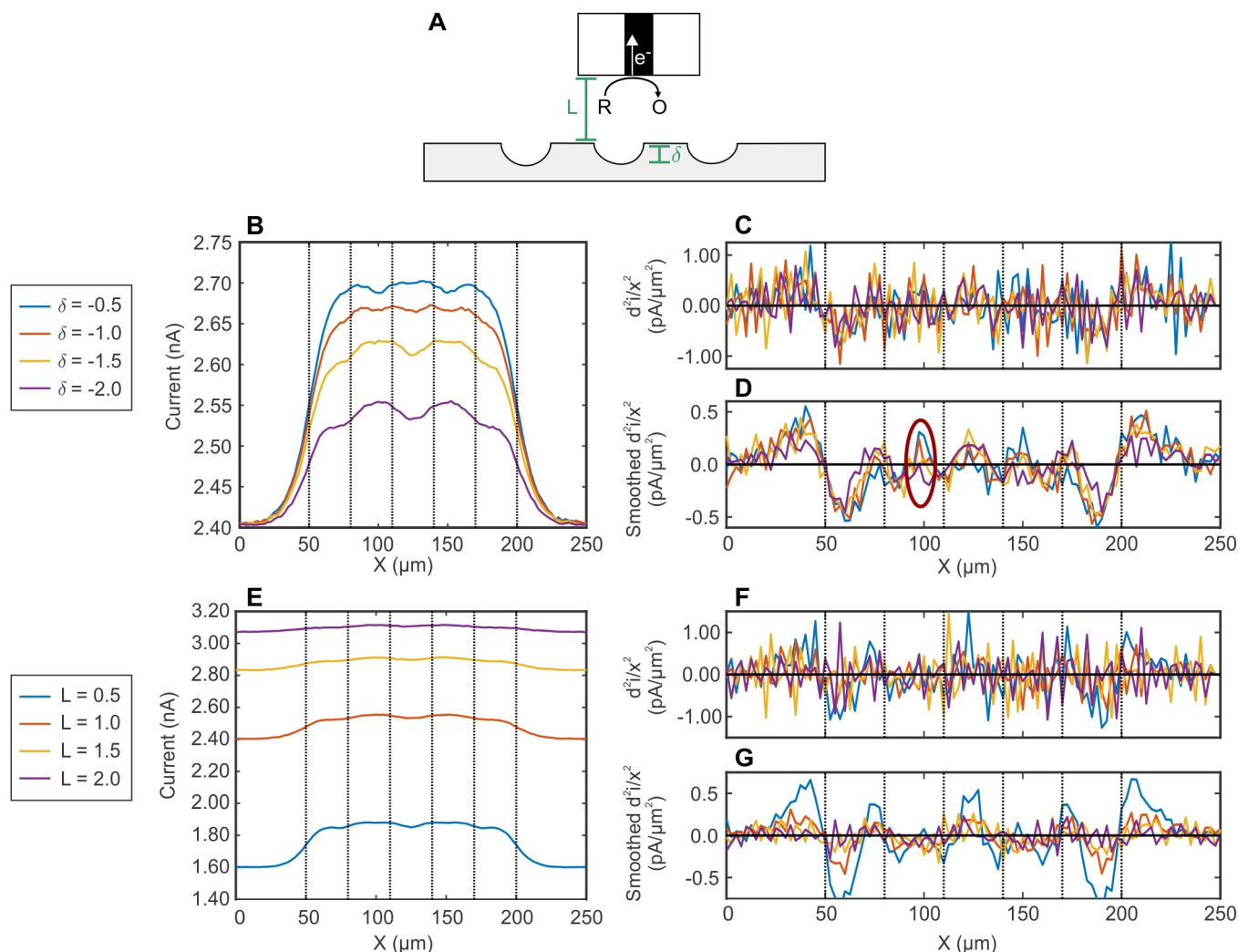


Figure 4.3 – (A) Schematic of the model system containing a substrate with three non-reactive grooves of 12.5 μm width and 25 μm center-center spacing. (B) Simulated line scans over the model substrate at varying tip-substrate distances (constant $\delta = 0.5$). (C-D) Second derivative of the line scans in (B), both original (C) and smoothed according to a 4-point moving average (D). (E) Simulated line scans over the model substrate at varying feature depths distances (constant $L = 1$). (F-G) Second derivative of the line scans in (E), both original (F) and smoothed (G). Dotted lines indicate the true feature edges. The red circle indicates a false positive, or detected edge with no corresponding feature.

effective for detecting topographical than reactive variations in a substrate; however, SECM is rarely used to examine exclusively topography, as methods such as SICM and AFM can

be integrated with SECM and exhibit improved topographical resolution. More commonly, topography plays a role in SECM in the context of convoluted topography and reactivity in images.

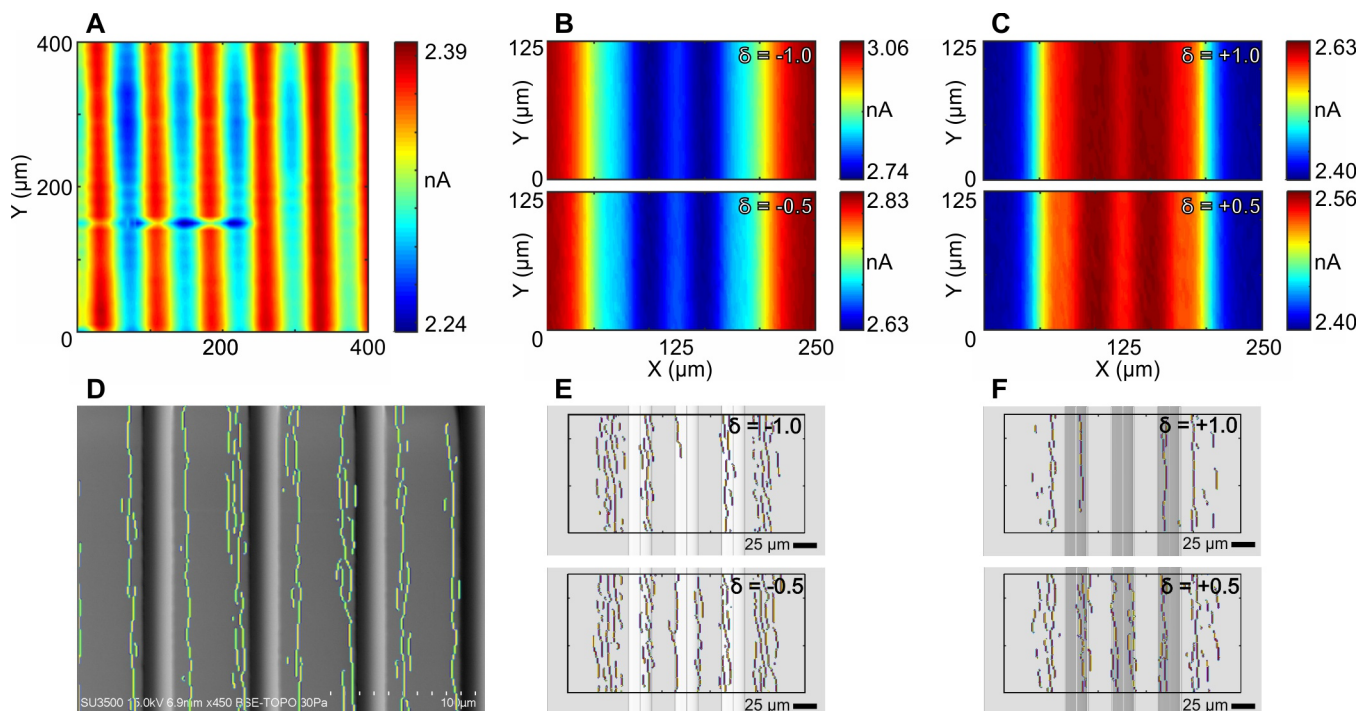


Figure 4.4 – (A) Experimental SECM image of a non-reactive substrate with 20 μm wide grooves with 75 μm center-center spacing at $L \approx 1$ (4001 x 41 points, 60 minutes). The substrate was imaged with a 25 μm diameter Pt electrode polarized at 300 mV vs. Ag/AgCl in a solution of 1 mM FcMeOH in 0.1 M KCl. Simulated SECM images of insulating substrates with 25 μm wide raised (B) and lowered (C) features of varying heights (251 x 126 points). (D-F) Detected edges in the SECM images overlaid on representative images of the true geometry obtained by SEM (D) or simulation (E-F).

4.3.3 Substrates Displaying Non-Ideal Behavior

In most cases, substrates do not display the ideal properties of the two model systems discussed in previous sections: they are not perfectly flat, uniformly reactive, or geometrically precise. To examine the accuracy of edge detection in a system displaying more complex behaviour, HEK293 cells were imaged in a solution of $\text{Ru}(\text{NH}_3)_6\text{Cl}_3$ (Figure 4.5 A). This is a cell impermeable redox mediator, and so monitoring the $\text{Ru}^{3+}/\text{Ru}^{2+}$ signal produces a response dependent mainly on topography.^{37,38} Compared to the Si/SU-8 substrates discussed previously, the edges detected in the SECM map agree more strongly with the optical image, well resolving multiple cells (Figure 4.5 B). Based on the reduced sensitivity to topography discussed earlier, the improved effectiveness in this case likely stems from the improved contrast in the image. This method works best when a high signal/noise ratio is present in the second derivative, which is always noisier than the original current trace. The cell dimensions and electrode size most strongly affect this S/N. Redox mediator concentration may improve it as well, but only to a certain point (Figure D.9).

For an individual cell or group of cells, the detected edges can then be used to construct a mask for the SECM image (Figure 4.5 C) in order to extract exclusively the currents measured over the cell. This might also be done by selecting a current cutoff below which is assumed to be background; however, given the continuous distribution of currents measured over the cell (Figure 4.5 D), this masking approach is better able to incorporate intermediate currents measured at the edge of the cell. Based on the mask, currents of the same magnitude are assigned to either the cell or the background (region of overlap in Figure 4.5 E) depending

on their location. In this way, the entire spatial data can be included in the analysis rather than the single point of largest signal.

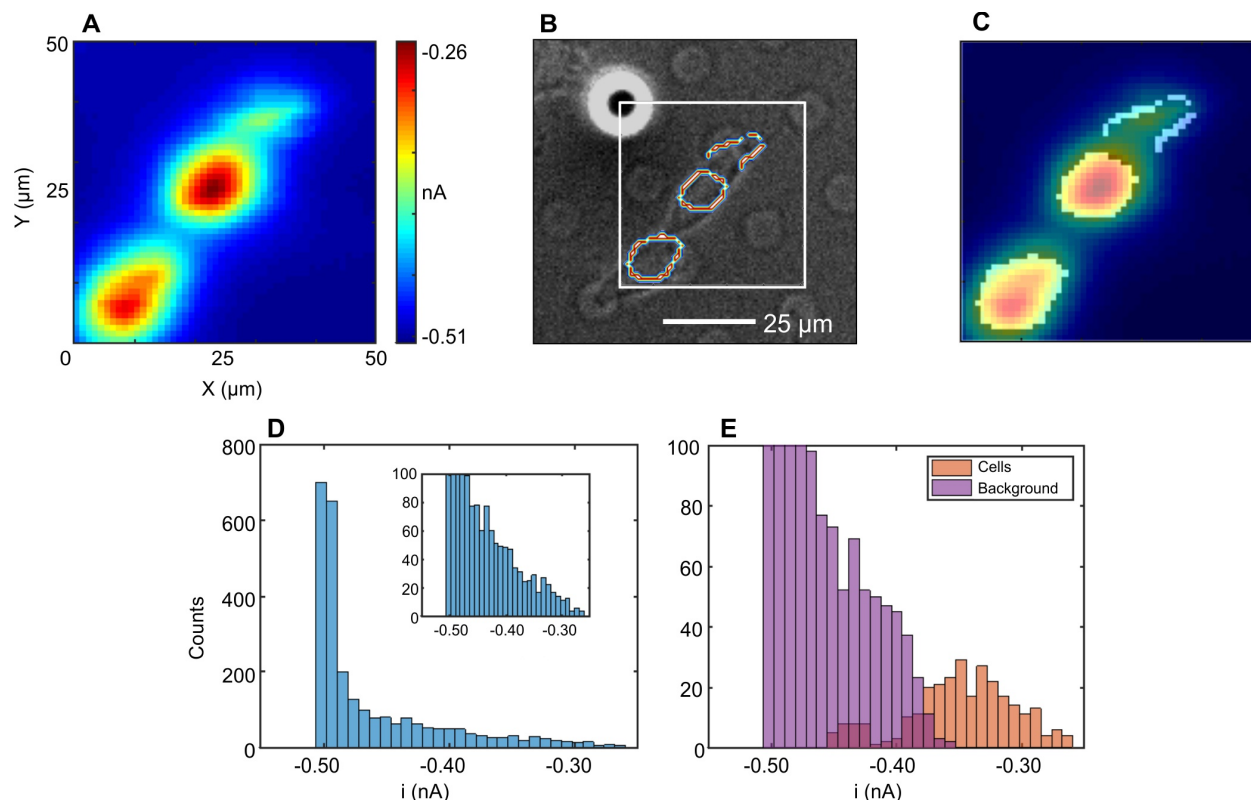


Figure 4.5 – (A) Experimental SECM image of a group of HEK cells (501 x 51 points, 7 minutes). (B) Detected edges in the SECM image (bounded by the white box) overlaid on the optical image. (C) Masked SECM image based on the detected edges. (D) Histogram of currents of the SECM image in (A). (E) Histogram of currents of the masked SECM image in (C). The cells were imaged using a 7 μm carbon fibre electrode polarized at -350 mV vs. Ag/AgCl at a tip-substrate distance of 6-7 μm in a solution of 0.5 mM $\text{Ru}(\text{NH}_3)_6\text{Cl}_3$ and 25 mM HEPES in DMEM⁻.

4.4 Conclusions

In this work, applying edge detection algorithms to feedback mode constant height SECM images has been shown to allow for the accurate estimation of feature size, the revelation of hidden details embedded in the original image, and the intelligent masking of SECM images to separate features from their background. In general, this approach is most effective when contrast in the SECM image is at a maximum, where there is a clear inflection point present in the current profile. Though these are the same conditions where the approximate shape is most prominent in the original image, the diffusional blurring obscures the position of the true edge and so can easily lead to inaccurate size estimation without further analysis.

Optimal accuracy is obtained when the sampling density is high and the image contains a large number of points, as might be obtained for line scan based scanning patterns. Performance is best when the feature is equal to or larger in size than the electrode. It may be possible to extend this methodology to other modes of SECM; success in this realm will depend on both the shape of the current profile and whether its inflection points hold the same meaning. This work has considered model substrates displaying pure and uniform feedback responses. The simulations suggest that while this method works with finite kinetics as well, non-uniform feedback behaviour could lead to current profiles displaying multiple inflection points, complicating interpretation of the data and increasing the chance of false positives.

This approach takes advantage of the well-studied Canny algorithm, which is a readily available function in many programming languages and is used in a wide variety of fields, simplifying its integration into a standard SECM imaging protocol. Though not investigated

here, protocols for high speed techniques with significantly reduced imaging time could be modified to be compatible, provided a high sampling density is used. It is most powerful for non-transparent substrates where aligning the imaged region between SECM and optical or electron microscopy is not a trivial task, though it provides potential uses for any experimental setup. Potential applications of this work include visualizing changes in cell shape or current distribution over time, image segmentation for feature recognition, and improved background subtraction. Future work will focus on extending this imaging processing approach to more quantitatively correct SECM images for diffusional blur, in addition to interpreting them in that context.

Acknowledgements

The authors would like to thank Susan P. Cole (Queen's University, Kingston, ON, Canada) for her generous donation of the HEK293 cells, Jason Ferreira (NRC) for help with the fabrication of the Au substrates, Mohini Ramkaran from the McGill Chemistry Characterization Facility for her assistance with AFM measurements, and the NSERC CGS-D program for funding.

References

- [1] Mirkin, M. V.; Nogala, W.; Velmurugan, J.; Wang, Y. *Physical Chemistry Chemical Physics* **2011**, *13*, 21196–21212.

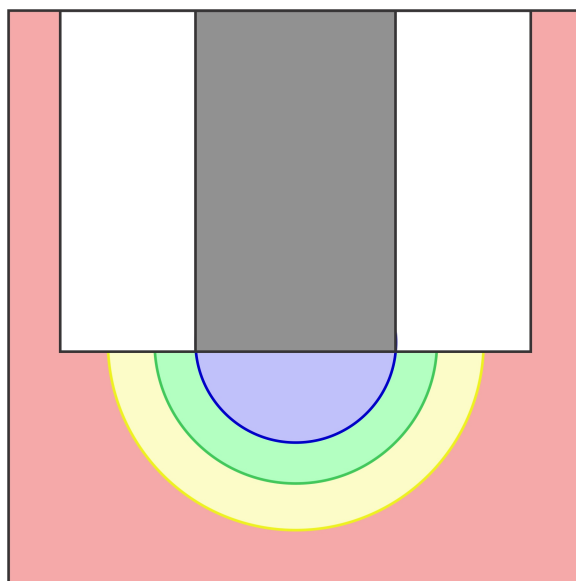
-
- [2] Bard, A. E.; Mirkin, M. E. *Scanning Electrochemical Microscopy*, 2nd ed.; CRC Press: Boca Raton, FL, USA, 2012.
- [3] Bergner, S.; Vatsyayan, P.; Matysik, F.-M. *Analytica Chimica Acta* **2013**, *775*, 1–13.
- [4] Polcari, D.; Dauphin-Ducharme, P.; Mauzeroll, J. *Chemical Reviews* **2016**, *116*, 13234–13278.
- [5] Sanchez-Sanchez, C. M.; Bard, A. J. *Analytical Chemistry* **2009**, *81*, 8094–8100.
- [6] Barton, Z. J.; Rodríguez-López, J. *Analytical Chemistry* **2014**, *86*, 10660–10667.
- [7] Wang, W.; Xu, L.; Sun, H.; Li, X.; Zhao, S.; Zhang, W. *Journal of Materials Chemistry A* **2015**, *3*, 5599–5607.
- [8] Xu, F.; Beak, B.; Jung, C. *Journal of Solid State Electrochemistry* **2012**, *16*, 305–311.
- [9] Barton, Z. J.; Rodríguez-López, J. *Analytical Chemistry* **2017**, *89*, 2716–2723.
- [10] Zhu, R.; Qin, Z.; Noël, J. J.; Shoesmith, D. W.; Ding, Z. *Analytical Chemistry* **2008**, *80*, 1437–1447.
- [11] Nowierski, C.; Noël, J. J.; Shoesmith, D. W.; Ding, Z. *Electrochemistry Communications* **2009**, *11*, 1234–1236.
- [12] Gateman, S. M.; Stephens, L. I.; Perry, S. C.; Lacasse, R.; Schulz, R.; Mauzeroll, J. *npj Materials Degradation* **2018**, *2*, 5.
- [13] Yang, M.-H.; Kriegman, D.; Ahuja, N. *IEEE Transactions on Pattern Analysis and Machine Intelligence* **2002**, *24*, 34–58.
- [14] Chaudhuri, S.; Chatterjee, S.; Katz, N.; Nelson, M.; Goldbaum, M. *IEEE Transactions on Medical Imaging* **1989**, *8*, 263–269.
- [15] van Dokkum, P. G. *Publications of the Astronomical Society of the Pacific* **2001**, *113*, 1420–1427.
- [16] Lee, C.; Wipf, D. O.; Bard, A. J.; Bartels, K.; Bovik, A. C. *Analytical Chemistry* **1991**, *63*, 2442–2447.
- [17] Kiss, A.; Nagy, G. *Electrochimica Acta* **2014**, *119*, 169–174.
- [18] Lee, Y.; Ding, Z.; Bard, A. J. *Analytical Chemistry* **2002**, *74*, 3634–3643.
- [19] Bard, A. J.; Fan, F.-R. F.; Kwak, J.; Lev, O. *Analytical Chemistry* **1989**, *61*, 132–138.
- [20] Pitta Bauermann, L.; Schuhmann, W.; Schulte, A. *Physical Chemistry Chemical Physics* **2004**, *6*, 4003–4008.

- [21] Kurulugama, R. T.; Wipf, D. O.; Takacs, S. A.; Pongmayteegul, S.; Garriss, P. A.; Baur, J. E. *Analytical Chemistry* **2005**, *77*, 1111–1117.
- [22] Shin, J. Y.; Park, J. Y.; Liu, C.; He, J.; Kim, S. C. *Pure and Applied Chemistry* **2005**, *77*, 801–814.
- [23] Polcari, D.; Hernández-Castro, J. A.; Li, K.; Geissler, M.; Mauzeroll, J. *Analytical Chemistry* **2017**, *89*, 8988–8994.
- [24] Kuss, S.; Polcari, D.; Geissler, M.; Brassard, D.; Mauzeroll, J. *Proceedings of the National Academy of Sciences* **2013**, *110*, 9249–9254.
- [25] Danis, L.; Polcari, D.; Kwan, A.; Gateman, S. M.; Mauzeroll, J. *Analytical Chemistry* **2015**, *87*, 2565–2569.
- [26] Stephens, L. I.; Mauzeroll, J. *Analytical Chemistry* **2018**, *90*, 6796–6803.
- [27] Atkins, P.; De Paula, J. *Physical Chemistry*, ninth ed.; Oxford University Press, 2010; pp 772–773.
- [28] Canny, J. *IEEE Transactions on Pattern Analysis and Machine Intelligence* **1986**, *PAMI-8*, 679–698.
- [29] Takahashi, Y.; Shevchuk, A. I.; Novak, P.; Babakinejad, B.; Macpherson, J.; Unwin, P. R.; Shiku, H.; Gorelik, J.; Klenerman, D.; Korchev, Y. E.; Matsue, T. *Proceedings of the National Academy of Sciences* **2012**, *109*, 11540–11545.
- [30] Lazenby, R. A.; McKelvey, K.; Unwin, P. R. *Analytical Chemistry* **2013**, *85*, 2937–2944.
- [31] Ballesteros Katemann, B.; Schulte, A.; Schuhmann, W. *Electroanalysis* **2004**, *16*, 60–65.
- [32] Etienne, M.; Schulte, A.; Schuhmann, W. *Electrochemistry Communications* **2004**, *6*, 288–293.
- [33] Macpherson, J. V.; Unwin, P. R. *Analytical Chemistry* **2000**, *72*, 276–285.
- [34] Kranz, C.; Friedbacher, G.; Mizaikoff, B.; Lugstein, A.; Smoliner, J.; Bertagnolli, E. *Analytical Chemistry* **2001**, *73*, 2491–2500.
- [35] Shi, W.; Baker, L. A. *RSC Advances* **2015**, *5*, 99284–99290.
- [36] Takahashi, Y.; Shevchuk, A. I.; Novak, P.; Murakami, Y.; Shiku, H.; Korchev, Y. E.; Matsue, T. *Journal of the American Chemical Society* **2010**, *132*, 10118–10126.
- [37] Liu, B.; Cheng, W.; Rotenberg, S. A.; Mirkin, M. V. *Journal of Electroanalytical Chemistry* **2001**, *500*, 590–597.

-
- [38] Li, M. S. M.; Filice, F. P.; Henderson, J. D.; Ding, Z. *The Journal of Physical Chemistry C* **2016**, *120*, 6094–6103.

Chapter 5

Flux: New Software for Analysing SECM Data



Chapter Abstract

Chapter 4 explored the idea of applying image processing algorithms developed for optical images to the analysis of electrochemical images. While this approach proved to be powerful, the MATLAB code developed was linked to a paid software license and involved a number of steps, making it less accessible. This chapter incorporates the procedure developed previously into open source Python software called Flux. This offers a number of advantages; Python is free and no paid license is required, making the code open source improves its transparency and allows it to be optimized or extended, and building a graphical user interface makes it more accessible to those without a programming background.

In addition to extending the image processing work of the previous chapter, Flux offers interfaces for performing standard analyses involved in SECM: two for electrode characterization via cyclic voltammograms and chronoamperograms, and two for surface characterization via approach curves and images. Flux allows users to input their experimental parameters, which is used to calculate theoretical values which can be overlaid on top of the experimental data for straightforward experiment/theory comparison.

The work presented in this chapter has been reproduced from:

Stephens, L.I.; Mauzeroll, J. Flux: New Software for Analysing SECM Data. *Journal of the Electrochemical Society* **2019**, 166(16), H861-H865.

5.1 Introduction

Scanning electrochemical microscopy (SECM) has become a common tool for characterizing the electrochemical reactivity of surfaces on the micro or nanoscale. Advances in microelectrode fabrication,^{1–3} instrumentation,^{4–6} and theory^{7–9} have made SECM more accessible in terms of both understanding and cost to researchers interested in a broad range of applications, which a number of recent subject specific reviews have discussed in more detail.^{10–22} Though a variety of SECM modes and microelectrode geometries have emerged with their own niches in terms of potential applications, most experiments still fall under one of four categories: cyclic voltammograms, approach curves, chronoamperograms, and images. Each of these categories possesses a standard set of analyses focused on qualitative or quantitative analysis of a localized process. While a renaissance in experimental development has focused on making the data collection accessible to all, much of the data processing is still done in-house using proprietary tools. In this work, we present a new software called Flux which provides a unified interface for performing these analyses.

Built in Python, Flux is both free and open source; in addition to its current scope of common analyses, this allows it to be modified or extended to accommodate advancements in theory and meet the changing needs of the community. In its current state, it supports input from a number of popular SECM manufacturers, and its code is written with readability in mind to ensure users can modify it to support any unique data sets they may have. The built-in theory (nonlinear curve fitting to extract geometric or kinetic parameters, calculation of a theoretical steady state current for normalization, etc.) is based on one of the most common

SECM configurations of disk microelectrodes operating in feedback mode. Importantly, the basic functionality supports a broader range of use cases, and the integration with existing theory can easily be extended to support other use cases.

SECM is part of a family of electrochemical scanning probe techniques, which also includes scanning ion conductance microscopy (SICM)^{23,24} and scanning electrochemical cell microscopy (SECCM),^{25,26} which have similar experimental methodologies and therefore similarly formatted output files. Flux has limited support for these additional techniques, but in many cases the analysis procedures diverge after plotting (for example, in the calculation of surface charge from approach curves). Currently, SECM-specific analyses are the focus of this work; however, we would like to extend this to support other electrochemical scanning probe techniques in the future.

A number of free software programs for analysis of scanning probe techniques have been developed in recent years.^{27,28} One commercial SECM software by the name of MIRA is available²⁹ which also supports analysis for a variety of input file formats and experimental types, but the paid nature of this software means the source code is not available and so cannot be extended by the end user as new developments in the field occur. By making an accessible open source platform available, Flux maintains a low entry barrier to SECM data analysis. In this way, the data treatment can be made as accessible as the data collection.

5.2 Implementation

Flux was built using Python 3.7 with the following packages: numpy (v1.16.2) and pandas (v0.24.1) were used for matrix computations, scipy (v1.2.1) for import of more complex data types, scikit-image (v0.14.2) for implementation of the Canny edge detection algorithm, matplotlib (v3.0.3) for plotting, and pyqt (v5.12) for Python bindings. A detailed overview of the source code is available in [Appendix E](#) describing how each of the data analysis tasks described in the following sections was implemented.

The software was designed to import files from a variety of instrument manufacturers. Currently supported formats include Bio-Logic Instruments/.txt, CH Instruments/.txt, HEKA Elektronik/.asc, HEKA Elektronik/.mat, and Sensolytics/.dat. The structure of these input files is detailed in [E.2](#).

5.3 Approach Curves

In an approach curve, the microelectrode is lowered in the z -direction towards the surface. As this happens, the measured current begins to deviate from its steady state value depending on the local reactivity of the surface. If the surface is insulating, diffusion to the electrode is hindered, decreasing the measured current. If the surface is conductive, the mediator may be regenerated at the surface and become available to react at the microelectrode again, increasing the measured current. If the surface is in between the two, this mediator regeneration is kinetic rather than diffusion limited, and a rate constant associated with the

surface reactivity may be assigned.

Typically, an approach curve may be performed to position the electrode close to the surface, estimate the electrode R_g for electrodes not visible optically, or quantify a local kinetic rate constant. The interface for processing approach curves is shown in [Figure 5.1](#). Flux supports processing of four types of common output files for image data, with the ability to customize the tip-substrate distance calibration, visibility of theoretical feedback lines, units, and normalization of currents according to experimental or theoretical values.

5.3.1 Normalization

When polarized at a sufficient overpotential, the currents at a disk microelectrode are diffusion limited, and diffusion of reactive species to the electroactive surface takes place with a hemispherical diffusion pattern. For an oxidation process, the magnitude of the steady state current is given by:

$$i_{ss} = 4nFD_Rc_R^*a\beta(R_g) \quad (5.1)$$

Where n is the number of electrons, F is Faraday's constant, D_R and c_R^* are the diffusion coefficient and concentration of the reduced species respectively, a is the radius of the microelectrode, and β is a parameter depending on the normalized glass radius, R_g . When thin glass sheaths are present (low R_g values), back diffusion along the sides of the glass can cause deviations from hemispherical diffusion which increase the steady state current observed. Several equations have been developed to approximate the $\beta(R_g)$ parameter from

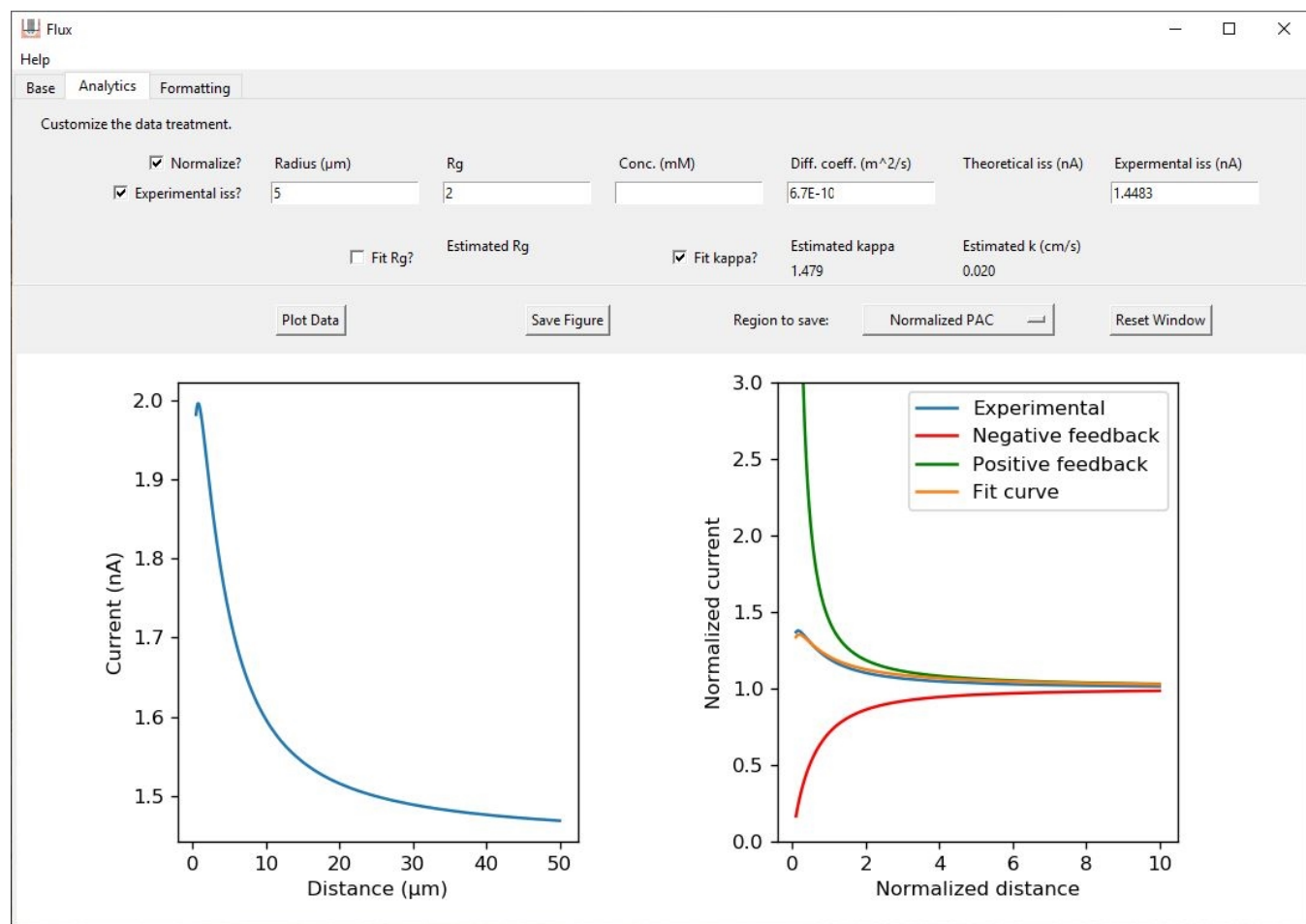


Figure 5.1 – A screenshot of the Flux interface for processing approach curves. The lefthand image shows the original data after calibrating the zero tip-substrate distance. The righthand image shows the normalized data, a theoretical curve with the κ estimated by curve fitting, and the theoretical pure feedback cases.

the measured microelectrode R_g ,^{30,31} the one implemented here⁹ is:

$$\beta(R_g) = 1 + \frac{0.23}{(R_g^3 - 0.81)^{0.36}} \quad (5.2)$$

In order to compare experiments done with different geometries of microelectrode or compositions of the imaging solution, both currents and distances may be normalized to account for these differences. For a disk microelectrode, distances are normalized to the electrode radius such that $L = d/a$, where L and d are the normalized and non-normalized tip-substrate distances respectively and a is the electrode radius. Currents are normalized to the steady state current such that $i_{norm} = i/i_{ss}$. Within Flux, the steady state current used for normalization can be either a theoretical value calculated according to the above equations or an experimental value (E.3.1), which supports a broader range of electrode geometries.

5.3.2 Calibrating Tip-Substrate Distance

To make use of further quantitative tools, approach curves are plotted in terms of tip-substrate distance rather than arbitrary distance, which requires calibration against the point $d = 0$. Robust electrodes may make contact with the surface and bend without breaking, during which time a current is still measurable, complicating this calibration. Here, three methods of calibrating the $d = 0$ point are available (E.3.2): no calibration, which uses the distances in the input file as is; first point with data, which sets the first point with an

associated current value as $d = 0$; and first derivative analysis, which sets the point where the derivative of the current is at a maximum as $d = 0$. The last option is better able to account for possible bending visible in the approach curve, though it may give erroneous results if the approach curve shows mixed kinetics or the electrode did not make contact with the surface.

5.3.3 Fitting R_g , κ

Once tip-substrate distance is calibrated, the approach curve can be treated quantitatively to estimate an unknown geometric or kinetic parameter of the system (E.3.3). For disk microelectrodes, a series of analytical approximations have been developed which generalize the shape of a normalized approach curve in terms of these parameters. A negative feedback approximation can be used in order to estimate the R_g of the electrode, and a mixed kinetics approximation to estimate the normalized rate constant κ , where $\kappa = ka/D$ of the surface at a particular point. The forms of these equations incorporated into Flux are given below:

The equation used to estimate negative feedback³¹ is:

$$Ni_T^{ins} = \frac{\left[\frac{2.08}{R_g^{0.358}} \left(L - \frac{0.145}{R_g} \right) + 1.585 \right]}{\frac{2.08}{R_g^{0.358}} (L + 0.0023R_g) + 1.57 + \frac{\ln R_g}{L} + \frac{2}{\pi R_g} \ln \left(1 + \frac{\pi R_g}{2L} \right)} \quad (5.3)$$

The equation used to estimate positive feedback³¹ is:

$$Ni_T^{cond} = \alpha(R_g) + \frac{1}{\beta(R_g)} \frac{\pi}{4 \text{ArcTan}(L)} + \left(1 - \alpha(R_g) - \frac{1}{2\beta(R_g)}\right) \frac{2}{\pi} \text{ArcTan}(L) \quad (5.4)$$

The equation used to estimate mixed kinetics³² is:

$$Ni_T^{mixed} = Ni_T^{cond} \left(L + \frac{1}{\kappa}, R_g \right) + \frac{Ni_T^{ins}(L, R_g) - 1}{(1 + 2.47R_g^{0.21}L\kappa)(1 + L^{0.006R_g+0.113}\kappa^{-0.0236R_g+0.91})} \quad (5.5)$$

$$\alpha = \ln(2) + \ln(2) \left(1 - \frac{2}{\pi} \text{ArcCos} \frac{1}{R_g} \right) - \ln(2) \left[1 - \left(\frac{2}{\pi} \text{ArcCos} \frac{1}{R_g} \right)^2 \right] \quad (5.6)$$

5.4 Images

In an imaging setup, a microelectrode is initially positioned close to a surface of interest. Under these conditions, the current measured depends on the geometry of the microelectrode, the characteristics of the imaging solution, and the nature of the surface itself. The microelectrode is then moved over the surface according to a particular scan pattern, and the current-position relationship is used to build up an electrochemical image of the surface over a larger region. The interface for processing images is shown in [Figure 5.2](#). Flux supports processing of five types of common output files for image data (Bio-Logic Instruments/.txt, CH Instruments/.txt, HEKA Elektronik/.asc, HEKA Elektronik/.mat, Sensolytics/.dat),

with the ability to customize the colourmap, units, and normalization of currents according to experimental or theoretical values.

5.4.1 Slope Correction

In 2D scan patterns such as raster, zigzag, or spiral, the electrode is moved in the x and y directions (constant z -height, variable tip-substrate distance), and the currents measured depend on both the reactivity and topography of the surface. In 3D scan patterns such as hopping or shear force, the electrode is moved in the x , y , and z directions (variable z -height, constant tip-substrate distance), and the currents measured are dependent only on the reactivity of the surface.

This description of constant height mode is the ideal case; in practice, it is more challenging. A tilt in the surface can cause a change in the intended tip-substrate distance entirely separate from the topography of the surface. This can be corrected for either on the instrument directly or through post-processing. On the instrument, a user-input slope is used to adjust the electrode movement to try and maintain constant height. In post processing, a line of the image where no reactive or topographical feature is present is used to estimate the slope in a particular direction and correct all parallel lines. Though the relationship between current and distance is not precisely linear, this approximation works well over small regions or shallow slopes. Flux supports post processing slope correction in both the x and y directions, with the line of best fit used for correction based on a user-specified edge of the image ([E.3.4](#)).

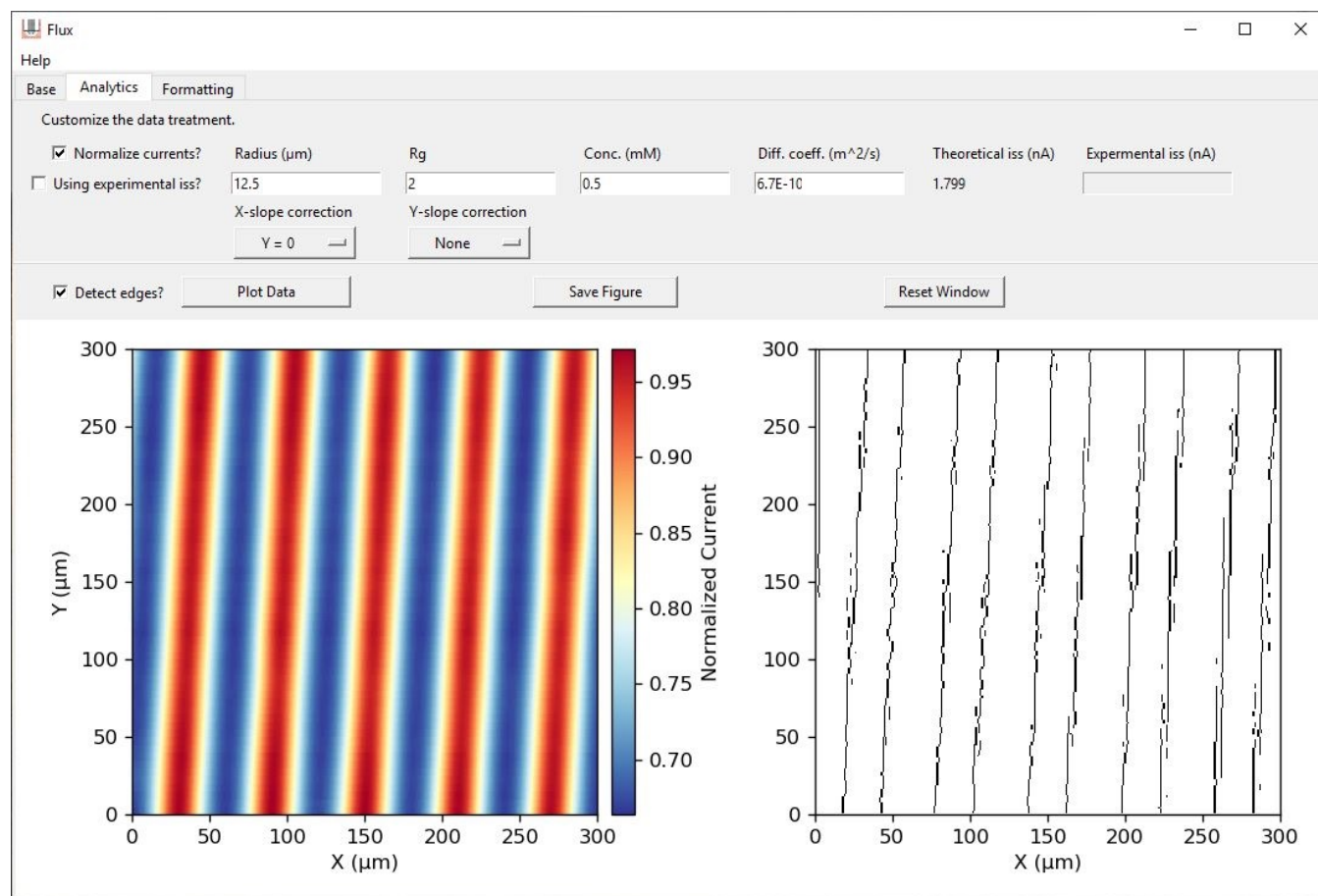


Figure 5.2 – A screenshot of the Flux interface for processing images. The raw SECM image visible on the left has been slope corrected in the x -direction and currents have been normalized based on a theoretical steady state value calculated based on input parameters for the experimental setup. The right image shows the edges detected in the image on the left.

5.4.2 Edge Detection

In our previous work,³³ we found that edge detection based on the Canny algorithm works well for estimating the boundaries of reactive features in an SECM image. This algorithm identifies the 2D-equivalent of inflection points in the current trace, which correlate well with the true feature boundaries in pure feedback cases. In Flux, this functionality is implemented through the scikit-image Python package ([E.3.5](#)).

5.5 Voltammetry

Voltammetry is commonly performed prior to a scanning probe experiment in order to characterize electrode performance. This commonly includes confirming the establishment and magnitude of a steady state current, determining the formal potential of a redox couple, or calculating the response time of an electrode. Flux supports processing of both cyclic voltammograms and chronoamperograms.

5.5.1 Cyclic Voltammetry

An example of a cyclic voltammogram (CV) processed using Flux is given in [Figure 5.3 A](#).

5.5.1.1 Formal Potential

During a CV at a macroelectrode, the formal potential of a redox couple is typically calculated as the average of the two potentials where anodic and cathodic currents are at a

maximum value respectively. In contrast, a CV at a microelectrode does not possess the same peak shape due to the establishment of a steady state current, and so this analysis cannot be performed directly. However, the first derivative of the current with respect to time does have a shape with distinct anodic and cathodic peaks (E.3.6). This has been used to calculate a formal potential, which should correlate well with the inflection point on the sigmoidal curve.

5.5.2 Chronoamperograms

An example of a chronoamperogram processed using Flux is given in Figure 5.3 B.

5.5.2.1 Response Time

The IUPAC definition of an electrode response time has been refined over time,³⁴ but a commonly used form is the time it takes the current to reach 110% of its steady state value (90% of change has occurred).³⁵ This metric is commonly used to evaluate the performance of biosensors, many of which use microelectrodes as a backbone that is then modified for selectivity to a particular biological compound. In Flux, this is calculated by first establishing two critical points: the experimental steady state current, taken as the average of the currents measured at the end of the data set; and the critical current (i_{crit} , which is the threshold for determining response time. The current trace is then examined in reverse time in order to determine the point where $\text{abs}(i > i_{crit})$. Taking the absolute value accounts for the sign differences between oxidation and reduction reactions, ensuring this procedure works for both (E.3.7).

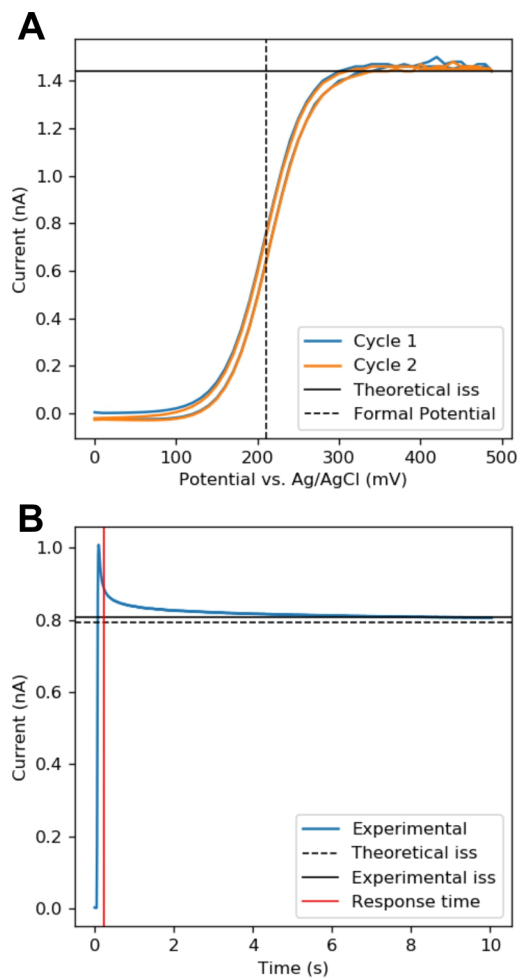


Figure 5.3 – (A) Processed data for a cyclic voltammogram, including a calculated formal potential and theoretical steady state current for comparison. (B) Processed data for a chronoamperogram, showing the theoretical and experimental steady state currents for comparison and calculated response time.

5.6 Conclusions

In general, Flux provides an accessible platform for data analysis of routine SECM experiments, lowering the entry barrier for those new to the field and reducing the analysis time for those more experienced. Though the built in theory is specific to one of the more common configurations (disk microelectrodes operating in feedback mode), many of the functions are versatile enough to support other configurations; normalization based on an experimental current can be performed for any microelectrode displaying a suitable steady state. As open source software, it can be modified freely and extended as new developments in the community occur.

The full source code can be found on Github (github.com/stepheli/fluxproject) and compiled in a self-contained .exe file (bioelectrochemistry.mcgill.ca/software.html).

References

- [1] Sun, P.; Zhang, Z.; Guo, J.; Shao, Y. *Analytical Chemistry* **2001**, *73*, 5346–5351.
- [2] Katemann, B. B.; Schuhmann, W. *Electroanalysis* **2002**, *14*, 22–28.
- [3] McKelvey, K.; Nadappuram, B. P.; Actis, P.; Takahashi, Y.; Korchev, Y. E.; Matsue, T.; Robinson, C.; Unwin, P. R. *Analytical Chemistry* **2013**, *85*, 7519–7526.
- [4] Takahashi, Y.; Hirano, Y.; Yasukawa, T.; Shiku, H.; Yamada, H.; Matsue, T. *Langmuir* **2006**, *22*, 10299–10306.

-
- [5] Kim, J.; Renault, C.; Nioradze, N.; Arroyo-Currás, N.; Leonard, K. C.; Bard, A. J. *Analytical Chemistry* **2016**, *88*, 10284–10289.
- [6] Meloni, G. N. *Analytical Chemistry* **2017**, *89*, 8643–8649.
- [7] Sun, P.; Mirkin, M. V. *Analytical Chemistry* **2006**, *78*, 6526–6534.
- [8] Galceran, J.; Cecília, J.; Companys, E.; Salvador, J.; Puy, J. *The Journal of Physical Chemistry B* **2000**, *104*, 7993–8000.
- [9] Lefrou, C.; Cornut, R. *ChemPhysChem* **2010**, *11*, 547–556.
- [10] Niu, L.; Yin, Y.; Guo, W.; Lu, M.; Qin, R.; Chen, S. *Journal of Materials Science* **2009**, *44*, 4511–4521.
- [11] Bertoncello, P. *Energy & Environmental Science* **2010**, *3*, 1620.
- [12] Souto, R. M.; Lamaka, S. V. V.; Gonzalez, S.; Gonzalez, S. *Microscopy: Science, Technology, Applications and Education*; Formatex: Badajoz, Spain, 2010; Vol. 3; pp 1769–1780.
- [13] Bard, A.; Mirkin, M. *Scanning electrochemical microscopy*, 2nd ed.; CRC Press: Boca Raton, 2012; pp 1–647.
- [14] Schuhmann, W.; Bron, M. *Polymer Electrolyte Membrane and Direct Methanol Fuel Cell Technology*; Elsevier: Philadelphia, PA, USA, 2012; Chapter 13, pp 399–424.
- [15] Bergner, S.; Vatsyayan, P.; Matysik, F.-M. *Analytica Chimica Acta* **2013**, *775*, 1–13.
- [16] Ventosa, E.; Schuhmann, W. *Physical Chemistry Chemical Physics* **2015**, *17*, 28441–28450.
- [17] Holzinger, A.; Steinbach, C.; Kranz, C. *RSC Detection Science*; 2016; pp 125–169.
- [18] Polcari, D.; Dauphin-Ducharme, P.; Mauzeroll, J. *Chemical Reviews* **2016**, *116*, 13234–13278.
- [19] Zoski, C. G. *Journal of the Electrochemical Society* **2016**, *163*, H3088–H3100.
- [20] Payne, N. A.; Stephens, L. I.; Mauzeroll, J. *CORROSION* **2017**, *73*, 759–780.
- [21] Izquierdo, J.; Knittel, P.; Kranz, C. *Analytical and Bioanalytical Chemistry* **2018**, *410*, 307–324.
- [22] Filice, F. P.; Ding, Z. *Analyst* **2019**, *144*, 738–752.
- [23] Hansma, P.; Drake, B.; Marti, O.; Gould, S.; Prater, C. *Science* **1989**, *243*, 641–643.
- [24] Chen, C.-C.; Zhou, Y.; Baker, L. A. *Annual Review of Analytical Chemistry* **2012**, *5*, 207–228.

-
- [25] Ebejer, N.; Güell, A. G.; Lai, S. C.; McKelvey, K.; Snowden, M. E.; Unwin, P. R. *Annual Review of Analytical Chemistry* **2013**, *6*, 329–351.
- [26] Ebejer, N.; Schnippering, M.; Colburn, A. W.; Edwards, M. A.; Unwin, P. R. *Analytical Chemistry* **2010**, *82*, 9141–9145.
- [27] Horcas, I.; Fernández, R.; Gómez-Rodríguez, J. M.; Colchero, J.; Gómez-Herrero, J.; Baro, A. M. *Review of Scientific Instruments* **2007**, *78*, 013705.
- [28] Nečas, D.; Klapetek, P. *Central European Journal of Physics* **2012**, *10*, 181–188.
- [29] BioLogic Science Instruments, MIRA: Microscope Image Rapid Analysis.
- [30] Zoski, C. G.; Mirkin, M. V. *Analytical Chemistry* **2002**, *74*, 1986–1992.
- [31] Lefrou, C. *Journal of Electroanalytical Chemistry* **2006**, *592*, 103–112.
- [32] Cornut, R.; Lefrou, C. *Journal of Electroanalytical Chemistry* **2008**, *621*, 178–184.
- [33] Stephens, L. I.; Payne, N. A.; Skaanvik, S. A.; Polcari, D.; Geissler, M.; Mauzeroll, J. *Analytical Chemistry* **2019**, *91*, 3944–3950.
- [34] Maccà, C. *Analytica Chimica Acta* **2004**, *512*, 183–190.
- [35] Lindner, E.; Tóth, K.; Pungor, E. *Pure and Applied Chemistry* **1986**, *58*, 469–479.

Chapter 6

Conclusions

6.1 Summary and Future Work

Electrochemists have been making measurements of current and potential dating back to the 1800's,¹ with state of the art modern potentiostats having a detection limit on the order of 10^{-15} A.² With this degree of sensitivity, the greater challenge lies in data analysis, which requires combining chemical insight regarding the reactions happening at the electrode surface with mathematical tools for quantification. In this way, electrochemical experiments can be interpreted in order to understand the behaviour of novel materials, optimize the performance of analytical techniques, and overcome theoretical limitations.

Chapter 1 presented a summary of the existing literature regarding mathematical methods for treating PDP and SECM quantitatively, which give access to macro and microscale studies of surface evolution respectively. The case study of a linear sweep voltammogram was used to explain how the conceptual model of any electrochemical cell can be translated to the underlying equations to study specific property-result relationships of interest and quantify local reactivity.

While mathematical modelling is a powerful tool for quantification of electrochemical experiments, it has two main drawbacks which are the focus of continued development work. Computationally, numerical methods represent a brute force approach to solving the characteristic system of equations, and the speed of these methods is highly dependent on the amount of computational power available in terms of processor speed and memory. The most complex models are often solved on distributed computing grids (“supercomputers”)

rather than on individual desktop machines. Chemical systems that commonly require this treatment include those with multiple mass transport mechanisms, complex geometries, or extremely long term predictions. Taking full advantage of distributed computing will be particularly crucial for corrosion applications, where the systems of interest involve all three of these complicating factors.³⁻⁵

Chemically, the accuracy of the model depends on the accuracy of the conceptual understanding. When constructing the characteristic set of equations, the modeller makes assumptions surrounding which chemical reactions occur, where they take place, and whether they contribute significantly to the measurement or can be omitted. When conceptual understanding of the system evolves, the models need to be refined to improve the accuracy of any extracted quantities such as the reaction rate constant or concentration profile. This is particularly important for mechanistic studies such as those involved in electrochemiluminescence, where new pathways or crucial intermediate species have been discovered over time.⁶⁻⁸

Chapter 2 described the challenges associated with analysing PDP for corrosion applications, where standardization was needed in order to make accurate comparisons between materials. By using an approximation equation that incorporates mass transfer limitations, a procedure was developed which can be applied to materials of vastly different reactivity.

This model assumes that corrosion takes place uniformly across the surface, an assumption that works well for low overpotentials. Consequently, in its current form it cannot be used to describe the onset of localized processes such as pitting corrosion, which is typically

present in a PDP as a sharp increase in current at high overpotentials where significant passive film breakdown occurs.^{9,10} While the crucial factors leading to pitting corrosion are a subject of intense debate in the literature,^{11–13} enhanced understanding of the critical conditions could be incorporated into this model in future work in order to provide more accurate treatment of systems where the dominant corrosion mechanism changes over time.

Chapter 3 considered multifunctional microelectrodes, a class of electrode that allows an electrochemical signal to be measured simultaneously with a second localized quantity. This chapter identified the unexpectedly strong dependence of the measured signal on the electrode shape, in addition to the already well-known dependence on electrode size. In particular, this work proposed that the same substrate imaged with both single and multifunctional microelectrodes could yield drastically different images under a critical set of conditions. As this type of electrode becomes increasingly more common due to its inherent advantages in terms of spatial and temporal alignment, this understanding will be needed to decouple the effect of the probe geometry on signal response.

This chapter considered the specific case of a dual barrel microelectrode operating in the SG-TC mode of SECM, a system which represents one of many possible configurations. Experimental proof-of-concept works already exist for SECM-SICM,^{14–17} SECM-AFM,^{18–21} and SECM-Raman.^{22,23} Many of these systems have not received an extensive theoretical treatment yet, making them more qualitative than quantitative. Extending the model built in this work to consider these systems will require overcoming some of the computational challenges discussed previously, such as the addition of migration as a significant mass trans-

port mechanism and the treatment of complex 3D geometries. Future work on this topic could further develop the geometry-current relationship for each of these configurations, with the following key objectives:

1. Generalizing the results to develop a theoretical steady state current approximation that could be used for rapid probe characterization.
2. Determining the optimal probe geometry, and refining the fabrication procedure to produce probes of this optimal geometry.
3. In cases where the probe geometry produces a SECM image of the substrate that is spatially distorted, correcting the distorted image to obtain a more accurate response.

Chapter 4 took a step towards the objective of image correction inspired by **Chapter 3** by successfully applying image processing algorithms to SECM images. It was demonstrated that the inflection points in an SECM signal correlate well with the true boundaries of reactive or topographical features on the surface, and that these can be rapidly identified using edge detection algorithms. The enhanced precision this procedure provides has the potential to improve structure-reactivity analyses. For example in the field of corrosion, reactive features are commonly associated with secondary phases in metallic alloys, which have a different composition to the bulk alloy.^{24–26}

Future work could extend this study in two key ways. The experimental systems chosen for the initial study all displayed pure feedback behaviours, where either local variations in reactivity or topography gave rise to the contrast in the SECM image. This procedure

could first be evaluated against substrates which do not display pure feedback (slow substrate surface kinetics), or where the two contributions of topography and reactivity are destructive rather than constructive. An example of this would be a raised reactive feature, where the increase in reactivity would increase the current and decrease in tip-substrate distance (in constant height mode) would decrease the current.

Second, this procedure could be incorporated into the broader goal of true image correction. There is some precedent for using the edges detected in an image as a guideline for an image correction algorithm²⁷ based on blind deconvolution, where the point spread function that acts to blur the ideal sharp image was not previously known. If this procedure can be translated to electrochemical images, the point spread function for any SECM image could be predicted and used to correct the experimental blurred image. This approach would have two major advantages: it could improve image resolution without requiring additional instrumentation (as opposed to the historical approach of improving resolution by fabricating smaller electrodes), and it could be retroactively applied. This method rests on the assumption that the point spread function is characteristic of the electrode shape and tip-substrate distance, and is independent of the sample being tested. In this way, the distortions observed in [Chapter 3](#) introduced by the asymmetrical electrode shape could be corrected. This leverages existing image processing algorithms in a way that is concretely linked to theory, which provides guidelines for procedural implementation that avoid the risks of arbitrary deblurring.

While the concept of image blurring translates well between optical and electrochemical images, there are fundamental differences between the two that may mean the procedures are

not applicable. The point spread function describes how the signal from a single point of negligible size is dispersed over a larger area. In optical microscopy the source of signal (photons) is localized in this way and so this approach is reasonable. For example in super-resolution fluorescence, the signal is assumed to emanate from single molecular fluorophores.^{28–30} In electrochemical microscopy the source of signal (chemical reaction) is not localized in the same way and takes place across the entire electroactive surface area. While single molecule studies have been carried out electrochemically,^{31,32} these setups usually involve a stationary electrode rather than one that is scanned during the imaging process.

Chapter 5 extended the work of **Chapter 4** to incorporate the edge detection procedure into open source software with a graphical user interface. In addition to image processing, Flux automated both electrode characterization via chronoamperometry and cyclic voltammetry, as well as surface characterization via approach curves and imaging. In this way, the theory developed for quantitative treatment of experimental data was made more accessible, demonstrating how the theory developed can be used in practice.

In a recent discussion of the analytical metrics recommended by IUPAC³³ in the context of SECM,³⁴ the major quantitative challenges identified as not yet solved include a high sensitivity to experimental conditions leading to poor robustness, a lack of protocols for identifying and correcting drift, and uncertain experimental accuracy associated with being unable to verify experimental results against certified reference values. To address these challenges, systematic data treatment methodologies are needed such as software provides. Image processing cannot create something from nothing, but the edge detection procedure

developed showed reduced sensitivity to experimental conditions that is promising for standardization. Geometrically precise substrates like the Au/SiO₂ samples used in **Chapters 4-5** could be used as reference substrates, and an experimental image compared to a reference image to determine if experimental drift has exceeded a threshold for recalibration. Though simulated data bears some differences from a certified reference material, the quantitative comparison of theoretical and experimental data is a step towards an independent verification of accuracy.

In addition to standardization, section 1.3.1.2 touched on some of the extensive theory development that has occurred in the SECM community since the inception of the technique. Some of these works have seen widespread adoption and further development (the approximation equations), while others had promising ideas but never caught traction (image processing algorithms and deconvolution). One of the deciding factors that controls which category a work falls into has been its accessibility. As the idea of treating SECM images using image processing algorithms like edge detection is explored further, this type of software development is needed for the methods developed to reach their full potential.

Future work could also extend Flux to support related electrochemical scanning probe techniques, for which the most logical initial extensions would be SICM and the scanning micropipette contact method (SMCM).

In SICM ([Figure 6.1 A](#)), a pipette with a narrow opening is used as the probe, and a potential is applied between a reference electrode within the pipette to one positioned outside in bulk solution. Restricted mass transport through the opening of the pipette creates a large potential gradient in solution, and significant migrational effects for ions in solution

that give rise to a contrast in signal. In SICM, approach curves are also commonly used for surface characterization, though the signal depends on topography and surface charge rather than topography and surface reactivity.³⁵ Equations have been developed that generalize the current-distance relationship for SICM³⁶ which could be incorporated into the software, though these have not yet been extended to include an adjustable parameter that describes a property of the surface such as porosity or surface charge.

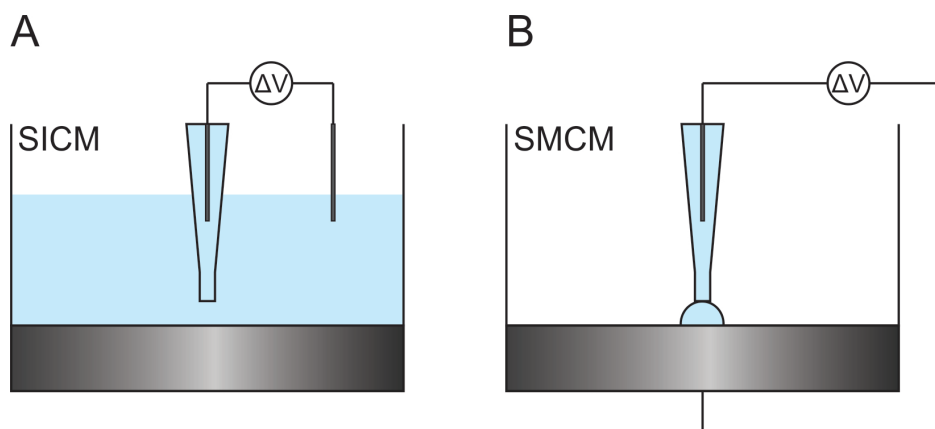


Figure 6.1 – Schematic of (A) Scanning ion conductance microscopy (SICM) and (B) Scanning micropipette contact method (SMCM).

SMCM (Figure 6.1 B) also uses a pipette with a narrow opening as a probe, but the solution is confined to the pipette and the substrate is not fully immersed. When the probe is brought close to the surface, a droplet wets the surface and forms a local electrochemical cell where any measurement can be carried out. The probe can be retracted and repositioned at a different location on the surface in a hopping pattern to build up a map of local reactivity. This has been used to carry out local PDP on a corroding sample,³⁷ an application which will likely see extensive development in the future. Future work could incorporate the

approximation equation in Chapter 2 to the Flux software, simplifying the entire analysis procedure.

6.2 Final Thoughts

Science is iterative, and while that means building on the understanding of those that came before us, it also means accepting the possibility that our current understanding needs to be refined too. The way we do this is by quantifying our approach. Equations give us an understanding of cause and effect, orders of magnitude give us the context of proportion, and statistical metrics give us decision criteria we can test against.

Advances in computing power have expanded the scope of what can be modelled using numerical methods. When algorithms for constructing and solving non-uniform meshes were initially optimized for electrochemical systems, it became possible to extract mechanistic insight from simulations of voltammetry.^{38–41} Since then, the scope of problems solved has expanded from a diffusion-centric focus to include convection and migration.^{42–44} Though these types of problems have become more accessible, new limitations have developed; simulations of fluid flow are still notoriously computationally challenging.^{45–47} Overcoming these limitations will depend not just on taking advantage of increased computer power, but optimizing the models and solvers to make the most of our existing capabilities, as was done in the early works.^{38–41} This will be particularly important for simulations of high-speed tandem scanning probe techniques like SECM-SICM, where all three mass transport mechanisms contribute to the measured signal.

As nanoscale experiments continue to explore the realm of single molecule electrochemistry,^{48–51} the gap between macroscale and microscale models introduced in 1.3.2.2.1 narrows. Microscale models such as density functional theory or molecular dynamics simulations could be used to explain traditionally macroscale measurements such as current, potential, and resistance. For example, if a heterogeneous rate constant is viewed through the lens of the Arrhenius equation as having a given pre-exponential factor, it may be possible to decompose that pre-exponential factor in terms of the experimental environment with respect to solvent effects. The reorganization energy associated with desolvation could also be connected to Marcus theory and used to explore fields like electrochemiluminescence.

Electrochemical systems are at the heart of corrosion, energy, and biology. When designing and optimizing these systems, we need to make decisions based on factors of time, cost, environment, and efficacy. While some of these factors are out of the scope of this thesis, the mathematical tools presented here pin down the last of these, efficacy. They enable us to identify steels that resist rusting, microstructures that produce stable macromaterials, and surpass system limits to achieve better spatial and temporal resolution than ever before.

References

- [1] Ampere, A. *Recueil d'observations electro-dynamiques*; Crochard: Paris, 1822.
- [2] HEKA Elektronik, *ElProScan*; 2019; pp 1–20.
- [3] Simillion, H.; Van den Steen, N.; Terryn, H.; Deconinck, J. *Electrochimica Acta* **2016**, *209*, 149–158.
- [4] Bösch, N.-C.; Höche, D.; Mittelbach, A.; Kainer, K. U. *Materials and Corrosion* **2017**, *68*, 699–710.
- [5] Xu, L.; Cheng, Y. *Corrosion Science* **2013**, *73*, 150–160.

-
- [6] Faulkner, L. R.; Bard, A. J. *Journal of the American Chemical Society* **1969**, *91*, 209–210.
- [7] Tachikawa, H.; Bard, A. J. *Chemical Physics Letters* **1974**, *26*, 246–251.
- [8] Miao, W.; Choi, J.-P.; Bard, A. J. *Journal of the American Chemical Society* **2002**, *124*, 14478–14485.
- [9] Casillas, N.; Charlebois, S.; Smyrl, W.; White, H. *Journal of the Electrochemical Society* **1994**, *141*, 636–642.
- [10] Muto, I.; Izumiyama, Y.; Hara, N. *Journal of the Electrochemical Society* **2007**, *154*, C439.
- [11] Frankel, G.; Li, T.; Scully, J. R. *Journal of the Electrochemical Society* **2017**, *164*, C180–C181.
- [12] Laycock, N. J.; Newman, R. C. *Corrosion Science* **1997**, *39*, 1771–1790.
- [13] Marcus, P.; Maurice, V.; Strehblow, H. H. *Corrosion Science* **2008**, *50*, 2698–2704.
- [14] Comstock, D. J.; Elam, J. W.; Pellin, M. J.; Hersam, M. C. *Analytical Chemistry* **2010**, *82*, 1270–1276.
- [15] Takahashi, Y.; Shevchuk, A. I.; Novak, P.; Murakami, Y.; Shiku, H.; Korchev, Y. E.; Matsue, T. *Journal of the American Chemical Society* **2010**, *132*, 10118–10126.
- [16] Morris, C. A.; Chen, C.-C.; Baker, L. A. *Analyst* **2012**, *137*, 2933.
- [17] Nadappuram, B. P.; McKelvey, K.; Al Botros, R.; Colburn, A. W.; Unwin, P. R. *Analytical Chemistry* **2013**, *85*, 8070–8074.
- [18] Davoodi, A.; Pan, J.; Leygraf, C.; Norgren, S. *Electrochemical and Solid-State Letters* **2005**, *8*, B21–B24.
- [19] Macpherson, J. V.; Unwin, P. R. *Analytical Chemistry* **2000**, *72*, 276–285.
- [20] Kueng, A.; Kranz, C.; Lugstein, A.; Bertagnolli, E.; Mizaikoff, B. *Angewandte Chemie International Edition* **2003**, *42*, 3238–3240.
- [21] Sklyar, O.; Kueng, A.; Kranz, C.; Mizaikoff, B.; Lugstein, A.; Bertagnolli, E.; Wittstock, G. *Analytical Chemistry* **2005**, *77*, 764–771.
- [22] Etienne, M.; Dossot, M.; Grausem, J.; Herzog, G. *Analytical Chemistry* **2014**, *86*, 11203–11210.
- [23] Schorr, N. B.; Jiang, A. G.; Rodríguez-López, J. *Analytical Chemistry* **2018**, *90*, 7848–7854.
- [24] He, H.; Zhu, R. K.; Qin, Z.; Keech, P.; Ding, Z.; Shoesmith, D. W. *Journal of the Electrochemical Society* **2009**, *156*, C87–C94.
- [25] Dauphin-Ducharme, P.; Matthew Asmussen, R.; Tefashe, U. M.; Danaie, M.; Jeffrey Binns, W.;

- Jakupi, P.; Botton, G. a.; Shoesmith, D. W.; Mauzeroll, J. *Journal of the Electrochemical Society* **2014**, *161*, C557–C564.
- [26] Nowierski, C.; Noël, J. J.; Shoesmith, D. W.; Ding, Z. *Electrochemistry Communications* **2009**, *11*, 1234–1236.
- [27] Joshi, N.; Szeliski, R.; Kriegman, D. J. PSF estimation using sharp edge prediction. 2008 IEEE Conference on Computer Vision and Pattern Recognition. 2008; pp 1–8.
- [28] Moerner, W. E.; Kador, L. *Physical Review Letters* **1989**, *62*, 2535–2538.
- [29] Hell, S. W.; Wichmann, J. *Optics Letters* **1994**, *19*, 780.
- [30] Dickson, R. M.; Cubitt, A. B.; Tsien, R. Y.; Moerner, W. E. *Nature* **1997**, *388*, 355–358.
- [31] Fan, F.-R. F.; Kwak, J.; Bard, A. J. *Journal of the American Chemical Society* **1996**, *118*, 9669–9675.
- [32] Zhang, J.; Kuznetsov, A. M.; Medvedev, I. G.; Chi, Q.; Albrecht, T.; Jensen, P. S.; Ulstrup, J. *Chemical Reviews* **2007**, *108*, 2737–2791.
- [33] International Union of Pure and Applied Chemistry, *Pure and Applied Chemistry* **2002**, *74*, 835–855.
- [34] Izquierdo, J.; Knittel, P.; Kranz, C. *Analytical and Bioanalytical Chemistry* **2018**, *410*, 307–324.
- [35] Klausen, L. H.; Fuhs, T.; Dong, M. *Nature Communications* **2016**, *7*, 12447.
- [36] Chen, C.-C.; Zhou, Y.; Baker, L. A. *Annual Review of Analytical Chemistry* **2012**, *5*, 207–228.
- [37] Yule, L. C.; Bentley, C. L.; West, G.; Shollock, B. A.; Unwin, P. R. *Electrochimica Acta* **2019**, *298*, 80–88.
- [38] Feldberg, S. W. *Journal of Electroanalytical Chemistry and Interfacial Electrochemistry* **1981**, *127*, 1–10.
- [39] Feldberg, S. W. *Journal of Electroanalytical Chemistry and Interfacial Electrochemistry* **1987**, *222*, 101–106.
- [40] Lerke, S. A.; Evans, D. H.; Feldberg, S. W. *Journal of Electroanalytical Chemistry and Interfacial Electrochemistry* **1990**, *296*, 299–315.
- [41] Feldberg, S. W. *Journal of Electroanalytical Chemistry and Interfacial Electrochemistry* **1990**, *290*, 49–65.

-
- [42] Rudolph, M. *Journal of Electroanalytical Chemistry* **1992**, *338*, 85–98.
- [43] Rudolph, M. *Journal of Electroanalytical Chemistry* **1994**, *375*, 89–99.
- [44] Britz, D.; Strutwolf, J. *Digital Simulation in Electrochemistry*; Monographs in Electrochemistry; Springer International Publishing: Cham, 2016.
- [45] Ladd, A. J. C. *Journal of Fluid Mechanics* **1994**, *271*, 285–309.
- [46] Schmid, P. J. *Journal of Fluid Mechanics* **2010**, *656*, 5–28.
- [47] Noyhouzer, T.; Perry, S. C.; Vicente-Luis, A.; Hayes, P. L.; Mauzeroll, J. *Journal of The Electrochemical Society* **2018**, *165*, H10–H15.
- [48] Fan, F.-R. F.; Bard, A. J. *Science* **1995**, *267*, 871–874.
- [49] Tao, N. J. *Physical Review Letters* **1996**, *76*, 4066–4069.
- [50] Haiss, W.; van Zalinge, H.; Higgins, S. J.; Bethell, D.; Höbenreich, H.; Schiffrin, D. J.; Nichols, R. J. *Journal of the American Chemical Society* **2003**, *125*, 15294–15295.
- [51] Xu, B. *Science* **2003**, *301*, 1221–1223.

Appendices

Appendix A

Supporting Information for Chapter 1

A.1 Introduction

The MATLAB code in this appendix will construct the finite difference model of a linear sweep voltammogram described in [1.2.1.3](#).

A.2 Code Outline

The script is composed of four main sections with the following structure:

1. **Simulation inputs.** In this section, universal constants and adjustable input parameters are defined. Units and recommended values are given in square and curly brackets respectively. Modifying the values in this section will change the appearance of the LSV when the simulation is run.
2. **Time 0 : Initial setup and time step.** Here, the grids needed for the finite difference simulation are created. Space, time, and concentration are discretized. Initial values for the potential and rate constant are calculated based on the input parameters. A reaction takes place in box 1 generating an initial current, and the concentration profiles are updated.
3. **Time > 0 : Time stepping.** The iterative procedure described in Equations 11-26 of the manuscript is implemented. For each time point, the potential and rate constant are updated, a chemical reaction producing an electrochemical current takes place in box 1, and the concentration profiles in all boxes are updated based on diffusion.

4. **Visualization of results.** Plots of the potential, current, rate constant, and concentration profiles are generated ([Figure A.1](#)).

A.3 Usage Notes

Some combinations of parameters may not appear to work ([Figure A.2](#)) at first glance. This is a discretization artifact. The default values for the number of total mesh points (*npts_x*) and number of total time points (*npts_t*) were selected for the default set of parameters. These values may need to be increased ([Figure A.3](#)) if changes in the system are happening more quickly.

A.4 MATLAB Script

```
%%%%%%%%%%%%%%%%%%%%%%%%%%%%%%%%%%%%%%%%%%%%%%%%%%%%%%%%%%%%%%%%%%%%%%%%
%% Section 0: Clean up workspace %%
%%%%%%%%%%%%%%%%%%%%%%%%%%%%%%%%%%%%%%%%%%%%%%%%%%%%%%%%%%%%%%%%%%%%%%%%
clear all
close all
clc

%%%%%%%%%%%%%%%%%%%%%%%%%%%%%%%%%%%%%%%%%%%%%%%%%%%%%%%%%%%%%%%%%%%%%%%%
%% Section 1: Simulation inputs %%
%%%%%%%%%%%%%%%%%%%%%%%%%%%%%%%%%%%%%%%%%%%%%%%%%%%%%%%%%%%%%%%%%%%%%%%%
%%% Constants %%%
F = 96485; % Faraday's constant [C/mol]
R = 8.314; % Gas constant [(C*V)/(mol*K)]
T = 298; % Temperature [K]

%%% Electrochemical parameters %%%
% Potential waveform
E_start = 0; % Start potential [V] {default: 0}
E_end = -0.8; % End potential [V] {default: -0.8}
E_0 = -0.4; % Standard potential [V] {default: -0.4}
```

```

nu = 10; % Scan rate [mV/s] {default: 10}

% Redox mediator
D = 1E-6; % Diffusion coefficient [cm^2/s] {default: 1E-6}
c_ox = 1; % Bulk concentration of oxidized species [M] {default: 1}
c_red = 1E-3; % Bulk concentration of reduced species [M] {default: 1E-3}
n = 1; % Number of electrons transferred during reaction {default: 1}
alpha = 0.5; % Transfer coefficient (unitless) {default: 0.5}

% Electrode
A = 1; % Electrode area [cm^2] {default: 1}
k_0 = 1E-1 ; % Heterogeneous rate constant [m/s] {default: 1E-1}

%%% Finite difference parameters %%%
npts_x = 100; % Number of mesh points {default: 100}
npts_t = 500; % Number of time steps {default: 500}

%%%%%%%%%%%%%%%%%%%%%%%%%%%%%%%%%%%%%%%%%%%%%%%%%%%%%%%%%%%%%%%%%%%%%%%%%%%%%%
%% Section 2: Time 0 / Initial Setup and Time Step %%
%%%%%%%%%%%%%%%%%%%%%%%%%%%%%%%%%%%%%%%%%%%%%%%%%%%%%%%%%%%%%%%%%%%%%%%%%%%%%%
% Discretize x
total_x = 0.1; % Maximum x value to simulate [cm]
del_x = total_x/npts_x; % x interval
x = [0:del_x:total_x]'; % Discretized x

% Discretize t
total_t = abs(E_end - E_start)/(nu/1000); % Maximum t value to simulate (1 LSV)
del_t = total_t/npts_t; % Time interval
t = [0:del_t:total_t]'; % Discretized t

% Set uniform concentration along discretized x
cox_x = repmat(c_ox, [npts_x,npts_t]);
cred_x = repmat(c_red, [npts_x,npts_t]);

% Setup empty matrices for time-dependent quantities that will be
% filled in as the simulation progresses
E_t = zeros(npts_t,1);
kred_t = zeros(npts_t,1);
i_t = zeros(npts_t,1);

% Calculate initial potential
E_curr = E_start; % E_curr = Current potential (single value)
E_t(1) = E_curr; % E_t = Potential waveform (matrix of values)

% Calculate formal potential according to the Nernst equation
E_eq = E_0 - ((R*T)/(n*F) * log(c_ox/c_red));

% Calculate initial rate constant according to the Butler-Volmer equation
eta = E_curr - E_eq; % Overpotential (V)

```



```

kred_curr = k_0*exp((-alpha*n*F*eta)/(R*T));

% Concentration in box 0 updated due to chemical reaction
cred_x(1,1) = cred_x(1) + (del_t*(kred_curr * cox_x(1,1))); % Equation 17
cox_x(1,1) = cox_x(1) - (del_t*(kred_curr * cox_x(1,1))); % Equation 20

% Current is calculated based on change in concentration
i_t(1) = -n*F*(del_x*(cred_x(1,1) - c_red) / del_t);

%%%%%%%%%%%%%%%%%%%%%%%%%%%%%%%%%%%%%%%%%%%%%%%%%%%%%%%%%%%%%%%%%%%%%%%%
%% Section 3: Time > 0: Simulation Continues %%
%%%%%%%%%%%%%%%%%%%%%%%%%%%%%%%%%%%%%%%%%%%%%%%%%%%%%%%%%%%%%%%%%%%%%%%%

for j = 2:npts_t+1 % Iterate over number of time points
    %% Pull concentration profiles from end of previous time step %%
    cred_x(:,j) = cred_x(:,j-1);
    cox_x(:,j) = cox_x(:,j-1);

    %%% Update concentration due to diffusion: Equation 26 %%%
    for i = 1:npts_x % Iterate over number of boxes
        % Note: a temporary variable is used here to make sure that the
        % concentration for this time step does not change as it is being
        % used in the calculation

        % In the first box (i=1), we use a modified diffusion equation since
        % there is no box with index (i-1)
        if i == 1
            cred_temp(i,j) = cred_x(i,j) + (D*del_t/(del_x^2))*...
                ((cred_x(i+1,j) - cred_x(i,j)));
            cox_temp(i,j) = cox_x(i,j) + (D*del_t/(del_x^2))*...
                ((cox_x(i+1,j) - cox_x(i,j)));

            % In the last box (i=max), we apply our boundary condition of
            % concentration = bulk concentration
            elseif i == npts_x
                cred_temp(i,j) = c_red;
                cox_temp(i,j) = c_ox;

            % In all other boxes, we use the diffusion expression
            % (Equation 26) as normal
            else
                cred_temp(i,j) = cred_x(i,j) + (D*del_t/del_x^2)*((cred_x(i+1,j) - 2*cred_x(i,
                    j) + cred_x(i-1,j)));
                cox_temp(i,j) = cox_x(i,j) + (D*del_t/del_x^2)*((cox_x(i+1,j) - 2*cox_x(i,j) +
                    cox_x(i-1,j)));
            end
        end

    end

    cred_x(:,j) = cred_temp(:,j);

```

```

    cox_x(:,j) = cox_temp(:,j);

    %% Update potential: Equation 12 %%
    E_curr = E_curr - del_t*(nu/1000);
    E_t(j) = E_curr;

    %% Update rate constant: Equation 14 %%
    eta = E_curr - E_eq; % Overpotential (V)
    kred_curr = k_0* exp((-alpha*n*F*eta)/(R*T));
    kred_t(j) = kred_curr;

    %% Chemical reaction in box 0: Equations 17 & 20 %%
    cred_x(1,j) = cred_x(1,j-1) + (del_t*(kred_curr * cox_x(1,j-1)));
    cox_x(1,j) = cox_x(1,j-1) - (del_t*(kred_curr * cox_x(1,j-1)));

    %% Calculate current: Equation 22 %%
    i_t(j) = -n*F*(del_x*(cred_x(1,j) - cred_x(1,j-1)) / del_t);

end

%%%%%%%%%%%%%%%%%%%%%%%%%%%%%%%%%%%%%%%%%%%%%%%%%%%%%%%%%%%%%%%%%%%%%%%%
%% Section 4: Figures %%
%%%%%%%%%%%%%%%%%%%%%%%%%%%%%%%%%%%%%%%%%%%%%%%%%%%%%%%%%%%%%%%%%%%%%%%%
% Settings applying to the appearance of all graphs
FontSize = 18;
DataLineWidth = 2;
PlotLineWidth = 2;

% Indices of times to plot concentration profiles
[index_time2,~] = find(i_t == min(i_t)); % Locate time index when current is largest
index_time1 = floor(0.9*index_time2); % Select a time point prior to peak
index_time3 = floor(1.1*index_time2); % Select a time point after peak

% Construct the megafigure
figure('units','normalized','outerposition',[0 0 1 0.9])

subplot(2,4,[1,2,5,6]) % Voltammogram
plot(E_t,i_t,'linewidth',2)
xlabel('Potential (V)')
ylabel('Current (A)')
axis([E_end E_start 1.25*min(i_t) -0.1*min(i_t)])
xL = get(gca,'XLim');
yL = get(gca,'YLim');
ytickformat('%,.1f')
line([E_t(index_time1) E_t(index_time1)],yL,'linewidth',DataLineWidth-0.5,'color',[0.8500
0.3250 0.0980])
line([E_t(index_time2) E_t(index_time2)],yL,'linewidth',DataLineWidth-0.5,'color',[0.9290
0.6940 0.1250])

```

```

line([E_t(index_time3) E_t(index_time3)],yL,'linewidth',DataLineWidth-0.5,'color',[0.4940
0.1840 0.5560])
legend('i(E)', 'Point 1', 'Point 2', 'Point 3', 'location', 'best')
set(gca, 'FontSize', FontSize, 'LineWidth', PlotLineWidth)
title('Voltammogram')

subplot(2,4,3) % Potential waveform
plot(t,E_t,'linewidth',DataLineWidth)
xlabel('Time (s)')
ylabel('Potential (V)')
xL = get(gca, 'XLim');
line(xL,[E_0, E_0], 'linestyle', '--', 'linewidth', DataLineWidth, 'color', 'k')
line(xL,[E_eq, E_eq], 'linestyle', ':', 'linewidth', DataLineWidth, 'color', 'k')
ytickformat('%,.1f')
legend('E(t)', 'E_{0}', 'E_{eq}', 'location', 'best')
set(gca, 'FontSize', FontSize, 'LineWidth', PlotLineWidth)
axis([-inf inf -inf inf])
title('Potential Waveform')

subplot(2,4,4) % Rate constant
plot(t,kred_t,'linewidth',DataLineWidth)
xlabel('Time (s)')
ylabel('k_{red} (cm/s)')
set(gca, 'FontSize', FontSize, 'LineWidth', PlotLineWidth)
title('Rate Constant')

subplot(2,4,7) % Normalized concentration profile of c_red
h = plot(1000*(x(1:npts_x)), cred_x(:, index_time1)./c_ox, ...
1000*(x(1:npts_x)), cred_x(:, index_time2)./c_ox, ...
1000*(x(1:npts_x)), cred_x(:, index_time3)./c_ox, 'linewidth', 2);
set(h(1), 'color', [0.8500 0.3250 0.0980])
set(h(2), 'color', [0.9290 0.6940 0.1250])
set(h(3), 'color', [0.4940 0.1840 0.5560])
xL = get(gca, 'XLim');
line(xL,[c_ox c_ox], 'linestyle', '--', 'color', 'k')
xlabel('x (mm)')
ylabel('c_R/c_{0} (bulk)')
set(gca, 'FontSize', FontSize, 'LineWidth', PlotLineWidth)
axis([0 1000*0.5*max(x) 0.5*c_red 1.2*max(max(cred_x/c_ox))])
legend('Point 1', 'Point 2', 'Point 3', 'c_{ox} (bulk)', 'location', 'southeast')
title('Concentration Profile')

subplot(2,4,8) % Normalized concentration profile of c_ox
h = plot(1000*(x(1:npts_x)), cox_x(:, index_time1)./c_ox, ...
1000*(x(1:npts_x)), cox_x(:, index_time2)./c_ox, ...
1000*(x(1:npts_x)), cox_x(:, index_time3)./c_ox, 'linewidth', 2);
set(h(1), 'color', [0.8500 0.3250 0.0980])
set(h(2), 'color', [0.9290 0.6940 0.1250])
set(h(3), 'color', [0.4940 0.1840 0.5560])

```

```

xL = get(gca,'XLim');
line(xL,[c_ox c_ox],'linestyle','--','color','k')
xlabel('x (mm)')
ylabel('c_0/c_{0 (bulk)}')
ytickformat('%,.1f')
set(gca,'FontSize',FontSize,'LineWidth',PlotLineWidth)
axis([0 1000*0.5*max(x) 0 1.2*c_ox])
legend('Point 1','Point 2','Point 3','c_{ox (bulk)}','location','southeast')
title('Concentration Profile')

```

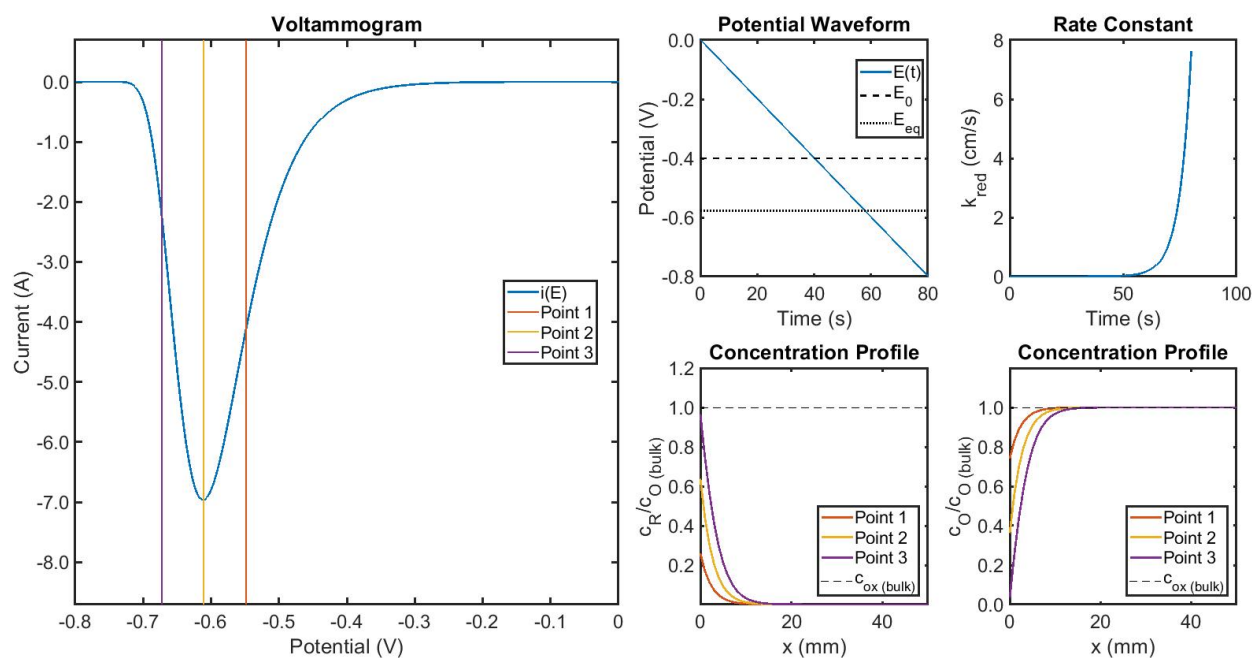


Figure A.1 – Script output for the default set of parameters.

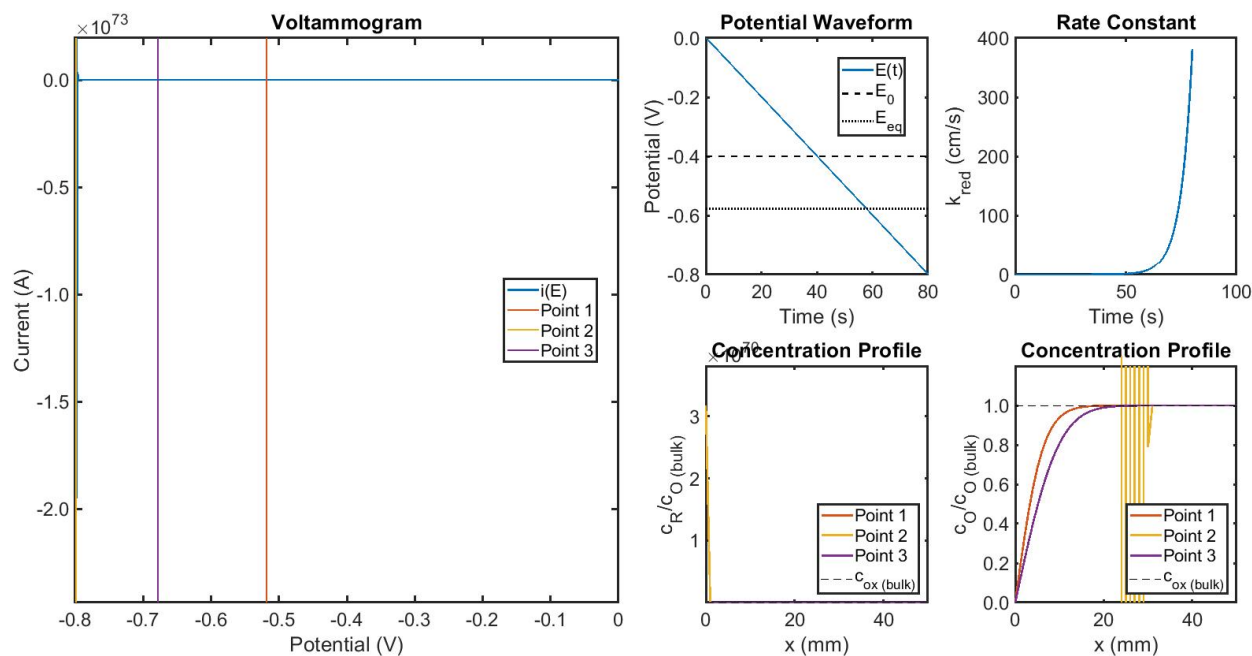


Figure A.2 – Script output for $k_0 = 5$ m/s and all other parameters having default settings.

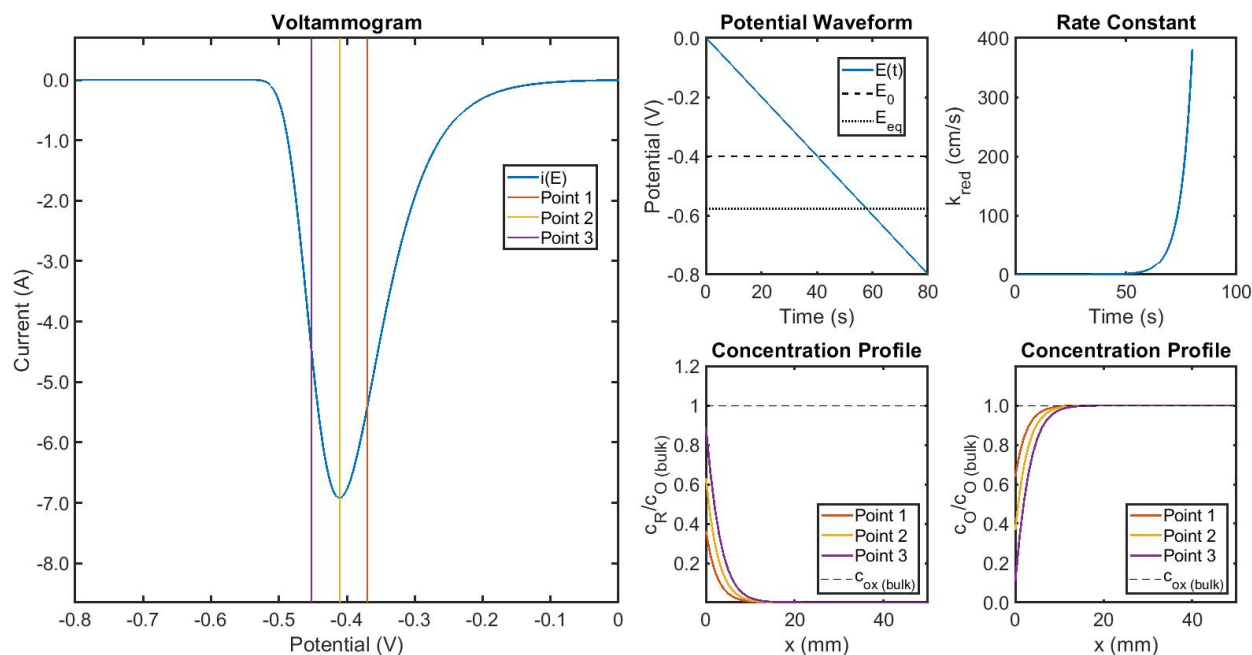


Figure A.3 – Script output for $k_0 = 5$ m/s, $npts_t = 5000$, and all other parameters having default settings.

Appendix B

Supporting Information for Chapter 2

B.1 Mathematical Description of Model Physics

Finite element simulations were performed using COMSOL Multiphysics 5.2a equipped with the Corrosion Module.

B.1.1 3D Model: Incorporating Effects of Overpotential

In this version of the model, the current at the electrode surface was calculated assuming a secondary current distribution, which solves the Nernst-Planck equation for mass transport of charged species in solution, accounting for overpotential but assuming negligible concentration gradients. Under these conditions, mass transport occurs exclusively due to diffusion. The kinetics of reactions at the WE and CE are described in terms of linear Tafel expressions, with both an anodic and a cathodic reaction defined for each electrode.

Within the electrolyte, the current distribution is given by:

$$\nabla \cdot i_l = Q_l \quad (\text{B.1})$$

$$i_l = -\sigma_l \nabla \phi_l \quad (\text{B.2})$$

Where i_l is the current within the electrolyte, Q_l is the charge within the electrolyte (resulting from double layer capacitance), σ_l is the conductivity of the electrolyte, and ϕ_l is the electric potential within the electrolyte.

Similarly, within the working electrode the current distribution is given by:

$$\nabla \cdot i_s = Q_s \quad (\text{B.3})$$

$$i_s = -\sigma_s \nabla \phi_s \quad (\text{B.4})$$

Where i_s is the current within the electrode, Q_s is the charge within the electrode (concentrated on the surface), σ_s is the conductivity of the electrode, and ϕ_s is the electric potential of the working electrode.

During a PDP simulation, ϕ_s is controlled according to a potential waveform given by:

$$\phi_s(t) = \nu t + E_{start} \quad (\text{B.5})$$

Where $\phi_s(t)$ is the potential as a function of time, ν is the scan rate, t the time elapsed since the beginning of the simulation, and E_{start} the potential at $t = 0$ s.

The total current at the surface of the working electrode is given by:

$$i_{total} = \sum_m i_{loc,m} + i_{dl} \quad (\text{B.6})$$

Where i_{total} is the total current at the electrode surface, $i_{loc,m}$ is the Faradaic current associated with reaction m , and i_{dl} is the non-Faradaic current associated with double layer capacitance.

$$i_{dl} = \frac{\partial(\phi_s - \phi_l)}{\partial t} c_{dl} \quad (\text{B.7})$$

The Faradaic current associated with a given reaction is calculated using [Equation B.8](#) or [Equation B.9](#) in the presence or absence of a mass transport limited current density respectively.

$$i_{loc} = \frac{i_{lim} i_{Tafel}}{i_{lim} + i_{Tafel}} \quad (\text{B.8})$$

$$i_{loc} = i_{Tafel} \quad (\text{B.9})$$

$$i_{Tafel} = i_{corr} \times 10^{\eta/\beta_m} \quad (\text{B.10})$$

$$\eta = \phi_s - \phi_l - E_{corr} \quad (\text{B.11})$$

Where i_{lim} is the mass transport limited current density, i_{corr} the corrosion current density, η the overpotential, β_m the Tafel slope associated with reaction m , and E_{corr} the corrosion potential.

The counter electrode is modelled as a porous domain to increase the effective surface area available for reaction without increasing the domain size. This results in a modification of the current distribution within both electrolyte and electrode components:

$$\nabla \cdot i_l = Q_l + i_{v,total} \quad (\text{B.12})$$

$$i_l = -\sigma_{l,eff} \nabla \phi_l \quad (\text{B.13})$$

$$\sigma_{l,eff} = \epsilon_l^{1.5} \sigma_l \quad \nabla \cdot i_s = Q_s - i_{v,total} \quad (\text{B.14})$$

$$i_s = -\sigma_{s,eff} \nabla \phi_s \quad (\text{B.15})$$

$$\sigma_{s,eff} = \epsilon_s^{1.5} \sigma_l \quad i_{v,total} = \sum_m i_{v,m} + i_{v,dl} \quad (\text{B.16})$$

$$i_{v,m} = s_v i_{loc} \quad (\text{B.17})$$

Where ϵ_l and ϵ_s are the electrolyte and electrode volume fractions respectively and s_v is the active specific surface area (defined as the surface area / domain volume ratio.)

The epoxy is defined as an electrical insulator through which no current can flow:

$$-\vec{n} \cdot i_l = 0 \quad (\text{B.18})$$

$$-\vec{n} \cdot i_s = 0 \quad (\text{B.19})$$

Where \vec{n} is the normal vector.

A boundary condition of electrolyte neutrality is applied to the faces of the electrolyte

that do not contain an electrode:

$$c_{i,bnd} = c_{i,initial} \quad (\text{B.20})$$

$$E_{l,bnd} = 0 \quad (\text{B.21})$$

When $c_{i,bnd}$ is the boundary concentration of species i , $c_{i,initial}$ is the starting concentration of species i , and $E_{l,bnd}$ is the electrolyte potential at the boundary.

B.1.2 2D Model: Incorporating Effects of Overpotential and Concentration Gradients

In this version of the model, the currents at the electrode surface were calculated assuming a tertiary current distribution, which solves the Nernst-Planck equation in its entirety accounting for all potential mass transport mechanisms.

Within the electrolyte, the current distribution is given by:

$$\frac{\partial c_i}{\partial t} + \nabla \cdot N_i = R_i \quad (\text{B.22})$$

$$N_i = -D_i \nabla c_i - z_i u_{m,i} F c_i \nabla \phi_l \quad (\text{B.23})$$

$$\nabla \cdot i_l = F \sum_i z_i R_i + Q_l \quad (\text{B.24})$$

$$\sum_m z_m c_m = 0 \quad (\text{B.25})$$

$$i_l = F \sum_i z_i N_i \quad (\text{B.26})$$

With respect to a given ion of identity i , c_i is the concentration, D_i the diffusion coefficient, z_i the charge, $u_{m,i}$ the ionic mobility, N_i the flux due to mass transport, and R_i the net flux. i_l is the current within the electrolyte, F is Faraday's constant, Q_l is the charge within the electrolyte (resulting from double layer capacitance), and ϕ_l is the electric potential within the electrolyte.

An additional zero flux boundary condition is applied to all electrolyte boundaries excluding electrode/electrolyte interfaces:

$$-\vec{n} \cdot N_i = 0 \quad (\text{B.27})$$

Within the working electrode the current distribution is defined in the same way as for the 3D geometry, according to [Equation B.3](#) and [Equation B.4](#). Also as before, the potential is

described by [Equation B.5](#).

During a chronoamperometry simulation, ϕ_s is controlled by a potential waveform given by:

$$\phi_s(t) = E_{test} \quad (\text{B.28})$$

The Faradaic current associated with a given reaction is calculated using [Equation B.8](#) or [Equation B.9](#) in the presence or absence of a mass transport limited current density respectively.

$$R_{i,m} = \frac{-\nu_{i,m} i_{loc,m}}{n_m F} \quad (\text{B.29})$$

With respect to aqueous species i , $R_{i,m}$ is the flux due to reaction m , $\nu_{i,m}$ is the stoichiometric coefficient in reaction m (positive for the reduced species, negative for the oxidized species) and n_m is the number of electrons involved in reaction m . These reaction kinetics are connected to the concentration of reacting species in solution according to:

$$-\vec{n} \cdot N_i = R_{i,tot} \quad (\text{B.30})$$

$$R_{i,tot} = \sum_m R_{i,m} + R_{i,dl} \quad (\text{B.31})$$

When the reaction of interest involves a dissolving/depositing solid species j , the change in concentration at the electrode surface is given by:

$$\vec{v} = \sum_j \sum_m \frac{R_{d,j,m} M_j}{\rho_j} \quad (\text{B.32})$$

$$\frac{\partial c_{d,j}}{\partial t} = \sum_m R_{d,j,m} \quad (\text{B.33})$$

Where M_j and ρ_j are the molar mass and density of solid dissolving species j , \vec{v} is the electrode growth velocity normal to the surface, and $R_{d,j,m}$ the net flux of species dissolved species d and solid species j involved in reaction m . The epoxy is defined as an electrical insulator through which no current can flow, as described by [Equation B.18](#) and [Equation B.19](#). Two boundary conditions are applied to the face of the electrolyte not containing an electrode or the axis of symmetry, which define bulk concentration and zero electrolyte potential conditions according to [Equation B.20](#) and [Equation B.21](#) respectively.

A pH equilibrium is added to the electrolyte by defining a chemical reaction within the electrolyte with the following reaction rates:

$$R_{OH^-} = k^0(K_W - [H^+][OH^-]) \quad (\text{B.34})$$

$$R_{H^+} = k^0(K_W - [H^+][OH^-]) \quad (\text{B.35})$$

$$R_{H_2O} = -k^0(K_W - [H^+][OH^-]) \quad (\text{B.36})$$

An arbitrary value of k^0 was selected which balanced model convergence with effectiveness

of the neutralization reaction.

B.1.3 Parameters

The kinetic parameters at the working electrode / corroding sample are specific to the sample of interest and have been described in the body of work. Parameters which do not depend on the substrate have been outlined below.

Table B.1 – Input model parameters.

Parameter	Description	Value	Reference
σ_l	Conductivity of electrolyte	5 S/m	[1]
σ_s	Conductivity of electrodes	1×10^7 S/m	[2]
$i_{0,Pt}$	Exchange current density of platinum counter electrode	7.9×10^{-4} A cm ⁻²	[3]
K_w	Equilibrium constant for autoprotolysis of water	1×10^{-14}	[4]
k^0	Rate constant for pH equilibrium	1×10^{-7} M/s	-
c_{dl}	Double layer capacitance of working and counter electrodes	20 μ F cm ⁻²	-
ϵ_l	Volume fraction of electrolyte within porous counter electrode	0.5	-
ϵ_s	Volume fraction of electrode within porous counter electrode	0.5	-

The diffusion coefficients employed for individual species are representative of their behaviour in bulk electrolyte. An effective reduction in the diffusion coefficient is expected to occur where an oxide film is present, but has not been explicitly modelled. Finite element simulations of adjacent domains of extremely different scales (cm thick sample, nm thick

passive film) pose an issue for model convergence. As the simulated kinetics used to examine individual systems are derived from experimental measurements, the effect of the oxide film has already been taken into account in the extracted parameters.

Table B.2 – Values used for the bulk concentrations and diffusion coefficients of aqueous species initially present, produced, or consumed during the corrosion reactions modelled. The bulk concentrations of dissolved gases are assumed to be the solubility limit at 20°C as given in reference 5.

Species	Bulk concentration (mol/L)	Diffusion coefficient (10^{-5} cm ² /s)
Na _(aq) ⁺	0.10	1.334 ⁶
Cl _(aq) ⁻	0.10	2.032 ⁶
H _{2(g)}	4×10^{-10}	4.50 ⁷
O _{2(g)}	2.26×10^{-4}	2.10 ⁷
H _(aq) ⁺	1×10^{-7}	9.331 ⁶
OH _(aq) ⁻	1×10^{-7}	5.273 ⁶
H ₂ O _(l)	18	2.2 ⁸
Fe _(aq) ²⁺	0	0.604 ⁶
Mg _(aq) ²⁺	0	0.706 ⁶

B.1.4 Mesh Density

When setting up the finite element simulation, a dense mesh (pictured in [Figure B.1](#)) was introduced to boundaries or volumes where chemical reactions occur; this corresponds to the surface of the working electrode (corroding sample) and throughout the volume of the porous counter electrode. A coarser mesh was applied to the remaining geometry.

The density of the final mesh was selected by increasing the mesh density and examining

changes in the calculated results. When a negligible change in calculated quantities was observed for increasing mesh density, the density was determined to be sufficient for further study. The minimal mesh meeting this criteria was selected as a balance between model accuracy and simulation time.

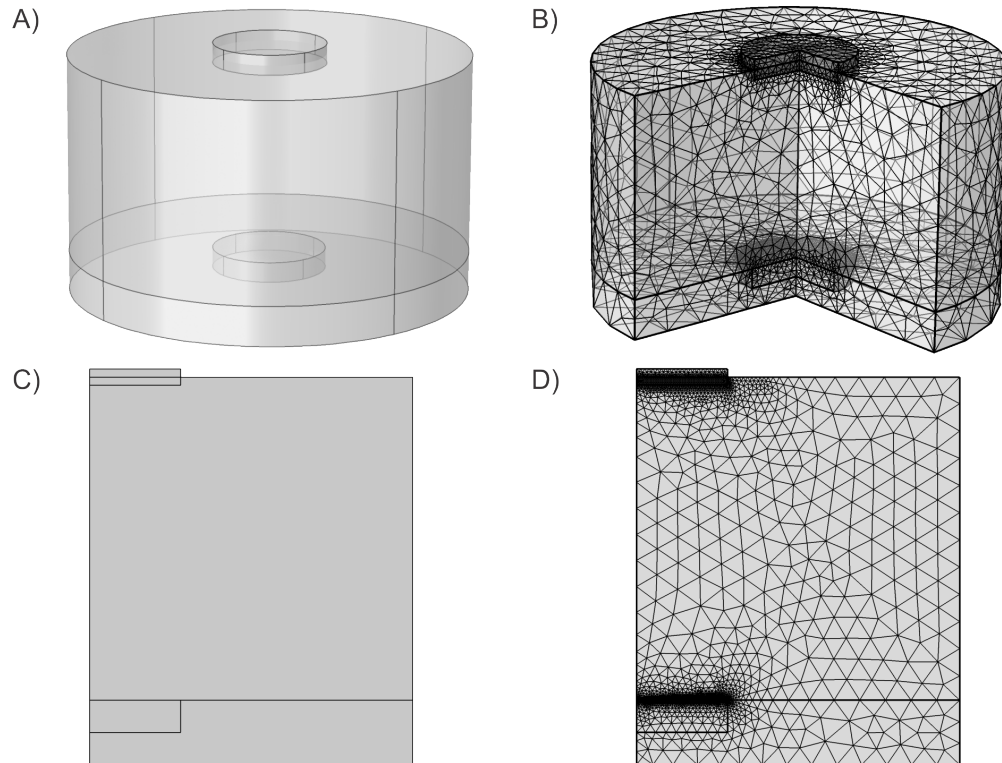


Figure B.1 – The geometry and mesh used for all 3D (A,B) and 2D-axisymmetric (C,D) simulations.

B.2 Additional Results

B.2.1 Variation in Transport Numbers with Time

The behaviour of the simulated electrolyte was validated through comparison of the simulated transport numbers to the literature during a chronoamperometric experiment run at a ϕ_s of $E_{corr} + 300$ mV. Within a simulation, these values fluctuate slightly over time as metal ions with a non-zero mobility are produced and the electrolyte composition changes: for this reason, values reported for comparison are from the initial time point of $t = 0$ s. The majority of the current is carried by the supporting electrolyte, with dilute ions in solution (H^+/OH^- , metal ions produced during corrosion) contributing the remainder.

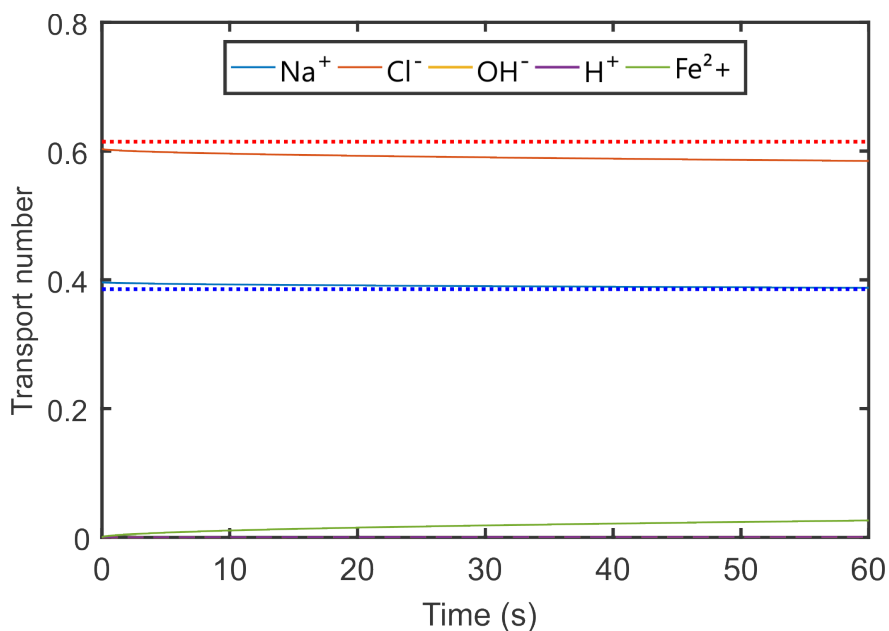


Figure B.2 – Variation of the simulated transport numbers with time. Solid lines indicate calculated values and dashed lines indicate literature values for an electrolyte of equivalent concentration.

B.2.2 Effects of Scan Rate and Range

The effect of scan rate, ν , on the kinetic parameters extracted was previously discussed. In addition to the extracted kinetics, the scan parameters influence the calculated concentration profiles.

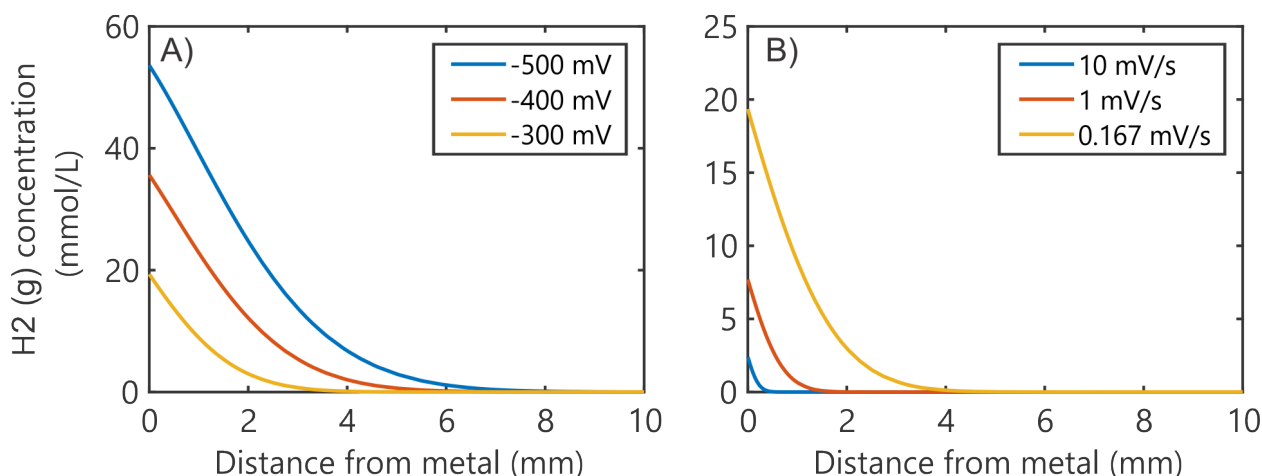


Figure B.3 – Effect of changing the scan parameters E_{start} and ν on the concentration profile of $H_2(g)$ calculated using pure Mg with the following kinetics: $E_{corr} = -1.192 \text{ V}$ vs. NHE, $j_{corr} = 80 \mu\text{A}/\text{cm}^2$, $\beta_a = 10 \text{ mV}/\text{decade}$, $\beta_c = -220 \text{ mV}/\text{decade}$, $j_{lim,c} = 3000 \mu\text{A}/\text{cm}^2$. All profiles are calculated for $\eta = 0$. A) Constant ν of 0.167 mV/s , variable E_{start} . B) Constant E_{start} of -300 mV vs E_{corr} , variable ν .

B.3 Calculation of Goodness of Fit Statistics

The simulated currents were calculated every 0.5 s (for a 0.167 mV/s scan rate, this corresponds to every 0.08 mV). A MATLAB script was then written to align the simulated ($j_{sim,i}$) and experimental ($j_{exp,i}$) currents for a matching potential i . Data for potentials without a corresponding current in both simulated and experimental scans were not considered in the

calculation of goodness of fit statistics.

The following formulas were used to calculate each goodness of fit statistic:

$$r = \sum_i \log j_{sim,i} - \log j_{exp,i} \quad (\text{B.37})$$

$$\%_d = \frac{1}{h} \sum_i \frac{(\log j_{sim,i} - \log j_{exp,i})}{\log j_{exp,i}} \times 100\% \quad (\text{B.38})$$

$$\chi^2 = \frac{1}{h} \sum_i \frac{(\log j_{sim,i} - \log j_{exp,i})^2}{\log j_{exp,i}} \quad (\text{B.39})$$

Where r is the residual and h is the number of total data points. The application of a goodness of fit metric to the entirety of a polarisation curve assumes that the accuracy of all data points is equal. In the case of our model, we are assuming Tafel behaviour at all potentials, where the log of current is proportional to the applied overpotential. This assumption is valid at high overpotentials, however for small overpotentials the current is instead proportional to the current, and so the predicted accuracy of the model is inherently reduced. This is clearly demonstrated when comparing simulated to experimental data zero overpotential. According to the model based solely on the Tafel plot, the log current at zero overpotential will tend towards negative infinity, whereas the experimental data can clearly be seen to give a more rational value. For this reason, a cursory inspection of the calculated residuals from the goodness of fit models reveals a sharp increase in the residual at zero overpotential, regardless of the model used (Figure 5). The magnitude of this spike in the residual was the primary contributor to the overall residual of the fit models, reducing the usefulness of the residual as a metric for the quality of the fit.

This lead to application of a weighting function to the residual analysis. The purpose of the weighting function is to reduce the impact of the deviation from Tafel behaviour on the quality of the fit, as determined by the calculated residuals. The weighted function is built around a simple cos function, which is translated on the x-axis so that it gives $f(E - E_{corr}) = 0$ at zero overpotential, with the cos function increasing towards one as the overpotential increases:

$$f(E - E_{corr}) = -0.5 \cos\left(\frac{3.2(E - E_{corr})}{E_{range}}\right) + 0.5 \quad (\text{B.40})$$

Here, E_{range} is the desired potential window of the weighting function. In this work, a value of 10 mV was chosen to give significant weighting at zero overpotential, whilst giving not weighting any data at significant overpotential where a Tafel slope could reasonably be applied. The factor $3.2/E_{range}$ controls the period of the cos function, so that $f(E - E_{corr})$ reaches one where $E - E_{corr} = \pm E_{range}$. An if function is then employed where the overpotential is greater than E_{range} or less than $-E_{range}$ so that data points outside of $E_{corr} \pm E_{range}$ are not affected by the weighting function. Weighted goodness of fit statistics are initially calculated using [Equation B.3](#).

$$r = \sum_i r_i \times f(E_i - E_{corr}) \quad (\text{B.41})$$

The test statistic for the chi-squared goodness of fit test, χ_{test}^2 , was calculated as the following:

$$\chi_{test}^2 = \sum_i \chi_i^2 \quad (\text{B.42})$$

The critical value used for comparison was selected at the 95% confidence level, where the degrees of freedom used were either $i - 4$ (no limiting current density present) or $i - 5$ (limiting current density present).

References

- [1] Haynes, W. *Electrical Conductivity of Aqueous Solutions: CRC Handbook of Chemistry and Physics*, 97th ed.; CRC Press/Taylor & Francis: Boca Raton, FL., 2017.
- [2] Haynes, W. *Electrical Resistivity of Pure Metals: CRC Handbook of Chemistry and Physics*, 97th ed.; CRC Press/Taylor & Francis: Boca Raton, FL., 2017.
- [3] Bard, A. J.; Stratmann, M.; Frankel, G. S. *Encyclopedia of Electrochemistry Volume 4: Corrosion and Oxide Films*; Wiley-VCH, 2003.
- [4] Harris, D. C. *Quantitative Chemical Analysis*, 8th ed.; W.H. Freeman and Company: New York, NY, USA, 2010.
- [5] Colt, J. *Computation of Dissolved Gas Concentration in Water as Functions of Temperature, Salinity and Pressure (Second Edition)*; 2012; pp 1–71.
- [6] Haynes, W. *onic Conductivity and Diffusion at Infinite Dilution: CRC Handbook of Chemistry and Physics*, 97th ed.; CRC Press/Taylor & Francis: Boca Raton, FL., 2017.
- [7] Cussler, E. *Diffusion: Mass Transfer in Fluid Systems*, 1st ed.; Cambridge University Press: New York, NY, USA, 2009; pp 117–234.
- [8] Jones, J. R.; Rowlands, D. L. G.; Monk, C. B. Diffusion coefficient of water in water and in some alkaline earth chloride solutions at 25°C. *Transactions of the Faraday Society* **1965**, *61*, 1384–1388.

Appendix C

Supporting Information for Chapter 3

C.1 Detailed Description of Model

A full 3D model was built using COMSOL Multiphysics 5.3a, with exclusively diffusion limited mass transport kinetics. The steady state Nernst-Planck equation (Equation C.1) was solved for each electrode position to determine the flux of all electroactive species. The flux of reacting species at a given electrode position was integrated over the electroactive surface to yield the corresponding current (Equation C.2). The x-position (x_{pos}) and y-position (y_{pos}) of the electrode were rastered using a parametric sweep in order to generate a current map of the substrate consisting of 51x51 points arranged in an evenly spaced grid (Figure C.1).

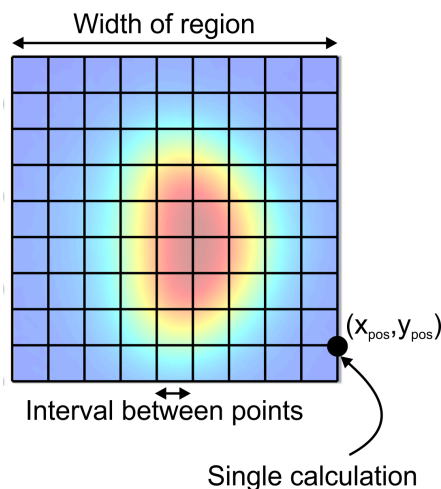


Figure C.1 – Schematic of sampling grid used to construct maps. A parametric sweep was used to make a single-point calculation of $i_{x_{pos}, y_{pos}}$ for every grid point, resulting in 2601 (51x51) points for each map presented.

$$\frac{\partial c_i}{\partial t} = 0 = \nabla \cdot (D_i \nabla c_i) + R_i \quad (\text{C.1})$$

$$i_{xpos,ypos,L} = nF \oint J_{(x,y)} \, dx \, dy \quad (\text{C.2})$$

Where c_i , D_i , and R_i are the concentration, diffusion coefficient, and reaction-induced flux of species i respectively, n is the number of electrons transferred during reaction ($n = 1$), F is Faraday's constant, and $J_{(x,y)}$ is the flux normal to the surface at mesh position (x, y) .

A square electrolyte domain of $100a$ in width was simulated (Figure C.2). A concentration boundary condition of $c_i = c_{i,bulk}$ was applied at boundary 1, where $c_{i,bulk}$ is the bulk concentration of species i . At boundaries 2 and 3, diffusion-controlled oxidations (Equation C.3) and reductions (Equation C.4) take place. A no flux condition (Equation C.5) is set at all other boundaries.

$$R_O = k_{tip} \times c_R \quad ; \quad R_R = -k_{tip} \times c_R \quad (\text{C.3})$$

$$R_O = -k_{tip} \times c_O \quad ; \quad R_R = k_{tip} \times c_O \quad (\text{C.4})$$

$$R_O = 0 \quad ; \quad R_R = 0 \quad (\text{C.5})$$

Where k_{tip} is the rate constant at the electrode, set to an arbitrarily large value of 1×10^4 to ensure diffusion controlled kinetics.

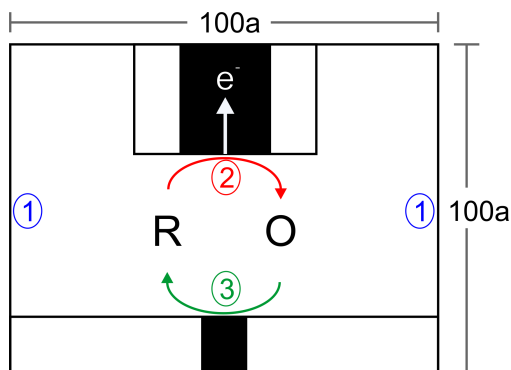


Figure C.2 – Simulation geometry and boundary conditions.

A dense mesh was introduced to the geometry with a maximum growth rate of 1.3 and maximum size restrictions of $0.075a$, $0.075b$, and a were added to the electroactive tip, surface feature, and electrode glass sheath respectively. The size restriction at the glass sheath was applied to prevent meshing errors caused by the high aspect ratio. This resulted in a mesh of approximately 100,000 finite elements (Figure C.3).

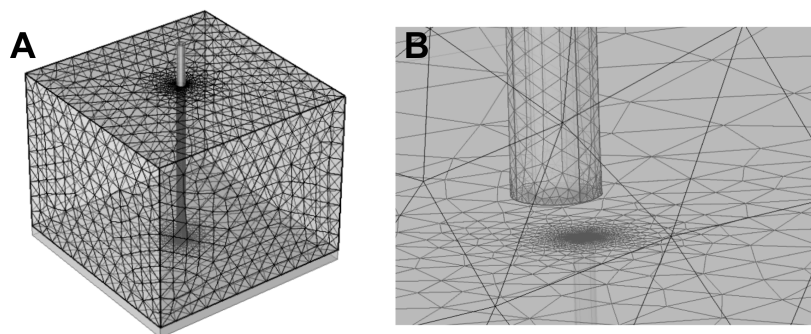


Figure C.3 – The mesh used in all simulations, with restrictions on the growth rate and maximum size at all electroactive features and the glass sheath. (A) View of the entire geometry. (B) Close-up view of the electroactive surfaces.

The effect of electrode orientation over the substrate was investigated using the single barrel electrode, rotating it about the center point of the insulating glass sheath (Figure C.4).

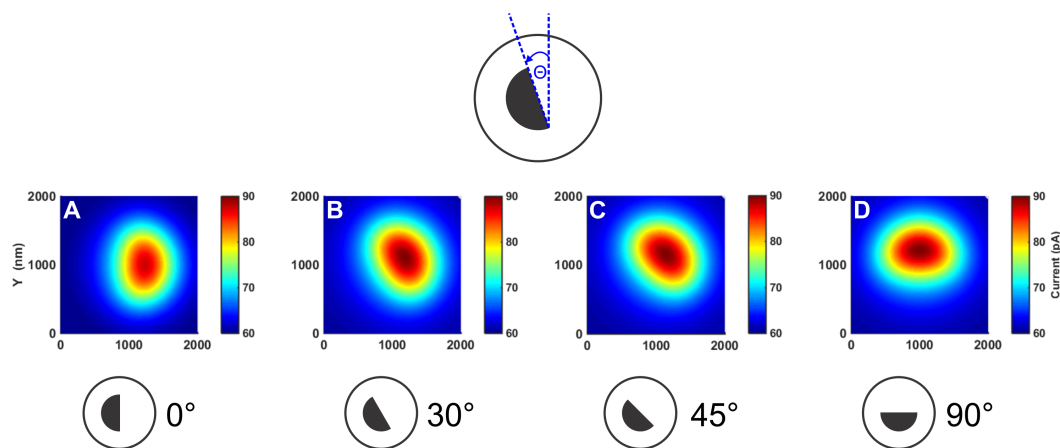


Figure C.4 – Effect of electrode orientation on the distortion obtained over a circular conductive feature using a single barrel electrode for an angle of (A) 0° (B) 30° (C) 45° (D) 90° from the y-axis. All other parameters were consistent with the standard set of initial conditions: $L = 0.5$, $b = 250$ nm, $a = 500$ nm, $R_g = 2$, and $f_R = 1.00$.

C.2 Validation of Linear Interpolation

To validate the linear interpolation performed on the calculated maps prior to contour extraction, a high resolution map was generated (large number of single point calculations) and compared to a standard resolution map (fewer number of single point calculations, and interpolation performed to generate a larger number of points). The residuals map comparing these two (Figure C.5D) shows negligible ($< 1\%$ difference in maximum current) differences with no systematic pattern, demonstrating the validity of this method for contour extraction.

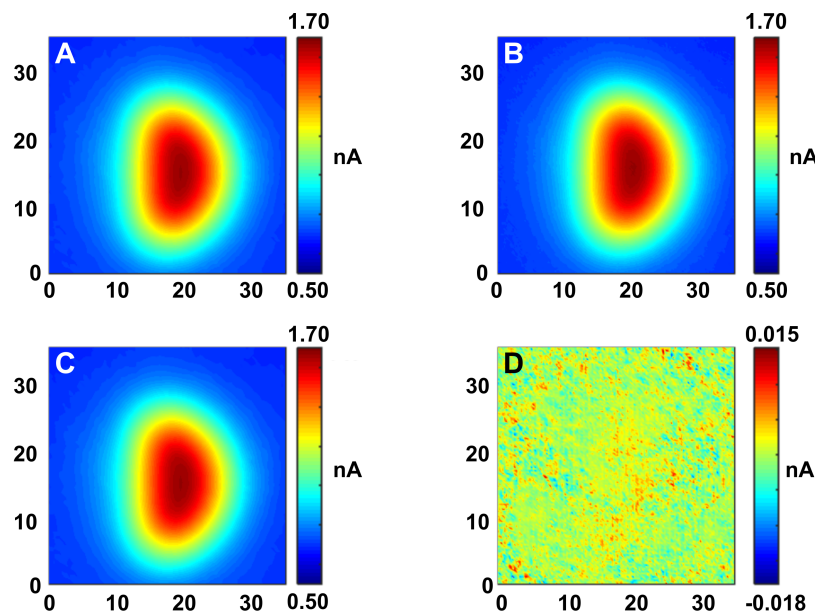


Figure C.5 – Current maps showing the negligible effect of linear interpolation for generating higher resolution maps for the purpose of contour extraction. All currents were calculated for $a = 10 \mu\text{m}$, $R_g = 2$, $b = 5 \mu\text{m}$, $L = 0.2$. (A) Calculated map of 3000 points. (B) Calculated map of 30 000 points. (C) Interpolated map of 30 000 points constructed from (A). (D) Residuals map of calculated (B) - interpolated (C) points.

C.3 Validation of Mesh and Solver Tolerance

The mesh and solver tolerance used were validated by comparing simulated approach curves for a disk electrode with $a = 500$ nm and $R_g = 2$ over uniformly reacting conductive and insulating substrates to the analytical approximations for positive (Equation C.6) and negative (Equation C.7) feedback.¹ Given the additional computational requirements associated with solving 3D models, this agreement is sufficient for balancing computational accuracy with solve time.

$$Ni_T^{\text{cond}} \simeq \alpha(R_g) + \frac{1}{\beta(R_g)} \frac{\pi}{4 \text{ArcTan} L} + \left(1 - \alpha(R_g) - \frac{1}{2\beta(R_g)}\right) \frac{2}{\pi} \text{ArcTan} L \quad (\text{C.6})$$

$$Ni_T^{\text{ins}} \simeq \left[\frac{2.08}{R_g^{0.358}} \left(L - \frac{0.145}{R_g} \right) + 1.585 \right] \left[\frac{2.08}{R_g^{0.358}} (L + 0.0023 R_g) + 1.58 + \frac{\ln R_g}{L} + \frac{2}{\pi R_g} \ln \left(1 + \frac{\pi R_g}{2L} \right) \right]^{-1} \quad (\text{C.7})$$

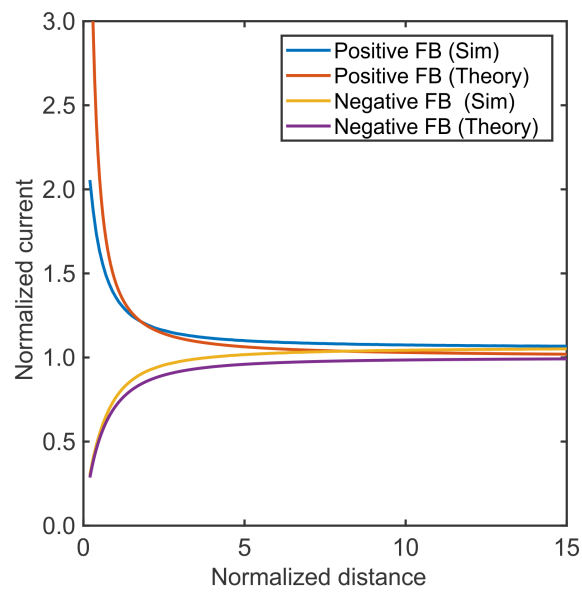


Figure C.6 – Comparison of simulated to theoretical approach curves over conductive and insulating substrates using a disk electrode to validate the mesh and solver tolerance used throughout all simulations.

References

- [1] Lefrou, C.; Cornut, R. Analytical Expressions for Quantitative Scanning Electrochemical Microscopy (SECM). *ChemPhysChem* **2010**, *11*, 547–556.

Appendix D

Supporting Information for Chapter 4

D.1 Electrochemical Setup

Au/SiO₂ substrates were designed to be transparent to allow for simultaneous SECM and optical imaging (Figure D.1). Optical images acquired immediately following the SECM raster scan were used to align the two images.

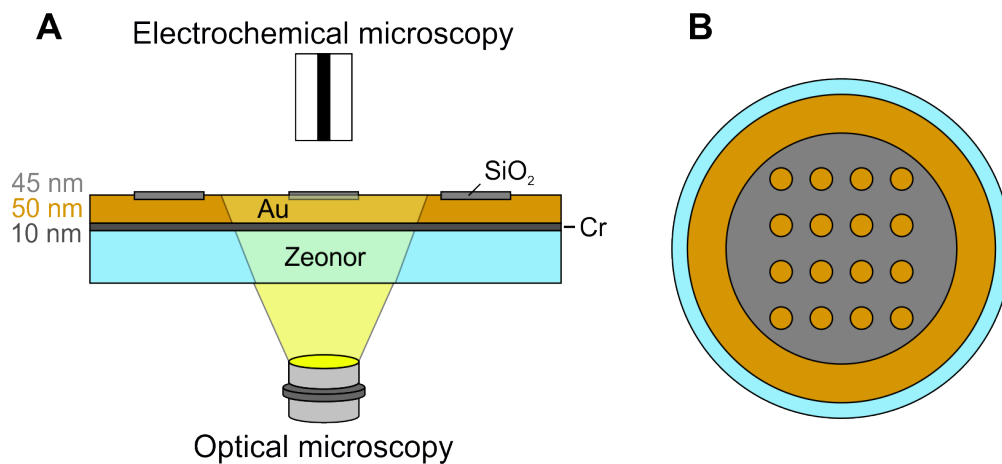


Figure D.1 – Schematic of the integrated electrochemical/optical microscope used to image the Au/SiO₂ substrates. (A) Side view. (B) Top view.

D.2 Finite Element Model

A 3D finite element model was built in COMSOL Multiphysics 5.3a with the Transport of Diluted Species module. This was used to solve the steady-state Nernst Planck equation under conditions of negligible convection and migration, with the boundary conditions described previously.¹ The position of the electrode was parameterized enabling SECM images to be calculated according to a parametric sweep.

An electrolyte domain of $100a \times 100a \times 80a$ ($x \times y \times z$) was simulated, where a is the radius of the microelectrode. For both topographical and reactive features, the feature spanned the entire width of the substrate. An electrode with radius $12.5 \mu\text{m}$ and $R_G = 3$ was used for all simulations.

A dense mesh was introduced to the domain with maximum size restrictions applied to the electrode and feature surfaces of $0.1a$ and $0.5a$ (Figure D.2) and maximum growth rate of 1.3 in the electrolyte domain. On average, this produced a final mesh with in excess of 300 000 elements.

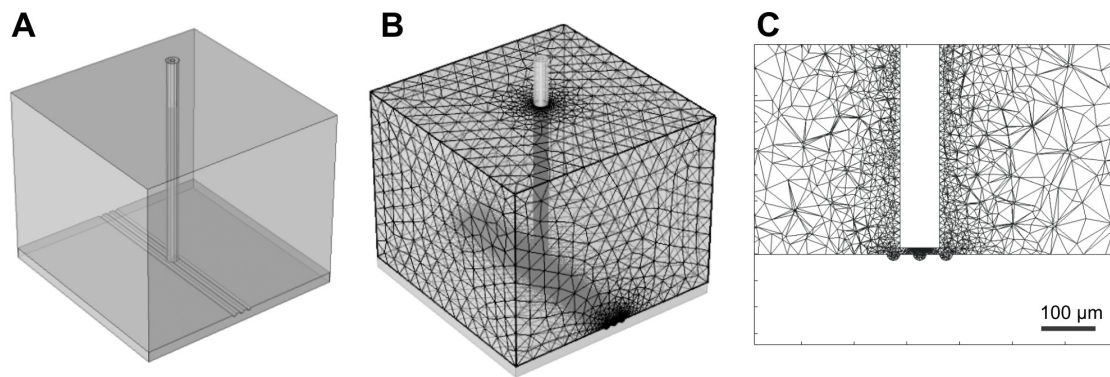


Figure D.2 – (A) Simulation geometry used for the groove simulations. (B) Meshed geometry. (C) Cross-section of the meshed geometry.

D.3 Enlarged Second Derivatives

For easier viewing, enlarged versions of the second derivative plots from the main manuscript have been included below. These were numerically calculated from simulated 1D line scans over reactive (Figure D.3 A-B) or topographical (Figure D.3 C-F) features. Zero-crossings of the second derivative indicate inflection points, dotted lines indicate the true feature edge.

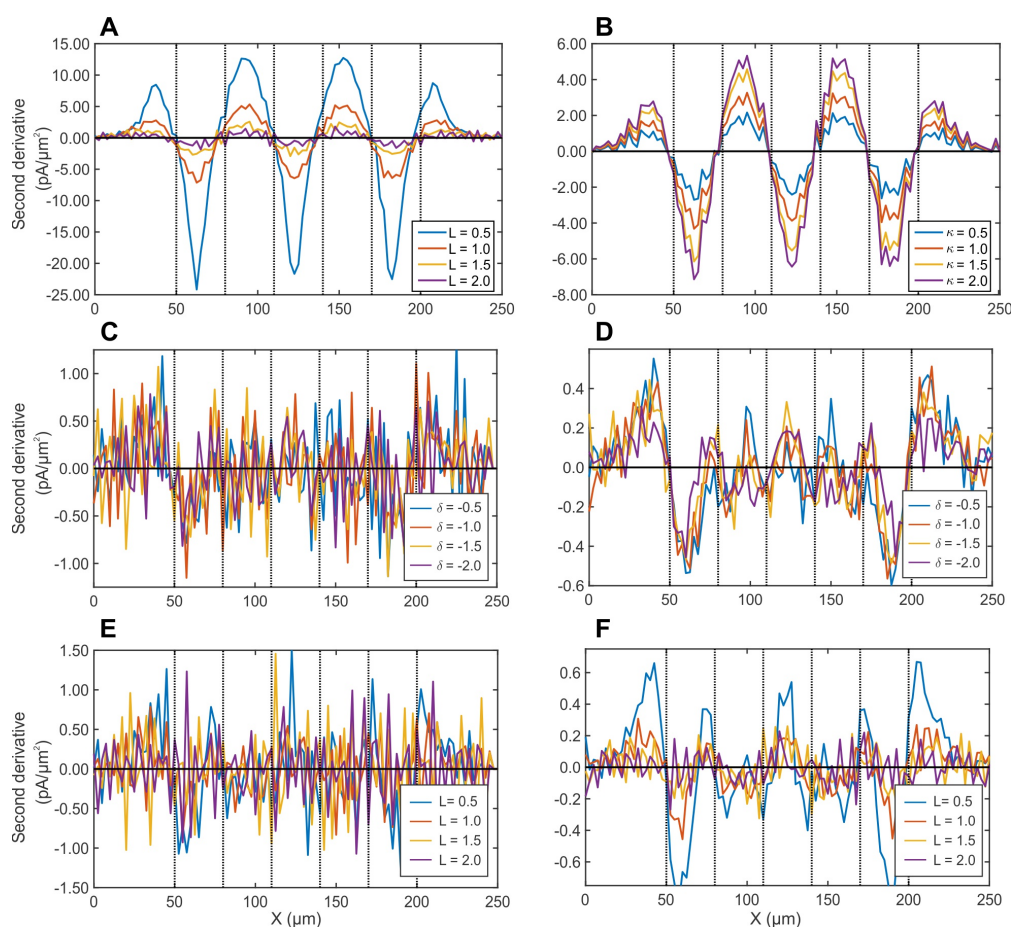


Figure D.3 – Enlarged versions of the second derivatives plotted in the main manuscript. (A,B) Figure 4.1 (B,C) respectively. (C,D) Figure 4.3 (C,D) respectively. (E,F) Figure 4.3 (F,G) respectively. Dotted lines indicate the true feature edges.

D.4 Atomic Force Microscopy

AFM data was collected on a MFP3D-SA atomic force microscope equipped with a 3D molecular force probe controller (Asylum Research, Santa Barbara, CA, USA). Experiments were performed in intermittent contact mode in air, using an OPUS 160AC-NA tip (Mikro-Mash, Sofia, Bulgaria) with a nominal spring constant of 26 N/m, frequency of 300 kHz, and radius of contact < 7 nm.

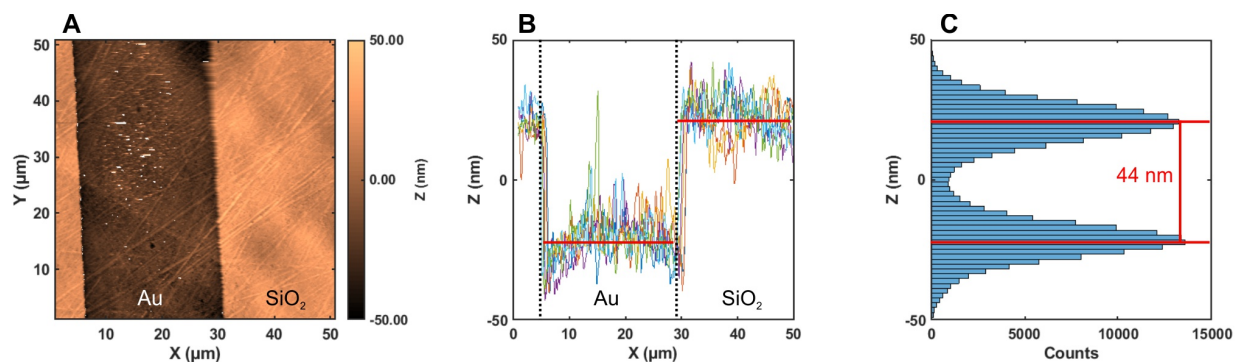


Figure D.4 – (A) AFM topography image of the Au/SiO₂ interface. (B) Selected line scans from the AFM image. (C) Histogram of all data to extract the average thickness of the SiO₂ layer.

D.5 Asymmetrical Reactive Features

To examine the effect of feature symmetry on method accuracy, edge detection was performed on both simulated (Figure D.5 A,B,D) and experimental (Figure D.5 C) SECM images. For the two moons of different size (Figure D.5 A,B), accuracy improves as the feature becomes larger relative to the electrode size, with the concave shape better represented, though accuracy is still not optimal at this scale. As the features become even larger (Figure D.5 C,D), improved agreement between the detected edges and true feature geometry is observed.

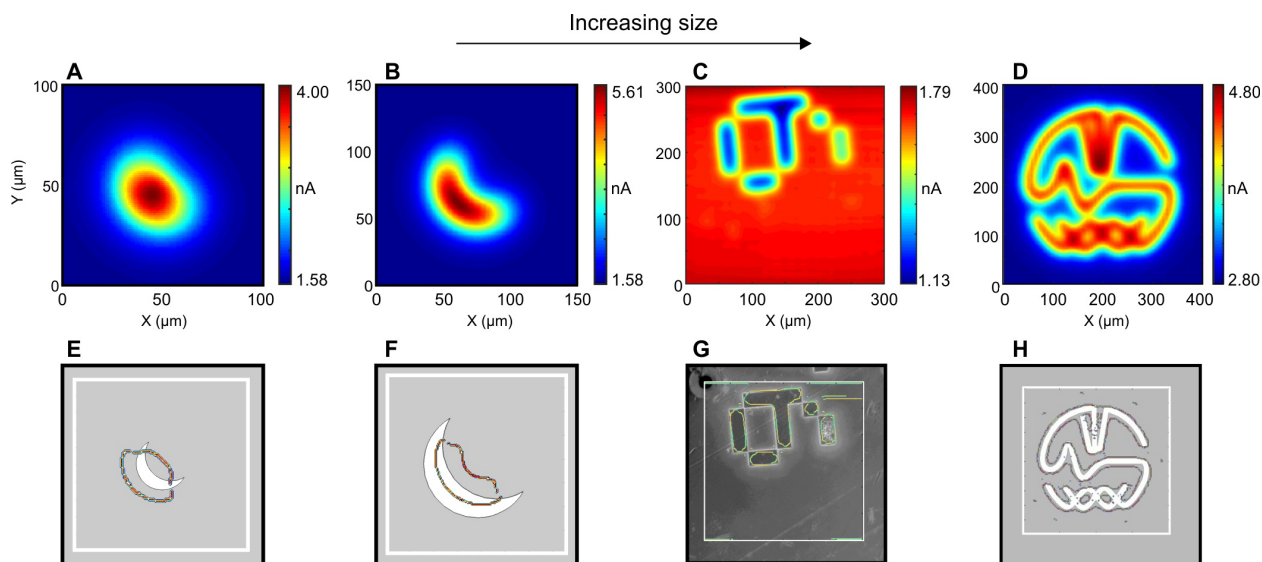


Figure D.5 – Edge detection on SECM images of asymmetrical reactive features. (A-B) Simulated image of a half moon feature (A) similar in size (B) larger than the electrode. (C) Experimental image of a number 6 (tilted sideways to the right-hand side). (D) Simulated image of our research group logo. (E-H) Detected edges in the SECM image (indicated by the frame in white) overlaid on the corresponding image of the true geometry determined through either (E,F,H) the simulation geometry or (G) a microscope image.

D.6 Accuracy and Feature Size

To examine the effect of feature size on method accuracy, edge detection was performed on simulated linescans over reactive circles of varying size. Optimal accuracy is observed, measured as agreement between the estimated feature diameter calculated from the detected edges and true feature diameter input into the simulation, for features the same size as the electrode or larger. For features smaller than this criteria, edge detection tends to overestimate the feature size.

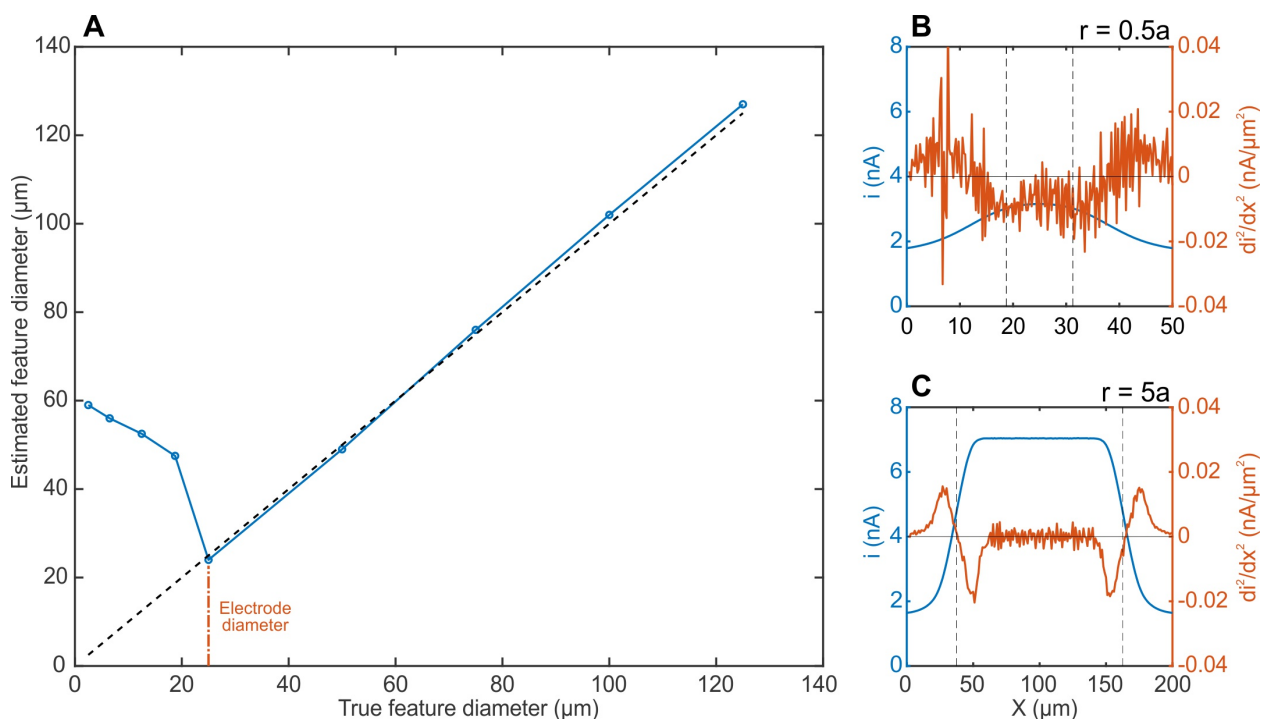


Figure D.6 – (A) The estimated feature size calculated from edge detection compared to the true feature size input into the simulation. (B,C) Raw currents and second derivatives for a simulated line scan over a circular feature with a radius of (B) $0.5a$ and (C) $5a$. Dotted lines indicate the true feature edges.

D.7 Effect of Groove Spacing

The relationship between feature spacing and edge detection accuracy of topographically varying substrates was examined by simulating three nonreactive grooves a variable distance apart (Figure D.7). In general, the algorithm tends to miss fewer edges (false negatives) as the features become further apart, but still tends to overestimate the true feature edges.

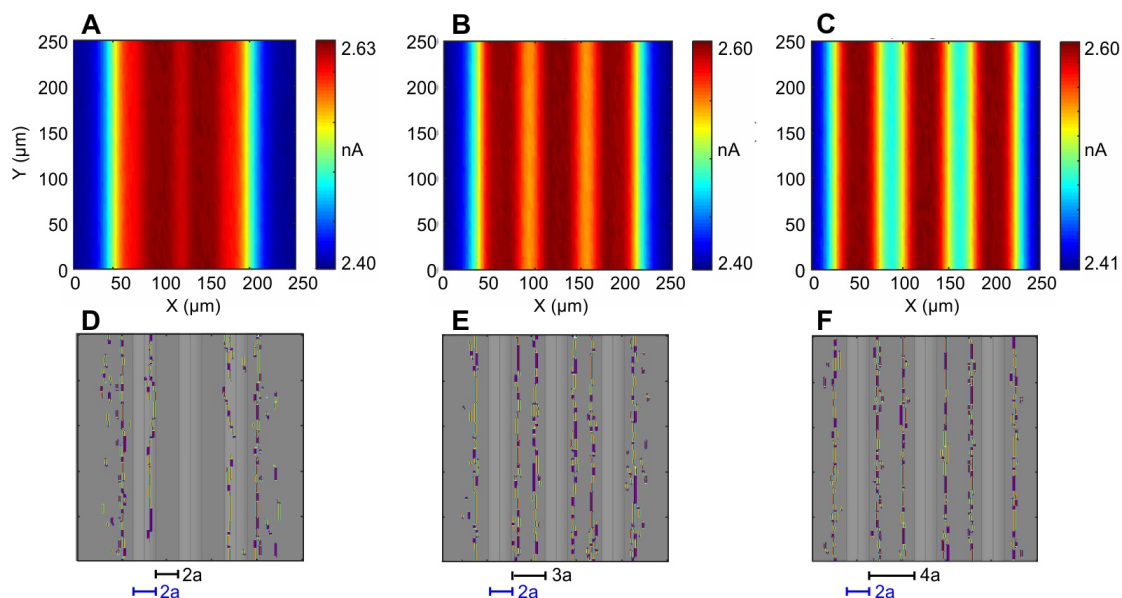


Figure D.7 – Comparison of the edge detection effectiveness for three grooves of the same depth separated by different distances. (A-C) Simulated SECM images for three identical grooves of depth a . (D-F) Edges detected in the SECM images overlaid on the true model geometry employed.

D.8 Scanning Ion Conductance Microscopy

Scanning ion conductance microscopy (SICM) was performed to confirm the groove depth (Figure D.8 A) and spacing (Figure D.8 B) of the topographically-variant non-reactive Si/SU-8 substrate. Pipettes were pulled from borosilicate glass capillaries (o.d. 1.2 mm and i.d. 0.69 mm) to a tip diameter of 1 μm using a Sutter 2000 pipette puller (Figure D.1).² A 250 μm diameter Ag/AgCl wire ($\geq 99.99\%$, Sigma) was used as the working electrode while a 1 mm diameter Ag/AgCl wire (annealed 99.99% Ag wire, Goodfellow) was used as QRCE. Measurements were carried out in 0.1 M KCl solution.

Table D.1 – Pipette pulling parameters.

	Heat	Fil	Vel	Del	Pul
Line 1	350	3	40	220	-
Line 2	350	3	40	180	100

Scanning ion conductance microscopy was performed using a DC hopping mode approach with a HEKA ELP-3 system. The probe was manually positioned within 100 μm of the surface and translated towards the surface at a speed of 10 $\mu\text{m}/\text{s}$ with sample interval of 10 nm while applying a voltage of 400 mV between the two Ag/AgCl electrodes. The probe movement was halted when a current change of 400 pA was observed (approx. 1% of bulk). The motor position was recorded and the probe was retracted by 20 μm before moving to a new location.

When the detected edges of the SECM image (Figure 4.4 A) are overlaid on the SICM

map, the same pattern of overestimation is observed as when overlaid on the electron micrograph (Figure 4.4 D).

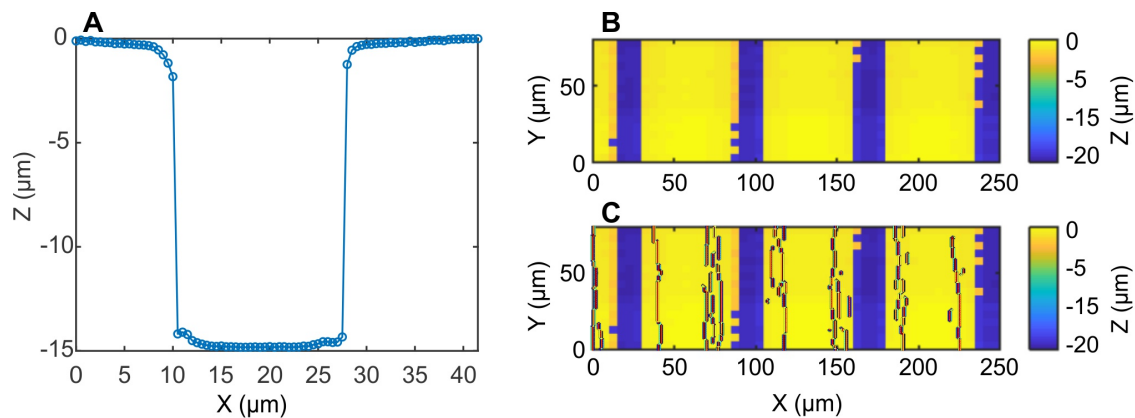


Figure D.8 – A) Line scan over a groove from the SICM image. (B) SICM map of the Si/SU-8 substrate. (C) Detected edges from a representative area of the SECM image overlaid on the SICM map.

D.9 Effect of Mediator Concentration

The effect of bulk mediator concentration on method performance was examined by simulating line scans over a reactive feature with different bulk concentrations. Provided a sufficiently high concentration giving a distinct signal is used, the apparent inflection point does not vary with increasing concentration and correlates well with the true feature edge.

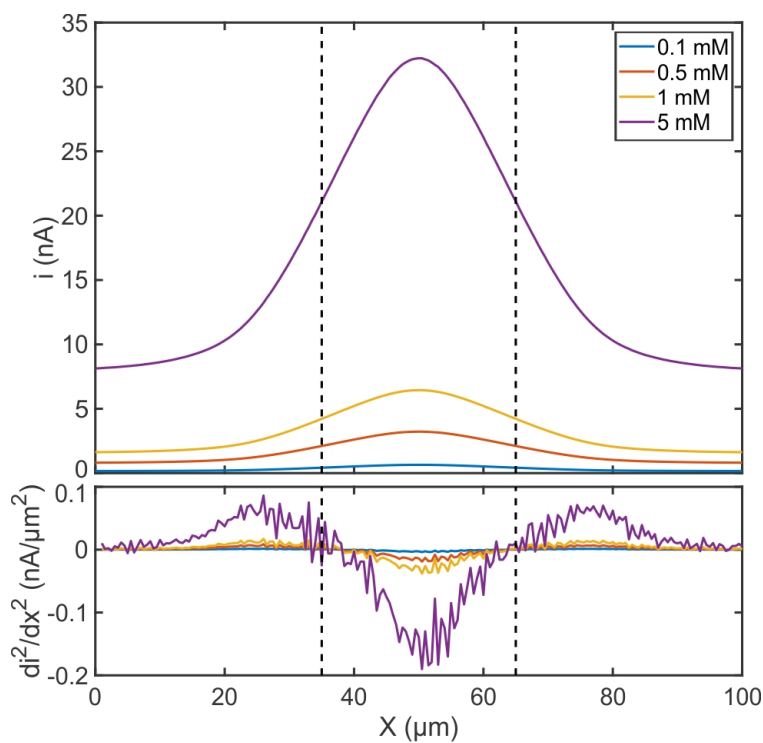


Figure D.9 – Simulated line scans over the center of a 30 μm radius circular reactive feature at varying initial concentrations of the redox mediator. Dotted lines indicate the true feature edge.

References

- [1] Stephens, L. I.; Mauzeroll, J. Altered Spatial Resolution of Scanning Electrochemical Microscopy Induced by Multifunctional Dual-Barrel Microelectrodes. *Analytical Chemistry* **2018**, *90*, 6796–6803.
- [2] Bentley, C. L.; Perry, D.; Unwin, P. R. Stability and Placement of Ag/AgCl Quasi-Reference Counter Electrodes in Confined Electrochemical Cells. *Analytical Chemistry* **2018**, *90*, 7700–7707.

Appendix E

Supporting Information for Chapter 5

E.1 Overview

E.1.1 Introduction

This document is written as an introduction to the source code of Flux. This does not contain the full source code, which is freely available on Github (<https://github.com/stepheli/fluxproject>). Instead, abbreviated snippets of the source code have been extracted to explain how the data analysis tasks described in the manuscript were accomplished.

The source code is written in the Python scripting language. It depends on a set of commonly used Python packages for support of specific functionality, as outlined in [Table E.1](#). In many cases, packages are imported with a commonly used alias (e.g. **import numpy as np**) to save space. A function from a specific package is called as **package.function**; examples of functions used from each package are given.

Table E.1 – List of the required Python packages.

Package (Alias)	Example	Overview	Version
numpy (np)	np.gradient	Numerical Python, provides matrix support	1.16.2
pandas (pd)	pd.DataFrame	Extension to numpy, supports more complex or mixed data structures	0.24.1
scipy	scipy.io.loadmat	Scientific Python, support for signal processing	1.2.1
scikit-image	skimage.feature	Extensions to scipy, provides image processing tools	0.14.2
matplotlib	matplotlib.figure	Plotting library	3.0.3
tkinter (tk)	tk.Label	Graphical user interface	Python 3.7
pyqt5	-	Python bindings that allow Python to use C libraries	5.12

E.1.2 Class Structure

For every experiment type supported by Flux, a separate Python class has been defined. This class is composed of a set of functions, where each function performs a single task such as setting up the initial appearance of the window, importing a file, or processing data. Though the setup for each class varies slightly, these share a common general structure, outlined below for the SECM image processing application.

```
class ImageApp:
    def __init__(self, master):
        # Set up appearance of analysis window by creating and positioning menus, buttons,
        # labels, entry fields, and graphs.
        ...
    def SelectFile(self):
        # Open a file dialogue window to let user select file.
        ...
    def ImportFile(self):
        # Depending on file type and manufacturer, parse the selected file to read data into
        # workspace.
        ...
    def ReshapeData(self):
        # With the imported data, perform any requested analysis and display the processed
        # data on the graph.
        ...
    def BoxesSelected(self):
        # Depending on user selections, enable or disable parts of the user interface.
        ...
    def SaveFig(self):
        # Save the current figure to an image file.
        ...
    def SaveTxt(self):
        # Save the processed data set to a text file.
        ...
    def ResetWindow(self):
        # Reset the user interface to its initial appearance.
        ...
```

To add a new experiment type, define a new class. To add a new analysis within an existing experiment, define a new function within the existing class. In each case, the user interface will need to be modified to trigger this new functionality (e.g. add a new entry in

the experiment dropdown menu or a new button in the user interface.)

E.1.3 Setting Up the User Interface

The creation and appearance of the user interface is controlled using the **tkinter** Python package. When an experiment is selected from the splash page, the `__init__` function in each class will set up the initial appearance of the analysis window. All elements on screen are composed of widgets of a given type ([Table E.2](#)) A widget of a given type is first created with given properties, and then positioned on the screen. A widget with the prefix **self** can be referenced by other functions within the class. For example, this may be used to update a label based on experimental data (e.g. reporting the number of data points in the file).

An example of each widget type in the source code can be found in [Table E.2](#).

Table E.2 – An example of the basic widget types used in Flux. This functionality is provided by the **tkinter** Python package. The syntax in this table assumes this package is imported with the alias **tk**.

Widget	Definition	Syntax
Frame	A rectangular region of the window where widgets can be placed	<code>tk.Frame(master)</code>
Label	Simple text box	<code>tk.Label(parentFrame, text="Label text")</code>
Button	Trigger for action	<code>tk.Button(parentFrame, text="Button text", command=self.FunctionName)</code>
Checkbox	Yes/no toggle	<code>tk.Checkbutton(parentFrame, text="Checkbox text?", variable=self.VariableName, command=self.FunctionName)</code>
Entry	Field for user input	<code>tk.Entry(parentFrame,state="enabled")</code>
Canvas	Region where graphics can be constructed	<code>FigureCanvasTkAgg(figure, master=parentFrame)</code>
OptionMenu	Dropdown menu	<code>tk.OptionMenu(parentFrame, variableName, menuChoices)</code>

```

# Notebook composed of tabs
tabs = ttk.Notebook(master)

# Frame which will contain all the widgets for a given tab
frameBase = tk.Frame(tabs)
tabs.add(frameBase, text=" Base ")

# Label which cannot be modified after creation
labelIntro = tk.Label(frameBase,text="Import experimental data to be plotted.") # Set up
label
labelIntro.grid(row=0,column=0,padx=20,pady=5,columnspan=3,sticky="WS") # Position label

# Label which can be modified after creation
self.labelXdim2 = tk.Label(frameBase,text="") # Set up label
self.labelXdim2.grid(row=1,column=4,sticky="W") # Position label

# Button which calls another function within the class when pressed
self.buttonFile = tk.Button(frameBase, text="Select File",command=self.SelectFile) # Set
up button
self.buttonFile.grid(row=1,column=1,sticky="W"+"E",padx=10) # Position button

# Checkbox which allows user to customize an aspect of the data processing
self.statusEdges = tk.IntVar() # Set up integer variable
self.checkEdges = tk.Checkbutton(framePlot, text="Detect edges?", variable=self.
statusEdges, command=self.BoxesSelected) # Set up a checkbox, link status of checkbox
to integer variable
self.checkEdges.var = self.statusEdges # Finish setting up variable
self.checkEdges.grid(row=0,column=0,sticky="E",padx=10,pady=5) # Position checkbox

# Entry field where user can input values
self.entryConc = tk.Entry(frameAnalytics,state="disabled") # Set up entry field,
initially disabled
self.entryConc.grid(row=2,column=3,padx=10,sticky="W") # Position entry field

# Canvas container for a matplotlib figure of data
self.fig = Figure(figsize=(9, 4), dpi=120) # Create figure of given size
self.ax1 = self.fig.add_subplot(121) # Create axis on figure
self.img = self.ax1.pcolormesh(xpos,ypos,currents,cmap=cm.RdYlBu_r) # Plot command
self.canvas = FigureCanvasTkAgg(self.fig, master=self.frameBottom) # Create canvas to
contain figure
self.canvas.get_tk_widget().grid(row=1,column=0,sticky="S") # Position canvas
self.canvas.draw() # Draw canvas on screen

# Dropdown menu to select from predefined list of options
self.colormapVar = tk.StringVar(master) # Create a variable to track choice
self.colormapVar.set('RdYlBu') # Set menu default
colormapChoices = { 'RdYlBu','coolwarm','jet','grayscale'} # Create dictionary with
potential options

```

```
popupColormap = tk.OptionMenu(frameFormatting, self.colormapVar, *colormapChoices) #  
    Create dropdown menu  
popupColormap.grid(row=2,column=1,sticky="W",padx=10) # Position dropdown menu  
self.colormapVar.trace('w', self.change_dropdown) # Trace the current menu selection
```

E.2 Importing Files

With the file selected by the user, the **ImportFile** function in each class will look at the file extension and user-specified manufacturer. If these match one of the predefined import configurations, then the function performs two tasks:

1. The file is parsed and numerical data is extracted.
2. The imported data is converted to a standardized format with consistent shape and units across file types. In the case of an image, three variables are created: two 1D numpy arrays which contain the sampled x/y positions in μm (self.xpos0, self.ypos0), and one 2D numpy matrix which contains the output currents in nA (self.currents0).

E.2.1 HEKA / .asc

In this file format, data is formatted as tab-separated text with currents expressed in the IUPAC convention. Each row corresponds to the current measured at a single point, where the image is built up from a series of consecutive line scans (Sweeps). A header separates individual line scans.

```
Series_4_1
Sweep_4_1_1 6.057607300E+04 16:49:36.073 2018/06/12 16:49:36.073
"Index" "Distance[m]" "Imon-1[A]"
    0    0.000000000E+00 2.904054774E-09
    1    1.000000000E-07 2.903139285E-09
...
    3999 3.999000000E-04 3.696291939E-09
    4000 4.000000000E-04 3.696597028E-09

Sweep_4_1_2 6.062463600E+04 16:50:24.636 2018/06/12 16:49:36.073
"Index" "Distance[m]" "Imon-1[A]"
    0    0.000000000E+00 3.190310016E-09
    1    1.000000000E-07 3.190920417E-09
```

This is imported by reading the file one line at a time, splitting the line into segments when a space or tab is detected. A data type test is then conducted on the first character of the line; if it is a number (numerical data), the line is appended to the data list. If it is a letter (header), the line is discarded. Data is then reshaped into two column vectors containing the x/y sampling positions and a 2D matrix containing the currents.

```
### Import data ###
# Open file
with open(self.filepath, 'r') as fh:
    for curline in fh: # Read file one line at a time
        try:
            curline = curline.split() # Split line where there is a space
            float(curline[0]) # Test if first character of line is a number or letter
            self.data.append(curline) # If the first character is a number (data), this code
                                     # will run and the line will be appended to the end of a list.
        except:
            pass # If the first character is a letter (header), the line will be skipped.
```



```

### Reshape into a common format ###
# Convert list to a matrix of values
self.df = pd.DataFrame(self.data, columns=["PtIndex", "xpos", "Current"], dtype='float')
self.df = self.df.values
# Convert units
self.df[:,1] = self.df[:,1]*1E6 # m --> um
self.df[:,2] = self.df[:,2]*1E9 # A --> nA
# Determine number of x and y points
self.nptsy = self.df[self.df[:,1] == 0]
self.nptsy = len(self.nptsy)
self.nptsx = int(len(self.df)/self.nptsy)
# Set up column vectors that contain list of unique x/y points
self.xpos0 = np.unique(self.df[:,1])
self.ypos0 = np.linspace(np.amin(self.xpos0), np.amax(self.xpos0), self.nptsy)
# Reshape column vector of currents into a 2D xy matrix
self.currents0 = self.df[:,2]
self.currents0 = self.currents0.reshape(self.nptsy, self.nptsx)

```

E.2.2 HEKA / .mat

In this file format, data is formatted as a MATLAB workspace consisting of variables which contain the numerical data and file metadata. Currents are expressed in the IUPAC convention. Variables containing numerical data are formatted as 2-column matrices, where the first column is the x-position and second column is the current.

__globals__	list	[]
__header__	bytes	MATLAB 5.0 MAT-file,...
__version__	str	1.0
Trace_4_1_1	float64	(4001,2)
Trace_4_2_2	float64	(4001,2)
...		

Using **scipy.io**, this is imported as a Python dictionary which contains an entry for each line scan (Trace) and the file metadata. The variables containing the file metadata are discarded. The remaining dictionary is read twice: the first read is used to determine the sampling dimensions of the image and construct an empty matrix, the second read is used to populate the empty matrix with the actual values.

```
### Import data ###
# Open file
matdata = scipy.io.loadmat(self.filepath)
# Delete metadata
del matdata['__header__']
del matdata['__globals__']
del matdata['__version__']
# Determine number of line scans
self.nptsy = len(matdata)
data = []

# Read matdata once to determine dimensions
for entry in matdata:
    trace = matdata[entry]
    self.xpos0 = trace[:,0]
    self.nptsx = len(self.xpos0)

# Construct an empty table with the the correct x/y dimensions
data = np.empty((self.nptsy, self.nptsx), dtype=float)

# Read matdata a second time and fill in the table
count = 0
for entry in matdata:
    trace = matdata[entry]
    data[count,:] = trace[:,1]
    count = count + 1

### Reshape into a common format ###
# Set up column vectors that contain list of unique x/y points
self.xpos0 = self.xpos0*1E6
self.ypos0 = np.linspace(np.amin(self.xpos0),np.amax(self.xpos0), self.nptsy)

# Convert units of current
self.currents0 = data*1E9
```

E.2.3 Biologic / .txt

In this file format, data is formatted as tab-separated text with currents expressed in the IUPAC convention. The data is given in two equivalent forms: an X-Y table (2D matrix) and Point Cloud (3 column vectors).

```

SECM Probe
X Axis: X-Position (micrometers)
Y Axis: Y-Position (micrometers)
Amplitude Axis: Probe Output (Amps)

Current Convention: European
Map Bias: 6.50000e-001V
Recorded by Potentiostat ID: 1

X-Y Table:
0 60 120 180 240 300 360 420 480 540 600 660 720 780 840 900 960
 1020 1080 1140 1200 1260 1320 1380 1440 1500
1.21243e-008 1.13949e-008 1.15797e-008 1.17744e-008 1.19950e-008 1.18596e-008 1.20026e
-008 1.23483e-008 1.60907e-008 1.86517e-008 1.87944e-008 1.88492e-008 1.88906e-008
 1.88725e-008 1.89481e-008 1.90003e-008 1.90166e-008 ...

Point Cloud:
X Y Z
0 750 1.21243e-008
60 750 1.13949e-008
...
1440 750 1.91948e-008
1500 750 1.92197e-008
0 690 1.22071e-008
60 690 1.15596e-008

```

This data is imported using a similar approach to the HEKA/.asc file type where the file is read one line at a time, with each line split into segments when a space or tab is detected. The only significant difference is that the line 'X Y Z' (immediately preceding the Point Cloud data table) is used as a trigger for when to begin storing the data.

```
### Import data ###
# Open file
with open(self.filepath, 'r') as fh: # Read file one line at a time
    for curline in fh:
        try:
            curline = curline.split() # Split line if there is a space
            if curline == ['X', 'Y', 'Z']: # Test if this is the critical line
                datastart = 1
            if datastart == 1: # If past the critical line, begin storing data
                float(curline[0]) # Check if line contains strings or numbers
                self.data.append(curline) # If number, add to dataframe
        except:
            pass # If string, skip to next line

### Reshape into a common format ###
# Convert list into a matrix of values
self.df = pd.DataFrame(self.data, dtype='float')
self.df = self.df.values
# Convert units
self.df[:, 2] = self.df[:, 2] * 1E9 # A --> nA
# Determine number of x and y points
self.nptsx = self.df[self.df[:, 0] == 0]
self.nptsx = len(self.nptsx)
self.nptsy = int(len(self.df) / self.nptsx)
# Set up column vectors that contain list of unique x/y points, set the origin as (0,0)
self.xpos0 = np.unique(self.df[:, 0])
self.xpos0 = self.xpos0 - np.amin(self.xpos0)
self.ypos0 = np.unique(self.df[:, 1])
self.ypos0 = self.ypos0 - np.amin(self.ypos0)
# Reshape column vector of currents into a 2D xy matrix
self.currents0 = self.df[:, 2]
self.currents0 = self.currents0.reshape(self.nptsy, self.nptsx)
```

E.2.4 CH Instruments / .txt

In this file format, data is formatted as comma-separated text with currents expressed in the polarographic convention. Each row corresponds to the current measured at a single point. Data is reported continuously, with no visual break between line scans.

```
Data Source: Experiment
Instrument Model: CHI920D
Header: 80 um Pt disk array with 10 um tip
Note:

Probe E (V) = 0.5
Sensitivity (A/V) = 1e-9
X Distance (um) = 250
Y Distance (um) = 250
Incr. Dist. (um) = 2.5
Incr. Time (s) = 0.0333
Long Move = X
Max Incr (um) = 0.5
Quiet Time (sec) = 20

X/um, Y/um, Current/A

0.0000, 0.0000, -7.0668932e-10
2.5000, 0.0000, -7.1113349e-10
...
245.0000, 0.0000, -1.0609460e-9
247.5000, 0.0000, -1.0678839e-9
0.0000, 2.5000, -8.2387447e-10
2.5000, 2.5000, -8.1248280e-10
```

This data is imported using a similar approach to the Biologic/.txt file where the file is read one line at a time, with each line split into segments on a comma. The line 'X/um, Y/um, Current/A' is used as a trigger for when to begin storing the data.

```
### Import data ###
# Open file #
with open(self.filepath, 'r') as fh:
    for curline in fh: # Read file one line at a time
        try:
            curline = curline.split(',') # Split line where there is a comma
            if curline == ['X/um', ' Y/um', ' Current/A\n']: # Test if this is the critical
                line
                datastart = 1
            if datastart == 1: # If past the critical line, begin storing data
                float(curline[0]) # Check if line contains strings or numbers
                self.data.append(curline) # If number, append to list
        except:
            pass # If string, skip to next line

### Reshape into a common format ####
# Convert list into a matrix of values
self.df = pd.DataFrame(self.data, dtype='float')
self.df = self.df.values
# Convert units
self.df[:,2] = self.df[:,2]*1E9 # A --> nA
# Determine number of x and y points
self.nptsx = self.df[self.df[:,0] == 0]
self.nptsx = len(self.nptsx)
self.nptsy = int(len(self.df)/self.nptsx)
# Set up column vectors that contain list of unique x/y positions, set the origin as
(0,0)
self.xpos0 = np.unique(self.df[:,0])
self.xpos0 = self.xpos0 - np.amin(self.xpos0)
self.ypos0 = np.unique(self.df[:,1])
self.ypos0 = self.ypos0 - np.amin(self.ypos0)
# Reshape column vector of currents into a 2D xy matrix
self.currents0 = self.df[:,2]
self.currents0 = self.currents0.reshape(self.nptsy, self.nptsx)
self.currents0 = self.currents0*(-1) # Polarographic --> IUPAC convention
```

E.2.5 Sensolytics / .dat

In this file format, data is formatted as comma-separated text with currents expressed in the IUPAC convention. Each row corresponds to the current measured at a single point. An empty line separates points from different line scans.

```
# Sensolytics: 1.2
# Channels:1
# Channel 1 Name: WE(1).Current
# Channel 1 Code: 101
# Channel 1 Unit: nA
# Rows: 140
# Lines: 140
# ArrayScan
...
# X [um], X rel. [um],Y [um],Y rel. [um], Z [um], Z rel. [um], Channel 1, Channel 2,...
50005.500,0.000,50712.620,0.000,49626.142,0.000,2.499,
50015.500,10.000,50712.620,0.000,49626.120,-0.021,2.390,
...
51395.500,1390.000,50712.620,0.000,49623.163,-2.979,2.222,
51405.500,1400.000,50712.620,0.000,49623.142,-3.000,2.237,

50005.500,0.000,50722.620,10.000,49626.120,-0.022,2.106,
50015.500,10.000,50722.620,10.000,49626.098,-0.043,2.121,
```

This data is imported using a similar approach to the Biologic/.txt file where the file is read one line at a time, with each line split into segments on a comma. Data files are assumed to have 23 header lines.

```

### Import data ###
# Open file #
with open(self.filepath,'r') as fh:
    for curline in fh: # Read file one line at a time
        index = index + 1 # Keep track of the line number
        if index <=23: # If the line number is less than or equal to 23, add to header list.
            try:
                curline = curline.split(',')
                header.append(curline)
            except:
                pass
        if index > 23: # If the line number is greater than 23, add to data list.
            try:
                curline = curline.split(',')
                float(curline[0])
                self.data.append(curline)
            except:
                pass
    fh.close()

### Reshape into a common format ###
# Convert list into a matrix of values, remove empty channel
self.df = pd.DataFrame(self.data, columns=['X','Xrel','Y','Yrel','Z','Zrel','Ch1','Ch2'],
                        dtype=float)
del self.df['Ch2']
self.df = self.df.values
# Determine number of x and y points from header
self.nptsx = int(header[5][1].strip(' \n')) + 1
self.nptsy = int(header[6][1].strip(' \n')) + 1
# Set of column vectors than contain list of unique x/y positions
self.xpos0 = np.unique(self.df[:,1])
self.ypos0 = np.unique(self.df[:,3])
# Reshape column vector of currents into a 2D xy matrix
self.currents0 = self.df[:,6]
self.currents0 = self.currents0.reshape(self.nptsy,self.nptsx)

```


E.3 Analysing the Data

This section will outline how the data analysis tasks described in the manuscript are implemented in the code.

E.3.1 Normalization

Within the **ReshapeData** function of all classes, an if statement will be run to determine whether the currents should be normalized, and what steady state current should be used for this normalization. This corresponds to the state of the binary variables **self.checkNormalize** and **self.checkNormalizeExp**. Depending on these values, one of three steady state currents will be used: 1 (no change), an experimental steady state (user entry for iss used directly), or a theoretical steady state (calculated from user entries for experimental parameters assuming a disk microelectrode.)

```
# Case 1: No normalization is requested
if self.checkNormalize.var.get() == 0:
    self.iss = 1 # Use a steady state current of 1 (values unchanged)

# Case 2: Normalization to experimental steady state current
elif self.checkNormalize.var.get() == 1 and self.checkNormalizeExp.var.get() == 1:
    self.iss = float(self.entryIssExp.get()) # Evaluate user entry for experimental iss

# Case 3: Normalization to theoretical steady state current
elif self.checkNormalize.var.get() == 1 and self.checkNormalizeExp.var.get() == 0:
    beta = 1+ (0.23/((((float(self.entryRg.get()))**3) - 0.81)**0.36)) # Calculate beta
    factor based on user-input Rg
    self.iss = 4*1E9*96485*beta*(float(self.entryDiff.get()))*((float(self.entryRadius.get())
    ())/1E6)*(float(self.entryConc.get())) # Calculate theoretical iss based on beta
    and other user-input experimental parameters
    self.labelTheoIssValue.config(text="{0:.3f}".format(self.iss)) # Update user interface
    to report calculated theoretical iss

# Divide all currents by the iss determined by the above if statements.
self.currents = np.divide(self.currents,self.iss)
```

E.3.2 Tip-Substrate Distance Calibration

Within the **ReshapeData** function of the **PACApp** class, an if statement will be run which checks the current state of the dropdown menu for how tip-substrate distances should be calibrated. This corresponds to the state of the text variable **self.zerodVar**.

```
### Preliminary processing ###
# Remove any points without numerical data
critrow = np.amin(np.where(np.isnan(self.currents) == False))
self.distances = self.distances[critrow:]
self.currents = self.currents[critrow:]

### Calibrate distances based on selection in dropdown menu ###
# Case 0: If no calibration is selected, no further processing will be performed.

# Case 1: Further calibration is requested.
if self.zerodVar.get() != 'No calibration':
    self.distances = self.distances - np.amin(self.distances) # Correct to min

# Case 1a: The first point with data is set to d = 0
if self.zerodVar.get() == 'First point with data':
    # Report how many points are left
    self.labelNpts4.config(text=len(self.distances))

# Case 1b: The peak in the first derivative is set to d = 0
elif self.zerodVar.get() == "First derivative analysis":
    # Perform a derivative analysis, take location of peak to be zero
    currentsderiv = abs(np.gradient(self.currents))
    maxderiv = np.where(currentsderiv == np.amax(currentsderiv))
    maxderiv = int(maxderiv[0])

    # Remove any points prior to the peak in the derivative. These are attributed to the
    # electrode bending upon surface contact ("negative" tip-substrate distance.)
    self.distances = self.distances[maxderiv:]
    self.currents = self.currents[maxderiv:]
```

E.3.3 Fitting R_g , κ

Within the **ReshapeData** function of the **PACApp** class, an if statement will be run which checks whether or not the normalized approach curve should be fit to extract ei-

ther R_g or κ . This corresponds to the state of the binary variables `self.checkFitRg` and `self.checkFitKappa`. If one of these is enabled, the normalized currents and distances are passed to a separate fit function (`self.negfbfit` or `self.kappafit`) within the class which contains the corresponding analytical approximation. A nonlinear curve fit is then performed using `scipy.optimize.curve_fit`. The code for fitting R_g is shown below.

```
def ReshapeData(self):
    ...
    ### Initial check for whether the data should be fit to extract Rg ###
    if self.checkFitRg.var.get() == 1:
        # The analytical approximations are only valid for L > 0.1; remove any points that
        # do not meet this criteria.
        critrow = np.amin(np.where(self.distancesnorm >= 0.1))
        self.distancesnorm = self.distancesnorm[critrow:]
        self.currentsnorm = self.currentsnorm[critrow:]

        ### If the check is passed, perform a curve fit ###
        try:
            self.estRg = scipy.optimize.curve_fit(self.negfbfit, self.distancesnorm, self.
                currentsnorm) # The curve fitting function will return the best fit Rg for the
                xdata (normalized distances) and ydata (normalized currents) against the fit
                function (analytical approximation for negative feedback.)
            self.estRg = float(self.estRg[0]) # Extract only the estimated Rg from all fit
                statistics
            self.labelEstRg2.config(text="{0:.3f}".format(self.estRg)) # Report the estimated
                Rg in the user interface
        except:
            self.labelEstRg2.config(text="Err") # Catch any errors from a failed fit function
        ...

    ### This function contains the analytical approximation for negative feedback. ###
    def negfbfit(self, distancesnorm, Rg):
        Lvalues = self.distancesnorm # Function input

        # Build up the analytical approximation
        currentsins_pt1 = ((2.08/(Rg**0.358))*(Lvalues - (0.145/Rg))) + 1.585
        currentsins_pt2 = (2.08/(Rg**0.358)*(Lvalues + (0.0023*Rg))) + 1.57
        currentsins_pt3 = (np.log(Rg)/Lvalues) + (2/(np.pi*Rg)*(np.log(1+(np.pi*Rg)/(2*Lvalues
            ))))
        currentsins = currentsins_pt1/(currentsins_pt2 + currentsins_pt3)

        return currentsins # Function output
```

E.3.4 Slope Correction

Within the **ReshapeData** function of the **ImageApp** class, an if statement will be run which checks whether or not x or y slope correction should be performed. This corresponds to the state of the text variables **self.slopeXVar** and **self.slopeYVar**. If one of these is requested, a straight line will be fit to the requested line to determine the slope. A correction term will then be applied to the original currents which takes into account the slope (**xslope0**) and the distance from the origin (**self.xpos[i] - self.xpos[0]**), which scales the amount of correction as necessary.

```
# Case 1: No slope correction is requested
if self.slopeXVar.get() == 'None':
    pass # Do nothing

# Case 2: Slope correction against the line Y = 0 is requested
elif self.slopeXVar.get() == 'Y = 0':
    xslope0 = np.polyfit(self.xpos,self.currents[0,:],1) # Fit a straight line, return the
    slope
    for i in range(0,(self.currents.shape[1])):
        self.currents[:,i] = self.currents0[:,i] - xslope0[0]*(self.xpos[i] - self.xpos[0])
        # Correct currents line by line

# Case 3: Slope correction against the line Y = Max is requested
elif self.slopeXVar.get() == 'Y = Max':
    xslopemax = np.polyfit(self.xpos,self.currents0[-1,:],1) # Fit a straight line, return
    the slope
    for i in range(0,(self.currents0.shape[1])):
        self.currents[:,i] = self.currents0[:,i] - xslopemax[0]*(self.xpos[i] - self.xpos
        [0]) # Correct currents line by line
```

E.3.5 Edge Detection

Within the **ReshapeData** function of the **ImageApp** class, an if statement will be run which checks whether or not edge detection should be performed. This corresponds to the state of the binary variable **self.checkEdges**. If edge detection is requested, the script first

does some pre-processing to put the data in a suitable form, and then applies the Canny algorithm (`scikit-image.feature.canny.`)

The Canny algorithm requires an even sampling interval in the x and y directions ("square pixels"). If this is not present, the script uses `griddata` to linearly interpolate the data. This requires reshaping the data from its initial form of two 1D position variables (`self.xpos`, `self.ypos`) and one 2D current matrix (`self.currents`) into a 3-column matrix (x,y,z). The data is then normalized to a 0-1 scale, and the Canny edge detection algorithm is applied on this evenly spaced, normalized image.

```
if self.checkEdges.var.get() == 1: # Runs if edge detection requested

    ### Step 1: Pre-processing / setup for edge detection algorithm ###

    ## 1a: Reshape data into 3 column vectors (x,y,z) ##

    # This step will construct the 'z' column of the matrix by reshaping the xy matrix of
    # currents into a single column.
    self.df = np.reshape(self.currents, (self.nptsx*self.nptsy))

    # This step will construct the 'y' column of the 3-column matrix. This is done using a
    # temporary calculation column modcol.
    ypos_int = np.amax(self.xpos)/((self.nptsy)-1) # Calculate y sampling interval as maxy
    /nptsy (note: due to earlier standardization procedures, miny = 0)
    self.dfycol = np.linspace(0,((self.nptsx*self.nptsy)-1),(self.nptsx*self.nptsy))
    # Create column vector with NxM total points;this will be updated in a later step
    # Ex: (0,1,2,...4001,4002,...)
    modcol = np.remainder(self.dfycol,self.nptsx)
    # Calculate remainder when integer is divided by number of points in a row
    # Ex: (0,1,2,...4001,4002,...) --> (0,1,2,...0,1,2)
    for i in range(0,len(modcol)):
        if modcol[i] == 0:
            self.dfycol[i] = self.dfycol[i] + 1
            # If the remainder is 0, make it 1 to make sure it is assigned to the correct
            # row.
            # Ex: (0,1,2,...0,1,2) --> (1,1,2,...1,1,2)
    self.dfycol = ypos_int*(np.floor(np.divide(self.dfycol,self.nptsx)))
    # First calculate integer index for y-position using floor, then convert to y-
    # position by multiplying by the previously calculated y-sampling interval
    # Ex: Divide (1,1,2,...) --> (0, 0.02, 0.04,...1,1.02,1.04)
    # Ex: Floor (0, 0.02, 0.04,...1,1.02,1.04) --> (0,0,0,...1,1,1)
    # Ex: Multiply by ypos_int (0,0,0,...1,1,1) ---> (0,0,0,...20,20,20)
```

```

    # This step will construct the 'x' column of the 3-column matrix by repeating the
    # unique x-values as many times as necessary.
    self.df = np.vstack((numpy.matlib.repmat(self.xpos,1,self.nptsy), self.df))

    # This combines the three assembled vectors, and transposes them so they are columns.
    self.df = np.vstack((self.dfycol,self.df))
    self.df = self.df.T

    ## 1b: Make sure x and y sampling intervals are equivalent (square pixels) ##
    try:
        try:
            if self.nptsx != self.nptsy: # This is true if the sampling intervals are UNEQUAL
                xpos_interp = np.linspace(np.amin(self.xpos), np.amax(self.xpos), np.amax(self.
                    xpos)+1)
                ypos_interp = xpos_interp
            else: # This is true is the sampling intervals are EQUAL
                xpos_interp = self.xpos
                ypos_interp = xpos_interp
            xpos_unigrid, ypos_unigrid = np.meshgrid(xpos_interp, ypos_interp)

            ## 1c: If needed, interpolate data ##
            currents_interp = griddata((self.df[:,1],self.df[:,0]),self.df[:,2],(xpos_unigrid,
                ypos_unigrid),method='cubic')
        except:
            print("Error interpolating data to uniform grid.")

        ### Step 2: Perform the edge detection ###
        currents_norm = (currents_interp - np.amin(currents_interp))/(np.amax(currents_interp)
            - np.amin(currents_interp))
        # Normalize currents to a 0 --> 1 scale (needed for this implementation of the
        # algorithm)
        self.currents_edges = feature.canny(currents_norm)
        # Apply the Canny algorithm. This returns a binary image with the original
        # dimensions, where 0 = no edge and 1 = edge.

    else: # Runs if no edge detection requested
        pass

```

E.3.6 Formal Potential

Within the **ReshapeData** function of the **CVApp** class, a formal potential may be calculated from the first cycle of an experimental cyclic voltammogram. This will be reported depending on the state of the binary variable **self.checkStdPot**. If this is requested, the

derivative of the current with respect to index will first be calculated using **numpy.gradient**. The potential associated with the maximum (forward sweep) and minimum (reverse sweep) value of this derivative will be evaluated, and these two potentials will be averaged to estimate the formal potential.

```
# Calculate derivative of current for first cycle (index 0)
current_deriv = np.gradient(self.currents_reshape[0,:])

# Find potential where current derivative is at a maximum
check_max = current_deriv == np.amax(current_deriv) # Find max value
max_index = np.where(check_max == True) # Find index associated with max value
max_index = int(max_index[0])
pot_max = self.potential[max_index] # Convert index to potential

# Find potential where current derivative is at a minimum
check_min = current_deriv == np.amin(current_deriv) # Find min value
min_index = np.where(check_min == True) # Find index associated with min values
min_index = int(min_index[0])
pot_min = self.potential[min_index] # Convert index to potential

# Average the two previously determined potentials
self.avg_pot = np.mean([pot_max,pot_min])

# If the user requests a formal potential, update the label in the user interface
if self.checkStdPot.var.get() == 1:
    self.StdPot2.config(text="{0:.3f}".format(self.avg_pot))
else:
    pass
```

E.3.7 Response Time

Within the **ReshapeData** function of the **CAApp** class, a response time may be calculated. This will be reported depending on the state of the binary variable **self.checkResponsetime**. If this is requested, then two points will be established: the steady state current (**self.expiss**, evaluated as the average of the last 20 points in the data set) and the critical current (**crit-value**, calculated as 110% of the steady state value (90% of change has occurred). The absolute values of the current will be searched in reverse order (**numpy.flip**) for the first

current value where the current is below the critical threshold, which will be reported as the response time.

```
def ImportFile(self):
    ...
    self.expiss = np.mean(df[-20:-1,2])
    # Establish experimental iss from last points in set
    ...

def ReshapeData(self):
    ...
    critvalue = abs(1.1*self.expiss) # Establish critical current

    # Procedure: Search trace from end to find the first point where the current is 110%
    # iss
    if self.expiss < 0: # This will run if the experimental iss is a reductive current
        rtcurrent = np.flip(np.absolute(self.currents))
    elif self.expiss > 0: # This will run if the experimental iss is an oxidative current
        rtcurrent = np.flip(self.currents)
    else: # Catch any errors
        print('Error in detecting iss. Cannot calculate response time.')

    modcol = rtcurrent > critvalue # Compare all currents to critical value
    critpt = np.amin(np.where(modcol == True)) # Look for index of first point where
    # threshold is crossed
    self.crittime = self.time[-critpt] # Convert index to time

    # Report calculated response time if requested
    if self.checkResponsetime.var.get() == 1:
        self.labelResponsetime.config(text="{0:.3f}".format(self.crittime))
    else:
        pass
    ...
```




Demystifying Mathematical Modeling of Electrochemical Systems



Author: Lisa I. Stephens, Janine Mauzeroll

Publication: Journal of Chemical Education

Publisher: American Chemical Society

Date: Oct 1, 2019

Copyright © 2019, American Chemical Society

Quick Price Estimate

This service provides permission for reuse only. If you do not have a copy of the article you are using, you may copy and paste the content and reuse according to the terms of your agreement. Please be advised that obtaining the content you license is a separate transaction not involving Rightslink.

Permission for this particular request is granted for print and electronic formats, and translations, at no charge. Figures and tables may be modified. Appropriate credit should be given. Please print this page for your records and provide a copy to your publisher. Requests for up to 4 figures require only this record. Five or more figures will generate a printout of additional terms and conditions. Appropriate credit should read: "Reprinted with permission from {COMPLETE REFERENCE CITATION}. Copyright {YEAR} American Chemical Society." Insert appropriate information in place of the capitalized words.

I would like to... ?

reuse in a Thesis/Dissertation ▼

Will you be translating? ?

No ▼

Requestor Type ?

Author (original work) ▼

Select your currency

CAD - \$ ▼

Portion ?

Full article ▼

Quick Price

Click Quick Price

Format ?

Print and Electronic ▼

QUICK PRICE

CONTINUE

To request permission for a type of use not listed, please contact [the publisher](#) directly.

ECS Copyright and Permissions

NOTICE: Beginning Monday, April 10, 2017, ECS has partnered with the Copyright Clearance Center (CCC) in order to manage permission requests.

- This service will allow authors to immediately receive permission, and will eliminate the need to complete ECS's permission request form.
- As of Monday, April 10, 2017, ECS will no longer accept permission request forms through email. All future requests must be made through CCC.
- Please note that there may be fees involved, depending on the type of material and reuse requested.
- **As has always been ECS's policy, authors are NOT required to request permission to reproduce their own figures or tables.**

Before requesting permission, please confirm the open access status of the article. **ECS does not hold the copyright on the open access articles published in its journals.** Please follow reuse instructions given by Creative Commons for its various licenses.

Guidelines for Use of ECS Material

- [Author Reuse Rights and Self-Archiving Policy](#)
- [Reusing Open Access Articles](#)
- [How to Ask for Permission](#)
- [Permission to Reproduce Full Articles](#)

Author Reuse Rights and Self-Archiving Policy

Before using ECS material or requesting to reproduce ECS material, please see the [ECS Transfer of Copyright Form](#) for the rights retained by authors and employers. **For example, authors may use their own tables and figures** in other scholarly research papers that they write, without writing to ECS for permission. Full credit to the original source should be given, for example:

Reproduced with permission from *J. Electrochem. Soc.*, 150, H205 (2003). Copyright 2003, The Electrochemical Society.

Permission is not needed if figures and/or tables from one ECS publication will be reused in another forthcoming ECS publication.

[Learn more about copyright and fair use.](#)

Authors may deposit the pre-print and/or published versions of their articles in their institutional repository, with no embargo, provided that the files prepared by and/or formatted by ECS (and its vendors) are not used for that purpose. Any posting made or updated after the acceptance of the article for publication should include a link to the online abstract in the ECS publication of origin or to the entry page of that publication.

If authors choose to make their articles open access through Author Choice Open Access, the Version of Record (VoR) will be immediately freely available in our digital library. Authors may also deposit the published PDF of these open access articles in their institutional repositories, if they wish.

Reusing Open Access Articles

ECS does not hold the copyright on the open access articles published in its journals. The copyright is held by the author(s). Please follow reuse instructions given by Creative Commons for its various licenses. ECS articles are published using either CC BY or CC BY-NC-ND licenses.

[CC BY](#)

[CC BY-NC-ND](#)

[Best Practices for Citing CC Licensed Articles](#)

How to Ask for Permission

Use one of the links below for the specific ECS title from which permission is requested:

[*Journal of The Electrochemical Society*](#)

[*ECS Journal of Solid State Science and Technology*](#)

[*ECS Transactions*](#)

[*Electrochemical and Solid-State Letters*](#)

ECS Electrochemistry Letters***ECS Solid State Letters******The Electrochemical Society Interface******ECS Meeting Abstracts***

- **PERMISSION IS NOT REQUIRED** to reuse your own content (i.e. reusing figures and/or tables from a paper you are an author on). Full credit to the original source should be given.
- **PERMISSION IS NOT REQUIRED** if figures and/or tables from one ECS publication will be reused in another forthcoming ECS publication.

Please click the button above and search for the ECS publication from which you wish to reuse content. You may search by the publication title (i.e. *Journal of The Electrochemical Society* or *ECS Transactions*), or the ISSN located in the lower right-hand corner of that publication's digital library page.

A fee may be assessed, depending on the use to which the reproduced material is put.

If permission is granted, the appropriate copyright credit line must be posted along with the ECS material; use of the material should not imply any endorsement by The Electrochemical Society.

You must print the ECS copyright credit line on the first page of the article or book chapter. For figures and tables, the credit may appear with the figure, in a footnote, or in the reference list. **For figures, tables, and journal articles, the standard credit line is:**

Reprinted with permission from [reference citation]. Copyright [year], The Electrochemical Society. [Example: Reprinted with permission from *J. Electrochem. Soc.*, 150, H205 (2003). Copyright 2003, The Electrochemical Society.]

Permission to Reproduce Full Articles

Reprographic copying of any article for internal or personal use beyond that permitted by ECS or by the fair use provisions of the Copyright Act of 1976 is granted to libraries and other users registered with the [Copyright Clearance Center](#), provided that any fees are paid directly to the Copyright Clearance Center, 222 Rosewood Drive, Danvers, MA 01923, USA; tel.: 1.978.750.8400; fax 978.750.4744; e-mail: info@copyright.com.

For additional assistance, please contact Copyright@electrochem.org.

[back to top](#)



RightsLink®

[Home](#)
[Account Info](#)
[Help](#)


ACS Publications
Most Trusted. Most Cited. Most Read.

Title:

Altered Spatial Resolution of Scanning Electrochemical Microscopy Induced by Multifunctional Dual-Barrel Microelectrodes

Logged in as:

Lisa Stephens

Account #:

3000992170

[LOGOUT](#)
Author:

Lisa I. Stephens, Janine Mauzeroll

Publication: Analytical Chemistry

Publisher: American Chemical Society

Date: Jun 1, 2018

Copyright © 2018, American Chemical Society

Quick Price Estimate

Permission for this particular request is granted for print and electronic formats, and translations, at no charge. Figures and tables may be modified. Appropriate credit should be given. Please print this page for your records and provide a copy to your publisher. Requests for up to 4 figures require only this record. Five or more figures will generate a printout of additional terms and conditions. Appropriate credit should read: "Reprinted with permission from {COMPLETE REFERENCE CITATION}. Copyright {YEAR} American Chemical Society." Insert appropriate information in place of the capitalized words.

I would like to...

reuse in a Thesis/Dissertation ▼

Requestor Type

Author (original work) ▼

Portion

Full article ▼

Format

Print and Electronic ▼

Will you be translating?

No ▼

Select your currency

CAD - \$ ▼

Quick Price

Click Quick Price

This service provides permission for reuse only. If you do not have a copy of the article you are using, you may copy and paste the content and reuse according to the terms of your agreement. Please be advised that obtaining the content you license is a separate transaction not involving Rightslink.

[QUICK PRICE](#)
[CONTINUE](#)

To request permission for a type of use not listed, please contact [the publisher](#) directly.

Copyright © 2019 [Copyright Clearance Center, Inc.](#) All Rights Reserved. [Privacy statement](#). [Terms and Conditions](#).
Comments? We would like to hear from you. E-mail us at customercare@copyright.com



RightsLink®

[Home](#)
[Account Info](#)
[Help](#)


ACS Publications
Most Trusted. Most Cited. Most Read.

Title:

Evaluating the Use of Edge Detection in Extracting Feature Size from Scanning Electrochemical Microscopy Images

Logged in as:

Lisa Stephens

Account #:

3000992170

[LOGOUT](#)

Author:

Lisa I. Stephens, Nicholas A. Payne, Sebastian A. Skaanvik, et al

Publication: Analytical Chemistry

Publisher: American Chemical Society

Date: Mar 1, 2019

Copyright © 2019, American Chemical Society

Quick Price Estimate

Permission for this particular request is granted for print and electronic formats, and translations, at no charge. Figures and tables may be modified. Appropriate credit should be given. Please print this page for your records and provide a copy to your publisher. Requests for up to 4 figures require only this record. Five or more figures will generate a printout of additional terms and conditions. Appropriate credit should read: "Reprinted with permission from {COMPLETE REFERENCE CITATION}. Copyright {YEAR} American Chemical Society." Insert appropriate information in place of the capitalized words.

I would like to... ?

reuse in a Thesis/Dissertation ▼

Requestor Type ?

Author (original work) ▼

Portion ?

Full article ▼

Format ?

Print and Electronic ▼

Will you be translating? ?

No ▼

Select your currency

CAD - \$ ▼

Quick Price

Click Quick Price

This service provides permission for reuse only. If you do not have a copy of the article you are using, you may copy and paste the content and reuse according to the terms of your agreement. Please be advised that obtaining the content you license is a separate transaction not involving Rightslink.

[QUICK PRICE](#)

[CONTINUE](#)

To request permission for a type of use not listed, please contact [the publisher](#) directly.

Copyright © 2019 [Copyright Clearance Center, Inc.](#) All Rights Reserved. [Privacy statement](#). [Terms and Conditions](#).
Comments? We would like to hear from you. E-mail us at customercare@copyright.com